DEVELOPMENT OF A MICROFABRICATED SILICON MOTOR-DRIVEN COMPRESSION SYSTEM

by

LUC G. FRÉCHETTE

B. Ing. Génie Méchanique, École Polytechnique de Montréal, 1994
S.M. Aeronautics and Astronautics, Massachusetts Institute of Technology, 1997

Submitted to the Department of Aeronautics and Astronautics
in partial fulfillment of the requirements for the degree of

DOCTOR OF PHILOSOPHY
at the
MASSACHUSETTS INSTITUTE OF TECHNOLOGY
September 2000

Author

Department of Aeronautics and Astronautics
August 14, 2000

Certified by

Professor Alan H. Epstein
R. C. Maclaurin Professor of Aeronautics and Astronautics, Committee Chairman

Certified by

Professor Jack L. Kerrebrock
Professor of Aeronautics and Astronautics

Certified by

Professor Mark S. Spearing
Esther and Harold E. Edgerton Associate Professor of Aeronautics and Astronautics

Certified by

Professor Martin A. Schmidt
Professor of Electrical Engineering and Computer Science

Accepted by

Professor Nesbitt W. Hagood, IV
Associate Professor of Aeronautics and Astronautics
Chairman, Department Graduate Committee

DEVELOPMENT OF A MICROFABRICATED SILICON MOTOR-DRIVEN COMPRESSION SYSTEM

by

LUC G. FRÉCHETTE

ABSTRACT

This thesis presents the design, fabrication, development, and test of the first microfabricated motor-driven compression system that integrates high speed rotating components for electrical-to-fluidic power conversion. This power MEMS device consists of a centrifugal compressor supported on gas-lubricated bearings and driven by an electrostatic induction micromotor, integrated on a 1.5 cm silicon chip through thin film processing, deep reactive ion etching, and wafer fusion bonding.

The development approach consisted of first building all-silicon devices to experimentally study the gas-lubricated bearings, and then integrating the thin film electrical components in the silicon structure to develop the micromotor and demonstrate the integrated system. The all-silicon devices consisted of a 4.2 mm diameter single crystal silicon microturbine rotor enclosed in a bonded stack of five deep reactive ion etched wafers. They were used to define a stable operating protocol for the low aspect ratio hydrostatic journal bearing, which is new to this type of device. The protocol allowed the rotation of a turbine-driven microrotor up to 1.4 million revolutions per minute (300 m/s peripheral speed).

The motor-driven devices were then built and tested to assess the micromotor and system operation. The electrical components were fabricated using thin and thick (10 μm) film processing, and integrated with the micromachined structures in a bonded five wafer stack. Testing of these devices demonstrated typical operation of the electrostatic induction motor, with a peak torque at a given frequency (5 MHz) and a quadratic dependence on applied voltage. The maximum speed achieved was 15,000 revolutions per minute (3 m/s peripheral speed), corresponding to a motor torque of 0.3 μNm and a shaft power of 0.5 mW. Operation was limited to 100V amplitude, beyond which breakdown occurred in the motor. The viscous drag on a bladeless rotor was measured using a transient spindown technique, inferring a peak electrostatic induction torque level of 65 $\mu Nm/kV^2$, which is one third the predicted value for the fabricated device. The cause for this discrepancy has not yet been determined.

This work opens the road for a new type of compact, potentially low-cost, high power density compression system, for applications such as air circulation through portable analytical instruments, pressurization of portable power generation devices, and cooling of electronics, sensors, or people.

Thesis Supervisor: Professor Alan H. Epstein
Title: R. C. Maclaurin Professor of Aeronautics and Astronautics

ACKNOWLEDGMENTS

My graduate experience and the results of this research would not be what they are without the contributions of many. I first extend my gratitude to Professor Alan Epstein, for proposing the concept pursued herein, for giving me the opportunity to live a unique graduate experience, and for mentoring me throughout. I also wish to thank Professors Jeffrey Lang and Martin Schmidt for sharing their knowledge and insightful suggestions, and Professors Jack Kerrebrock and Mark Spearing for providing valuable guidance.

I have also had the privilege to work with an exceptional group of researchers and students part of the MIT Microengine team, whom I would like to thank. In particular, I am grateful to Dr Stuart Jacobson for his design work, bearing testing, and numerous discussions. I am also greatful to Professor Reza Ghodssi, Dr Xin Zhang, Dr Arturo Ayon, Dr Ravi Khanna and others on the fabrication team for their help and insight in microfabrication; Steve Nagle and Dr Steve Umans for teaching me about electromechanics theory and providing invaluable help with the electrical testing; Dr C.C. Lin, Chee Wei Wong, Dr Fred Ehrich, Professor Kenny Breuer, and Dr Carol Livermore for help in bearing testing and with the experimental apparatus; Paul Warren, Jimmy Letendre, Viktor Dubrowski, and Bill Ames for the countless hardware components, so necessary for testing; as well as Lory, for her smile and for keeping us well fed. I am also greatful to Dr Vicky Diadiuk and the Microsystems Technolgy Laboratories (MTL) staff, namely Kurt Broedrik, Joe Walsh, and Bernard Alamariu for their hands-on help and guidance. The microfabricated devices presented herein were developped and fabricated in the MTL facilities.

My experience at MIT would not have been has much fun without the friendship of Amit, Adam, Zolti, Rory, Spad, and Erik. Thanks guys. Finally, I wish to thank my parents, my brothers, and my wife Elise for their unconditional love, encouragement, and support througout this journey. Sincerely, Luc.

This research was supported by DARPA (DAAG55-98-1-0365, DABT63-C-0004) under Dr. R. Nowarck and Dr. J. McMichaels, respectively, and by the Army Research Office (DAAH04-95-1-0093) under Dr. R. Paur. Support from the Fonds pour la Formation de Chercheurs et l'Aide á la Recherche is also appreciated.

CONTENTS

LIST OF FIGURES

LIST OF TABLES

NOMENCLATURE

Roman

C	capacitance (pF)
C_p	specific heat at constant pressure (J/kg K)
dc	electrode duty-cycle, ratio of electrode area to total area
f	force per unit area, Pa (force per unit radius in App. A)
k	wave number, such that wavelength = $2\pi/k$
g	motor gap (m)
h	blade height (m)
h_t	trench height (m)
J	rotor inertia
K_v	viscous torque constant: $T_{visc} = K_v\ \Omega$ (μNm / rad/s)
l	characteristic length scale (m)
L	inductance (μH)
$\dot{m}$	mass flow (kg/s)
m	number of poles
n	harmonic number
p	number of electrodes per pole
P_{comp}	power consumed by the compressor(W)
P_{elec}	mechanical power delivered by the motor (W)
P_{ir}	inter-row pressure (psi)
ΔP	axial pressure differential across the journal bearing gap (psi)
P_t	total pressure (Pa)

r	radius (m)
R	resistance (Ω)
R_i	inner radius (m)
R_o	outer radius (m)
S	Slip, Eqn 2.13
t	time (s)
T_{elec}	torque of electrostatic origin (μNm)
T_{visc}	viscous torque (μNm)
T_t	total temperature (K)
U	tip speed $= \Omega r_2$ (m/s)
V	velocity (m/s)
$\lvert\hat{V}\rvert$	amplitude of voltage (Volts)
w_e	electrode width (m)
w_t	trench width (m)
$\dot{W}_{visc}$	viscous power dissipated (W)

Greek

α	conductivity parameter, Eqn 2.13
β	gap parameter, Eqn 2.13
β_2'	relative trailing edge flow angle
Δ	rotor insulator thickness
ϵ	rotor eccentricity
ϵ_o	permittivity of free space
$\epsilon_r i$	permittivity of rotor insulator
π	total pressure ratio $= P_{t,2}/P_{t,1}$
ρ	density (kg/m^3)
Ω	rotational speed (RPM or rad/s)
ω	electrical frequency (rad/s)
ω_n	bearing natural frequency

σ_{rfs}	rotor film sheet conductivity
σ_{ri}	rotor insulator conductivity
σ_{eff}	effective rotor film conductivity, Eqn 2.13
μ	fluid viscosity

Subscripts

1	location at inlet of compressor (leading edge)
2	location at exit of compressor (trailing edge)
c	compressor
jb	journal bearing
m	motor
r	radial component
i	inner radius
o	outer radius
z	axial component
θ	tangential component

Acronyms

2D	two-dimensional (z and θ)
3D	three-dimensional (r, z and θ)
CFD	computational fluid dynamics
DAQ	data acquisition
FEM	finite element model
MCBR	Motor-Compressor Bearing Rig
M/T	motor-assisted turbine
M/C	motor-driven compressor
M/D	motor-driven disk (no blades)

MEMS	micro-electromechanical systems
RPM	revolutions per minute
SCCM	standard cubic centimeters per minute
ATB	aft thrust bearing
FTB	forward thrust bearing
JPP	journal pressurization plenum
MOP	motor outer plenum
AEP	aft end plate
AFP	aft foundation plate
FEP	forward end plate
FFP	forward foundation plate
RP	rotor plate
BOE	buffered-oxide etch
CMP	chemical-mechanical polishing
DRIE	deep reactive ion etching
STS	deep reactive ion etcher from Silicon Technology Systems Limited
TBOS	thick buried oxide in silicon (Sec. 3.3.3)
PECVD	plasma enhanced chemical vapor deposition

CHAPTER 1

INTRODUCTION

A technology which has greatly impacted our society over the previous four decades, is undeniably semiconductor manufacturing for microelectronics. This fabrication technology for silicon-based materials has enabled the advent of computing and signal processing microchips, which have taken an important role in our lives. Computer chips, comprised of millions of electrical components, are mass produced and sold for tens and hundreds of dollars. The semiconductor microfabrication technology developed to create these compact integrated circuits has been a major factor in the widespread use of microprocessors, by enabling cost-effective mass production of reliable, compact, and powerful information processing systems.

Beyond building electrical components, this fabrication technology has been extended to integrate mechanical elements. Micro-electromechanical systems, or MEMS, have been built which combine simple mechanical elements, such as membranes, springs, and gears with electronic circuitry on a compact chip. The single-crystal silicon substrate and thin films typically used in microelectronics become structural elements. In addition to controlling the motion of electrons, these microsystems physically interacts with the environment, moving molecules, heat, and light. The new world that micromachines can open has long been recognized [16]. In addition to creating new tools for the scientific field, multi-functional microsystems hold great commercial promise, since they can be manufactured with the similar mass-production and cost-efficient approach as microprocessors. It has been recognized since the 1980's that this capability opens the road for new compact devices to be introduced for applications previously unimaginable, or only viable with larger, heavier, and more expensive devices.

Although these possibilities have not yet been fully commercially exploited, some MEMS devices have successfully reached the market over the past decade, for specific applications. The main examples are ink jet printer heads, automotive pressure sensors, automotive airbag accelerometers, and data storage read/write heads. The market segment taken by these products was on the order of \$1.7 Billion in 1996 and is expected to grow to over \$5 Billion by 2003 [55]. New applications for MEMS technology are emerging, such as optical switching, Radio Frequency (RF) devices for wireless communication, and microfluidic lab-on-a-chip devices. In the microfluidic area, biomedical, as well as chemical testing and processing applications for MEMS are growing [60], and microfabricated valves are commercially available from Redwood Microsystems [64] and Hewlett-Packard [6]. Figure 1-1 shows the estimated MEMS sales by technology area [55], predicting a large growth in the microfluidics and chemical testing and processing area.

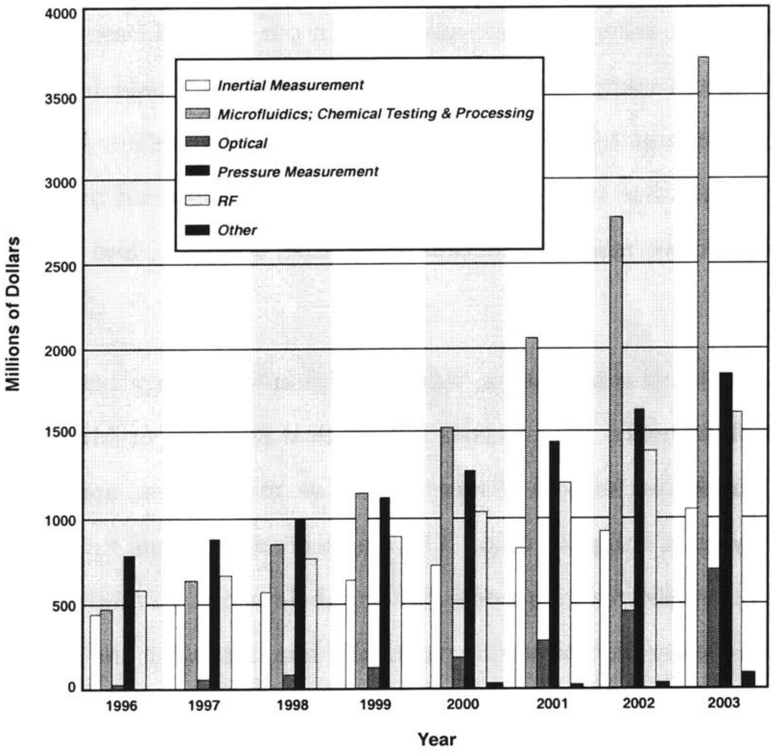

Figure 1-1: Estimate sales of MEMS products by technology area (Courtesy of System Planning Corporation [55])

The popularity of MEMS mostly stems from the potential cost advantage, and from the unprecedented functionality they can offer. Current MEMS devices are typically low energy, low power devices, useful to sense or lightly actuate on the environment. However, single crystal silicon, a common starting material in microfabrication, offers great structural characteristics [42]. In particular, the high strength-to-density ratio makes it a promising candidate for high speed rotating machinery. It is therefore credible to imagine compact, high performance micromachines based on high speed rotating machinery for high power applications. These devices could integrate an electrical motor or generator, with turbomachinery to convert energy between the fluidic, mechanical and electrical domains for applications requiring compact power components. A potential type of microfluidic MEMS therefore consists of *energy converting microsystems*, or *Power MEMS* [10].

The focus of this work has been to design, fabricate, and demonstrate a millimeter-scale compression system, driven by an integrated electric micromotor, using electrical power to deliver a pressurized gas. This motor-compressor device is envisioned for use in microfluidic systems, such as compact fuel cells for power generation, portable analytical instruments for air sampling, and micro-refrigeration for cooling of electronics, microprocessors, or people. The approach is to use microfabrication technologies from the semiconductor industry and MEMS fields to create the compact system. It therefore holds the promise to be reliably batch produced and available for tens of dollars per unit, bringing a capability usually reserved for high-end applications to a broader consumer market.

This chapter will first state the objectives of this work, followed by a review of previous work on related micro-electromechanical systems and compact compression systems. The development approach will then be presented, as well as the outline of the thesis, and the expected contributions.

1.1 Motivation and Objectives

As portable power generation and compact fluidic applications increase in popularity, the need for adequate components will rise. In particular, there will be a need for fluid pumping and compression systems for applications where size, weight, and cost are important parameters.

Two specific applications will be considered here, used to define a set of specifications to guide the design:

- μ**Compressor:** Pressurization of portable fuel cells in the range of 50-100W
    - Mass flow: 0.1 g/s (5000 sccm, 5 l/min, 0.2 CFM) of air
    - Pressure ratio: 2:1 (1 atm, 15 psig, 410" H_2O, 101kPa)
    - Fluid power[1]: 7.3 W
- μ**Blower:** Air circulation through analytical instruments such as gas analyzing systems
    - Mass flow: up to 0.3 g/s (15000 sccm, 15 l/min, 0.6 CFM) of air
    - Pressure ratio: 24" H_20 (0.06 atm, 0.9 psig, 6 kPa)
    - Fluid power: 1.5 W

These devices could serve in many fluidic applications, either as part of thermodynamic cycles which require compression, or simply to provide air flow through a constrained circuit. For example, the μCompressor device could be used for compression in compact cooling or refrigeration systems for microprocessors, electronics, or people.

The technological approach chosen to create such a device is through *MEMS technology*, since:

- Single crystal silicon and recent fabrication techniques allow the level of performance in MEMS to be pushed to that of macro-systems;
- High-speed turbomachinery promises high power-density micro-devices;
- Thin film processing technology allows the on-chip integration of an electrical motor to drive the compressor;
- Microfabrication allows batch processing, promising mass production at reasonable costs.

Based on this motivation and objectives, the following goals were defined for this research:

---

[1] Fluid power noted is the ideal compression work for the prescribed mass flow and pressure ratio, for standard conditions.

- Explore the feasibility of a microfabricated turbomachinery-based compression system;
- Determine the physical and technological issues which guide the design of such a micro-scale system;
- Develop the microfabrication techniques and methodology which allow the fabrication and successful operation of high-speed and high-power micromachines, and;
- Demonstrate such a device

1.2 Review of previous work and related technologies

In order to put the objectives of this work in context, this section will review previous work on similar microsystems and related technology. First, typical compression systems will be summarized, followed by microfabricated and traditional fluid pumping systems and components.

1.2.1 Typical compression systems

Various approaches are used to increase the pressure of a gas in conventional scale applications. Low mass flow approaches typically achieve high pressure ratios, and consist of constraining the gases in a closed reservoir and reducing the volume through a movable wall. The most common examples include reciprocating pistons and diaphragms. Rotary vanes operate on the same principle, but deliver a higher mass flow with a compromise on pressure ratio. Turbomachinery is a very high mass flow alternative, since the fluid does not come to a rest, i.e. high throughflow velocities are possible. The increase in pressure comes from the work done by imparting angular momentum to the flow, through the rotating machine. High pressure ratio is achievable if the impeller is operated at high tangential velocities, or by serially repeating the process. Among these alternatives, turbomachinery offers the highest power density, and will be the method adopted herein.

1.2.2 MEMS compressors, motors, and bearings

A variety of microfabricated fluid pumping system have been developed for microfluidic applications. They have mostly been pumps, for liquids, as opposed to compressors, for gases. The most common type has been volume displacement *diaphragm* pumps, activated by electrostatic [52], piezoelectric [14, 28], electromagnetic [1], electrohydrodynamic [48], or electro-thermopneumatic [36] forces. The chamber is usually connected to a pair of active or passive valves, controlling the inflow and outflow from the chamber. Diffuser valves have also been demonstrated, with no moving parts [54, 40]. A number of such micropumps have been reported in the literature, with flow rates ranging from tens to thousands of μl/min. These configurations provide at least three orders of magnitude less flow rate than desired for the μCompressor and μBlower applications (which must be on the order of 5-15 l/min), precluding them for high power applications.

A variety of micromotors have also been demonstrated over the past decade. They mostly were variable-capacitance motors built by surface micromachining of thin polysilicon layers [15, 34]. As will be discussed further in Chapter 5, these micromotors are six to eight orders of magnitude less powerful than necessary for the desired Power MEMS applications, mostly due to the small active area and low speeds (up to 25,000 RPM).

The highest peripheral speed microrotor found in the literature is the 50 μm diameter gear driven by a pair of orthogonal linear comb drive actuators [53]. It has reached up to 300,000 RPM, which is near 1 m/s tip speed[2].

Most of these devices have been supported by dry friction on a center pin and bushing. Gas film lubrication has also been investigated, mainly to lift the rotor from the substrate [23]. Other micro-devices use gas film lubrication to support sliding motion, such as data storage writing heads, and more recently, cantilevers for atomic force microscope tips [47].

Finally a few microfabricated turbomachines have also been demonstrated, such as the Micro-Turbo-Generator by Wiegele [61]. Operation was however limited to tip speeds of 3.5 m/s, which is significantly less than desired for power applications.

Overall, previous work shows that most types of components are realizable through micro-

---

[2] Tip speed is defined as the tangential velocity at the outer edge of the rotor

fabrication, but not to the level of performance necessary for the envisioned Power MEMS applications. It therefore remains to be proven that high-power components can be designed and micromachined for high levels of performance.

Miniaturized components and compression systems fabricated using conventional processes will be reviewed next.

1.2.3 Other miniature compression systems and components

Other motor-driven compressors and blowers Various motor-driven compressors manufactured using conventional techniques are currently available on the market. Prices are typically in the few hundreds of dollars for high pressure ratio devices (2:1), such as the rotary vane compressor shown in Figure 1-2. We notice the large power density difference with the proposed MEMS μCompressor. Smaller diaphragm compressor are available for this pressure ratio, but offer less mass flow. A combination of 4 devices in parallel would be necessary to provide sufficient mass flow, as illustrated in Figure 1-2.

Similarly, a pair of diaphragm motor-driven compressors would be necessary for the μBlower specifications, as shown in Figure 1-3. The proposed MEMS μBlower still promises a significant power density advantage compared to its large scale counterpart. Typical fans used for cooling electronics are low speed and provide 1" H_2O, which is 20 times less than necessary for this application.

The use of high power density microturbomachinery and drive technology in a batch fabricated MEMS device offers the possibility to miniaturize gas compression devices, and offer them at a relatively low cost.

Miniature turbomachinery, motors, and bearings Other applications have motivated the development of the main components of a motor-driven compressor. For example, air-driven dentist drills have prompted the development of high-speed miniature ball bearings, currently reaching up to 500,000 RPM at a 6.35 mm outer diameter (i.e. an outer rim speed of 170 m/s) [57]. Foil bearings have also been developed for high speed applications such as cryocoolers, with diameters as small as 1.65 mm (Creare [8]).

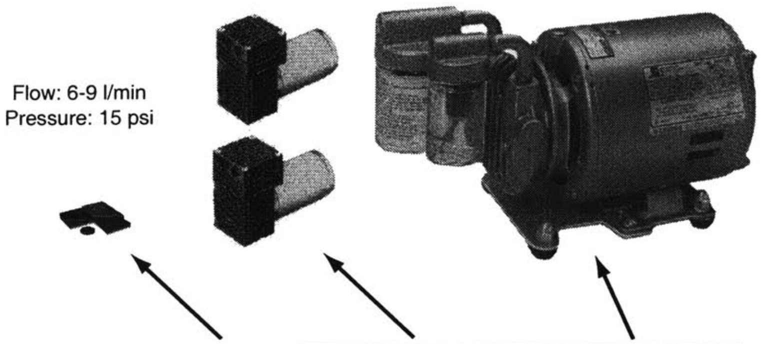

	μCompressor (predicted)	KNF Neuberger (4 N86 units)	Gast (model 0211)
Overall efficiency	18 %	25 %	5 %
Power/weight	1440 W/kg	7 W/kg	2 W/kg
Power/volume	4 W/cm^3	0.1 W/cm^3	0.02 W/cm^3

Figure 1-2: Comparison of proposed μCompressor to commercially available motor-driven compressors.

Both of these applications also integrate millimeter scale turbomachinery. Creare cryocooler impellers integrate three-dimensional, shrouded blades within a monolithic rotor, built by electro-discharge machining (EDM). The geometric flexibility of this fabrication approach comes however at the expense of low throughput, resulting in high unit costs.

Very small motors have also been developed, mostly for high frequency actuation in compact systems. For example, the smallest magnetic motor offered by Smoovy [49] is 3 mm in diameter, and provides a torque of 15 μNm at a speed of 60,000 RPM. Unfortunately, this corresponds to 0.1 W, which is approximately 50 times less power than necessary.

In order for the proposed MEMS Motor-Driven Compressor to be viable compared to these other available technologies, it should achieve the performance level of conventional compression systems, but with the cost advantage of MEMS batch fabrication. Its higher power density could also be considered as a competitive advantage, but to date, commercial MEMS success has mostly been characterized by the cost savings they provide.

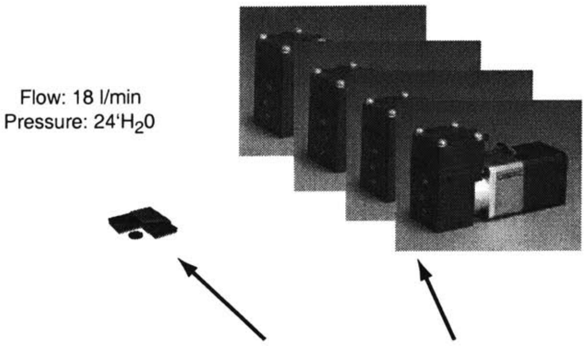

	μBlower (predicted)	KNF Neuberger (4 UNMP30 units)
Overall efficiency	18 %	12 %
Power/weight	320 W/kg	4 W/kg
Power/volume	0.8 W/cm^3	0.04 W/cm^3

Figure 1-3: Comparison of proposed μBlower to commercially available low pressure motor-driven compressors.

1.3 Development Approach

1.3.1 MIT Microengine Project

The Motor-Compressor development was part of a larger research project at MIT, aiming to demonstrate turbomachinery-based, energy conversion MEMS devices and technology, i.e. *Power MEMS* [10, 13]. In addition to the Motor-Compressor, the other microengines considered are: a centimeter-scale gas turbine engine for propulsion of Micro Air Vehicles (MAV), a gas turbine generator for portable electrical power generation, and a bi-propellant micro-rocket engine with turbopumps [32, 46] for satellite attitude keeping or future micro-launch vehicles [18]. Many components and processing techniques are shared between devices, leveraging the microfabrication experience gained and the unique knowledge base developed for these devices.

The MIT Microengine project is structured along two axes: device-oriented development and disciplinary research. Disciplinary teams focus on the original research necessary in the fields of turbomachinery, bearings and rotordynamics, electromechanics, combustion, structures and materials, and microfabrication. Specific device development then crosses the necessary fields, guiding the disciplinary research efforts to satisfy device requirements. By the year 2000, over 50 researchers from the departments of Aeronautics and Astronautics, Electrical Engineering and Computer Science, Material Science and Engineering, and Mechanical Engineering formed the collaborative research and development team.

Inter-disciplinary interaction was necessary to guide the research and determine the adequate balance between technological innovation, implementation risks, and timely achievement of project milestones. For example, the Motor-Compressor development required a compromise between achievable system performance, high speed bearing operation, and manufacturability.

1.3.2 Motor-Compressor related work

The Motor-Compressor development path consisted of first establishing expected levels of component performance achievable with the given resources; then developing the necessary knowledge base, designing the components and the system, developing the fabrication techniques, building and demonstrating the components and the integrated system.

The disciplinary activities related to the Motor-Compressor project will be detailed in the relevant Chapters later in the thesis, but can be summarized as:

1. Electromechanics: analytical modeling and experimental verification of micro-motor design and power electronics [37, 38];
2. Bearings and Rotordynamics: modeling and experimental development of viable bearing designs and operating protocols [41, 44, 50, 19];
3. Turbomachinery: computational and experimental development of viable compressor configurations [33, 51];
4. Microfabrication: unit process development, assessment of integration issues, and device fabrication [29, 21].

The limited diagnostics available at the small scale has pushed the initial effort mostly toward analytical and numerical work, and scaled-up experimental testing. Macro test rigs of the gas-lubricated bearings [41] and compressor [51] provided extremely valuable demonstration of those components, which are characterized by non-conventional geometries and operating regimes.

Microfabricated devices also played a critical role in the Motor-Compressor development. The MicroBearing Rig was a development platform for the basic techniques to create a fusion bonded 5-stack of double-side etched silicon wafers [31, 30, 29]. The device was also a platform for microfabricated gas bearing development. Work by Lin [29] mostly investigated the hydrostatic bearing operation. This microbearing rig work guided the Demo Motor-Compressor design and testing, and established the process flow for the silicon structure of the Motor-Compressor.

Secondly, a tethered version of the micromotor was developed in parallel with the Demo Motor-Compressor, by Nagle [37, 38]. It is a 2-wafer device, consisting of the electrical stator and rotor of the electrostatic induction micromotor. The rotor is held by flexible tethers, which allow a measurable rotation of the rotor under electrostatic torque. The device aims to measure the electrostatic torque, validate the motor modeling, and concurrently develop fabrication processes for the thin film electric stator and rotor.

Furthermore, a turbine-driven generator is currently being developed based on the Motor-Compressor configuration [12]. High efficiency electrical components are being developed for this application, which will eventually be directly beneficial to a Motor-Compressor.

1.3.3 Device development plan

Top-level view The approach has been first to develop an experimental *Demo Motor-Compressor*, before pursuing the development of the μBlower and μCompressor devices, with the intent of limiting the level of risk. Component designs and fabrication processes were largely based on the valuable, although limited, experience gained by other researchers in the Microengine team.

The Demo Motor-Compressor development effort therefore focused on the unique and critical aspects of this type of device, mainly the fabrication of a 5-stack device with integrated thin film components, and the high-speed journal bearing, micromotor, and integrated system operation.

This initial development phase aims to determine the validity of the proposed approach and identify the main challenges both at the component and system levels. The Demo

Motor-Compressor development will set the guidelines for the implementation of application specific devices. Although the system level designs of the μBlower and μCompressor configurations will be proposed, they have not been experimentally pursued.

Experimental device development Two types of devices were fabricated and tested: a second generation bearing rig and a set of motor-driven microrotors. The new bearing rig device was directly derived from the Demo Motor-Compressor design, and will be referred to as the *MC-Bearing Rig.* As described in Chapter 4, it was instrumental in developing the hydrostatic journal bearing and demonstrating high rotational speeds.

The motor-driven devices then go one step further from the all-silicon MC-Bearing Rig, and integrate the thin film micromotor in the 5-wafer stack to drive the rotor. In order to explore experimentally the operation of the electrostatic micromotor and demonstrate system level operation, three variants of motor-driven devices were built, which only differ in the blading:

1. Motor/Compressor: Disk with motor and compressor blades, intended for system-level demonstration;
2. Motor/Disk: Flat disk with motor but no blades, intended for viscous drag and micromotor torque assessment;
3. Motor/Turbine: Disk with motor and turbine blades, intended for high speed bearing assessment and micromotor torque assist to achieve higher speeds.

Terminology The general configuration adopted here, of a planar motor driving a disk with compressor blades on the reverse side, will be referred to as a *Motor-Compressor.* The experimental motor-driven devices will be usually referred to as the *Demo Motor-Compressor*, since they share the same fabrication process flow and were built simultaneously on the same wafer. Finally, the proposed configurations for the pressurization of fuel cells and aspiration for analytical instruments applications will be referred to as the μCompressor and μBlower respectively.

1.4 Scope of the Thesis

Figure 1-4 illustrates the topics covered and the various devices built as part of this work, mostly focusing on the demonstration of microscale components and systems. First, bearing rig work was pursued (Bearing Rig v.2, referred to herein as the MC-Bearing Rig) to demonstrate microscale hydrostatic journal bearing operation, and the operation of high-power density microturbomachinery. The set of motor-driven devices were then fabricated and tested, to study the operation of the micromotor, and that of the integrated microsystem.

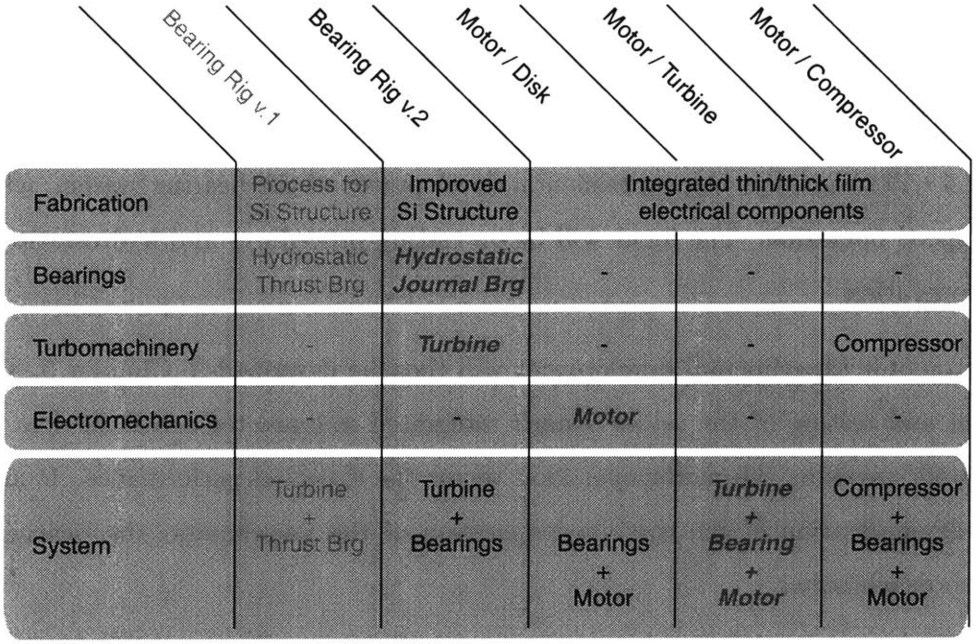

	Bearing Rig v.1	Bearing Rig v.2	Motor / Disk	Motor / Turbine	Motor / Compressor
Fabrication	Process for Si Structure	Improved Si Structure	Integrated thin/thick film electrical components		
Bearings	Hydrostatic Thrust Brg	***Hydrostatic Journal Brg***	-	-	-
Turbomachinery	-	***Turbine***	-	-	Compressor
Electromechanics	-	-	***Motor***	-	-
System	Turbine + Thrust Brg	Turbine + Bearings	Bearings + Motor	***Turbine + Bearing + Motor***	Compressor + Bearings + Motor

Figure 1-4: Illustration of the experimental devices built and tested to demonstrate critical Power MEMS components and systems.

1.5 Thesis Outline

The work for this thesis extends along both main axes of the MIT Microengine Project: device oriented development and disciplinary research. Along one axis, original work has focused on system design, fabrication, and testing of the Motor-Compressor. Along the other axes, research in the disciplinary areas of microfabrication, electromechanics, and gas-lubricated bearings was undertaken when necessary for the successful operation and integration of the components in the Motor-Compressor. The thesis is structured to cover both axes, namely: the modeling and design, the microfabrication, and the experimental development and demonstration of the components and the integrated system.

Chapter 2 provides an overview of the Motor-Compressor, and describes the component and system design. It will also present a summary of disciplinary work, by the author and by others, related to the Motor-Compressor development. The system design section will describe the main trade-offs in this unique design space and the suggested device configurations.

Chapter 3 will present the fabrication process, the results, and the experience gained in building the devices as part of this work. Major challenges in using deep reactive ion etching, wafer bonding, and thin film processing will be discussed, along with the techniques applied to successfully build the MEMS devices.

Chapter 4 will summarize the experimental development of the bearing system, which led to high speed operation. The focus will be on testing procedures and hydrostatic journal bearing operation.

The micromotor experimental development will then be described in Chapter 5. Characterization and testing of the set of 5-stack integrated micromotor-driven devices will be summarized, assessing the motor operation versus the expected performance. It also provides a demonstration of the combined operation of the micromotor, the bearings, and microturbomachinery.

Finally, Chapter 6 summarizes the main aspects and contributions of the work presented herein, and suggests further disciplinary and device-oriented work.

CHAPTER 2

SYSTEM AND COMPONENT DESIGN

This chapter will define the design basis for a microfabricated silicon motor-driven compressor. First, an overview of the baseline configuration will be presented, setting the stage for the following three sections, which will describe the function of each main component: turbomachinery, electromechanics, and bearings. The focus will mainly be on aspects which are important for system level design.

Disciplinary technology development for the components (especially the turbomachinery and bearing design) has mostly been the effort of other researchers. Important parts of their work will be included herein for completeness, and will be referenced accordingly. The author's contributions in micromotor fluidic and electromechanical modeling, as well as system-level design, constitutes the main substance of this chapter. The system design section uses a combination of component models to predict the device performance and efficiency, and explores the design space for this new type of device. Optimum configurations are suggested for the envisioned applications, based on the specific technology developed and on the unique limitations of silicon microfabrication. The design of the Demo Motor-Compressor and MC-Bearing Rig development devices will be presented, as the basis for the experimental work presented in the other chapters of the thesis.

2.1 Baseline System Overview

The motor-compressor is composed of the following components, illustrated in the schematic cross-section (Figure 2-1):

1. Radial impeller and diffuser
2. Journal and thrust bearings
3. Electrostatic induction motor
4. Fluid piping and electrical connections

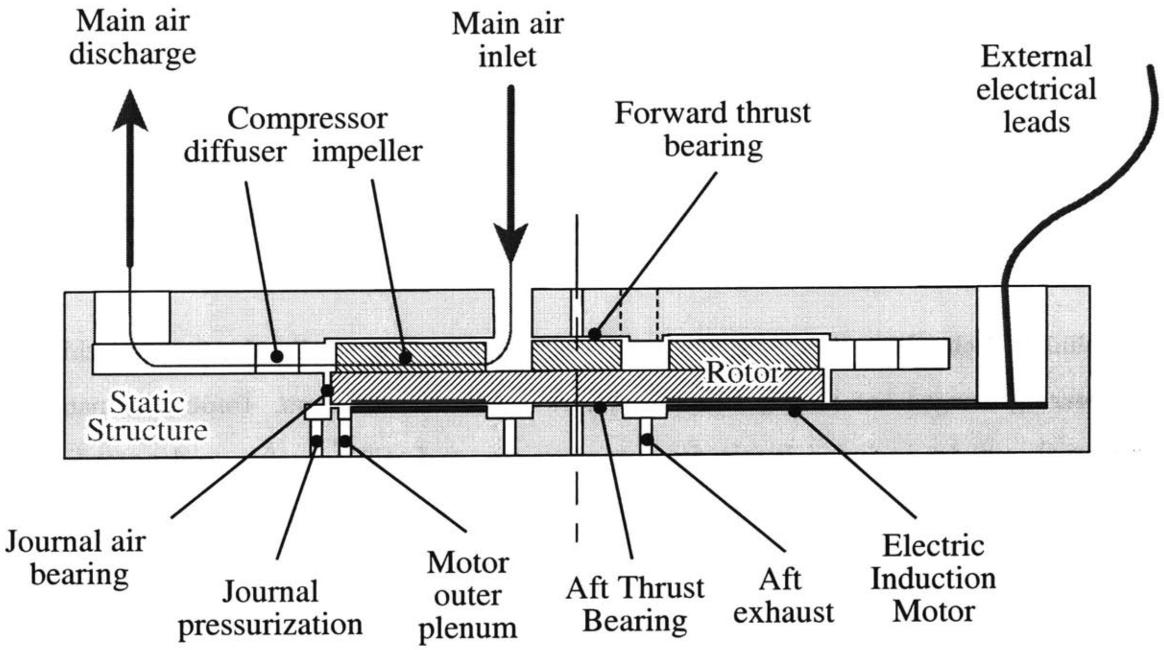

Figure 2-1: Cross-section schematic of the motor-driven compressor.

After fabrication, the motor-compressor consists of one moving part, the rotor, enclosed in the static structure. The rotor is a low aspect ratio disk with the turbomachine rotor blades on the front side and the electric motor on the back side. The in-plane motion of the rotor disk is supported by a gas journal bearing on its periphery, and the axial motion is restrained by central thrust bearings on each side of the disk. The electrostatic induction motor applies torque on the rotor by inducing charges on the back side of the disk, across an air gap, and dragging them tangentially. This applied torque spins the disk and the impeller blades on the front side. The pressure rise created by the compressor entrains air from the inlet to the discharge, feeding an external system such as a fuel cell or an air analysis system.

The main system design challenge consists of defining the components of a system delivering the prescribed fluid power, within the constraints of state-of-the-art microfabrication and reasonable new technology development.

Before discussing the system design, the design of the turbomachinery, the electrostatic-induction motor, and the gas bearings will be summarized.

2.2 Turbomachinery

The approach in achieving compression is based on high-speed turbomachinery. The design space differs from conventional turbomachinery due to the small-scale and the limited fabrication flexibility, as will be discussed in the following sections.

2.2.1 Turbomachinery scaling

Since thermodynamic cycles do not change with size, the pressure rise required from a micro-compressor is similar to that required from a conventional scale machine, when the application is miniaturized. Since fluid power delivered can be approximated by the product of pressure rise and volume flow, it scales with the mass flow. Furthermore, if high through-flow velocities are maintained, the mass flow, and fluid power will scale with the through-flow area l^2, where l is a characteristic dimension of the flow path. This suggests that the power density of a miniature turbomachine should not degrade, but increase inversely with the scale:

$$\begin{aligned} \frac{\text{Power}}{\text{Volume}} &\approx \frac{\dot{m}\,\Delta P_t/\rho}{l^3} \\ &\approx \frac{Vl^2\,\Delta P_t}{l^3} \\ &\propto \frac{1}{l} \quad \rightarrow \quad \text{for constant } V, \Delta P_t \end{aligned}$$

This scaling is only valid if the same level of pressure rise is achievable in a microturbomachine as in its large-scale counterpart. Since the pressure rise is proportional to level of turning across the blade row, high tangential velocities (tip speed) and high through-flow velocities are necessary (i.e. similar velocity triangles). To first order, if the spacing between blades is reduced with the chord (as shown in Figure 2-2), the diffusion within the blade passage and the turning achievable will remain constant (for constant velocities). This implies that similar power per unit area can be expected for high performance micro and macro scale turbomachines. The reduction in scale however delivers this power per unit area over a shorter length. The scaling law described above can therefore be interpreted simply in terms of shorter turbomachinery, for constant power per unit through-flow area:

$$\begin{aligned} \frac{\text{Power}}{\text{Volume}} &= \frac{\text{Power}}{\text{Area}}\frac{1}{\text{chord}} \\ &\propto \frac{1}{\text{chord}} \quad \rightarrow \quad \text{for constant power per unit area} \end{aligned}$$

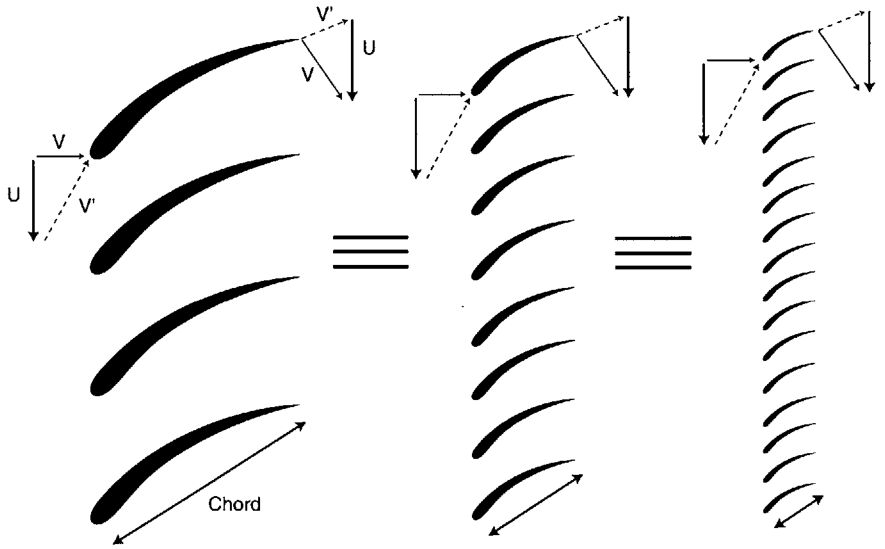

Figure 2-2: Scaled blade row, conserving the non-dimensional geometry.

It is important to note that the necessity for high tip speed drives the requirement for other components in the systems (the bearings and the motor), as well as the strength requirements of the rotating structure.

The power density benefit of micro-turbomachinery must be traded-off with efficiency. The small-scales, for similar flow properties and velocities, are characterized by higher viscous losses, represented by lower Reynolds Numbers. Figure 2-3 quantifies this effect by plotting the loss coefficient as a function of scale (i.e. Reynolds Number) for a centrifugal compressor. The numerical study was done by Jacobson [25] using the CFD code MISES [9] on the baseline Motor-Compressor geometry. The figure suggests a practical limit to turbomachinery miniaturization, beyond which the component inefficiency will overwhelm the benefit of higher power density, for a specific application.

In addition to low Reynolds number operation, the geometric constraints imposed by microfabrication strongly impact the turbomachinery design. This constrained design space led to a non-standard blading design, as described next.

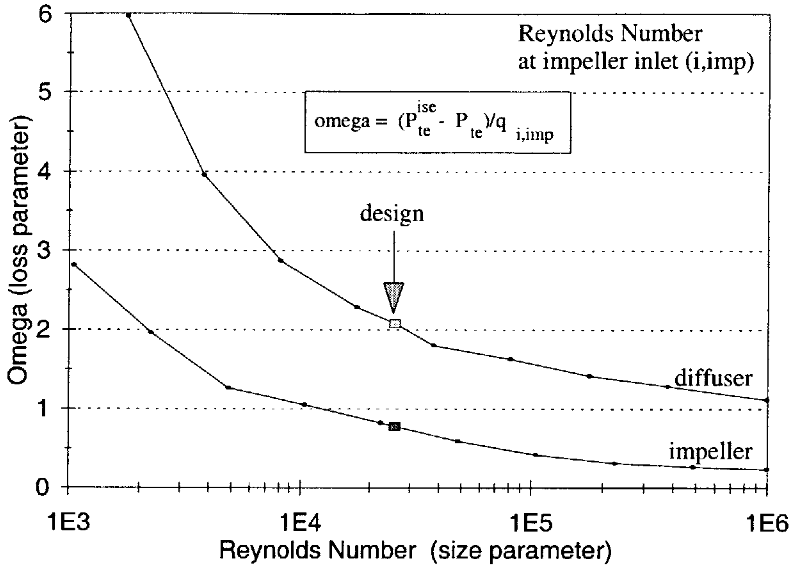

Figure 2-3: Loss coefficient as a function of Reynolds Number, representing the effect of higher viscous losses at small scale (by Jacobson [25]).

2.2.2 Compressor design

Given the planar fabrication approach, the compressor geometry was chosen to be a constant blade height, radial outflow centrifugal compressor.

Blade profiles for a pressure ratio of up to 2:1, mass flow of 0.1 g/s, tip speed of 400 m/s, and a radius of 2 mm were designed by S. Jacobson using the computational tool MISES [9]. As discussed by Jacobson [25], the main design challenge consisted of keeping the boundary layers attached, even thought the area tends to increase with radius since the blade height remains constant. As illustrated by the final geometry in Figure 2-4 and Table 2.1, the flow channel area was kept relatively constant by sweeping the blades to a high angle and tailoring the blade thickness. A vaned diffuser then straightens the flow towards the radial direction, converting some of the tangential kinetic energy into pressure rise.

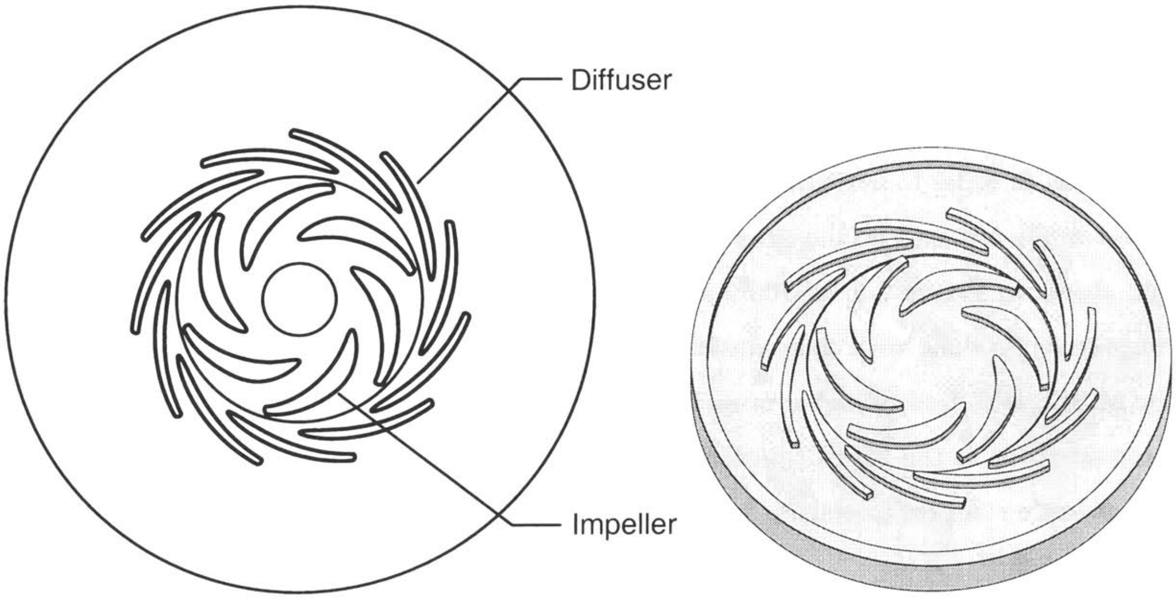

Figure 2-4: 2D and 3D view of the baseline compressor, designed by S. Jacobson [24].

	Impeller	Diffuser
Design	MIT-I99	MIT-H36
Inlet radius (mm)	0.98	2.37
Exit radius (mm)	1.95	2.96
Number of blades	6	11
Blade height	200 μm	200 μm

Table 2.1: Motor-Compressor baseline turbomachinery geometry, by S. Jacobson.

2.2.3 Assessment of compressor performance

Analysis of the three-dimensional flow field in the compressor was carried out by Mehra [33] and Gong [22], suggesting that the 3D losses are approximately double the losses predicted in 2D calculation. Although the micromachined geometry is largely 2D, the flow field is three-dimensional. The right angle turn into the impeller, the hub and shroud, and diffuser vanes with spanwise constant stagger all contribute to undesirable secondary flows and additional losses.

The compressor fluid dynamics were also investigated experimentally, using a macro-scale test rig [51]. The compressor geometry was scaled-up by a factor of 75 and operated in a closed loop at $\frac{1}{75}$ of an atmosphere in order to match the microscale Reynolds numbers and allow for conventional instrumentation. The rotor was also designed for high speed operation in order to match the Mach numbers. Tip speed was limited to 400 m/s due to stress limits imposed on the titanium rotor. Measurements of pressure rise and mass flow are shown in Figure 2-5 for 100% and 42% design speed (400m/s and 168m/s tip speed respectively), along with computational results. The design speed characteristic predicted by MISES is shifted to higher mass flows since blockage due to the 3D flow is not entirely accounted for in the 2D calculations. Overall compressor efficiency measurements in the macro-scale compressor test rig were done by Shirley [51], and are shown for both speeds in Table 2.2.

Speed	42 % (168 m/s)	100 % (400 m/s)
Adiabatic efficiency	26 %	41 %

Table 2.2: Measured compressor efficiency in the unshrouded macro-scale compressor test rig, from Shirley [51].

2.2.4 Modeling for system design purposes

From an overall power balance perspective, the compressor can simply be viewed as a load, and the system designed to provide sufficient power to drive it.

The power necessary to drive the turbomachine is the sum of the fluid power delivered and the losses incurred in doing so, including all related losses such as the tip clearance drag and mixing losses, but excluding disk windage[1] and bearing losses (which will be accounted for separately).

For design purposes, the compressor power consumption was based on the experimental measurements of pressure rise, mass flow, and efficiency, chosen near the maximum efficiency

---

[1] Windage refers to the fluid drag on the disk, other than that in the bearings and attributed to the compressor.

point. The shaft power is calculated from these values following the basic relations:

$$P_{comp} = \dot{m}_c C_p (T_{t,2} - T_{t,1}) \tag{2.1}$$

$$\eta_c = \frac{\pi_c^{(\gamma_c - 1)/\gamma_c} - 1}{T_{t,2}/T_{t,1} - 1} \tag{2.2}$$

$$\pi_c = \frac{P_{t,2}}{P_{t,1}} \tag{2.3}$$

The power and pressure rise are then extrapolated to lower speeds by scaling the velocity triangles. This is achieved by adjusting the throttle during operation to keep the incidence on the blades constant, implying that the mass flow changes linearly with tip speed ($\dot{m}_c = \rho_1 V_{r,1} A$). Based on the Euler turbine equation [26], the work per unit mass flow will scale with the square of the tip speed:

$$\frac{P_{comp}}{\dot{m}} = C_p(T_{t,2} + T_{t,1}) = \Omega(r_2 V_{\theta,2} - r_1 V_{\theta,1}) \tag{2.4}$$

$$= \Omega r_2 V_{\theta,2} \quad \rightarrow \quad \text{for radial inlet flow} \tag{2.5}$$

$$= \Omega r_2(\Omega r_2 - V_{r,2} tan(\beta_2')) \tag{2.6}$$

$$= U^2 - U\ V_{r,2} tan(\beta') \tag{2.7}$$

where:

$$U = \Omega r_2 \quad \rightarrow \quad \text{tip speed} \tag{2.8}$$

$$\beta_2' \quad \rightarrow \quad \text{relative backswept flow angle exiting the impeller} \tag{2.9}$$

$$V_{r,2} \quad \rightarrow \quad \text{radial flow velocity exiting the impeller} \tag{2.10}$$

Therefore, the power is to first order proportional to the tip speed cubed: $P_{comp} \propto U^3$. The pressure ratio can then be derived from the expression for adiabatic efficiency, assuming a linear variation of efficiency as a function of speed[2]. The efficiency at both tip speeds of interest (400 m/s, and near 200 m/s) were measured in the macro-scale compressor rig, showing a significant reduction at lower speeds (Table 2.2).

---

[2] Since efficiency had been measured at two different speeds at the time of this system study, only a linear fit to the macro-scale experimental data was possible.

Conclusion: The experimental and computational assessment of this initial geometry positions the turbomachinery as a relatively low risk component that is expected to meet the requirements for the development stage of the Motor-Compressor. Use of this baseline blading for the first devices built is justified by the availability of numerical and scaled experimental data, to compare to the micro-scale results. Most effort has therefore been focused on higher risk components, namely the high-speed bearings and the electrostatic-induction micromotor.

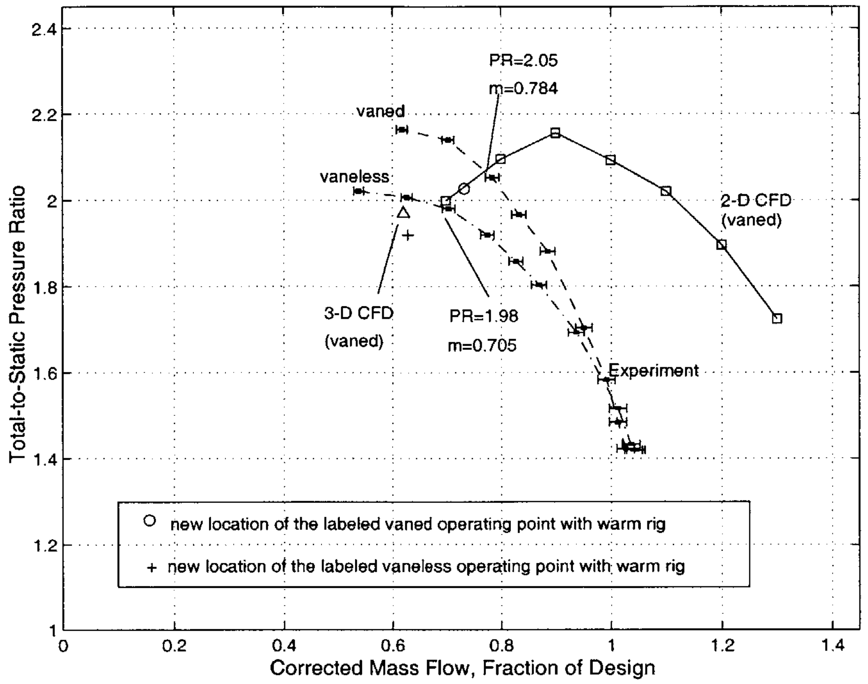

(a) 100 % Design speed - 400 m/s

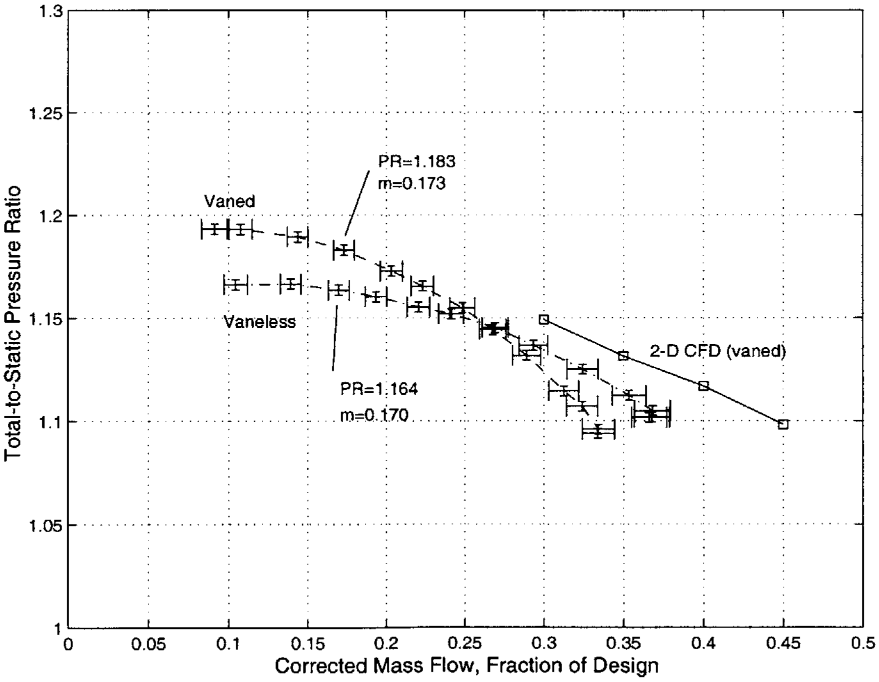

(b) 42 % Design speed - 168 m/s

Figure 2-5: Experimental macro-scale compressor pressure rise characteristic for the Motor-Compressor baseline turbomachinery design (from Shirley [51]).

2.3 Electromechanics

The approach chosen to drive the rotor was by electrostatic induction. An electric machine was chosen over a magnetic one, mainly since the microfabrication technology for electric components is compatible with microelectronics processes, especially when compared to the relatively primitive process maturity for magnetic materials. Furthermore, initial estimates suggested that the induction approach could provide sufficient power, and would be compatible with high speed rotation (high operating frequencies and no rotor contact), although it would require that the operating conditions and fabrication limits were pushed aggressively [11].

Unfortunately, electric micromotors found in the literature did not provide the requisite power, nor operate at sufficiently high rotational speeds. Design and development of a high-speed, high-power micromotor was therefore necessary. The design requirements for the Motor-Compressor differ from those of micromotors which are intended as actuators for micro-mechanisms, and can be summarized as:

- Power output: sufficient to overcome viscous drag and to drive the compressor;
- Torque per unit area: compact enough to reside on the back side of the rotor disk;
- Rotational speed: compatible with high-speeds necessary for compressor;
- Energy conversion efficiency: sufficient for intended applications;
- Integration: with silicon micromachined high-speed rotating micromachinery.

The development started with analytical modeling of the motor performance and efficiency, then design of a baseline motor configuration, fabrication process development of the rotor and stator electrical structures, and demonstration at the micro-scale. Basic analysis, motor design, and some process development were the focus of S. Nagle, and are described elsewhere [38, 37]. Process development for the stator electrical structure was a collaborative effort and is described by Ghodssi *et al.* [21].

The original work presented in this section consists of additional modeling which was necessary to design the Motor-Compressor device. The fabrication and micro-scale demonstration will be detailed in subsequent chapters. Section 2.3.2 will detail the electrical modeling and Section 2.3.3 will summarize the viscous drag modeling in the micromotor. A short description of the electrostatic induction principle will first be presented for completeness.

2.3.1 Electrostatic Induction Principle

Torque in an electrostatic induction motor comes from the tangential component of the electrical field between induced charges in the rotor and an applied potential on the stator. As illustrated in Figure 2-6, a potential wave is externally applied on the stator surface, inducing charges in the rotor film across the air gap. When the stator waveform is made to travel faster than the rotor in the circumferential direction, the field lines will slant and drag the charges along the film. For finite rotor film conductivities, the induced charges will feel a resistance and the rotor waveform will lag behind the traveling stator potential. The tangential component of the electrical field lines in this quasi-static scenario is the source of torque on the disk. The gross mechanical power delivered to the rotor is simply the product of this torque and the rotational speed, and will be referred to as P_{elec}. The normal component results in an attraction force between the stator and rotor.

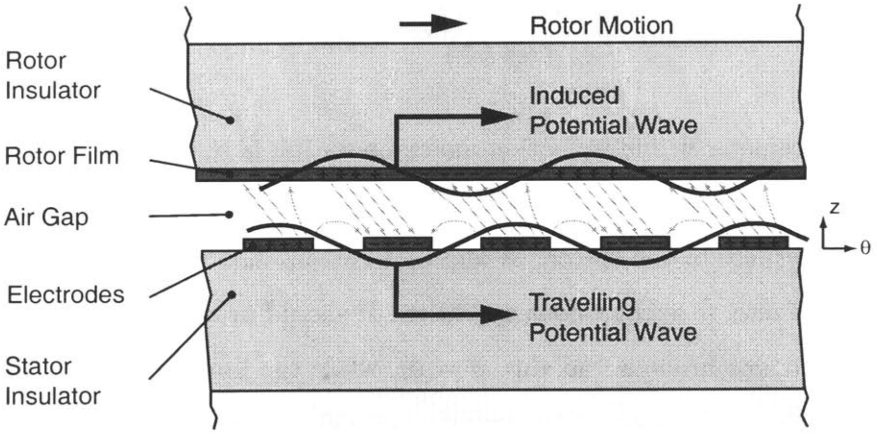

Figure 2-6: Principle of operation of the electrostatic-induction motor.

Basic modeling of the electric fields and resulting forces from the electrostatic induction principles are described by Bart and Lang [5], and Nagle and Lang [38]. For a given sinusoidal waveform on the stator surface, the induced charge distribution and resulting electrical fields across the air gap and in the rotor were solved for analytically. The stator potential is defined by its frequency ω, wavelength $2\pi/k$, and amplitude $|\hat{V}|$; the air gap is defined by its height g_m, and permittivity ϵ_g; the rotor insulator is characterized by its thickness Δ, permittivity ϵ_{ri}, and conductivity σ_{ri}; and the rotor film is characterized by its sheet conductivity σ_{rfs}. The tangential electrostatic forces per unit area are expressed analytically as:

$$f_\theta = \frac{\epsilon_g k^2 |\hat{V}|^2}{2\beta \sinh(kg_m)} \cdot \frac{\alpha\beta S}{1 + (\alpha\beta S)^2} \tag{2.11}$$

while the axial force per unit area is:

$$f_z = \epsilon_g \left[\frac{k|\hat{V}|}{2\beta \sinh(kg_m)}\right]^2 \frac{\beta^2 + (\alpha\beta S)^2[(\beta - \cosh(kg_m))^2 - (\sinh(kg_m))^2]}{1 + (\alpha\beta S)^2} \tag{2.12}$$

with the following parameters defined for convenience:

$$\begin{aligned}
S &= \frac{\omega - kU}{\omega} && \text{(Slip)} \\
\sigma_{eff} &= k\sigma_{rfs} + \sigma_{ri}\frac{\cosh(k\Delta)}{\sinh(k\Delta)} && \text{(Effective rotor film conductivity)} \\
\alpha &= \frac{\omega\epsilon_g}{\sigma_{eff}\ \sinh(kg_m)} \\
\beta &= \cosh(kg_m) + \frac{\epsilon_{ri}}{\epsilon_o}\frac{\cosh(k\Delta)}{\sinh(k\Delta)}\sinh(kg_m)
\end{aligned} \tag{2.13}$$

An important parameter in the induction motor operation is S, the *slip*. It represents the velocity of the potential wave in the reference frame of the rotor, which is traveling at a velocity U with respect to the stator. A slip of 1 corresponds to the case of a stationary rotor, and a slip of zero, to synchronous operation. It should be noted that the normal force, f_z, is maximum at synchronous (no slip, $S = 0$), while the tangential force, f_θ, reaches a maximum at $\alpha\beta S = 1$. At synchronous speed, the field lines are mostly vertical across the air gap. In the range of $0 < \alpha\beta S < 1$, the tangential component of the field lines grows as the slip increases. For $\alpha\beta S > 1$ however, less charges are induced in the rotor film, and the field intensity decreases along with the induced charges. The optimal value of $\alpha\beta S = 1$ happens when the time scale for charges to relax over a length l in the rotor film is of the order of the time the stator waveform travels the same distance.

The effective rotor film conductivity σ_{eff} has a large influence on the slip at which the maximum tangential force occurs, making it a critical design parameter. As shown by the definition of α (Eqn 2.13, it is inversely proportional to σ_{eff}, and σ_{rfs}. At maximum torque, $S|_{maxtorque} = \frac{1}{\alpha\beta}$, so $S|_{maxtorque} \propto \sigma_{rfs}$. The point of maximum torque ($\alpha\beta S = 1$) will occur closer to synchronous (i.e. at lower slip, S) for less conductive films (lower σ_{rfs}). Further discussion of these characteristics and other aspects of induction machines can be found in Woodson and Melcher [63].

The following section describes the application of this basic electrostatic induction model to the Motor-Compressor configuration.

2.3.2 Micromotor Modeling and Design

The micromotor configuration consists of a polar array of radial stator electrodes laying beneath the rotor disk, separated by a small air gap. A circumferential waveform is created on the stator surface by applying a prescribed voltage to discrete electrodes. Figure 2-7 illustrates a discretized sinusoidal waveform using a set of six electrodes, forming a pole of circumferential extent $\lambda = 2\pi/k$ (the choice of six electrodes will be discussed later). Similar poles are repeated m times in a polar array, creating a continuous high frequency waveform in the circumferential direction.

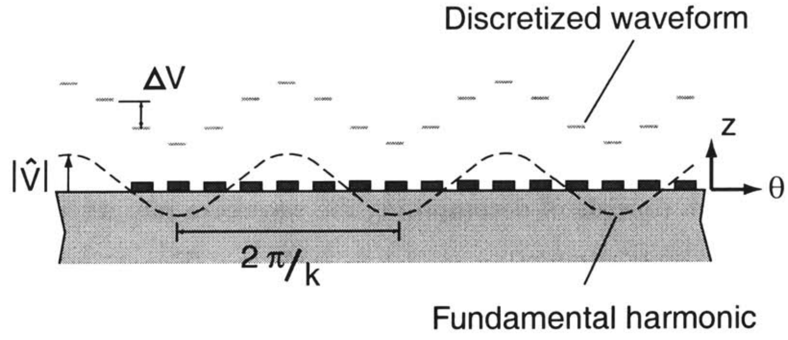

Figure 2-7: Stator potential, discretized by six electrodes.

Each sixth electrode can be connected together, forming a phase. By alternating the applied voltage to each phase, the waveform can be made to travel circumferentially. The chosen stator excitation scheme consists of applying a sinusoidal signal to each phase, shifted by 60°. Spatially, the waveform takes a discretized sinusoidal shape. This non-ideal waveform contains a strong fundamental harmonic, but also higher-order harmonics, of smaller magnitude. Figure 2-8 illustrates such a waveform at one moment in time, with its first three non-zero harmonics $n = 1, -5, 7$ (to be discussed later).

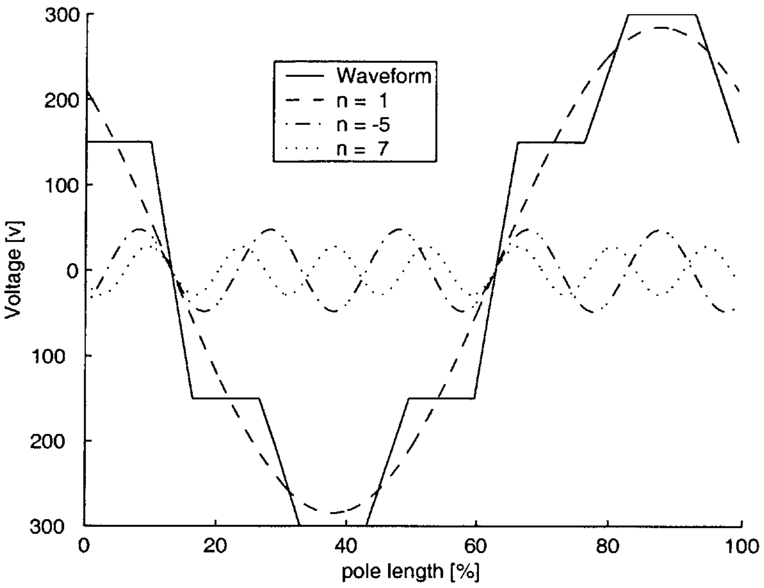

Figure 2-8: Stator potential distribution at one moment in time, and its harmonic decomposition

This sinusoidal electrode excitation scheme creates harmonics of constant magnitude that travel at constant speeds. The electrical fields can be considered quasi-steady in the reference frame of each stator harmonic, and can then be independently calculated. Modeling that allows time-varying harmonic magnitude and speed can be found in Reference [37].

Integration of the electromechanical forces on the disk

The modeling approach consists of decomposing the waveform into its harmonics, and applying the basic electrostatic-induction model to each one (Equations 2.11, 2.12). The geometry is segmented in rings of width dr, each assumed to be represented by the rectilinear configuration at their mean radius r. The total force is summed for the first N harmonics and integrated over the active motor area:

$$T_{z,elec} = \int_{R_i}^{R_o} r \sum_{n=1}^{N} f_{\theta,n}(r) \quad 2\pi r \, dr \tag{2.14}$$

$$F_{z,elec} = \int_{R_i}^{R_o} \sum_{n=1}^{N} f_{z,n}(r) \quad 2\pi r \, dr \tag{2.15}$$

The forces per unit area of a circular strip, at a radius r, are modeled using the basic analytical expressions, noting that one wavelength ($\frac{2\pi}{k}$) is equal to $\frac{2\pi r}{nm}$ such that $k = nm/r$ (m is the number of poles, i.e. number of repeated waveforms around the circumference). The analytical expressions therefore become:

$$f_{\theta,n} = \frac{\epsilon_g \left(\frac{nm}{r}\right)^2 |\hat{V}|^2}{2\beta \ \sinh(\frac{nm}{r} g_m)} \cdot \frac{\alpha\beta S}{1 + (\alpha\beta S)^2} \tag{2.16}$$

$$f_{z,n} = \epsilon_g \left[\frac{\frac{nm}{r} |\hat{V}|}{2\beta \sinh(\frac{nm}{r} g_m)} \right]^2 \frac{\beta^2 + (\alpha\beta S)^2 [(\beta - \cosh(\frac{nm}{r} g_m))^2 - (\sinh(\frac{nm}{r} g_m))^2]}{1 + (\alpha\beta S)^2} \tag{2.17}$$

with:

$$S = \frac{\omega - \frac{nm}{r} U}{\omega} \qquad \text{(Slip)} \tag{2.18}$$

$$\sigma_{eff} = \frac{nm}{r} \sigma_{rfs} + \sigma_{ri} \frac{\cosh(\frac{nm}{r} \Delta)}{\sinh(\frac{nm}{r} \Delta)} \qquad \text{(Effective rotor film conductivity)} \tag{2.19}$$

$$\alpha = \frac{\omega \epsilon_g}{\sigma_{eff} \sinh(\frac{nm}{r} g_m)} \tag{2.20}$$

$$\beta = \cosh(\frac{nm}{r} g_m) + \frac{\epsilon_{ri}}{\epsilon_o} \frac{\cosh(\frac{nm}{r} \Delta)}{\sinh(\frac{nm}{r} \Delta)} \sinh(\frac{nm}{r} g_m) \tag{2.21}$$

$$\tag{2.22}$$

A closed form analytical solution can also be obtained given a few assumptions:

1. only the fundamental harmonic, $n = 1$, will be considered, neglecting the torque from the higher harmonics;
2. the magnitude of the harmonic is considered constant over the entire radial span;
3. the rotor conductivity will be assumed to vary with radius such that the slip at all radial locations is at the point of maximum torque ($\alpha\beta S = 1$);
4. linear approximations: $\sinh(\frac{nmg_m}{r}) \approx \frac{nmg_m}{r}$ and $\beta = 1 + \frac{\epsilon_b g_m}{\epsilon_o \Delta}$;

The electrostatic induction torque can then be approximated as:

$$T_{elec} = \frac{\pi m \epsilon_o V^2}{4 g_m (1 + \frac{\epsilon_b g_m}{\epsilon_o \Delta})} (r_{mo}^2 - r_{mi}^2) \tag{2.23}$$

and, assuming a small slip such that $m\Omega = \omega = 2\pi f$, the approximate gross mechanical power delivered by the motor becomes:

$$\begin{aligned} P_{motor,elec} &= \Omega \times T_{elec} \\ &= \Omega \frac{\pi m \epsilon_o V^2}{4 g_m (1 + \frac{\epsilon_b g_m}{\epsilon_o \Delta})} (r_{mo}^2 - r_{mi}^2) \\ &= \frac{\pi^2 f \epsilon_o V^2}{2 g_m (1 + \frac{\epsilon_b g_m}{\epsilon_o \Delta})} (r_{mo}^2 - r_{mi}^2) \end{aligned} \tag{2.24}$$

This representation will be used in the system design to explain trends, while the numerical solution of the actual discretized stator potential (Eqn. 2.16) will be used for all calculations.

The use of discrete electrodes to create the stator waveform introduces important considerations in order to accurately predict the gross mechanical power and determining the operating limits of the motor. The following sections will detail the effects of discrete electrodes on the magnitude of the harmonics and on the voltage limits to prevent breakdown between adjacent electrodes.

Number of phases

One main design parameter is the number of phases, i.e. the number of electrodes used to discretize one period of the waveform. Two competing effects guide the number of phases will be discussed, motivating the choice of a 6 phase configuration.

Minimal electrode line width and spacing The electrode line width and spacing are limited to a practical value l_{min} which is constrained by fabrication capabilities. There is therefore a maximum number of electrodes practically achievable for a circumference of $2\pi r$. The total number of electrodes is split into m poles of p electrodes each, such that: $p\, m\, 2l_{min} \leq 2\pi r$, or otherwise stated $p \propto 1/m$. From the approximate expression of electromechanical torque (Eqn. 2.23), the number of poles should be maximized in order to achieve higher power, suggesting that the least number of phases is preferable.

Inter-electrode breakdown limits Breakdown considerations however limit the maximum voltage difference which can be sustained between adjacent electrodes. A limit of 300

V difference is suggested by Paschen's curve [59] in order to prevent breakdown in air, and is taken as a maximum design value. The voltage difference ΔV between two sinusoidally excited adjacent electrodes of a pole discretized with p electrodes is illustrated in Figure 2-7, and can be expressed as:

$$
\begin{aligned}
\Delta V &= V_i - V_{i+1} && (2.25)\\
&= |\hat{V}|\Big(sin(\omega t) - sin\Big(\omega t - \frac{2\pi}{p}\Big)\Big) && (2.26)
\end{aligned}
$$

which reaches a maximum during one period when:

$$\frac{\partial \Delta V}{\partial t} = |\hat{V}|\,\omega\,(cos(\omega t) - cos(\omega t - \frac{2\pi}{p})) = 0 \tag{2.27}$$

corresponding to:

$$cos(\omega t) = cos(\omega t - \frac{2\pi}{p}) \quad \rightarrow \quad \omega t = -\omega t + \frac{2\pi}{p} \quad \rightarrow \quad (\omega t)_{\Delta V_{max}} = \frac{\pi}{p} \tag{2.28}$$

The highest alternating voltage magnitude $|\hat{V}|_{max}$ which can be applied to the electrodes, while respecting the maximum ΔV_{max} admissible before breakdown, is then expressed by substituting 2.28 into 2.26 as:

$$\frac{|\hat{V}|_{max}}{\Delta V_{max}} = \frac{1}{2\,sin(\pi/p)} \tag{2.29}$$

Since the power delivered by the motor is a function of the square of the applied voltage, it is desirable to discretize each pole with more electrodes. Figure 2-9 quantifies this effect by plotting the square of $|\hat{V}|_{max}/\Delta V_{max}$, a measure of maximum achievable torque, for two to six electrodes per phase.

Combined effect The number of phases for maximum motor power is a combination of the limited number of electrodes and the breakdown limit between adjacent electrodes. This is simply expressed by $|\hat{V}|^2_{max}/p$ (since $P_{elec} \propto m|\hat{V}|^2$ and $m \propto 1/p$, and illustrated in Figure 2-10.

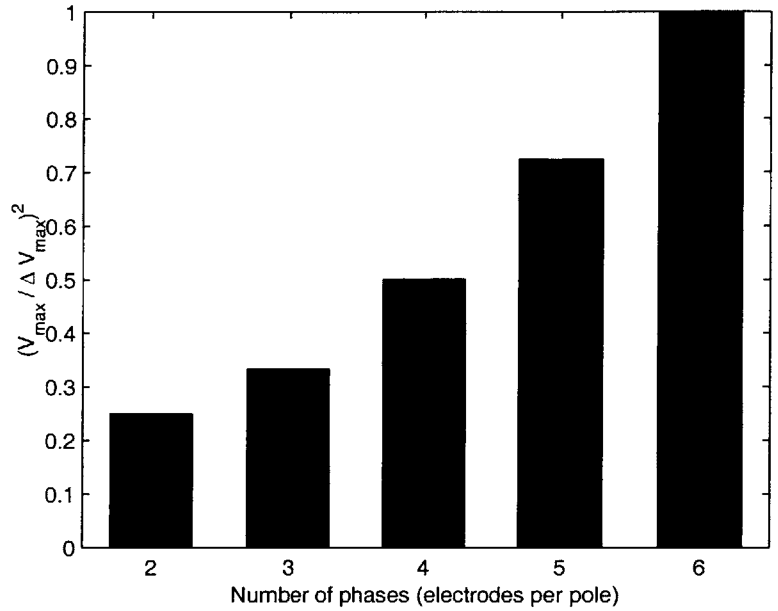

Figure 2-9: A measure of motor power as a function of the number of electrodes used to discretize the waveform, for constant voltage breakdown limit between adjacent electrodes (sinusoidal excitation).

A 6-phase design was finally chosen since it provides a high level of power, while allowing the possibility to operate the motor as a 2-phase or 3-phase machine by externally re-wiring the phases. As will be discussed in the following section, a high number of phases is even more beneficial, due to the presence of backward traveling waves in discretized waveforms.

Backward traveling potential waves

The decomposition of the traveling waveform yields harmonics which travel in the same direction, and others which travel in the opposite direction. In the case of the 6 phase discretization, the fundamental and seventh harmonics ($n = 1, 7$) travel in the direction of the waveform, while the fifth harmonic ($n = -5$) travels in the opposite direction. Figure 2-11 illustrates the waveform and these three harmonics, as a function of time, illustrating their direction of travel.

The backward traveling harmonics will apply a counter-rotating torque, effectively reducing the net power delivered by the motor. It is therefore desirable to minimize their occurrence. Figure 2-12 illustrates the magnitude of the harmonics for the 6 phase discretization, showing the dominance of the fundamental.

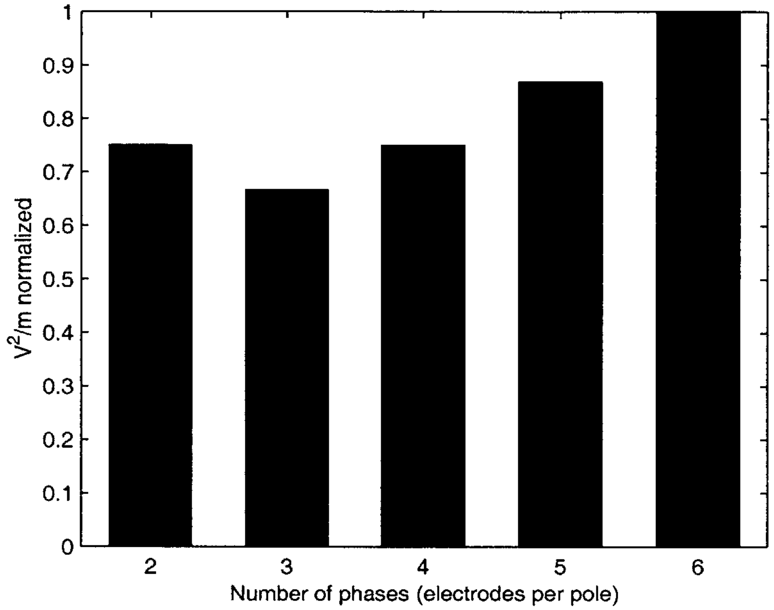

Figure 2-10: A measure of motor power as a function of the number of electrodes used to discretize the waveform.

Inter-electrode potential

Adjacent electrodes must be insulated from each other and separated by a gap to prevent leakage and breakdown. In order to calculate electrostatic forces using the analytical expressions, the potential over the entire stator surface[3] must be known, including its value between the electrodes. The inter-electrodes potential is floating, and assumed to vary from a linear profile between electrodes to a uniform average value of adjacent electrodes. Figure 2-13 shows the impact of two extreme potential distributions on the motor power, as a function of electrode duty-cycle[4]. The dashed lines assume a linear distribution of potential, while the solid lines assume that the potential between electrodes is grounded. A large difference is noted, motivating further investigation.

An iterative combination of the analytical electrostatic induction modeling and Finite Element Modeling (FEM) was used to study the fields in the stator structure. As a result, it was found that the profile varies from a linear distribution to a constant value of the average between adjacent electrodes. The average profile was then used for all subsequent

---

[3] The electrode surface is defined as the plane level with the top of the electrodes.

[4] The electrode *duty-cycle* is defined as the proportion of active electrode area with respect to total stator area. A value approaching 1 indicates wide electrodes and thin inter-electrode gaps, while a duty-cycle approaching 0 represents thin electrodes and large gaps.

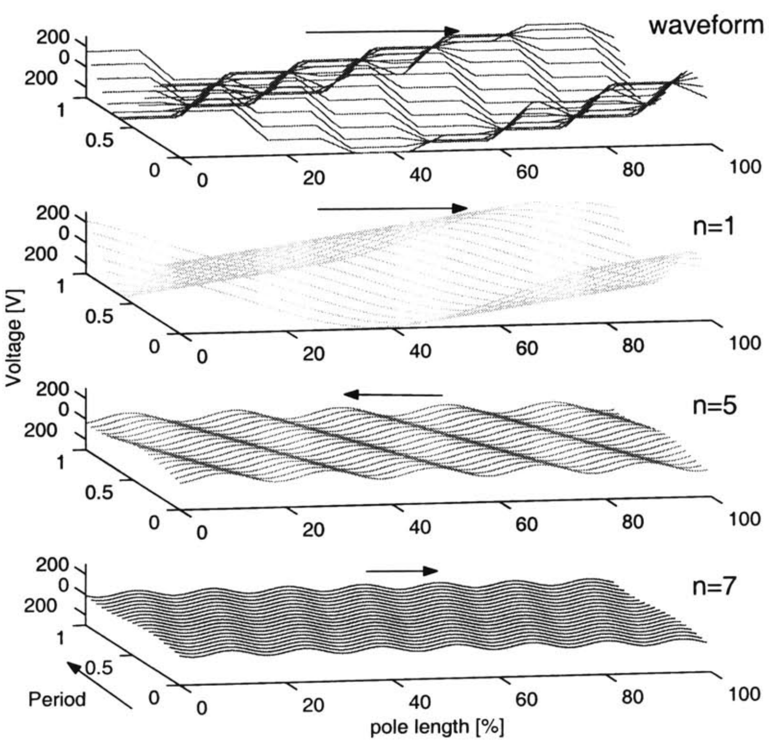

Figure 2-11: Stator potential distribution as a function of time: discretized waveform (top plot) and its harmonic decomposition, n = 1,-5,7 in second, third and forth plots respectively. Potential distribution is shown as a function of time, for one period of the discretized waveform.

design purposes, since it results in conservative predictions of motor torque.

Spacing between the electrodes also affects the viscous drag in the motor gap, since etched areas between electrodes locally increase the gap. This possibility prompted detailed analysis of the viscous flow in the motor gap, which will be the topic of the following section.

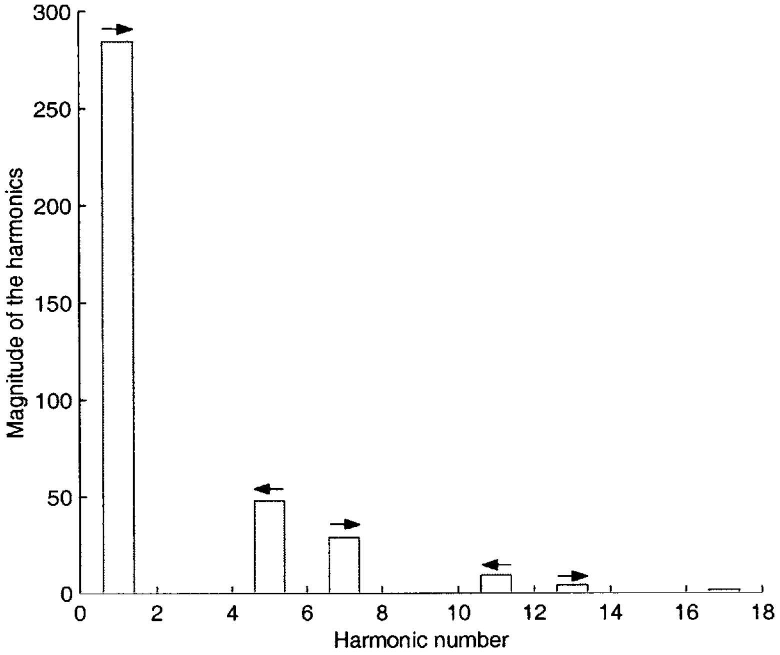

Figure 2-12: Magnitude of the harmonics forming the stator potential when discretized with 6 electrodes. Arrows to the right and left indicate forward and backward traveling waves, respectively.

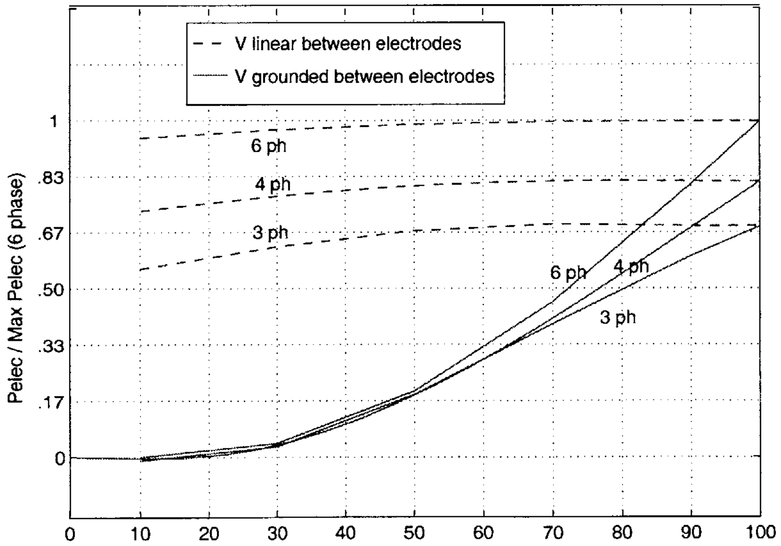

Figure 2-13: Predicted motor power as a function of duty-cycle, for 3, 4, or 6 electrodes per pole.

2.3.3 Viscous flow in the motor gap

The combination of a high-speed rotor and a small gap results in highly sheared flow in the motor, as illustrated in Figure 2-14. This viscous dissipation was found to be significant compared to the motor electrical power, and deserved special attention. This section summarizes the analysis of the flows in the motor gap, while a more detailed presentation of the analysis is given in Appendix A.

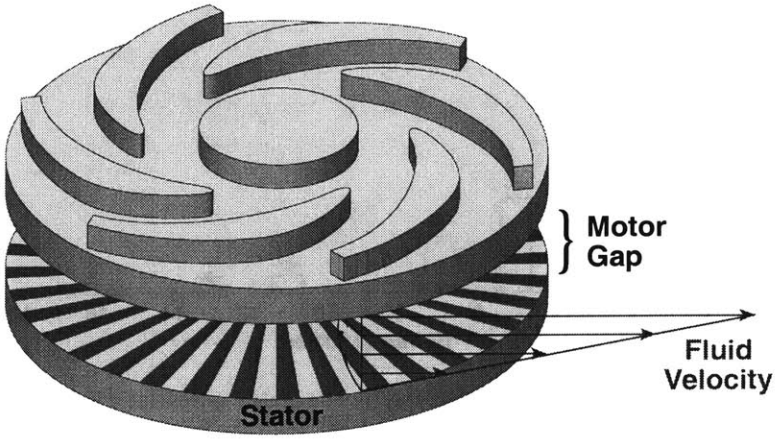

Figure 2-14: Schematic of viscous drag in the motor gap (axial dimension of the gap has been exaggerated for illustration purposes).

In general terms, the motor gap area can be viewed as an annular disk region extending from an inner motor radius r_{mi} to an outer radius r_{mo}. The bottom surface is stationary, while the top surface rotates. Static pressures can be applied at the outer radius (P_{mo}) and inner radius (P_{mi}), with $P_{mo} > P_{mi}$ for the nominal Motor-Compressor configuration. At atmospheric pressures, rarefaction of the air starts to become apparent for gaps of less than 1 micron [45]. Since the nominal gap is 3 μm , and usually pressurized slightly above the ambient pressure (by the journal and thrust bearing hydrostatic pressures), the fluid can be treated as a continuum and modeled by the Navier-Stokes equations. Two cases are described in this section: that of a motor gap with a smooth electric stator (electrode surface) and with a grooved electric stator.

Smooth stator Two velocity components are of interest: tangential and radial. The radial velocities define the mass flow through the motor gap, while the tangential velocities near the disk define the viscous torque. From the order of magnitude analysis presented in Appendix A, viscous effects dominate the motor gap flow. The inertial terms (including Coriolis and centrifugal forces) do not affect the tangential velocity profile, such that the tangential component of the Navier-Stokes equations simplifies to simple Couette flow, giving a shear stress per unit area of:

$$\tau_\theta = \mu \frac{\partial V_\theta}{\partial z} = \mu \frac{\Omega r}{g_m} \tag{2.30}$$

The fluid shear stress is therefore a linear function of radius, rotational speed, and viscosity; and is inversely proportional to the motor gap height. The viscous torque in the motor gap is the integral from the inner to outer radius of the product of shear stress, radius, and unit area:

$$T_{visc,motor} = \int_{r_{mi}}^{r_{mo}} r \cdot \tau_\theta \, dA = \mu \frac{\pi \Omega}{2 g_m} (r_{mo}^4 - r_{mi}^4) \tag{2.31}$$

The power dissipated in the motor gap is then:

$$P_{visc,motor} = \Omega \cdot T_{visc,motor} = \mu \frac{\pi \Omega^2}{2 g_m} (r_{mo}^4 - r_{mi}^4) \tag{2.32}$$

The negligible inertial effects due to rotation were confirmed through a numerical calculation of the motor gap flows. These CFD calculations have also shown that the flow entering the motor gap at the outer radius is rapidly set into fully developed rotation, i.e. the inertia in the entrance region is negligible. The simple Couette flow approximation is therefore appropriate for modeling the flow in a motor with a smooth electrode surface. Appendix A expands on the effects of rotation and the validity range of this approximation.

Grooved stator

The actual electrode fabrication will not result in a smooth stator, since the electrodes will be formed by patterning a 1 μmthick polysilicon layer. Furthermore, etching deeper trenches between the electrodes can potentially reduce the viscous drag in the motor. The motor gap geometry is therefore a disk rotating over several hundred thin radial trenches, which can be deep or shallow. Numerical predictions of the motor gap flows with a grooved stator were performed in order to determine the effect of these trenches on drag. Comparison of 2-D and 3-D solutions has shown that the radial flow, centrifugal, and Coriolis effects do not significantly affect the drag prediction. The 3-D domain was therefore modeled as a sum of 2-D sections, taken in the circumferential direction. Figure 2-15 shows a 2-D section, labeled with the main geometric parameters describing the geometry at a given radius: the motor gap height (g_m), the electrode and trench widths (w_e and w_t respectively) and the trench depth (h_t).

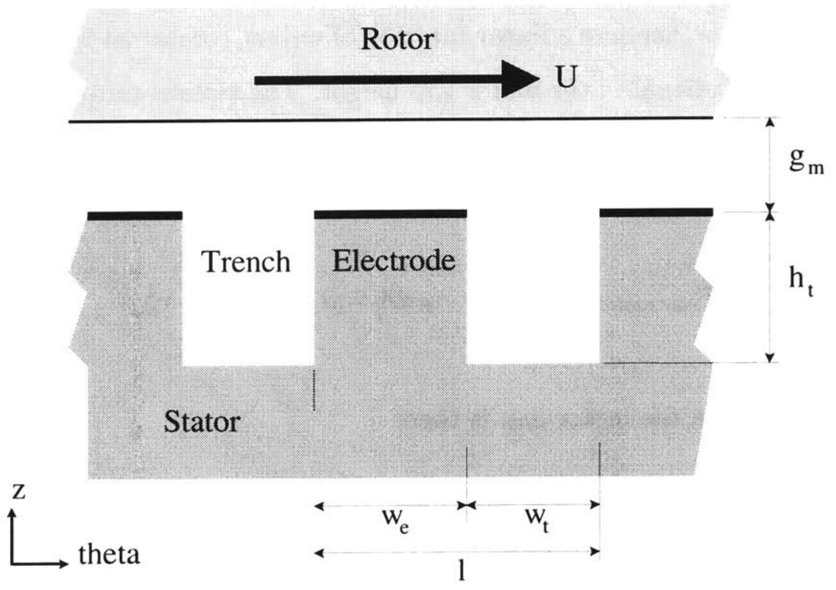

Figure 2-15: Section through the motor gap, taken in the circumferential direction.

The drag on the rotor for such a configuration can be represented by four non-dimensional parameters, of which *dc* is referred to as the duty-cycle and Re_g, the gap Reynolds number:

$$l^* = \frac{w_e + w_t}{g_m};\ h^* = \frac{h_t}{g_m};\ dc = \frac{w_e}{w_e + w_t};\ Re_g = \frac{\rho \Omega r g_m}{\mu} \tag{2.33}$$

The relevant graphs for design are shown in Appendix A, in which the percentage drag reductions from the smooth stator case are shown as a function of the three first non-dimensional parameters: l^*, h^*, and dc (initial analysis has shown that the Reynolds number has very little influence on the drag in our range of interest[5]). We notice that the drag is

---

[5] The Reynolds number for Couette flow has no significance, since the flow is purely viscous. In the case with trenches, inertial effects appear as the flow transitions from the small gap to the trench region and vice

always reduced by the presence of inter-electrode trenches, and that deeper, wider trenches are better.

Baseline design Drag reduction of up to 25 % was predicted, but can only be achieved for excessively wide and deep trenches (only 15% of electrode area). Given this limited benefit and the fabrication complexity in creating such a geometry, the design settled for 1 μm deep and 4 μm wide grooves naturally created when etching the electrodes. The duty-cycle varies from 73% to 50% from the outer to inner radii. The CFD calculations predict a 4% drag reduction for this configuration. In comparison, the assumption that the local gap increase directly reduces the drag according to the Couette flow expression (inversely proportional to the local gap) would predict a 9% drag reduction. This discrepancy is even more pronounced for deeper trenches, confirming the need for this CFD analysis.

Alternate motor gap geometries

The potential for drag reduction in the motor gap was further explored by relaxing the fabrication concerns. Various features on the stator and rotor were analytically and computationally evaluated for their drag reduction potential. In addition to the smooth and grooved stator, Figure 2-16 illustrates two other configurations: floating electrodes and beveled electrodes.

The floating electrodes configuration represents undercut electrodes, allowing tangential flow under the electrodes. The benefit was negligible compared to the grooved stator, mostly from the fact that the drag in the small gap over the electrodes completely dominates the overall drag. It was found that the flow goes through a sharp pressure gradient as it enters the gap area over the electrode (shown by the shaded contours in Figure 2-16), resulting in a large velocity gradient on the disk (local drag increase). When the electrode surface is slanted, as in the beveled electrode configuration, the pressure gradient is reduced, and so is the integral of drag in the disk. This configuration reduced the drag by as much as 30%, but requires fabrication capabilities currently unavailable to make the electrode surface at an angle.

---

versa. The Reynolds number would therefore be better represented by $Re_g \times l^*$. Either way, the effect on drag was not noticeable for variation of this parameter in the possible range for our application.

Smooth Wall

Grooved Wall

Floating Electrodes

Grooves with Beveled Electrode

Figure 2-16: Various stator configurations for drag reduction. Section through the motor gap, taken in the circumferential direction. Pressure field and velocity field are shown by the contours and vectors respectively.

In summary, the drag in the motor gap is mainly dominated by the shear flow between the electrode and the spinning disk, and that increased clearance between electrodes has a limited effect. The drag reduction due to this clearance is less than that predicted from simple Couette flow, and was calculated using CFD. Implementation of higher drag reduction geometries was not judged worth the fabrication complexity, especially for a first generation Motor-Compressor. The relatively large viscous dissipation in the motor gap does not preclude operation, although it imposes larger power requirements on the drive source and reduces the system efficiency. Design trade-offs concerning the motor will be discussed in Section 2.5.

Fluid dynamics of components other than the motor, such as the bearings, were also of importance, as will be discussed in the following section.

2.4 Bearings and Rotordynamics

As for any rotating machine, bearings are required to support the rotor and allow it to rotate freely while constraining its motion in the other degrees of freedom. A wide variety of bearings are available for conventional scale rotating machinery, such as ball bearings, roller bearings, gas or liquid lubricated bearings, foil bearings, and magnetic bearings. A similar selection has not yet been developed for microfabricated devices.

In the Motor-Compressor and Bearing Rig configuration, a pair of thrust bearings support the axial motions of the rotor, and a journal bearing on the periphery of the disk supports the in-plane motion (illustrated in Figure 2-1). The requirements on this bearing system can be summarized as:

- Load capability: counteracting pressure forces, inertial forces, and imbalance loads
- Stability: stable operation up to high rotational speeds;
- Low friction: the high ratio of surface area to volume at small scales suggests that friction losses become more important than at large scale, so low friction bearings are desirable;
- Compatibility of lubrication fluid (if any): with electrical and fluidic components;
- Manufacturability: according to silicon microfabrication capabilities;
- Integration: with high-speed micro-turbomachinery and the micromotor.

Gas-lubricated bearings were chosen, mostly for their compatibility with the last four requirements. The low viscosity of gases reduces the impact of high surface to volume ratio, compared to liquid lubrication or dry friction. The same gas as the compressor can be used (typically air), precluding the need for a secondary lubricating system. The bearings can be manufactured in the silicon wafer, in parallel with the other components. Furthermore, the geometry does not include any additional free parts, which is convenient since conventional configurations (such as ball or roller bearings) are not readily reproducible with silicon micromachining.

Of primary concern has been the stability of gas journal bearings in the design space accessible using microfabrication technology (low aspect ratio). An experimental investigation of the operating space using a scaled-up bearing test rig was pursued by Orr [41], while Piekos conducted extensive numerical modeling of these gas bearings [44]. Low order modeling of the rotordynamics was also done by Savoulides [50], based on analytical bearing modeling and numerical results from Piekos. The performance of gas thrust bearings was modeled by Jacobson [24] and further studied numerically and experimentally by Lin [29].

Gas bearing principles of operation Two modes of operation were considered for the micro-gas bearings: hydrodynamic and hydrostatic. *Hydrodynamic* gas bearings operate on the principle that pressure in a lubricating film can be created from the motion of one of the bearing surfaces. *Hydrostatic* gas bearings make use of pressurized gas provided to the bearing in order to sustain the lubrication film. Stiffness is achieved by devising a geometry which creates restoring pressure forces on the rotor when it is displaced from its steady-state equilibrium position.

Originally, hydrodynamic journal and thrust bearings were preferred, since they are simpler to microfabricate, do not require external components, and were predicted to be adequate at the high design rotational speeds. In practice, hydrostatic bearings have been chosen for experimental devices, since their stiffness can be controlled independently from the rest of the system. Although the bearing fluids are currently supplied from an external pressurized tank, they could theoretically be tapped from an optimum location in the compressor flow path[6]. This level of inter-dependent component interaction was however undesirable for the initial experimental devices.

This section provides an overview of the microfabricated bearing operation and modeling for system design purposes. Further details can be found in the body of work listed above.

2.4.1 Hydrostatic thrust bearing operation

The Motor-Compressor development devices use a pair of central hydrostatic thrust bearings, operating from externally pressurized gases.

---

[6] Based on results presented later in the thesis, 15-30% of the main compressor flow would be necessary to operate the hydrostatic bearings, although it is inconclusive if the available pressures from the compressor will be sufficient. In particular, the thrust bearings have only been operated as low as 35 psig, which is more than the pressure delivery of the compressor at design speed (15 psig).

Applying a high pressure to the feed plenum, the gases flow through two main restrictor elements in series: axial orifices (capillary resistance), and a radial outflow gap (Figure 2-17). The pressure in the center of the thrust bearing gap is equal to the feed pressure minus the drop across the orifices. Flow is then driven radially outward through the gap between the rotor and the stator thrust bearing pad. This second resistor varies with the position of the rotor, since the axial clearance changes. This variable resistance creates a restoring axial force on the rotor: if the rotor moves upwards (towards the forward thrust bearing), the gap in the forward thrust bearing is reduced, restricting the flow rate. This results in a lower pressure drop across the orifices, and hence a higher pressure in the gap, for a constant feed pressure. The higher pressure on the front side of the disk creates a downward force, pushing the rotor back to its original position. Both thrust bearings provide such a restoring force, adding to the axial stiffness. Since independent orifices are distributed circumferentially at a radius r_i from the center, the same stiffness principle acts as a restoring torque when the rotor is tilted.

The thrust bearing design for axial balance and tilting stiffness will be presented in the following sections, but first, the secondary flow system will be described.

2.4.2 Secondary flow configuration

The pressurized gases are brought to the bearings through micromachined channels and plena within the silicon die. Relatively large ports (100's μm in diameter) are located on the top and bottom surfaces on the die, as an interface with the packaging. Internal passages then channel the flows through the outer wafers, through the micron scale bearing features, and back out through relatively large exhaust channels. Some of the bearing flow also combines with the compressor main flow path. Piping for the secondary flows (i.e. for the bearings) constitutes most of the features on 4 of the 5 wafers, and are an integral part of the device.

Of main interest is the back side of the disk. It serves many functions, such as providing axial and tilting stiffness, axial and lateral load balance, as well as electromechanical energy transmission to the rotor.

Figure 2-18 shows a drawing of the top side of the aft end plate (which faces the back side

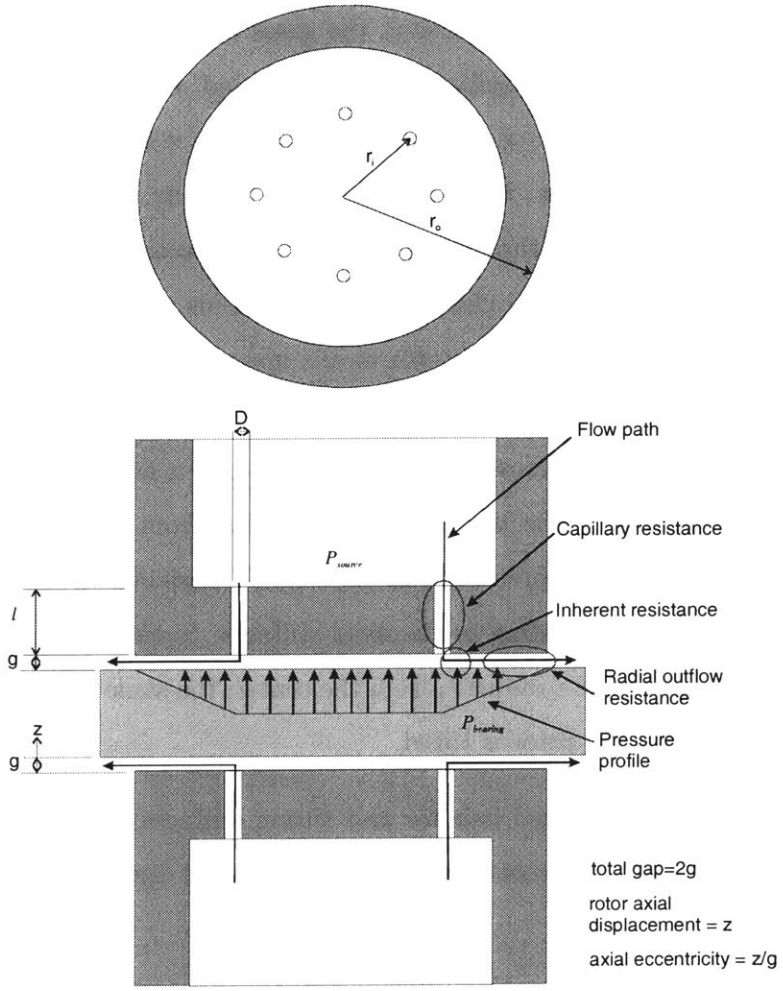

Figure 2-17: Schematic of hydrostatic thrust bearings (from Lin [29]).

of the rotor). In the center, is located the Aft Thrust Bearing (ATB) and a circumferential aft exhaust plenum surrounding it. Further outwards, is located the electrostatic induction motor. Although the active motor area nominally extends from a radius of 1.0 mm to 1.9 mm, extra radial extent is necessary at the inner and outer radii to accommodate fabrication tolerances and to allow for slight process flow variations. The motor is then surrounded by a plenum, referred to as the Motor Outer Plenum (MOP). It serves as an axial load balance piston, changing the static pressure in the motor gap, through an externally controlled MOP pressure. Although it does not provide axial stiffness, it can apply an axial force on the rotor to change the axial position, independently of the thrust bearing or other pressures.

Two symmetric plena surround the MOP, which are aligned with the aft end of the journal bearing gap, and are referred to as the high and low journal pressurization plena (High JPP

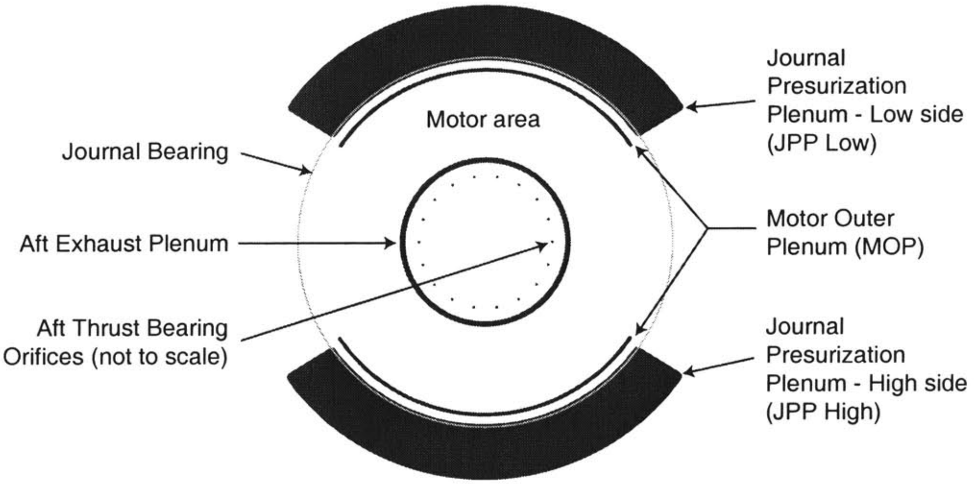

Figure 2-18: Aft plenum configuration. The motor (not shown here) occupies the area between the Motor Outer Plenum and the Aft Exhaust Plenum.

and Low JPP). The journal pressurization plena are separated from the motor outer plenum (MOP) by a simple flat face seal. The nominal gap between the seal face and the rotor is designed to be the same as the ATB gap (1.5 μm). This is therefore the point of contact if the rotor tilts excessively. This mechanical stop prevents the rotor and stator electrical components from coming into contact. Two opposing bridges extend from the motor area between the symmetric MOP and JPP to support the electrical leads of the stator. Each JPP occupies 120°, leaving $2 \times 60°$ for the electrical leads.

Figure 2-19 illustrates the internal flow paths in the die. Trenches or cavities in the microfabricated device are shown here in reverse polarity, as piping and reservoirs. For example, the forward thrust bearing flow path enters the port on the die surface, flows along a lateral pipe, to a circular reservoir and finally out of the array of capillary orifices. Similarly, the compressor flow path is shown, as opposed to the blades themselves.

2.4.3 Thrust bearing design: stiffness, load balance, and drag

The axial forces acting on the rotor are illustrated in Figure 2-20. Most pressure forces are not a function of the axial position of the rotor, and are externally controlled. Since the MOP pressure serves the sole function of providing axial balance, other components may be operated for their main function without affecting the axial force balance.

In particular, the thrust bearings in this device are mainly intended to provide a restoring

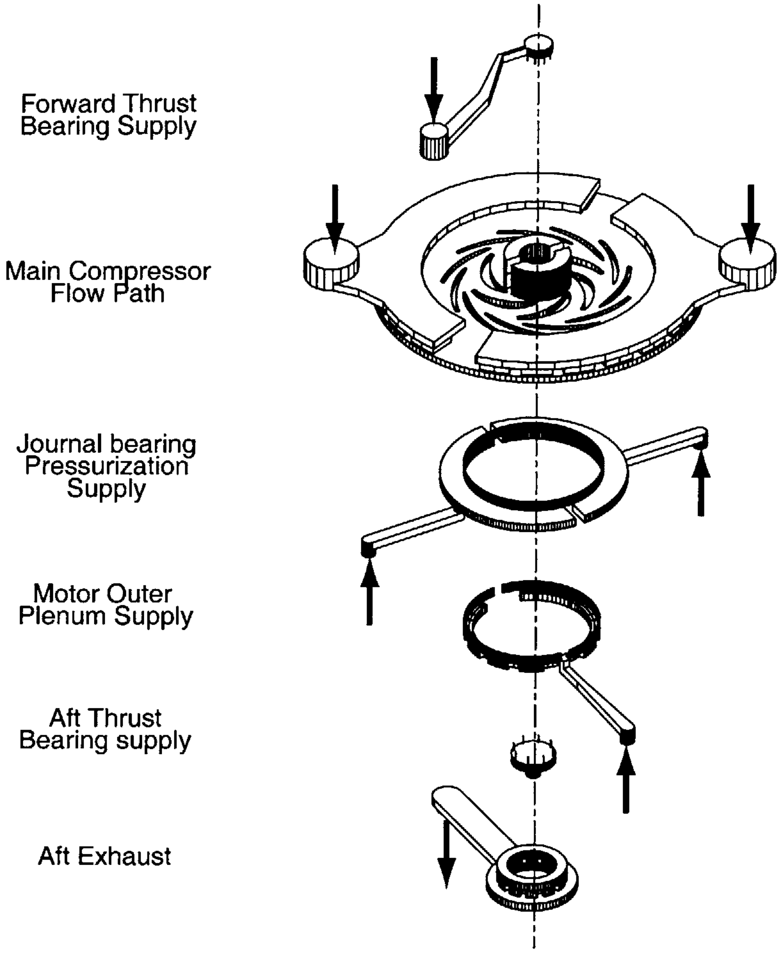

Figure 2-19: 3D view of the secondary flow piping.

axial and tilting stiffness, which must overcome the destabilizing electrostatic forces.

Stiffness from the hydrostatic thrust bearings was found to be maximal when approximately half of the pressure drop occurs over the orifices. A design study varying the forward and aft thrust bearing geometries yielded the configuration described in Table 2.3. The forces and flows were predicted using a combination of empirical flow restriction models, developed by Jacobson [24] and investigated by Lin [29]. The thrust bearings in this device are larger than those implemented by Lin [29] in the first generation bearing rig, due to the additional requirement to withstand the electrostatic forces from the micromotor.

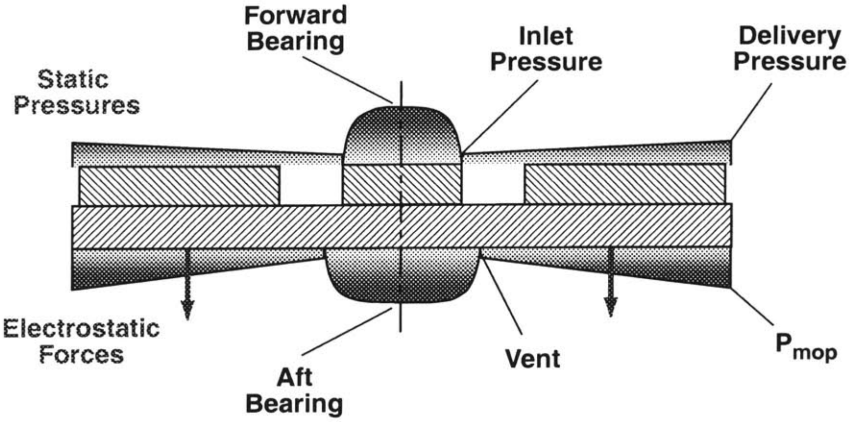

Figure 2-20: Schematic of axial pressure and electrostatic forces acting on the rotor.

Component		
Forward Thrust Bearing	Type	Hydrostatic
	Axial gap	1.5 μm
	Outer radius	0.7 mm
	Orifices: number and location	14 r=0.55mm
	Orifice diameter	10 μm
	Orifice length	100 μm
Aft Thrust Bearing	Type	Hydrostatic
	Axial gap	1.5 μm
	Outer radius	0.9 mm
	Orifices: number and location	18 r=0.75mm
	Orifice diameter	10 μm
	Orifice length	100 μm

Table 2.3: Thrust Bearing Geometry for the Demo Motor-Compressor.

The change in axial pressure force from the thrust bearings is plotted in Figure 2-21, as a function of distance off-equilibrium. Also plotted is the change in electrostatic attraction force from the motor, based on Eqn. 2.17. We notice that the thrust bearings provide a restoring force larger than the opposing electrostatic force, over an operating range of at least 0.5 μm on either side of the central position (3 μm motor gap). The electrostatic forces were calculated using the modeling approach presented in Section 2.3.2.

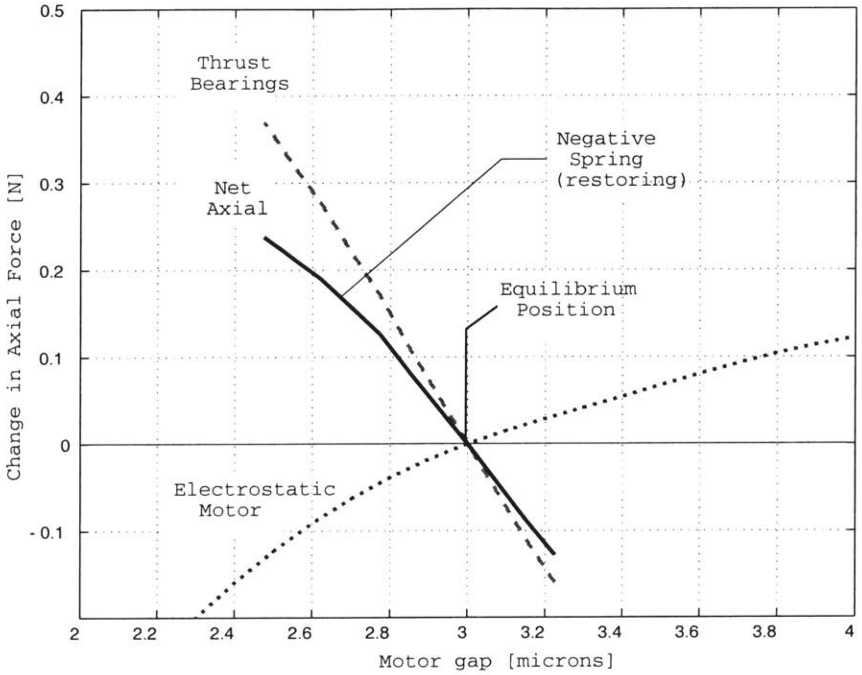

Figure 2-21: Axial bearing pressure forces and motor electrostatic forces acting on the rotor as a function of displacement from equilibrium (motor gap of 3 μm).

Tilting stiffness

Destabilizing torques are created by the electrostatic induction motor, and were modeled by accounting for the varying gap around the circumference when integrating the normal force equation 2.17 over the motor area. Restoring tilting moment from the thrust bearings were calculated by R. Walker from Draper Laboratories using a model developed by MTI [35] for the bearing configuration in Table 2.3, and found to be larger than the electrostatic moment.

Drag prediction

The drag in the thrust bearings is approximated by the same equation as the drag in the motor gap with a smooth stator, repeated here for convenience. Once again, the tangential flow is dominated by viscous effects, such that it can be represented by simple Couette flow.

$$P_{visc,tb} = \Omega \cdot T_{visc,tb} = \mu \frac{\pi \Omega^2}{2 g_{tb}} (r_o^4 - r_i^4) \tag{2.34}$$

The other areas on the aft side of the disk will also incur losses, and will also be modeled as fully developed Couette flow. To reduce the drag on these areas, the depth of the plena was increased up to 200 μm.

2.4.4 Journal bearing

The journal bearing is formed by the thin air gap surrounding the disk. This gap is created by etching a deep and narrow circular trench from the back side of the rotor wafer, simultaneously cutting out the rotor disk. The baseline configuration consists of a plain circular bearing with a minimum width of 10 μm and maximum depth of 300 μm , limited by the fabrication technology. This constraint positions viable designs out of the traditional gas journal bearing design space, since it limits the geometry to a relatively short gap. Hydrodynamic and hydrostatic modes of operation applicable to our unique configuration will be presented next.

Hydrodynamic operation In-plane stiffness was initially intended to come from hydrodynamic pressure forces. By applying a lateral force on the rotor, it is displaced off-center, and the moving rotor surface creates a pressure build-up in the region of smaller gap (Figure 2-22). At low eccentricity, this hydrodynamic pressure force is typically orthogonal to the applied force, inducing the rotor into a whirling orbit. As the rotor is pushed to higher eccentricity, the hydrodynamic pressure force vector rotates in-line and opposite to the applied force, allowing for a stable operating position. As detailed by Piekos [44], microfabricated plain journal bearings must operate at eccentricities on the order of 90% or higher for stable operation[7]. The journal pressurization plena can be used to apply the lateral force, by supplying a pressure difference between the high and low plena.

---

[7] For a 10 μm journal bearing gap, this implies operating only 1 μm clearance from the static structure.

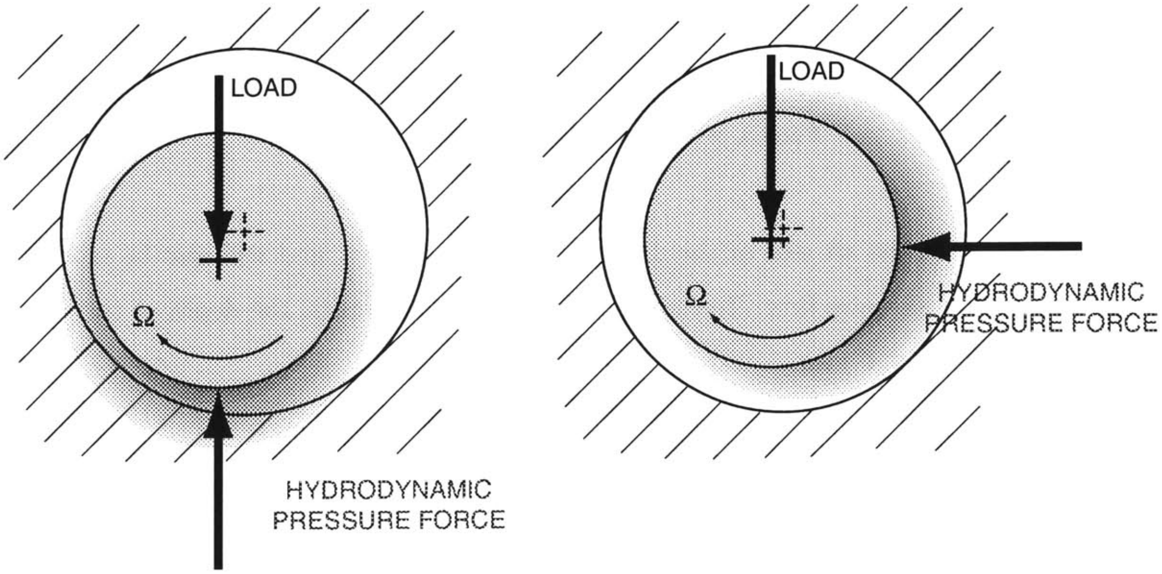

(a) High eccentricity: stabilizing

(b) Low eccentricity: destabilizing

Figure 2-22: Illustration of change in orientation of hydrodynamic journal bearing forces for low and high eccentricity.

Hydrostatic operation An alternative mode of operation was experimentally demonstrated by Orr [41], using externally pressurized gases. In hydrostatic journal bearing operation, a pressure difference between the journal pressurization plena and the front side of the disk drives the gases axially through the journal gap. Figure 2-23 illustrates the hydrostatic operation. When the rotor is centered, axial flow sets a pressure distribution along the gap, which is symmetric on both sides. The pressure profile is defined by the entrance losses of the flow entering the gap, followed by a linear pressure gradient once the flow is fully-developed[8]. Upon a disturbance, the rotor is displaced, increasing the gap and flow rate on one side, while decreasing them on the other. The higher entrance loss on the large gap side results in a lower local pressure force, and vice-versa on the small gap side[9]. The result is a restoring net pressure force on the rotor. This approach was used throughout the experiments here to support the in-plane motion. In this case, pressures in the High and Low JPP are equilibrated, even though they are independently controlled.

---

[8] The pressure profile in the fully-developed will be parabolic for compressible flow.

[9] Two possible sources of entrance loss has been identified: the development of the boundary layers in the journal bearing gap (Piekos [44] and Orr [41]), and the flow transition from the journal pressurization plena into the narrow journal bearing gap (Jacobson [24]).

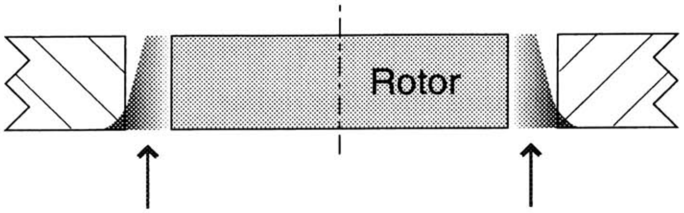

(a) centered rotor

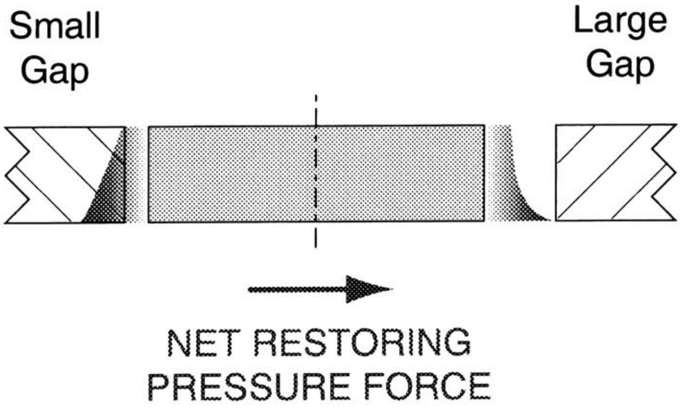

(b) off-centered rotor

Figure 2-23: Hydrostatic journal bearing operating principle.

Journal bearing drag When the journal bearing nominally operates at a certain eccentricity, circumferential pressure gradients are created. The tangential velocity profile between the rotor outer rim and the stationary journal is therefore a superposition of Couette and Poiseuille flows. Since the pressure is periodic around the annulus, the increase in drag on the disk in the positive pressure gradient region on the annulus was found to compensate for the decrease in drag in the adverse pressure gradient region [45]. An approximate drag prediction can be given by integrating the shear stress due to a pure Couette flow around an off-centered rotor, at an eccentricity ϵ:

$$T_{visc,jb} = \frac{1}{\sqrt{1-\epsilon^2}} 2\pi \, \mu \, \Omega r_{jb}^3 \, \frac{l}{c} \tag{2.35}$$

$$P_{visc,jb} = \Omega T_{visc,jb} = \frac{1}{\sqrt{1-\epsilon^2}} 2\pi \, \mu \, \Omega^2 \, r_{jb}^3 \, \frac{l}{c} \tag{2.36}$$

When the rotor is centered ($\epsilon = 0$), the square root in the denominator become unity and the drag is minimized. This is the case for hydrostatic journal bearing operation. The increase in drag as the rotor is moved off-center is shown in Figure 2-24. We notice the strong increase in drag at eccentricities above 0.9. This implies larger journal bearing losses in the hydrodynamic journal bearing operating regime.

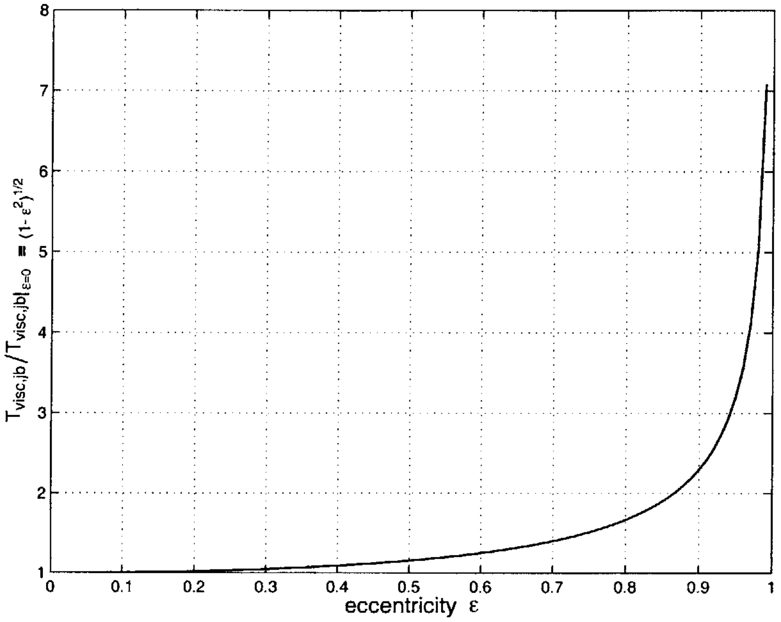

Figure 2-24: Increase in journal bearing viscous drag as a function of eccentricity.

2.5 System Design

To define the dimensions and operating parameters of the Motor-Compressor, simple models of the components were used to predict the behavior of the complete system. This section describes the major system design trade-offs, summarizes the design of the Demo Motor-Compressor, and outlines proposed configurations for μBlower and μCompressor applications.

2.5.1 Power balance and system design trade-offs

At design conditions, the system must be sized such that the power delivered by the motor is sufficient to drive the compressor and overcome all viscous losses in the system. For a pressure ratio of 2:1, a mass flow of 0.1 g/s and a compressor efficiency of 65%, 10W of net mechanical power must be available to drive the turbomachine. To explore design trade-offs, the power accounting is viewed in terms of torque balance on the rotor. The main metric will be the power available for compression (P_{comp}), which is equal to the gross mechanical power from the motor (P_{elec}) minus sum of the viscous losses in the motor gap ($\dot{W}_{visc,motor}$), in the bearings ($\dot{W}_{visc,bearings}$), and over the aft seal and plena ($\dot{W}_{visc,other}$). Based on the models presented in the previous sections, we can calculate the P_{comp} for a given geometry and operation settings:

$$P_{comp} = P_{elec} - (\dot{W}_{visc,motor} + \dot{W}_{visc,bearings} + \dot{W}_{visc,other}) \tag{2.37}$$

One of the main parameters to be determined is the dimensions of the motor. As discussed in Section 2.3, other motor parameters have been determined for maximum power: the number of phases was chosen to be 6, the maximum voltage 300V, the minimum electrode width 4 μm, and inter-electrode spacing also 4 μm. The motor inner and outer radii will be determined here, trading between viscous drag in the motor gap and electrostatic induction torque.

Effect of disk radius

Figure 2-25(a) shows the net mechanical power available for compression work for the baseline Motor-Compressor configuration, as a function of motor outer radius. Each line is for a rotor disk of different diameter. Along each line, the motor outer radius is varied until it reaches the journal bearing radius. Figure 2-25(b) shows the corresponding energy conversion efficiency, from electrical power into the microfabricated device, to net mechanical compression power available.

We first note that the output power level increases with diameter, which is simply the result of increased motor active area (i.e. increased P_{elec}). For a given rotor diameter, there is a motor outer radius for which net power reaches a maximum. As the motor outer radius is initially increased, increments in active area increase the motor electrical power, as well as viscous losses but in a smaller fraction. At a certain point, identified by the maximum in the efficiency curves, the percentage increase in motor electrical power is equal to the percent increase in viscous drag in the motor gap. The net power still grows, but with no further improvement in efficiency. Adding motor active area beyond this radius adds more viscous torque than electrical torque. This limits the net mechanical power output, and reduces the electrical to net mechanical power conversion efficiency.

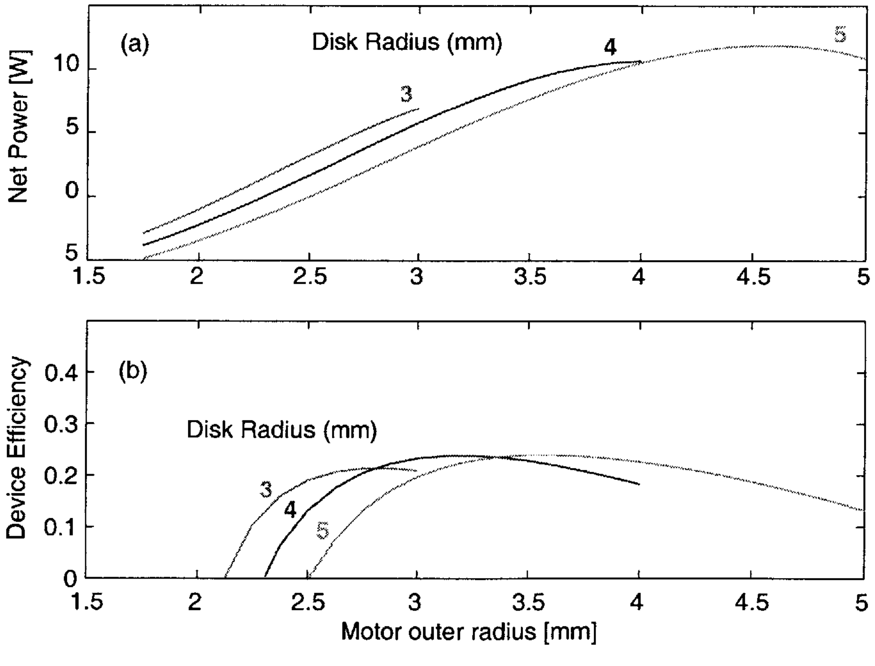

Figure 2-25: Predicted performance as a function of motor outer radius, for different rotor diameters, and constant tip speed of 400 m/s.

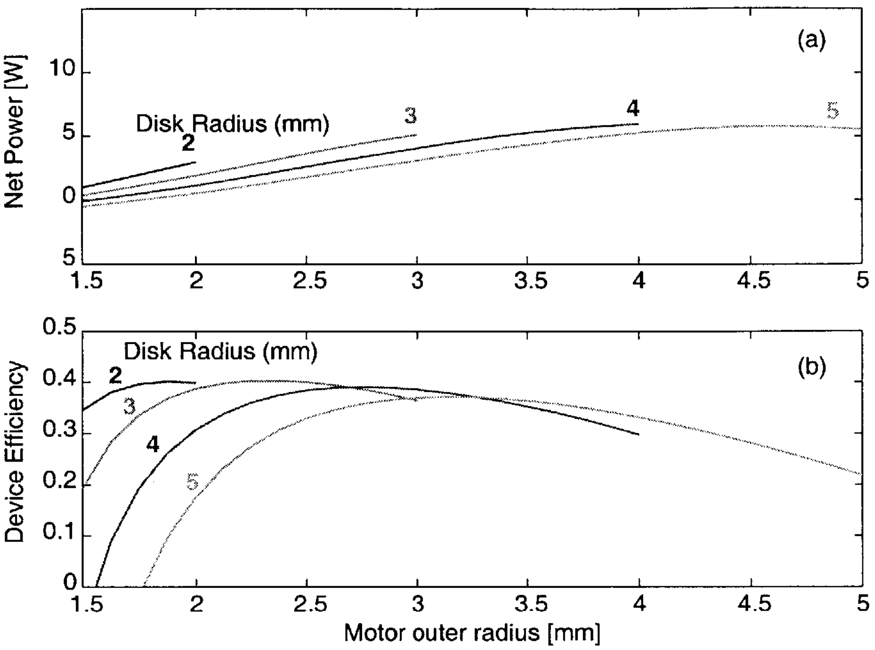

Figure 2-26: Predicted performance as a function of motor outer radius, for different rotor diameters, and constant tip speed of 200 m/s.

Effect of tip speed

Figure 2-26 shows the same design trades as Figure 2-25, but for a lower tip speed of 200 m/s as opposed to 400 m/s. Comparing both figures, We notice that less power is available for compression work, but on the other hand, the energy conversion efficiency is higher.

This is shown by the simplified equations. Since the electric power is proportional to tip speed, while the viscous dissipation is proportional to tip speed squared, lower speed results in higher efficiency.

Overall, these studies have identified the main trend that increasing disk radius increases the power output, while lowering the tip speed mainly improves the efficiency.

2.5.2 Demo Motor-Compressor design

This section summarizes the design of an experimental motor-compressor development test-bed, referred to as the "Demo Motor-Compressor". It aims to validate the Motor-Compressor concept and guiding the design and development path for application specific devices. It will allow a first demonstration of an integrated micromotor-driven turbomachine supported on gas bearings, by aiming to:

1. Develop the fabrication process to integrate the thin film micromotor in a bonded silicon wafer stack;
2. Demonstrate simultaneous operation of the microfabricated gas bearing, micromotor technology, and microturbomachinery;
3. Validate the modeling assumptions and basic understanding of the integrated operation;

Inherited design specification

Unfortunately, all the components forming this device reside in uncharted design spaces. The development risk of a system integrating all new components was reduced by limiting the design parameters to geometries previously studied by other researchers as part of this project. Three main design parameters were constrained in order to build on the limited experience gained in related work:

- The *rotor disk diameter* was chosen to be on the order of 4 mm, to build on previous bearing rig fabrication and operating experience;
- A plain *journal bearing* configuration with an aspect ratio of 30:1 was chosen to take advantage of the extensive numerical and macro-scale experimental experience in operating stable bearings, and to have reasonable expectations from the microfabrication;
- The *baseline compressor design* was chosen since it has been experimentally and numerically investigated and shown to provide the requisite pressure rise, at high tip speeds.

Baseline design: Demo Motor-Compressor device

Based on these choices, and on compressor, micromotor, and bearing aspects highlighted in the previous sections, the experimental device configuration summarized in Table 2.4 was chosen.

Component		
Disk	Outer radius	2.1 mm
Compressor	Impeller:	
	Blade design	MIT-I99 (2 : 1)
	Number of blades	6 blades
	Blade extent	r= 0.98 to 1.95 mm
	Diffuser:	
	Blade design	MIT-H36 (2:1)
	Number of blades	11 blades
	Blade extent	r= 2.37 to 2.96 mm
Motor	Type	Electrostatic induction
	Number of poles and phases	131 x 6 phases
	Number of electrodes	786 electrodes
	Excitation	±300 Volts, sinusoidal at 2.6 MHz
	Air Gap	3 μm
	Electrode extent	R=1 to 1.9 mm
	Spacing	4 μm , constant w/ radius
	Width	4 to 11.2 μm
	Inter-electrode spacing	4 μm , constant w/ radius
	Rotor film thickness	0.5 μm
	Rotor film conductivity	200 $\mathrm{M}\Omega_{\square}$
	Rotor insulator thickness	10 μm
Forward Thrust Bearing	Type	Hydrostatic
	Axial gap	1.5 μm
	Outer radius	0.7 mm
	Orifices: number and location	14 at r=0.55mm
	Orifice diameter	10 μm
	Orifice length	100 μm
Aft Thrust Bearing	Type	Hydrostatic
	Axial gap	1.5 μm
	Outer radius	0.9 mm
	Orifices: number and location	18 at r=0.75mm
	Orifice diameter	10 μm
	Orifice length	100 μm
Journal Bearing	Type	Plain Hydrostatic
	Length	300 μm
	Width	10-15 μm

Table 2.4: Design parameters for the Demo Motor-Compressor.

The load and motor power curves are shown in Figure 2-27, at the intersection of which is the predicted steady-state design point of 200 m/s tip speed. A relatively high slip of 30 % was chosen for ease of operation for this initial device. It provides a large starting torque and a broad peak at high power operation. A lower slip would reduce the rotor inductive losses, improving efficiency at the expense of lower starting torque and a narrow operating range for maximum power. Also shown in the figure, is the operating line of a disk with no blading (dashed), along which the load is simply viscous drag on the disk.

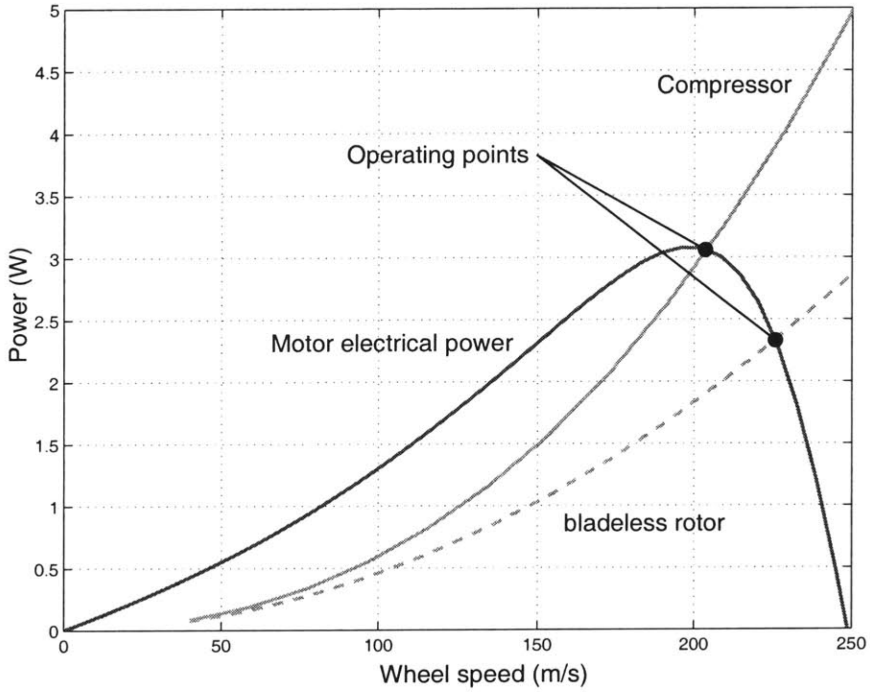

Figure 2-27: Predicted load and motor power curves as a function of tip speed. Steady state operating point is found at their intersection.

2.5.3 Future configurations

Relaxing the inherited design specifications, such as the disk radius and the tip speed, the design space was explored to identify the potential performance for this type of device. The metrics are the power available for compression work and the overall energy conversion efficiency.

Figure 2-28 illustrates three possible configurations: (a) the current motor-compressor 5-stack, (b) increased diameter, 3-stack configuration (by replacing the hydrostatic thrust bearings with a hydrodynamic design); (c) double-motor 4-stack symmetric configuration.

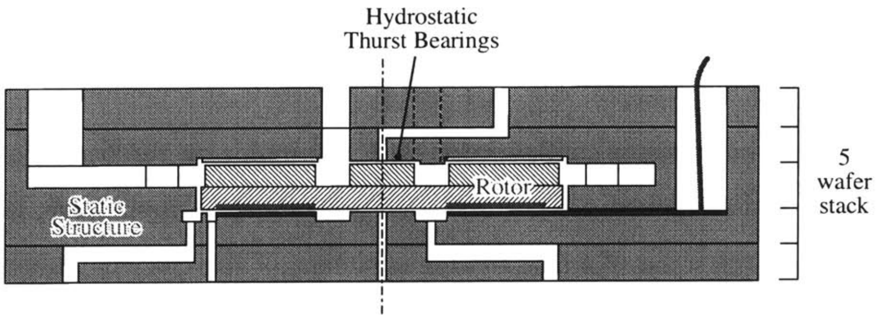

(a) Baseline 5-stack configuration

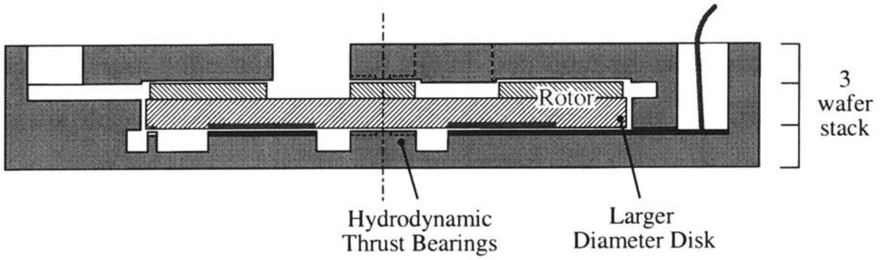

(b) Enlarged 3-stack configuration

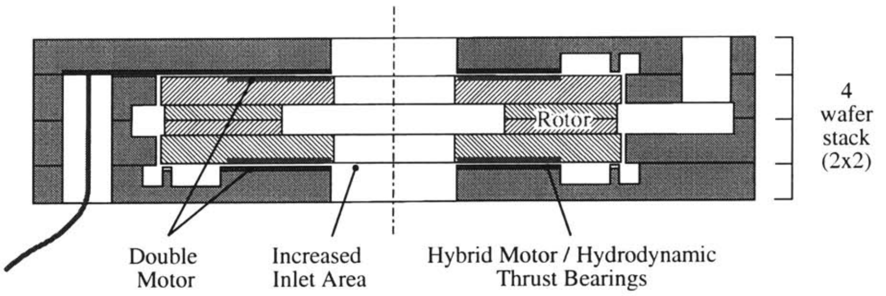

(c) Double-motor 4-stack configuration

Figure 2-28: Alternate Motor-Compressor configurations.

Tables 2.5, 2.6, and 2.7 summarize suggested configuration for the μCompressor and μBlower devices, compared to the experimental Demo Motor-Compressor.

The motor power is increased by first increasing the rotor diameter from 4 mm to 8 mm (while increasing the journal bearing depth to 500 μm for stability). The motor power also increased by reducing the minimal line width from 4 to 3 μm and slightly reducing the motor gap from 3 μm to 2.5 μm. Capacitive and resistive losses are minimized in the stator by replacing the polysilicon conductors with metals, and the compressor efficiency is expected to increase to 65%. The power electronic losses are reduced using inductors with a quality factor Q of 60 (Quality factor: $Q = \omega L/R$, where ω is the frequency, L is the inductance, and R is the internal resistance of the inductor).

Although the motor-compressor configuration with one motor on the backside of the disk is predicted to provide sufficient power for the 2:1 pressure ratio application, it suffers low overall efficiency on the order of 5 %. Taking advantage of the efficiency improvement at lower tip speed, a two-stage compressor is proposed. Two motor-compressors operating at lower tip speed (200 m/s) can operate in series, each providing the square root of the desired pressure ratio.

Alternatively, two motors can be mounted on one disk in a shrouded impeller configuration. The motor outer radii can be reduced since the individual power requirement is halved, resulting in higher energy conversion efficiency. This configuration is illustrated in Figure 2-28(c), for which the electrodes could be laid out in a spiral fashion instead of purely radial, acting as hydrodynamic thrust bearings. The center thrust pad would no longer be necessary, opening up the inlet. This configuration would only require the development of 2 wafers, used to create a symmetrical 4 wafer stack.

	Development Device Demo	Blower Application μBlower	Compressor Application μCompressor
Airflow	0.05 g/s	0.33 g/s	0.11 g/s
Pressure rise	1.02:1 (8" of H_2O)	1.06:1 (25" of H_2O)	2:1 (15 psi)
Electric power required	8.4 W	8.3 W	38 W
External bearing air required	Yes	No	No
Device size	15 x 15 x 2.5 mm	20 x 20 x 1.5 mm	20 x 20 x 3.0 mm
Device heat dissipation	6 W	5 W	22 W
Electronics heat dissipation	2 W	1 W	5 W

Table 2.5: Summary of Motor-Compressor configurations: Overall Description

	Development Device	Blower Application	Compressor Application
	Demo	μBlower	μCompressor
Airflow	0.05 g/s	0.33 g/s	0.11 g/s
Pressure rise	1.02:1 (8" of H_2O)	1.06:1 (25" of H_2O)	2:1 (15 psi)
Electric power in	8.4 W	8.3 W	38 W
Electric losses - Electronics	2.6 W	1.0 W	4.6 W
Electric losses - Stator	3.1 W	0.9 W	4.0 W
Electric Losses - Rotor	0.7 W	1.9 W	9.0 W
Gross motor power	2.0 W	4.5 W	20 W
Viscous losses - Motor gap	1.1 W	1.2 W	5.8 W
Net motor power	0.9 W	3.3 W	15 W
Viscous losses - Bearings	0.6 W	0.8 W	2.8 W
Compressor power	0.3 W	2.5 W	12 W
Compression losses	0.2 W	0.9 W	4.6 W
Net mech. power delivered	0.1 W	1.6 W	7.4 W
Overall system efficiency	1 %	18 %	19 %

Table 2.6: Summary of Motor-Compressor configurations: Predicted Performance

	Development Device Demo	Blower Application μBlower	Compressor Application μCompressor
Number of motors per stage	1	1	2
Wheel speed	190 m/s	150 m/s	200 m/s
Rotor diameter	4 mm	8 mm	8 mm
Rotational speed	922,000 RPM	358,000 RPM	477,000 RPM
Motor outer radius	1.9 mm	3.25 mm	3.35 mm
Motor inner radius	1.0 mm	2.0 mm	2.0 mm
Motor air gap	3.0 μm	3.0 μm	2.5 μm
Peak Voltage	300 V	300 V	300 V
Electrical frequency	2.6 MHz	2.6 MHz	3.4 MHz
Number of phases	6	6	6
Number of electrodes	786	1800	1800
Inter-electrode spacing	4 μm	4 μm	4 μm
Minimum electrode width	4 μm	3 μm	3 μm
Stator conductor	Polysilicon	Tungsten	Tungsten
Rotor insulator thickness	10 μm	20 μm	20 μm
Stator insulator thickness	10 μm	20 μm	20 μm
Inductor Q	30	60	60
Compressor efficiency	25 %	65 %	65 %
Compressor bleed air	5 % of main air	5 % of main air	5 % of main air
Operating air temperature	273 K	298 K	298 K
Journal bearing diameter	4 mm	8 mm	8 mm
Journal bearing eccentricity	80 %	80 %	80 %

Table 2.7: Summary of Motor-Compressor configurations: Design Detail

Power flow

The power consumption per component is illustrated in Figure 2-29 for the proposed μCompressor device. It illustrates the power flow along the electrical to fluid energy conversion path.

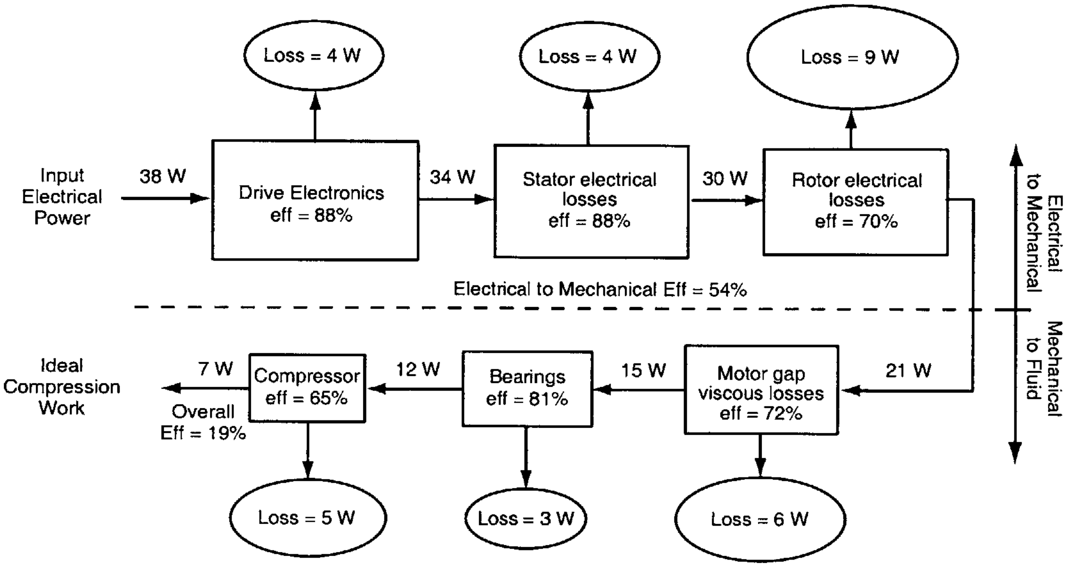

Figure 2-29: Power flow illustrating the power consumption of a Motor-Compressor designed for the high pressure ratio application.

One point to notice is the serial nature of the power flow. This implies that the overall energy conversion efficiency is the product of all the component efficiencies along the serial power flow:

$$\eta_{overall} = \eta_{power\ elec} \cdot \eta_{stator} \cdot \eta_{rotor} \cdot \eta_{visc,motor} \cdot \eta_{visc,bearing} \cdot \eta_{comp} \tag{2.38}$$

Fractional change in one component efficiency directly affects the overall system efficiency. This is important in judging the system benefit of technology improvement of one component versus another.

Another interesting aspect of the serial power flow is the importance of a components position in the sequence. Increase in power consumption of an element downstream in the power flow, such as the compressor, will require more power to flow through all upstream components, incurring additional losses at each stage, for constant component efficiencies. For the current example, to obtain an additional 1 watt to the compressor, 4 watts extra must be supplied to the power electronics, 3 of which are dissipated in various components.

2.5.4 Thermal balance considerations

At high-speed, power dissipated in small air gaps produces considerable heat, which will increase the operating temperature of both the fluid and the structure. High temperature is undesirable from many standpoints: 1) gas viscosity is larger, increasing viscous losses; 2) rotor creep increases; 3) motor electrical properties will change; and 4) compression work increases. Due to the relatively high thermal conductivity of silicon and the short length scales, the rotor and static structure will each reside at approximately uniform temperature (however different from each other).

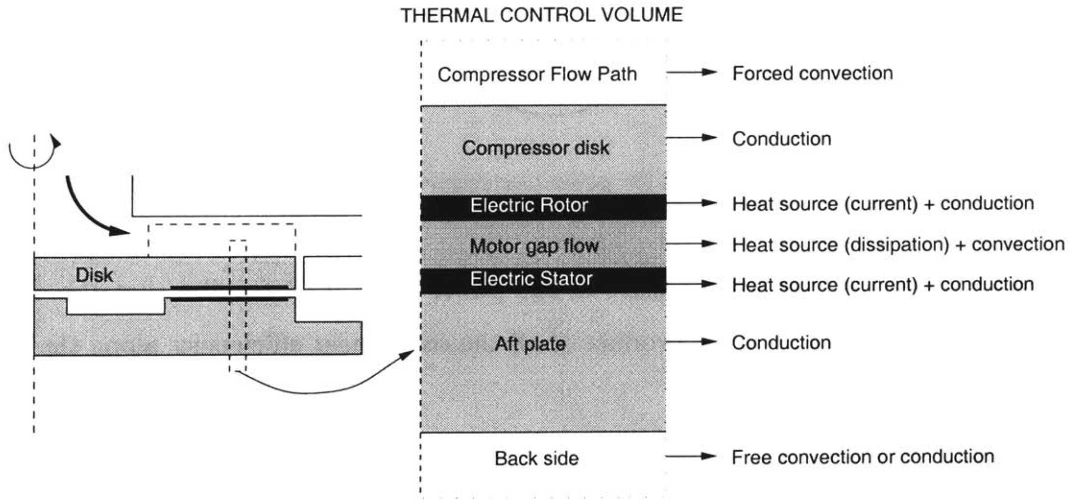

Figure 2-30: Schematic of conjugate heat transfer analysis for the Motor-Compressor configuration. Heat is generated by viscous and ohmic losses in the motor gap area, and conducted to the compressor flow path and surroundings.

To assess the thermal equilibrium, a conjugate heat transfer model was developed using Fluent, a commercial CFD code [17]. The model includes the solution for the Navier-Stokes equation of the non-isotropic flow in the motor gap, the heat transfer through the structure, and external heat transfer boundary conditions. A schematic of the control volume analyzed is shown in Figure 2-30. Initial analysis predicts that the rotor will equilibrate at a temperature of 40-50°C above the static structure for the 4 mm diameter compressor at 400 m/s tip speed. The temperature level is governed by the heat transfer rates to the impeller flow path, and to the surrounding (outer die surfaces). The precise location of the heat sources (such as the motor gap) is not important since the high thermal conductivity and small length scales essentially create a thermal short across the structure. The main flow path through the impeller and the diffuser serves to cool both the rotor and static structure.

Additional cooling to the static structure, and consequently the rotor, can be accomplished through convection or conduction to the surroundings. Acceptable operating temperatures will be guaranteed for experimental devices through external cooling. Packaging for specific applications will require attention to the thermal boundary conditions applied to the silicon device.

2.5.5 Stress and Mechanical deflection considerations

Mechanical integrity of the rotating structure and deformation under centrifugal loads are always a concern for high-speed rotating machinery. The Motor-Compressor is especially sensitive to out-of-plane deflection since the 4 mm rotor is enclosed with 1.5 μm gaps (thrust bearings). The structural integrity of the rotor was analyzed using finite element modeling by Kuo-Shen Chen [7] for the macro-scale compressor test rig. When scaled for the micro-compressor rotor, the analysis suggests acceptable maximum stresses (at the blade leading edge, the most critical region) and a downwards deflection at the outer rim of 0.37 μm at 200 m/s tip speed. The aft seal clearance can be modified if necessary by moving the rotor upward, reducing the minimal 1.5 μm gap forward thrust bearing gap.

2.6 Design conclusions and implications

Overall, the system performance is largely impacted by the characteristics of the micromotor. Most noticeable is the limited electrical power per unit area achievable with the electrostatic motor technology. It requires most of the high area on the back side of the disk to be used in order to provide sufficient torque. The small motor gap adds viscous losses in regions of high tangential velocities. This trade-off limits the maximum net mechanical power density achievable.

Since this trade-off is more forgiving at lower tip speeds, this suggests that the level of impeller backsweep could be reduced, lowering the necessary tip speed for a given pressure rise requirement. This would typically come at the expense of lower compressor efficiency, which may at some point counteract the intended improvement. This trade-off has not been pursued, since the microturbomachinery design space remains unexplored; the baseline compressor design in the only configuration which has been experimentally and numerically investigated.

Within this framework, configurations were proposed, which are predicted to achieve the pressure rise and mass flow goals at an overall energy conversion efficiency in the range of 15-20 %.

As a first step towards developing this type of device, the effort has focused on the experimental demonstration of an integrated micromotor-driven turbomachine. The Demo Motor-Compressor presented here was used as a test vehicle for the development of necessary microfabrication technology, the high-speed bearing development, and the integrated micromotor, which constitute the topics of the following chapters.

CHAPTER 3

MICROFABRICATION

This section describes the fabrication approach and summarizes the experience gained in building the MC-Bearing Rig and Demo Motor-Compressor devices. The first section reviews the microfabrication technology base, since it considerably differs from traditional macro-scale fabrication technology. The following two sections are the core of this chapter, describing the process flow and fabrication experience, first for the all-silicon MC-Bearing Rig, then for the Motor-Compressor, which integrates thin films within the silicon structure. Section 3.4 then describes two main processes developed as part of this work, and finally, Section 3.5 describes the mechanical rotor release strategy, also developed as part of this work.

The Motor-Compressor designs presented in the previous chapter can only be useful if implementable in a real device. Thus, the goal of this chapter is not only to establish a record of the device fabrication, but mainly to identify and demonstrates critical fabrication steps used to build this MEMS device, judging the viability of some fabrication approaches and identifying the pitfalls of others.

The two main criteria to judge the success of a fabrication approach are: 1) does it yield a complete device; 2) does the device satisfy the functional requirements. This chapter will describe the fabrication details, while the functional demonstration of the high speed micromachined rotor and the integrated micromotor will be the focus of the next two chapters.

Although this chapter mostly presents original work, contributions from other researchers will also be included for completeness. In summary, the design of the thin film process flow design presented here and the basic unit process development (not presented) were a collaborative effort, with S. Nagle, R. Ghodssi, and X. Zhang. This silicon structure fabrication presented here builds on the experience gained on previous multi-stack all-silicon devices, by C. C. Lin, A. Ayón, R. Ghodssi, R. Khanna, and X. Zhang. Their contributions were instrumental in the success of this work, and will be acknowledged throughout.

3.1 Microfabrication Technology Base

Available materials and fabrication techniques have traditionally been responsible for the power limitations of high performance systems, such as gas turbine engines. For example, the high rotation speed of the turbomachinery components, necessary for high power density, imposes challenging stresses on the rotating components. Over the years, metal superalloys have been introduced, along with fabrication techniques, which allow the fabrication of blades as single crystal structures. Such an advanced "macro-fabrication" technology base allows complex geometries to be manufactured, which withstand the high stresses, while fulfilling the intended aerodynamic functions.

The semiconductor industry has developed a different technology base, enabling the fabrication of micron-scale electrical components and circuits. Single crystal silicon ingots are grown and sliced to form thin circular wafers of high purity. Integrated circuits (IC) are formed on the silicon substrate by depositing, growing, and/or patterning thin films of insulating and conducting materials, such as silicon dioxide and polycrystalline silicon. Electrical components are patterned in the thin films using photolithography techniques, which allows sub-micron features. An extensive set of compatible fabrication processes and materials have been developed to mass produce cost-effectively reliable microelectronic chips used in widespread electronics.

An additional set of microfabrication techniques have emerged from the desire to build micro-electromechanical system (MEMS) out of silicon. Mechanical elements have been created by releasing thin film structures or by directly creating structures in the silicon substrate. Examples include springs, membranes, channels, mirrors, gears and other mechanisms. These mechanical elements can be integrated with electronic components to form integrated micro-scale systems. Such systems are commonly envisioned for sensing and actuating in ways not possible with their larger counterparts. These new devices have led to an extension of the processing techniques developed for planar IC fabrication. Of particular interest, the MEMS field has motivated deep silicon etching and wafer bonding to create quasi-three-dimensional structures.

These processing techniques and materials developed by the IC and MEMS fields form the technology base for high power density micro-motors and micro-turbomachines. They are briefly discussed in Appendix B for the reader who is less familiar with this fabrication technology.

The benefits of using microfabrication to build micro-rotating machinery, such as the Motor-Compressor, include:

- the availability of single crystal silicon as a structural material;
- the ability to define features within microns of tolerance;
- the potential integration of electrical components within the silicon structure;
- minimal number of parts and assembly;
- batch fabrication for eventual low cost-large volume production.

The high strength-to-density ratio of single-crystal silicon enable micro-turbomachines to withstand the stresses at high speeds, with less complex structural design. Such a benefit is welcome, since the microfabrication technology does not yet allow to create complex three-dimensional structures from the silicon wafers.

Additional microfabrication techniques were developed to allow the fabrication of the motor-compressor. These were necessary in order to deliver the level of functionality from the device components. The development of thick insulating layers and deep reactive ion etching of high aspect ratio trenches, as well as rotor release strategies will be described in sections 3.4 and 3.5. First, the process flow to create the MC-Bearing Rig and Demo Motor-Compressor devices will be detailed in Sections 3.2 and 3.3.

3.2 MC-Bearing Rig Fabrication

This section describes the fabrication process flow to create the MC-Bearing Rig, which is also the silicon structure of the Demo Motor-Compressor device. A picture of a MC-Bearing Rig die is shown in Figure 3-1. The fabrication approach builds on the process developed for the all-silicon 5-wafer stack micro-bearing rig [29].

This section will first present the double-side through wafer etching process, followed to process flow for the MC-Bearing Rig. Design guidelines and limitations governing this process flow are then summarized. The basic microfabrication techniques are summarized in Appendix B and will not be discussed here.

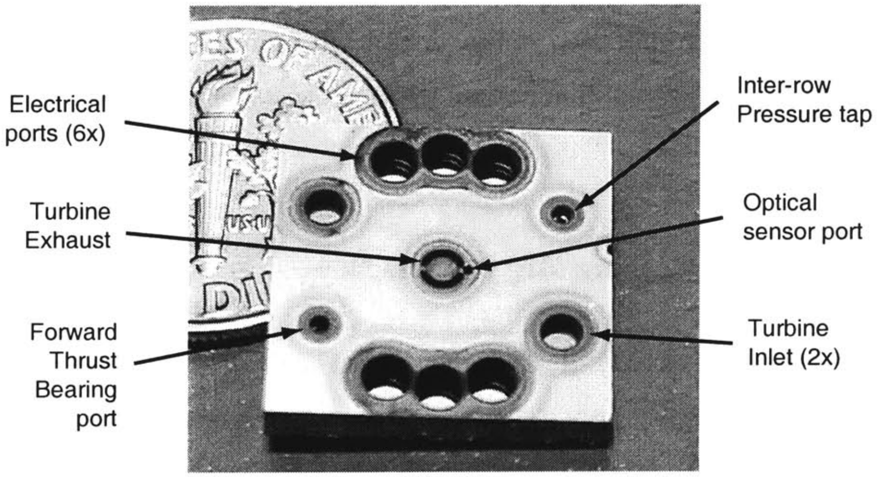

Figure 3-1: Optical photograph of a MC-Bearing Rig die (from *MCBR1* build). The 5-wafer stack device is 15 mm square and 2.3 mm thick. It encloses a 4 mm diameter microturbine rotor.

3.2.1 Aligned double-side through wafer DRIE process

As described by Lin [29], the basic process to create a silicon wafer with through-etched features using deep reactive ion etching (DRIE) consists of:

1. Photolithography on the first side of the wafer and surface protection of the opposite side;
2. First deep silicon etch part way through the wafer thickness;
3. Photolithography on the second side of the wafer and surface protection of the etched

side;

4. Attach a handle wafer on the etched side of the wafer;
5. Second deep silicon etch, reaching the cavities formed during the first deep etch;
6. Remove the handle wafer and the surface protection.

This process creates plena and piping with rectangular cross-sections on both sides of the wafer, which connect where the deep etches overlap. Flow channels are completed upon bonding of the micromachined wafers.

Features on opposite sides of the wafer can be aligned to micron level accuracy. The approach is to etch shallow small linewidth features on one side of the wafer and use them as the alignment marks for both deep etches. Alignment from the opposite side of the wafer is achieved using either infrared illumination through the wafer or combined front-to-back optics.

3.2.2 Baseline MC-Bearing Rig process flow

The fabrication process of the MC-Bearing rig is based on deep reactive ion etching (DRIE) and aligned fusion bonding of silicon wafers. An exploded view of the five-wafer stack device is shown in Figure 3-2. The fabrication approach was developed and first presented by Lin et al. [31, 30, 29], and remains the foundation for this second generation bearing rig. This section summarizes the fabrication sequence, while section 3.4 will provide more detail on deep reactive ion etching (DRIE).

Process overview The end plates (wafers #2 and #4) first receive shallow silicon etches on the sides facing the rotor. All the wafers are then deep-etched halfway through their thickness, except for wafer #1, which is etched completely through from its bottom side. Wafers #2, #4 and #5 are then deep etched on the opposite side until through-flow channels are created. Wafer #3 is then bonded to wafer #2 and etched from the bottom side to define the journal bearing gap. Finally, wafers #1, #4, and #5 are fusion-bonded to wafer pair #2-3 in a single step. Figures 3-3 to 3-8 illustrate this process.

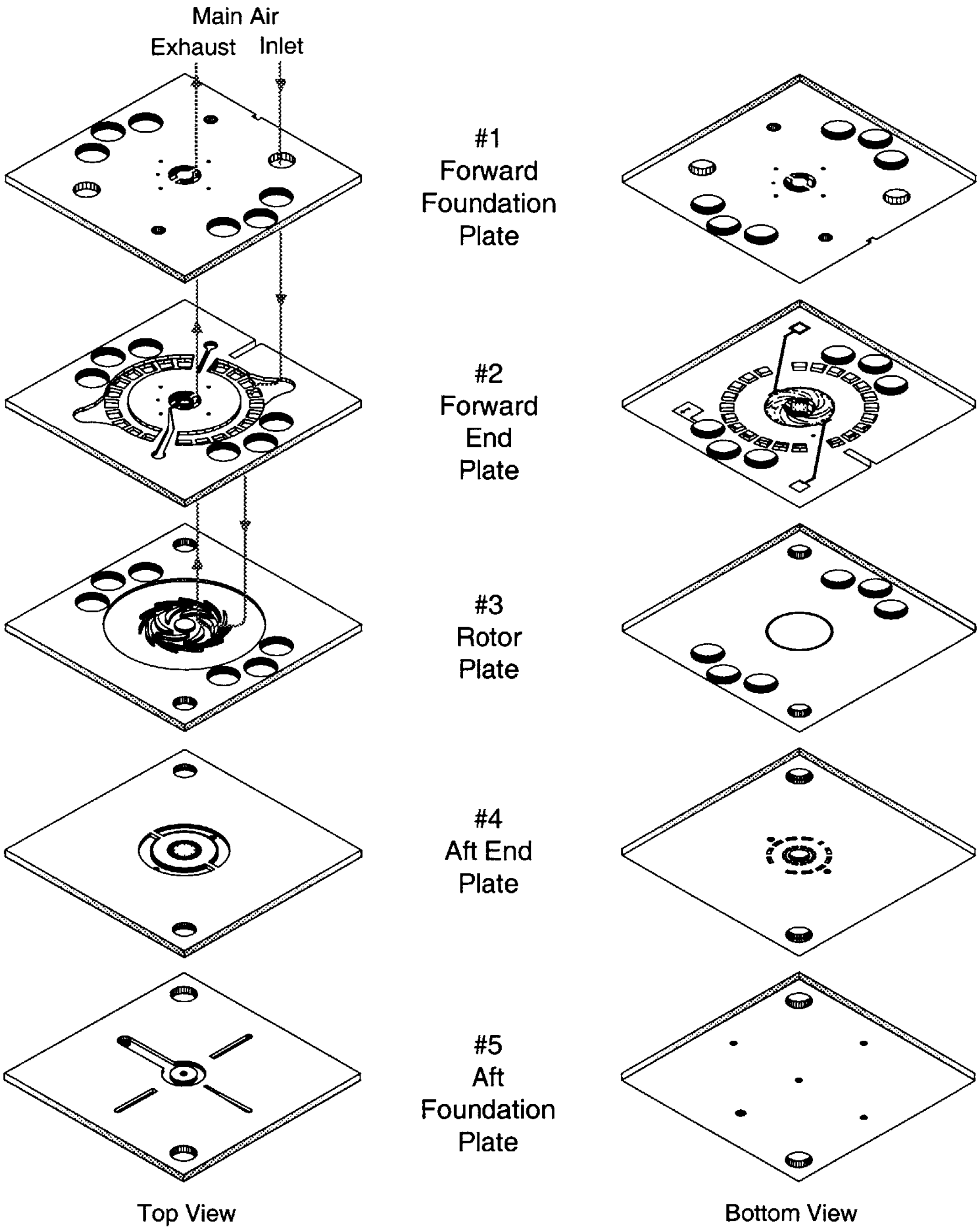

Figure 3-2: Exploded view of the 5-wafer stack MC-Bearing Rig. One die viewed from the top (left) and from the bottom (right). Drawing is to scale, where the die is 15 mm per side.

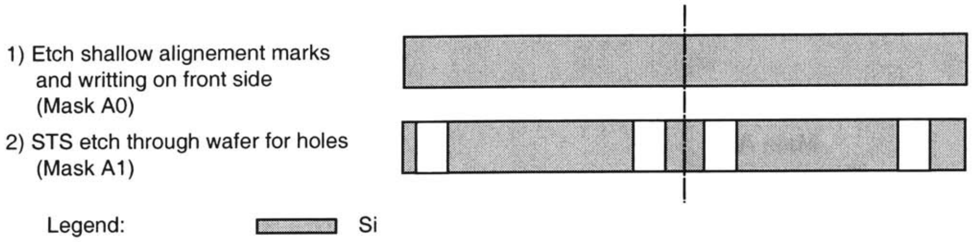

1) Etch shallow alignement marks and writting on front side (Mask A0)

2) STS etch through wafer for holes (Mask A1)

Legend: ▨ Si

Figure 3-3: Wafer #1: Forward foundation plate process flow

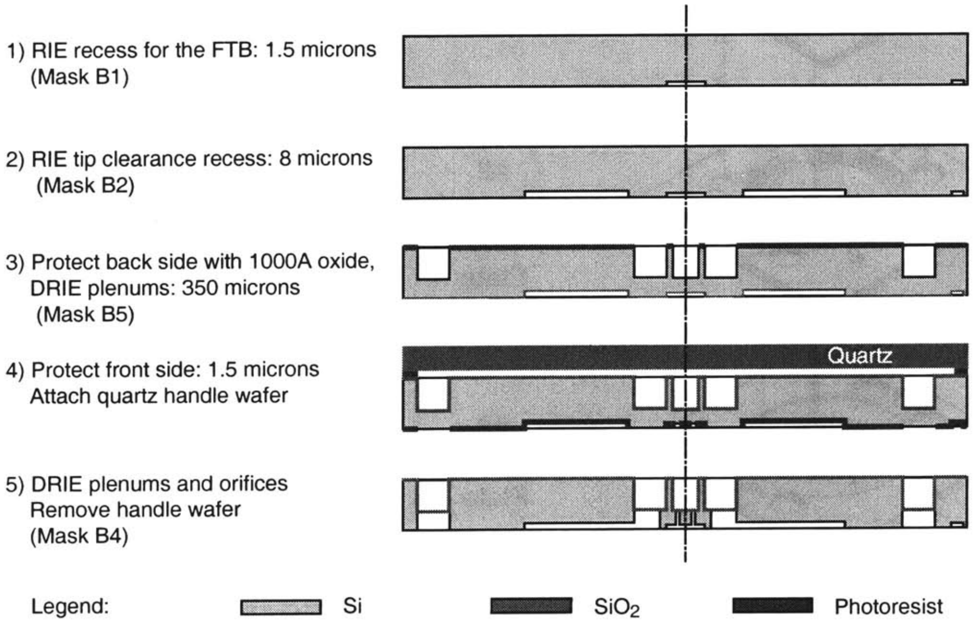

1) RIE recess for the FTB: 1.5 microns (Mask B1)

2) RIE tip clearance recess: 8 microns (Mask B2)

3) Protect back side with 1000A oxide, DRIE plenums: 350 microns (Mask B5)

4) Protect front side: 1.5 microns Attach quartz handle wafer

5) DRIE plenums and orifices Remove handle wafer (Mask B4)

Legend: ▨ Si ▩ SiO2 ■ Photoresist

Figure 3-4: Wafer #2: Forward end plate process flow

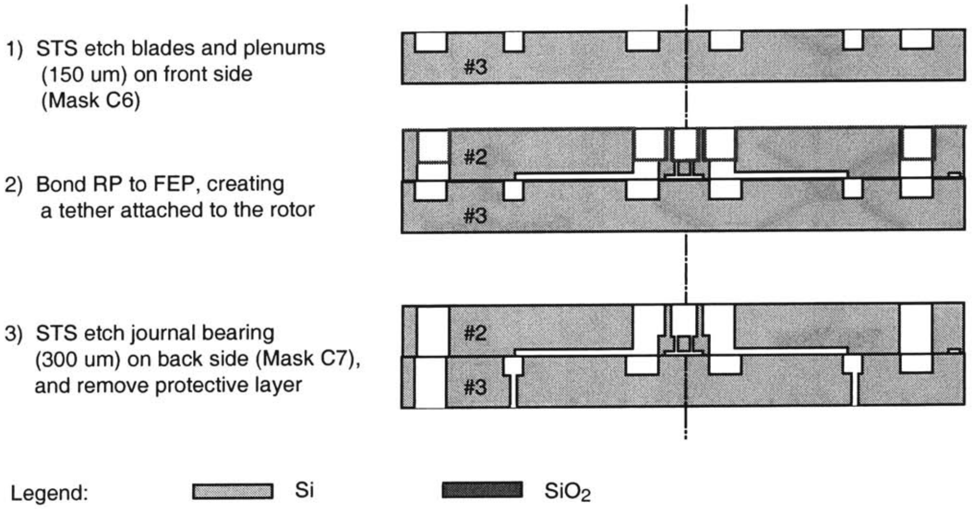

1) STS etch blades and plenums (150 um) on front side (Mask C6)

2) Bond RP to FEP, creating a tether attached to the rotor

3) STS etch journal bearing (300 um) on back side (Mask C7), and remove protective layer

Legend: ▨ Si ▩ SiO2

Figure 3-5: Wafer #3: Rotor plate process flow

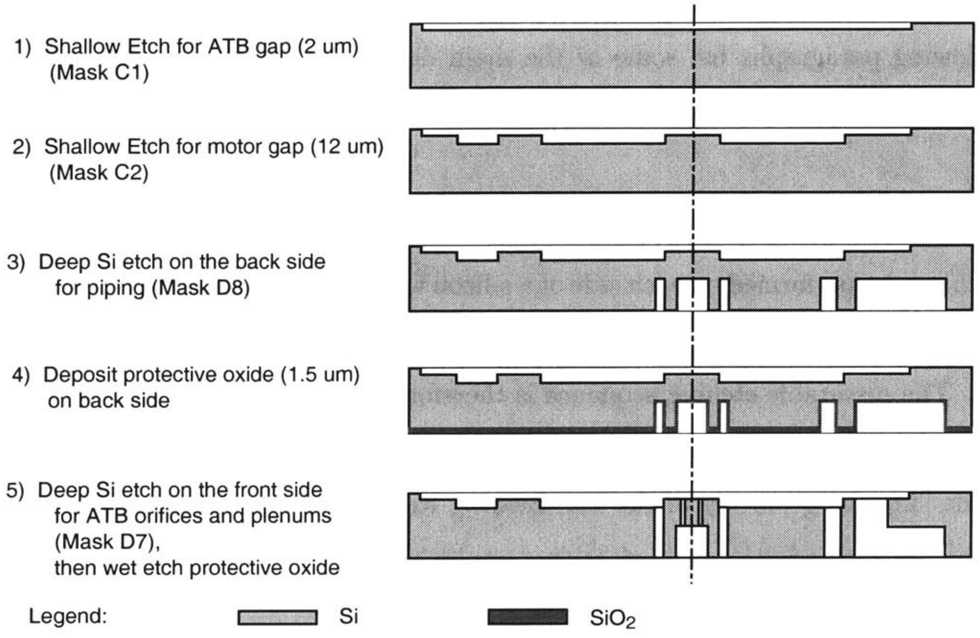

Figure 3-6: Wafer #4: Aft end plate process flow

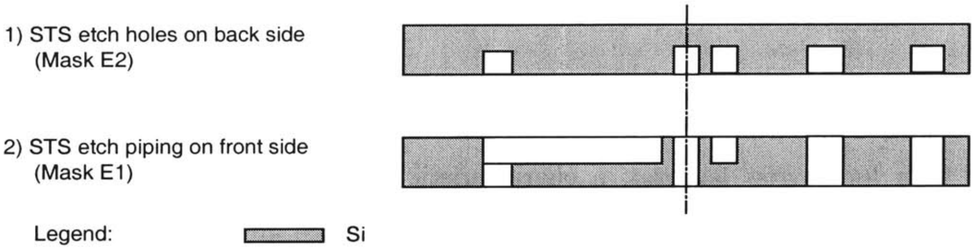

Figure 3-7: Wafer #5: Aft foundation plate process flow

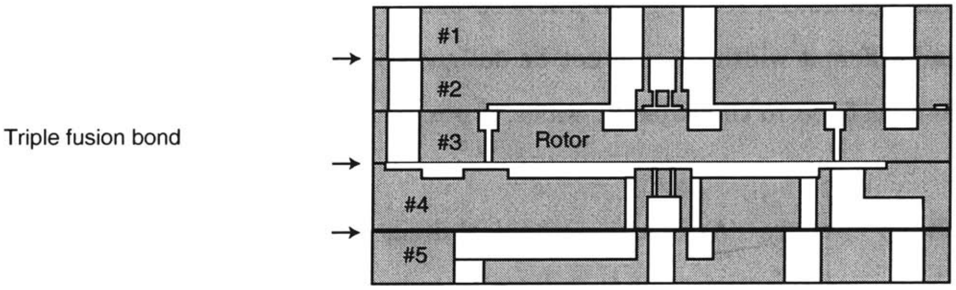

Figure 3-8: Final MC-Bearing Rig 5-wafer stack bond

3.2.3 Silicon structure - Design guidelines and limitation

The following paragraphs list some of the main design guidelines in defining the process flow and masks for the silicon structure, imposed by this fabrication approach.

Combination of deep and shallow silicon etches Multiple shallow etches and one deep etch can be performed on each side of a silicon wafer. Spin coating for photolithography on a surface with etches deeper than 10 μmwas found to be challenging and was subsequently avoided. The preferable etching sequence is therefore to start with the shallow etches first, then the deep etch. Although a nested mask approach allows more than one deep etch per wafer side [32], the geometry of the MC-Bearing Rig and Motor-Compressor was designed not to require such additional fabrication complexity.

Avoid overlapping edges of shallow and deep etched features If a step from a previous etch is within the unmasked area of a subsequent DRIE etch, a silicon wall may remain at the location of the edge. Shallow-etched regions should ideally enclose subsequent shallow or deep etches.

Accommodate aspect-ratio dependent etching The DRIE etch rate in large features is faster than for narrow features, a characteristic referred to as *aspect-ratio dependent etching* or ARDE. Specific etch recipes can be chosen which minimize the ARDE [3], but often at the expense of sidewall perpendicularity and selectivity. Tight tolerance geometries must often be etched with tailored recipes, so the design should accommodate non-uniform etch depths. For example, 10 μm diameter holes are etched 100 μm deep (for the hydrostatic thrust bearing nozzles), creating 350 μm deep plena in the process. Two features of critical depths and different widths should not be designed on the same wafer surface; one feature should be transfered to the adjacent wafer, if possible.

Avoid sharp corners As in any mechanical design, stress concentration should be minimized. In microfabrication, this translates to rounded features in the photolithographic pattern. Corners of a square etched cavity can act as stress concentration and promote crack initiation. They can be avoided by rounding the corners or replacing the square with a circle. Sharp corners of a square pillar will modify the local electrical field and create localized asperities (such an example can be found in Figure 3-30). Once again, this can be avoided by rounding the corners of the convex surface.

Avoid enclosed cavities If etched features create enclosed cavities during wafer bonding, plastic deformation or wafer delamination can be driven by the expanding gases during the high temperature bonding anneal. This is avoided by etching the through-wafer channels before bonding, ensuring a path for enclosed gases to escape. Shallow features up to 4 μm (such as the alignment marks, 1x3 mm) have shown not to be problematic.

Protect wafer surface during processing and handling Since the wafer surfaces are ultimately used for wafer-level fusion bonding, they must preferably be smooth to within 5 nm [2]. Polished wafers are purchased with surfaces ready for bonding. During wafer processing, care must be taken to protect the surfaces from damage and undesired residue accumulation. During etching, the bonding surfaces on the front side of the wafer are naturally protected by the etch mask. The back side of the wafer however is exposed to the wafer handling equipment and to some etch gases[1]. The approach taken here was to coat the surfaces with a thin sacrificial oxide film (1000 Å PECVD SiO_2), which will only be removed before bonding. This approach is not viable for wafers with electrical components, such as stator and rotor wafers in the Motor-Compressor (Sec. 3.3). In these cases, a thin photoresist layer covered the back-side of the wafer.

The back-side layers mainly protect against three sources of damage:

1. Fluorocarbon residue (Teflon-like) from the C_4F_8 passivation step during DRIE[2];
2. Ion bombardment of the wafer back-side by reflection of the underlying quartz handle wafer;
3. Surface Scratches from machine handling (mostly the AME5000 thin film etcher)

---

[1] In IC semiconductor processing, the back side of wafers are not polished and the surface roughness is not a concern. Some equipment is therefore not designed to be "back-side friendly".

[2] DRIE surface contamination is clearly visible in Figure 3-1. We notice dark regions surrounding the through holes, due to the C_4F_8 passivation residue. Wafer #1 was etched from the bottom side, opposite to the visible surface.

Minimize wafer bow Experience suggests that a maximum wafer bow of 10 μm is preferable in order not to increase the challenge of bonding stacks of multiple wafers. Although bonding of wafers with larger bow is possible, starting material should be restricted to wafers with less than 10 μm bow.

3.2.4 Fabrication results for the MC-Bearing Rig

Two 5-wafer stacks of microturbine-driven bearing rigs, based on the Motor-Compressor design, were built as part of this work, with the help of Drs R. Ghodssi, X. Zhang, and R. Khanna. They will be referred to as *MCBR1* and *MCBR2*. An optical photograph of the cross-section of an *MCBR1* die is shown in Figure 3-9. During fabrication of the MC-Bearing Rigs, special attention was given to protecting the surface for bonding and creating the bearing geometries to the design specifications. These devices were also the first application of the snap-off tab approach for rotor release (detailed in Section 3.5). The following paragraphs will summarize this fabrication experience.

Bonding yield The 5-wafer stack was created in two bonding steps. As presented in the process flow, the rotor wafer (#3) was first bonded to the forward end plate (#2) and annealed, and the journal bearing was etched. The other wafers were bonded to the FEP-Rotor pair in one process using the Electric Vision Aligner-Bonder with inverted optics:

1. RCA clean all the wafers
2. Insert the aft foundation plate (wafer #5), up-side down
3. Align cross hairs to front side of wafer
4. Insert the aft end plate (wafer #4), up-side down
5. Align the wafer to the cross hairs, and contact the pair
6. Align the cross hairs to the front side of the aft end plate (wafer #4);
7. Insert the FEP-Rotor pair (bonded pair of wafer #2-3), up-side down;
8. Align the wafer pair to the cross hairs, and contact both pairs;
9. Align the cross hairs to the front side of the forward end plate (wafer #2);

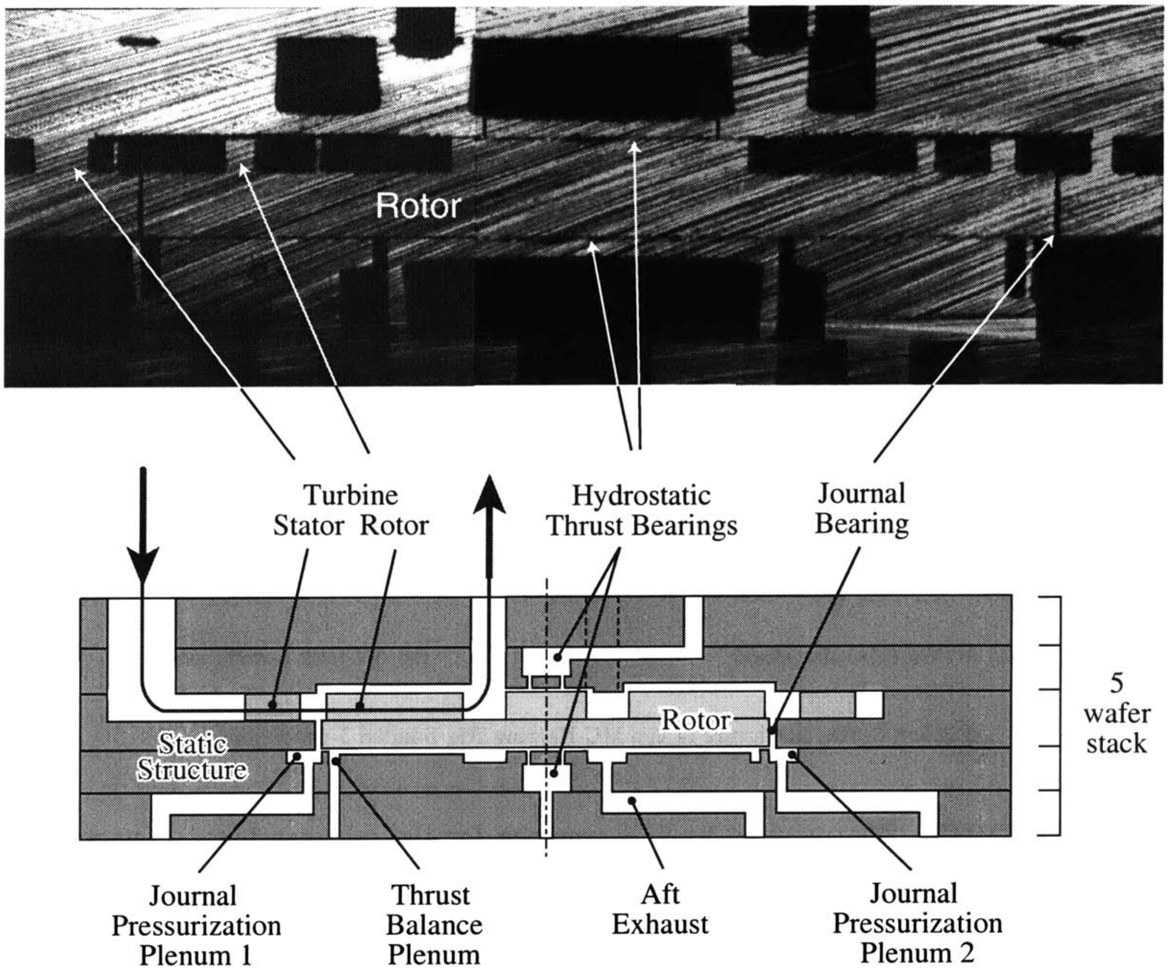

Figure 3-9: Cross-section of the 5-wafer stack MC-Bearing Rig with schematic. The device, *MCBR1* die #12, was cast in epoxy and cut through the center.

10. Insert the forward foundation plate (wafer #1);

11. Align the wafer to the cross hairs, and contact the last wafer to the 4-stack

The 5-wafer stack was annealed at 1100°C for 1 hr in a nitrogen ambient. Infrared pictures of the bonded *MCBR1* and *MCBR2* stacks are shown in Figure 3-10, showing a clear image over the device area. Dark spots and fringes usually appear when the surfaces are not in intimate contact, as shown along the edges of the bonded stacks). This one-step multi-wafer bonding approach was demonstrated here for the first time to create a DRIE MEMS device. This process is preferred to a repeated single-wafer bond and anneal process, which was used for the first generation bearing rig, since it reduces wafer handling and high temperature cycling.

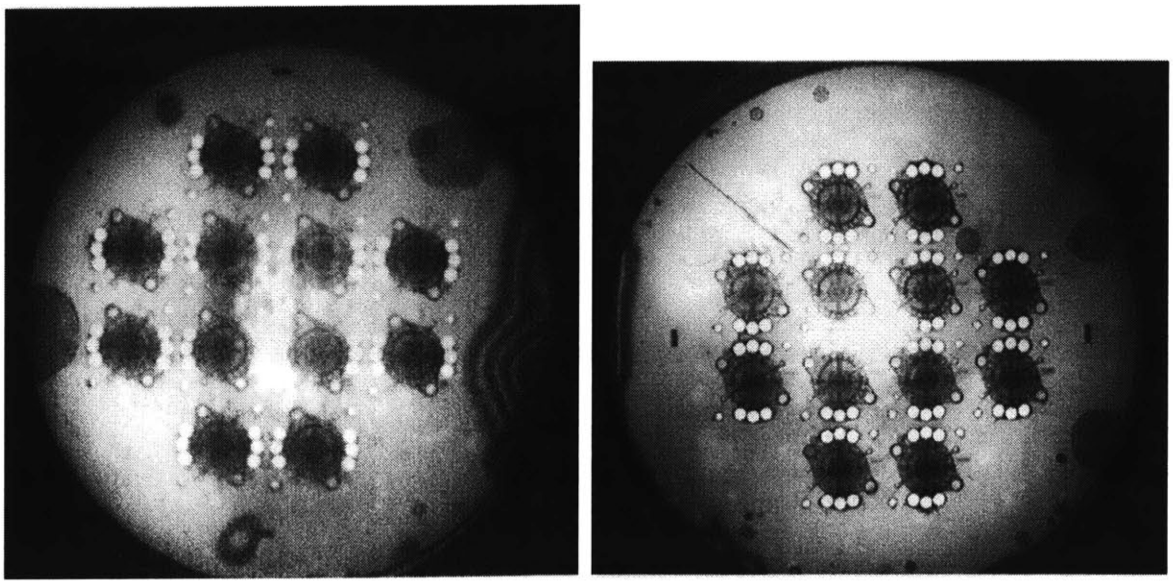

(a) *MCBR1* 5-wafer stack (b) *MCBR2* 5-wafer stack

Figure 3-10: IR picture of the MC-Bearing Rig bonded 5-wafer stacks.

Precision DRIE The required level of accuracy for the micromachined geometries is driven by their functionality. The two outermost wafers provide external fluidic and optical ports to the die, resulting in dimensions of the order of hundreds of microns without stringent precision requirements. Moving inwards toward the rotor, the end plates (wafers #2 and #4) feature pressurized plenum (on their outer side) and 10 μm diameter by 100 μm long orifices for the thrust bearings (on their side facing the rotor). Accurate dimensions are critical since the axial stiffness of the thrust bearing depends on the pressure drop across the orifice, which is a strong function of its diameter. Orifices with a diameter of 10-11 μm were reproducibly achieved by exposing a 7 μm diameter circle on the mask through a 6 μm thick resist (AZ4620). The optimized process resulted in an 8-9 μm diameter opening in the resist, and 1 μm larger feature in the silicon after 90 minutes of DRIE.

The rotor is cut from the back of the center wafer by a high-aspect ratio circumferential trench, which simultaneously creates the journal bearing geometry. From an initial 4 μmline width in the mask, a final DRIE trench tapering from 17 to 9 μm wide and 300 μm deep was achieved using a 10 μm thick photoresist. The process development of the journal etching will be described further in Section 3.4. It should be noted that the taper precludes hydrodynamic operation of the journal bearing, since the rotor cannot be pushed to the minimum eccentricity for stable operation of at least 90%. Instead, the journal bearing will be operated hydrostatically, since near wall operation is not necessary.

In both processes, the minimum feature size consistently achievable was limited by the trade-off between the photoresist thickness necessary to withstand the etch duration, the increase in etch duration for smaller features, and the lower selectivity of DRIE recipes which create vertical sidewalls.

Insufficient backside protection Although the wafer surfaces were protected against contamination and scratching, ion scattering off the handle wafer created severe pitting on the back side of the forward end plate (wafer #2). As illustrated in figure 3-11(a), the ion bombardment through large areas (which etch through first) reflected off the quartz handle wafer. This rapidly removed the 1000 Å SiO_2 covering the back side, and damaged the silicon surface. Figure 3-11(b) shows the damage occurred, where the dark area is a pitted recess, reaching up to 20 μm deep. This was completely prevented in the second build by using a thicker 1.5 μm back side protective SiO_2 layer.

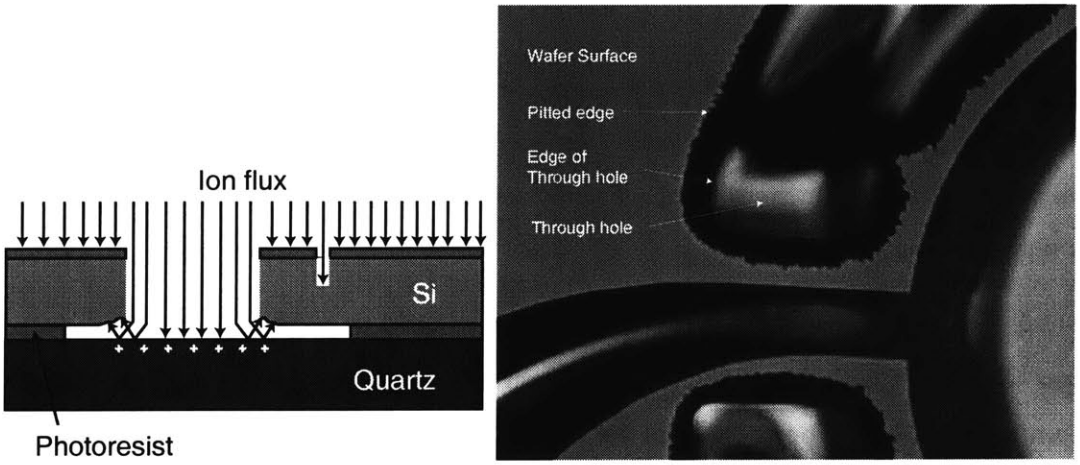

(a) Schematic illustration of the cross-section

(b) Optical photograph of the forward end plate (wafer #2) back side in the plane view

Figure 3-11: Illustration of backside pitting.

Wafer bonding alignment Severe misalignment occurred between wafers #3 and #4 during bonding of the first stack (*MCBR1*). This resulted in the aft plenum and seal to be misaligned with respect to the bottom side of the journal bearing gap. Figure 3-12 is an overlay of the masks, displaced by the measured misalignment. We notice that the motor outer plenum (MOP) is shorted to the journal pressurization plenum by the journal bearing gap. This will limit the functionality of the aft plenum, but did not prevent hydrostatic journal bearing operation. Misalignment was minimized in subsequent builds by calibrating the equipment before processing the device wafers, allowing a wafer-to-wafer alignment to the micron level. Noticeable 5-stack wafer misalignment was not measured (less than 5 μm) on the second MC-Bearing Rig stack (*MCBR2*).

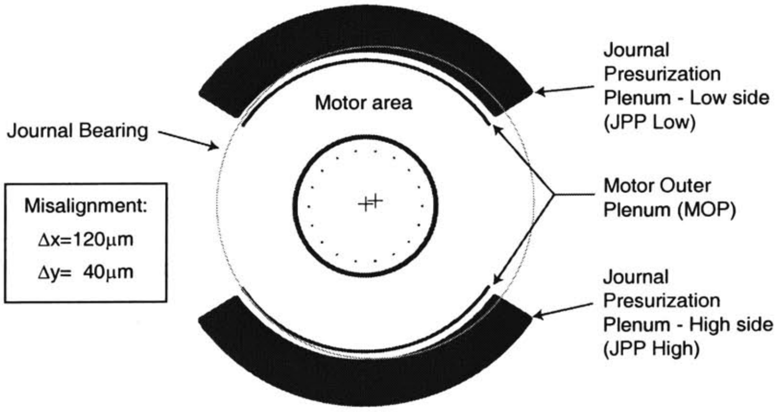

Figure 3-12: Illustration of the misalignment between wafers #3 and #4 of *MCBR1*.

Lateral etching As seen in the cross-section (Figure 3-9), the vertical plenum walls are not perfectly perpendicular to the wafer surface. Most, if not all plenum etches, exhibit a certain level of re-entrant anisotropy. This is not detrimental, unless adjacent plenum are only separated by a thin wall.

The etch recipe for the front side of wafer #4 was tailored to produce vertical walls for the 10 μm diameter thrust bearing nozzles. Larger areas, such as the journal pressurization plenum and the motor outer plenum are created during the same etch and exhibit non-optimum anisotropy. The 50 μm wide seal was thinned down at its base, as seen in the cross-section of *MCBR1* (Figure 3-9). To accommodate this effect, the mask was redesigned with a wider seal between the plenum for the *MCBR2* build. This is a prime example of the compromise imposed by the parallel processing approach.

3.3 Motor-Compressor Fabrication

In addition to the silicon structure fabrication, thin film processing is integrated in the process flow to create the electrical components. The overall approach consists of:

1. Building the thin film electrical components;
2. Deep etching the flow paths through the bulk silicon wafer;
3. Bonding the patterned wafers, completing the flow channels and enclosing the rotor and electric motor.

This section will summarize the approach to create the rotor wafer with thin films and two approaches to create the stator wafer. These were defined after considering a multitude of options, based on the fabrication complexity, the electrical performance limits, and the ability to integrate the motor components. In addition to building the electrical components, a major challenge resides in integrating these films within the bonded silicon structure, and these challenges will be detailed in the last part of this section.

3.3.1 Baseline Motor-Compressor process flow

The motor-compressor process flow is based on the MC-Bearing Rig process, to which is added front-end thin film processing to create the electrical components, before doing the deep etches. An exploded view of a 5-stack motor-compressor die is shown in Figure 3-13. The electric stator is built in the top side of the aft end plate (wafer #4), and the electrical rotor films are built on the bottom side of the rotor plate (wafer #3). Recesses previously created with shallow etches on wafers #3 and #4 are now realized as part of the thin film processing.

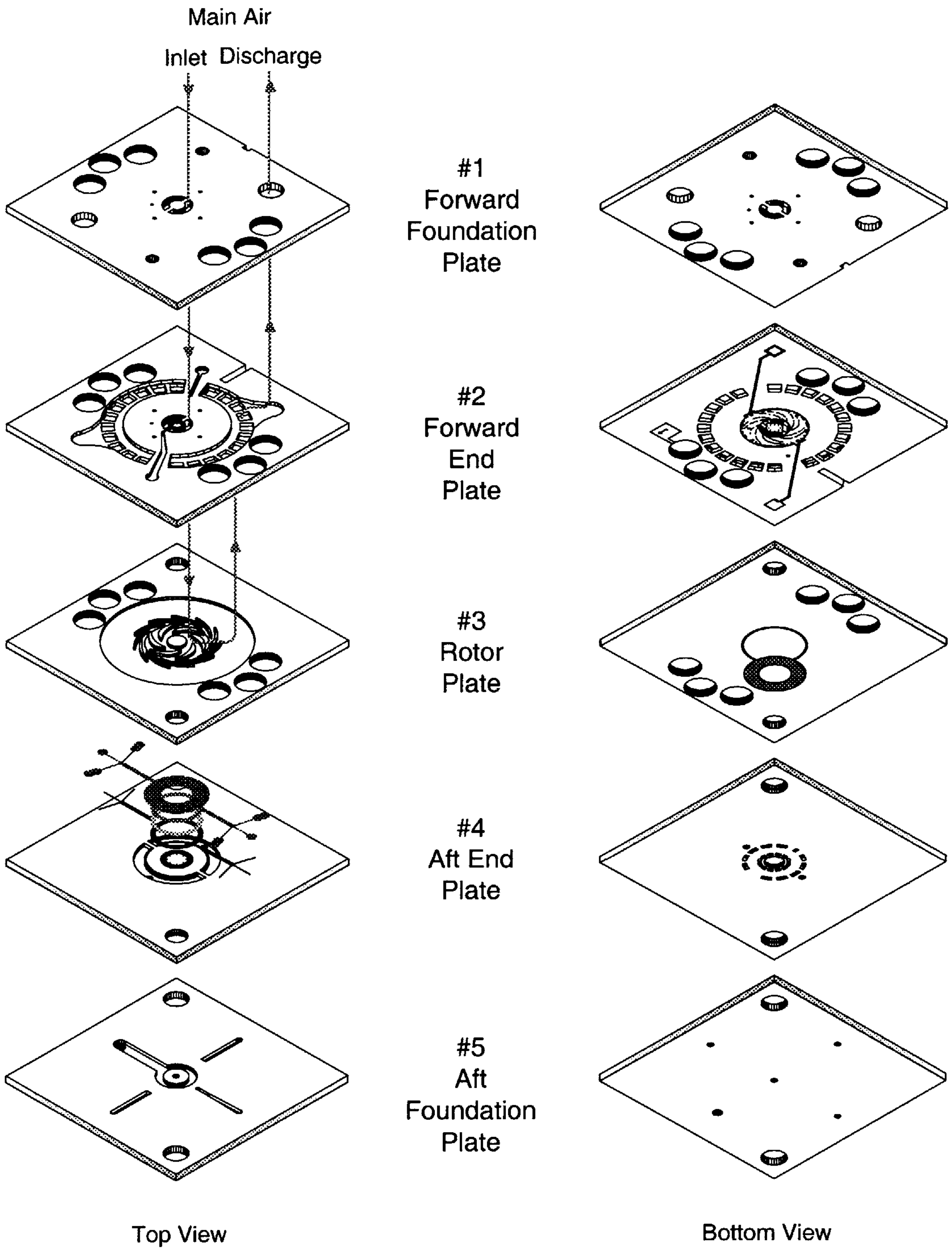

Figure 3-13: Exploded view of the 5-wafer stack Motor-Compressor.

3.3.2 Rotor process flow

The process flow for the rotor wafer of the motor-compressor device is illustrated in Figure 3-14. First, thin and thick film processing forms the rotor conductor in a recessed cavity. A thick 10 μm PECVD oxide is used as a dielectric, isolating the rotor silicon substrate from the motor electrical fields. The rotor conductor film is formed on the thick oxide by depositing and doping a thin polysilicon layer. The implantation and drive-in process necessary to achieve a rotor film resistivity of 200 $M\Omega_\square$ was determined by Nagle [38].

The films are removed outside of the active electrical area to allow bonding to the silicon substrate and to facilitate the journal deep etching. Then the blades are formed using DRIE. The rotor wafer is then ready for bonding to the FEP and journal etching, similar to the MC-Bearing Rig process. A major difference is the back-side protection of the FEP (wafer #2) during the journal etch; photoresist was used instead of oxide, since the removal of oxide on one side would also potentially attack the rotor insulating oxide. Figure 3-16 shows the front side of the FEP after bonding and journal etching.

3.3.3 Stator process flow #1 - Thick Buried Oxide in Silicon (TBOS)

The original approach pursued for the stator fabrication consisted of creating thick buried oxide patches in the silicon substrate, on top of which is built a two-level polysilicon interconnect and electrode structure. The surface was planarized using chemical-mechanical polishing (CMP) before depositing each of the two polysilicon layers. The planarized surface allowed thin photoresist to be used to patterning of the thin features, such as the 2 μm via holes in the interlevel dielectric and 4 μm gaps between electrodes. The process flow is described in Figures 3-17 and 3-18. Results using this thick buried oxide in silicon (TBOS) approach were presented by Ghodssi *et al.* [21].

3.3.4 Stator process flow #2 - Recessed Oxide Islands

An alternate process was also pursued for the stator fabrication. It differs from the TBOS approach by the absence of CMP for planarization of surface topology. The design constraint of a planar electrode surface here is relaxed to reduce the fabrication complexity.

Photolithography of the small features on the surface with trenches was possible using higher viscosity photoresist (35 centipoise). The process flow is described in Figure 3-19. The top side of a final stator die is shown in Figure 3-20, after processing of the electrical layers and deep etches on both sides.

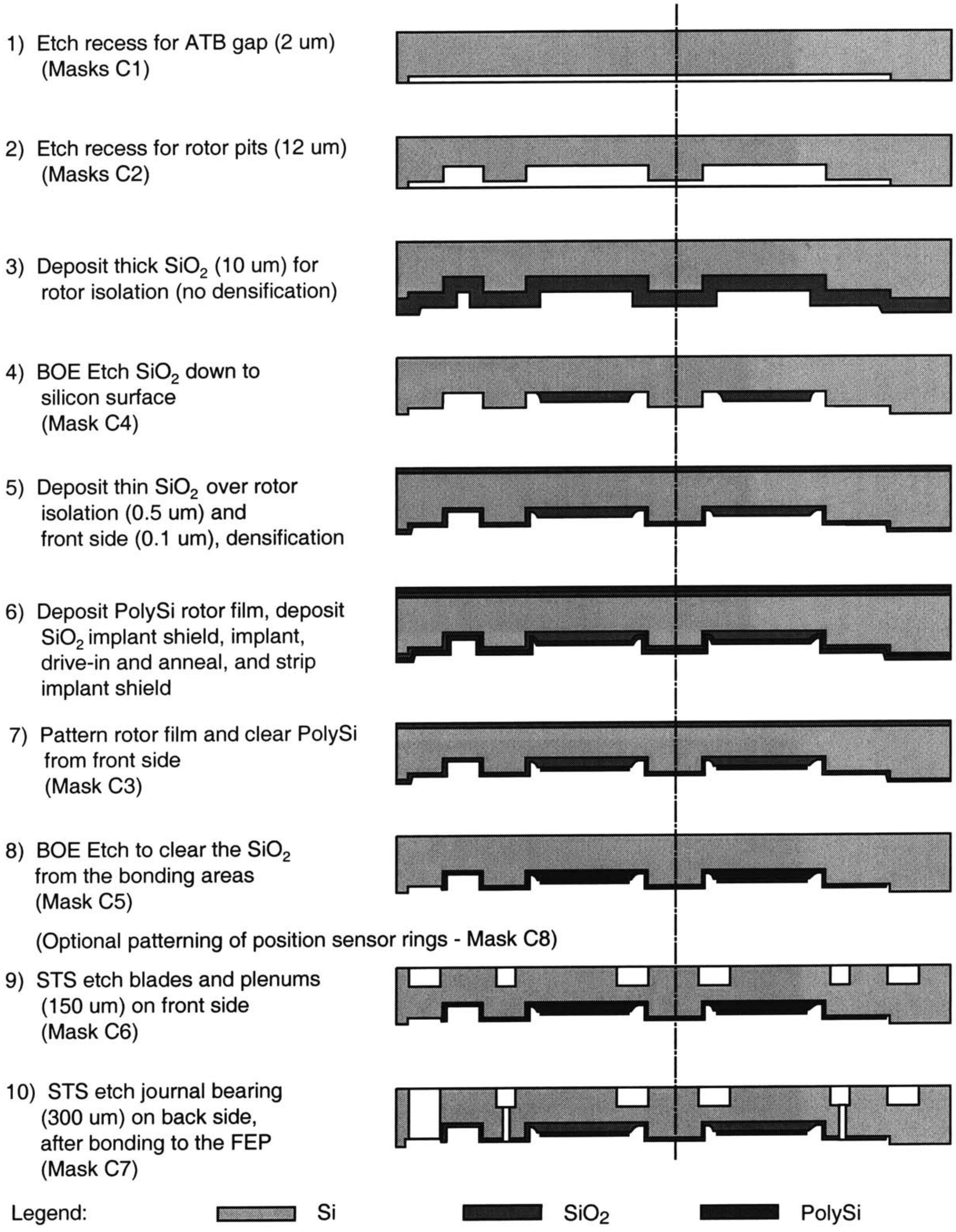

1) Etch recess for ATB gap (2 um) (Masks C1)

2) Etch recess for rotor pits (12 um) (Masks C2)

3) Deposit thick SiO_2 (10 um) for rotor isolation (no densification)

4) BOE Etch SiO_2 down to silicon surface (Mask C4)

5) Deposit thin SiO_2 over rotor isolation (0.5 um) and front side (0.1 um), densification

6) Deposit PolySi rotor film, deposit SiO_2 implant shield, implant, drive-in and anneal, and strip implant shield

7) Pattern rotor film and clear PolySi from front side (Mask C3)

8) BOE Etch to clear the SiO_2 from the bonding areas (Mask C5)

(Optional patterning of position sensor rings - Mask C8)

9) STS etch blades and plenums (150 um) on front side (Mask C6)

10) STS etch journal bearing (300 um) on back side, after bonding to the FEP (Mask C7)

Legend: ▨ Si ▩ SiO_2 ■ PolySi

Figure 3-14: Rotor process flow for the Motor-Compressor.

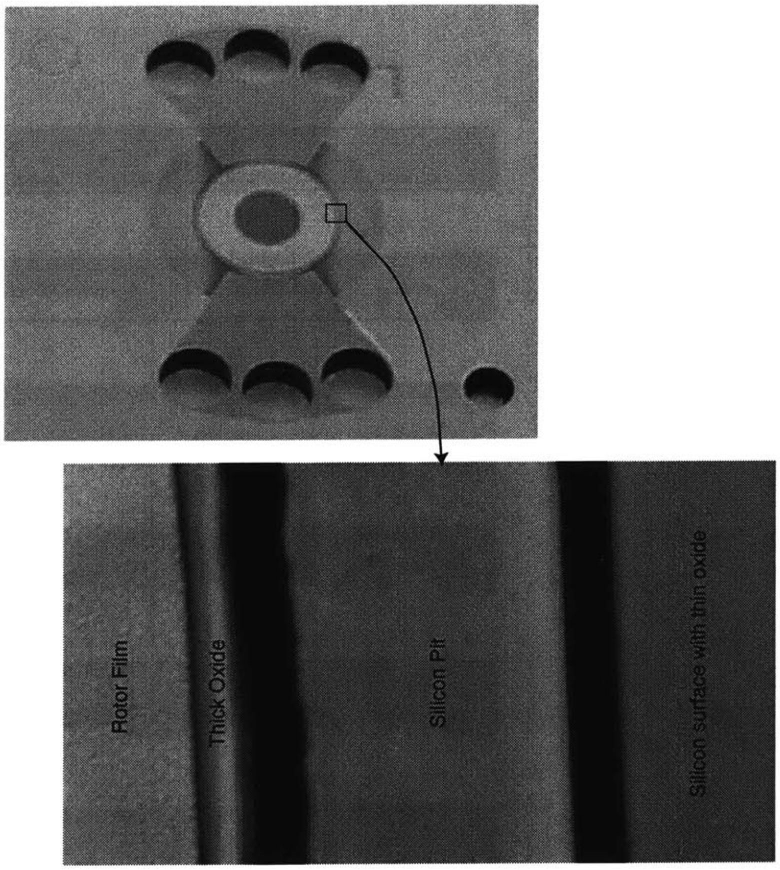

Figure 3-15: Bottom side of *MC1* Rotor plate, after thin film processing and deep reactive ion etching.

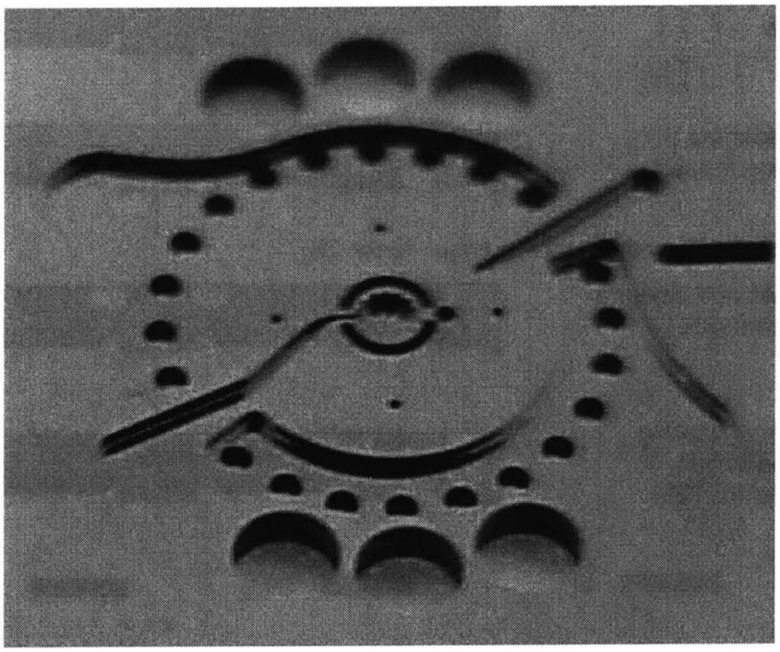

Figure 3-16: Top side of *MC1* FEP after having been bonded to the rotor plate and the journal being etched.

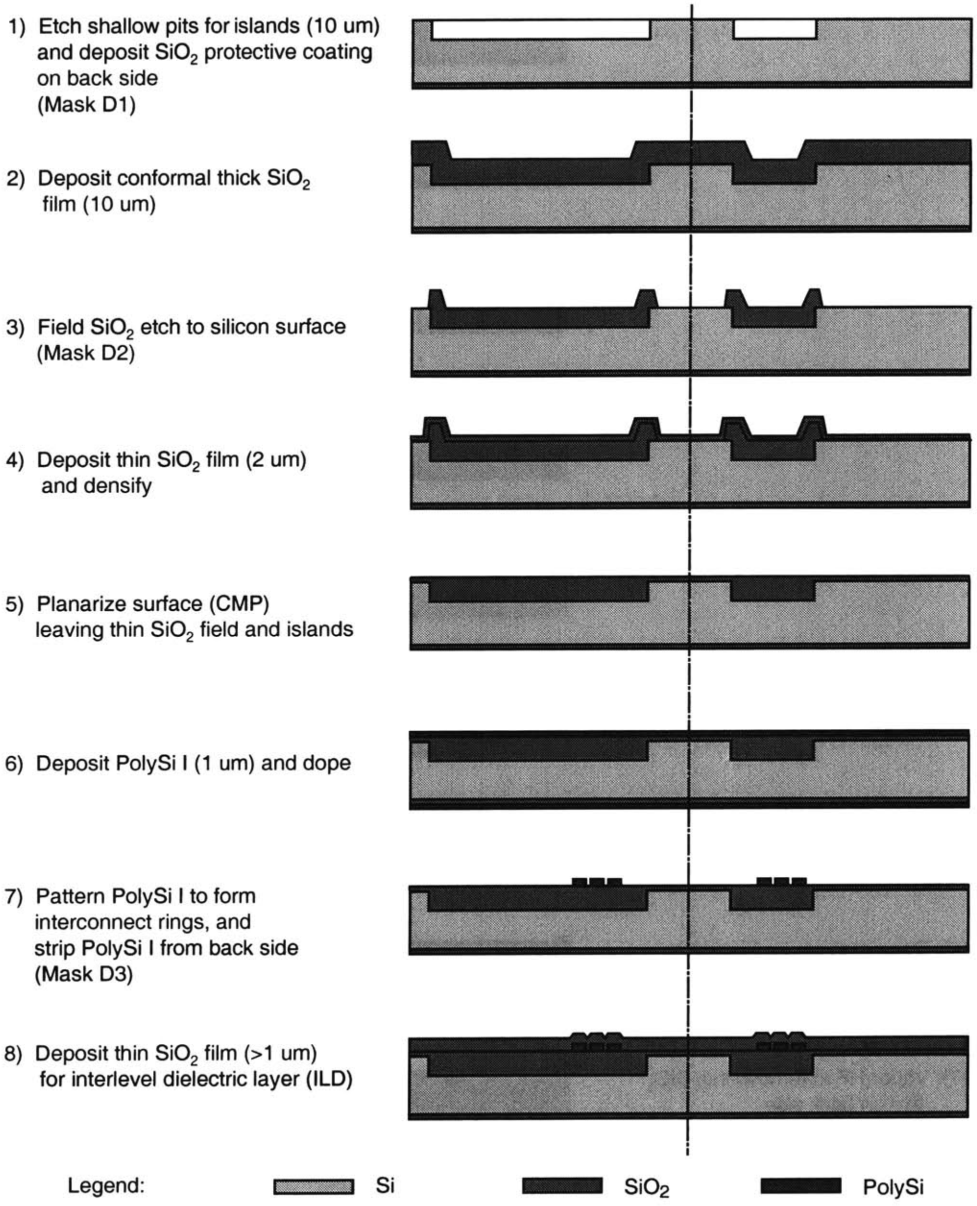

1) Etch shallow pits for islands (10 um) and deposit SiO_2 protective coating on back side (Mask D1)

2) Deposit conformal thick SiO_2 film (10 um)

3) Field SiO_2 etch to silicon surface (Mask D2)

4) Deposit thin SiO_2 film (2 um) and densify

5) Planarize surface (CMP) leaving thin SiO_2 field and islands

6) Deposit PolySi I (1 um) and dope

7) Pattern PolySi I to form interconnect rings, and strip PolySi I from back side (Mask D3)

8) Deposit thin SiO_2 film (>1 um) for interlevel dielectric layer (ILD)

Figure 3-17: TBOS stator process flow - part 1

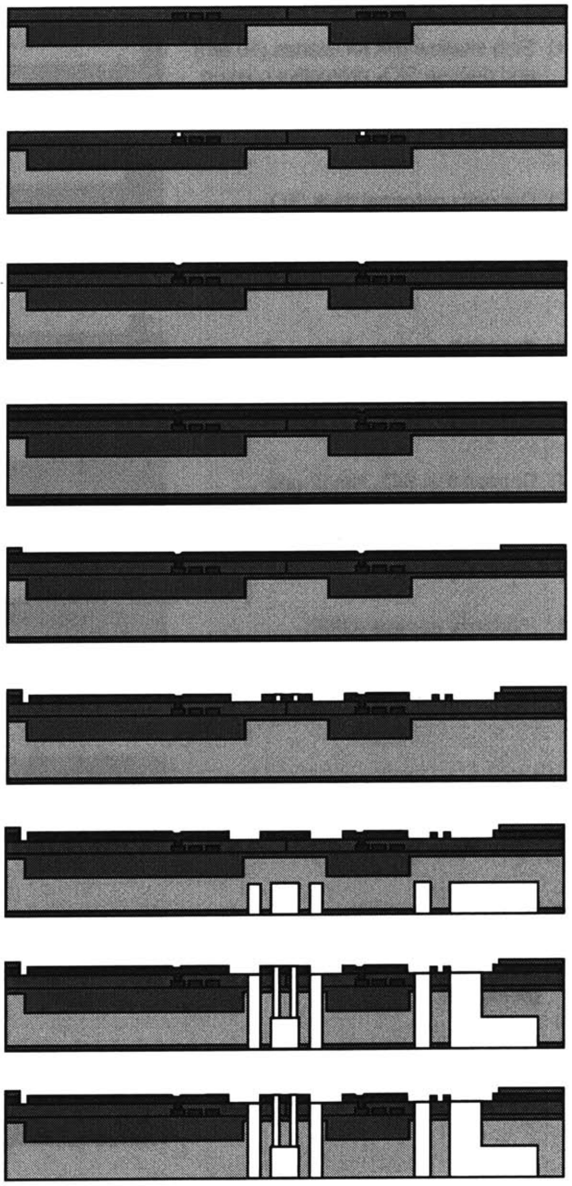

9) Planarize ILD surface (CMP)

10) Pattern the vias through the ILD (Mask D4)

11) Deposit PolySI II (1 mm) and dope

12) Deposit thin SiO_2 film, and polish for bonding (CMP)

13) Pattern bonding SiO_2 (Mask D5), and strip PolySi II from back side

14) Pattern PolySi II to form the electrodes (Mask D6)

15) Deep etch on the back side for piping (Mask D8)

16) Deep etch on the front side for ATB orifices and plenums (Mask D7)

17) Vapor HF to remove thin SiO_2 film on back side

Legend: ▨ Si ▨ SiO_2 ■ PolySi

Figure 3-18: TBOS stator process flow - part 2

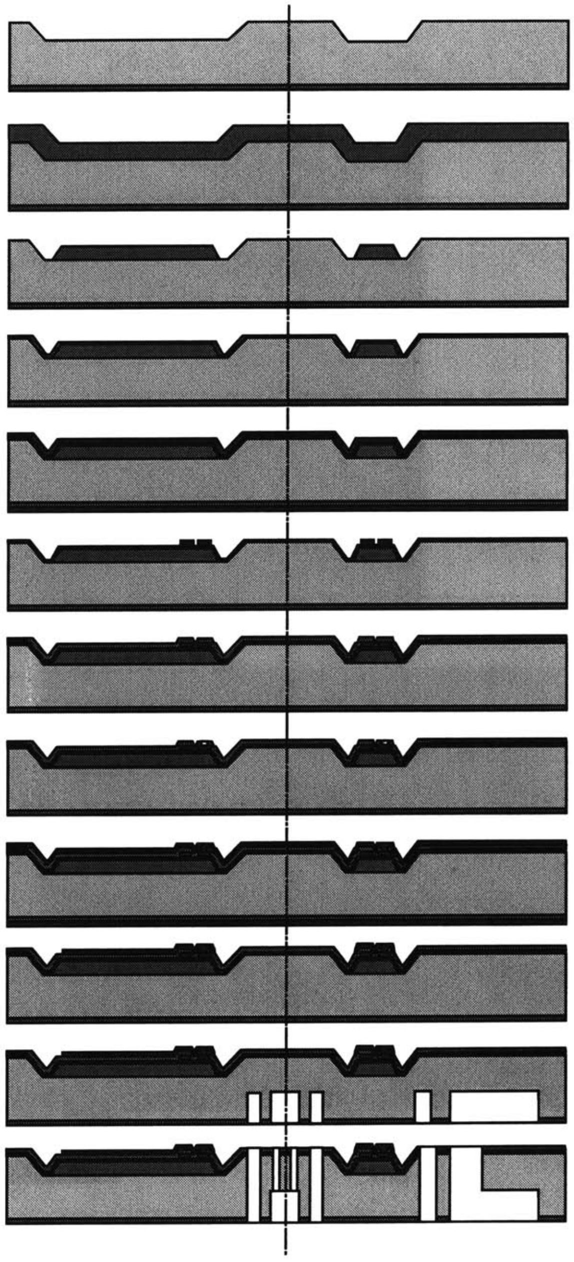

1) Etch shallow pits for islands (12 um) and deposit SiO$_2$ protective coating on back side (Mask D1)

2) Deposit conformal thick SiO$_2$ film (10 um)

3) Wet etch of Field SiO$_2$ to silicon surface (Mask D2)

4) Deposit thin SiO$_2$ film (0.1 um) as etch stop, densify

5) Deposit PolySi I (1 um) and dope

6) Pattern PolySi I to form interconnect rings, and strip from back side (Mask D3)

7) Deposit thin SiO$_2$ film (>1 um) for interlevel dielectric layer (ILD)

8) Pattern the via holes through the ILD (Mask D4)

9) Deposit PolySI II (1 um) and dope

10) Pattern PolySi II to form electrodes, remove from backside (Mask D6)

11) Polish both sides for bonding (CMP)

12) Oxide wet etch and Deep Si etch on the back side for piping (Mask D8)

13) Oxide wet etch and Deep Si etch on the front side for ATB orifices and plenums (Mask D7)

Legend: ▨ Si ▬ SiO$_2$ ■ PolySi

Figure 3-19: Recessed Oxide Islands (ROI) stator process flow

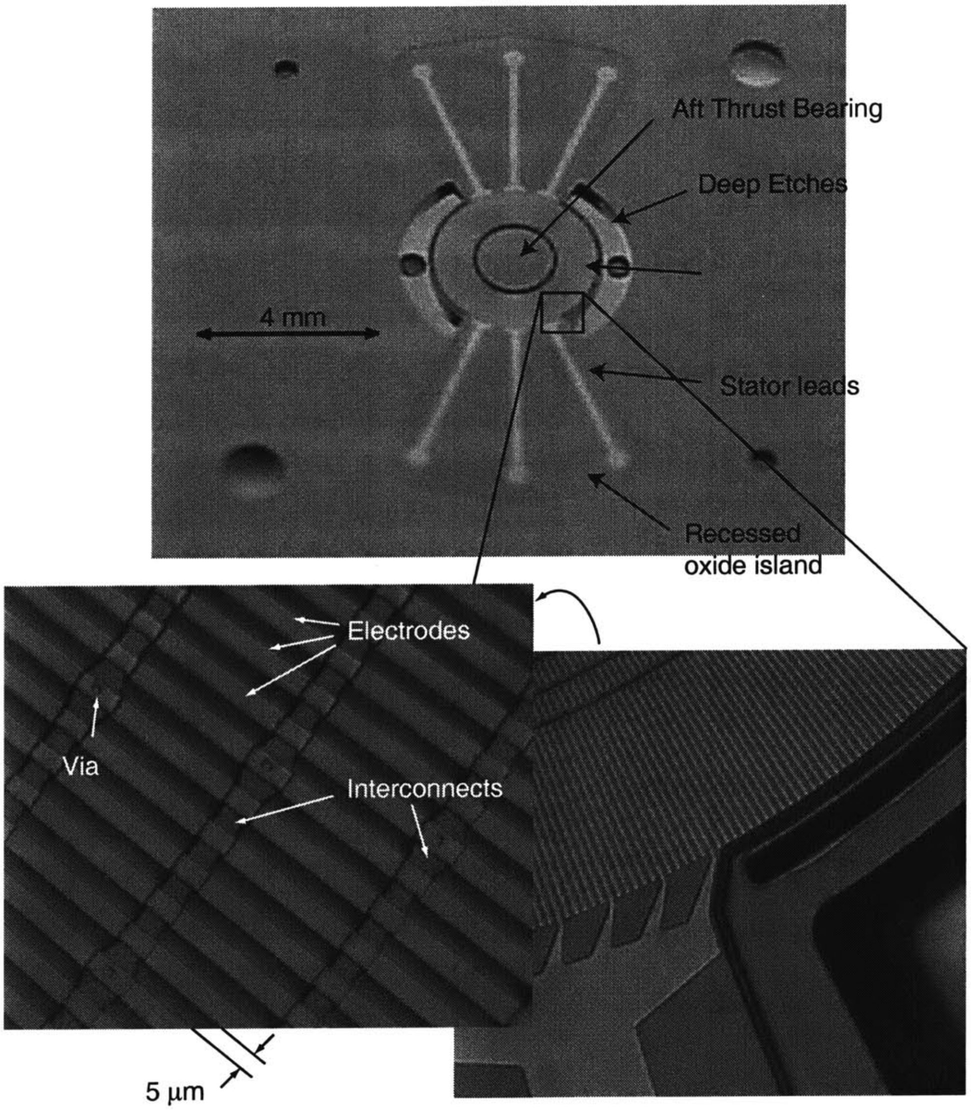

Figure 3-20: Optical photograph of a die of the *MC1* stator wafer after processing of the electrical layer and the deep etches, built using the Recessed Oxide Island Approach.

3.3.5 Thin film integration - design guidelines and limitations

Specific fabrication issues arose due to the integration of thin films within the silicon structure. They impose unique requirements on the process flow and mask design for the motor-compressor.

Thick insulation layers Thin films are typically limited in thickness to about 1 μm in IC processing and 2-3 μm in MEMS fabrication. The high voltages and electrical frequencies driving the motor-compressor raise the need for insulating layers of 10 μm or more to provide adequate insulation [37]. The development of thick (relatively to the state-of-the-art) PECVD SiO_2 was necessary and will be described in section 3.4.1.

Individual wafer processing: thin film then deep etches The approach to integrate the electrical components with the silicon structure is first to complete all the thin film processing, then do the deep etches in the substrate. Attention must be given to minimize the increase surface topography created by repeated thin film processing. Thicker photoresist must be used with increasing topology, sacrificing minimal achievable line width. It was found that regions of deep etches should not be closer than 50 μm from trenches or protrusions of 5 μm or more.

Polysilicon and oxide for high temperature compatibility After thin film processing and deep etches, the wafers are assembled by fusion bonding. Since a strong bond is established by annealing the bonded wafer pair at 1100°C for 1 hour, the thin film materials must retain their electrical characteristics and mechanical integrity at this high temperature. The materials of choice are low stress insulators such as SiO_2 as a dielectric, and doped polysilicon as the conductor. Compatibility with the overall process must be assured when considering other materials.

Bonding of wafers patterned with thin films The presence of multi-layered thin films on the wafer surfaces imposed significant challenges to the wafer bonding process. Three main issues are raised:

1. Surface roughness must be in the range of 5 nm or less to ensure intimate surface contact. Deposited or grown thin films may necessitate polishing to satisfy this criteria.
2. No protrusions must remain over the entire bonding surface. If thin films are removed from bonding areas, extra care must be taken during photolithography and etching to ensure that the etched areas are completely clear to prevent spots of the material to remain, protruding from the bonding surface. Polishing can also be used to planarize surface topology.
3. The ratio of bonding surface to wafer bow must be maximized. The normal surface force between wafers during bonding acts against the thin film stresses which tend to curve the wafer. Larger contact area will increase the normal force and improve the bonding of bowed wafers.
4. Edges of patterned films should not overlap with bonding areas, in order to prevent bonding complications. Even if a surface is planarized to reduce the topology, it is rarely perfectly flat. Therefore, the bonding areas should not enclose edges of patterned films.

3.3.6 Fabrication results for the Motor-Compressor

Two FEP-Rotor wafer pairs were fabricated, and the second pair pursued to form a complete Motor-Compressor 5-wafer stack, referred to as *MC1*. The stator was built using the Recessed Oxide Island approach described above. After bonding and die sawing, 10 dies out of 12 yielded viable devices. Figures 3-21 and 3-22 show pictures of one delaminated die and of the rotors before final bonding, respectively. Details of the processing are summarized Appendix C. Assistance is acknowledged from X. Zhang for help with the forward end plate etching, and from A. Hoelke for help with the rotor thin film processing.

In addition to building the rotor and stator wafers (#3 and #4) with thin films, major challenges remained in bonding these wafers with the others to form the 5-stack device. The following paragraph describe the challenges faced, the approach, and the results.

Thick oxide film patterning Wet etch patterning of the thick oxide proved to be challenging due to the low adhesion of photoresist to the oxide. As shown in Figure 3-23, the

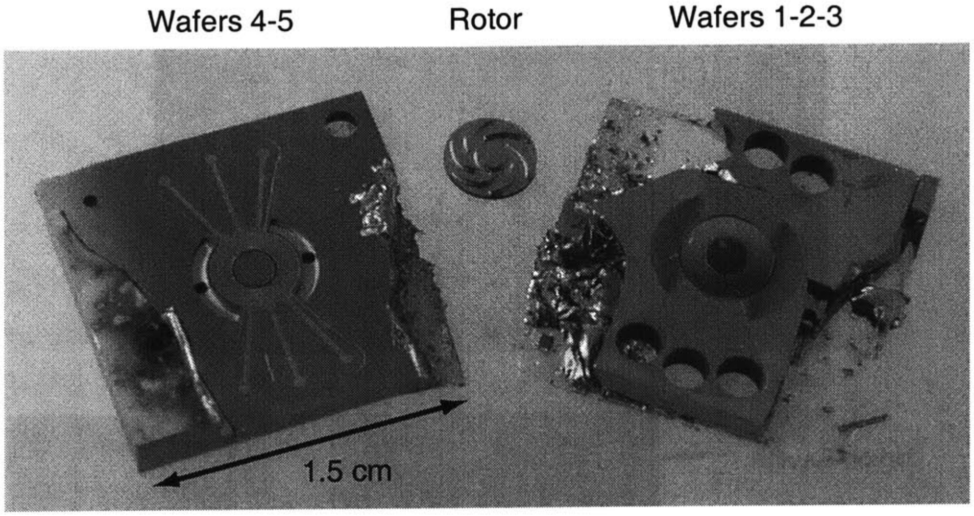

Figure 3-21: Photograph of a delaminated Motor-Compressor die. To the left is the stator, and to the right, the back side of the rotor. An extra 4 mm impeller is also shown in between both halves of the die.

edge of a 4 mm diameter circle of resist showed curling along the edges. This results in an undercut by the wet etchant. This was minimized by limiting the resist post-bake to 30 min at 90°C , therefore reducing the stress in the film.

FEP-Rotor bonding Bonding of the forward end plate (wafer #2) to the rotor plate (wafer #3) was prevented by unusually poor surface contact. The problem was attributed to the rotor wafer top surface. Extended buffered oxide etch (BOE) was necessary during the rotor thin film processing, exposing the top silicon surface of the wafer for at least 30 min. Although the etch rate of silicon in BOE is negligible, a short loop experiment exposing polished silicon wafers to BOE for extended periods of time suggested that it can create regions of high roughness [27].

Increased time and compression force The quality of the contact of the first FEP-Rotor pair was improved by keeping the wafers in compression for extended periods of time after alignment and initial contact. Figure 3-24 illustrates the contact quality, improving over time. Annealing at high temperature did not improve the contact area, as illustrated in the final subfigure (however, the anneal is desirable, since it increases the bond strength in the regions of good contact, establishing a permanent wafer bond).

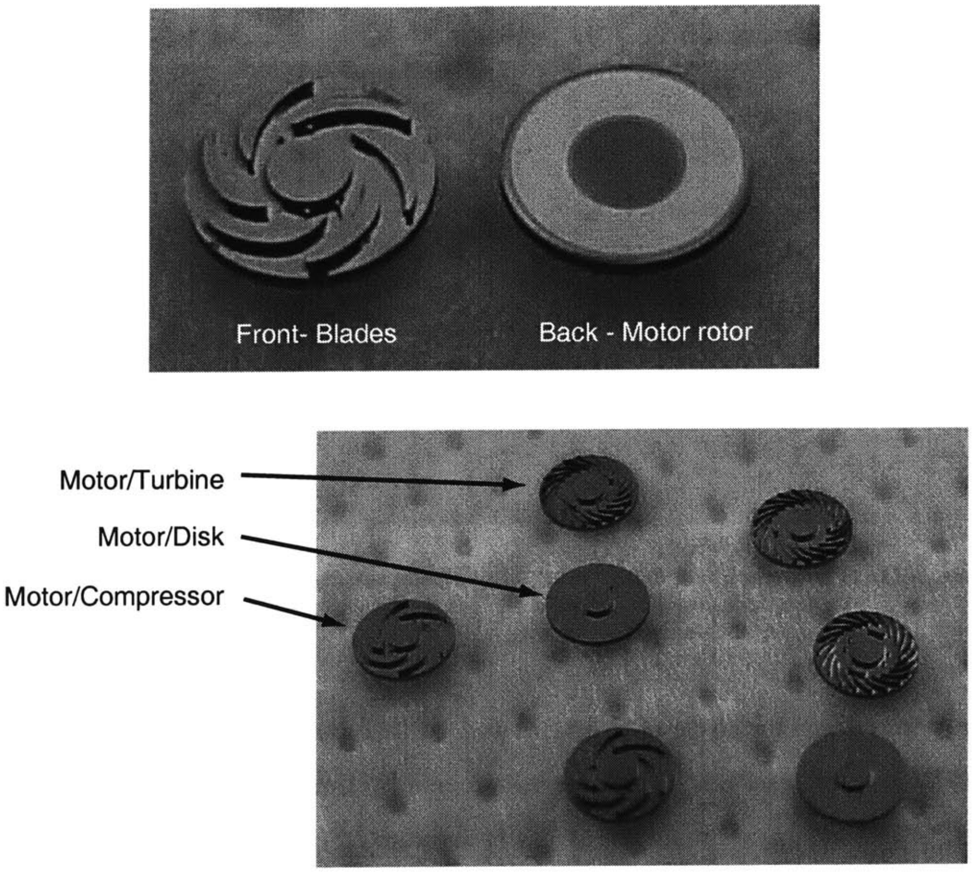

Figure 3-22: Photograph of the microrotors before bonding, showing the three types of motor-driven devices that where built: with turbine blades (Motor/Turbine), compressors blades (Motor/Compressor), or no blades (Motor/Disk)

CMP to improve bond quality Before attempting to bond the second FEP-Rotor pair, the wafer surfaces were polished to reduce the surface roughness. Since the wafers were already patterned, a conformal polishing approach was used, which does not preferentially remove the highest features, but instead mostly conforms to the wafers surface. Bonding of the second FEP-Rotor pair was successful and did not require the extended compression cycle. After etching the journal bearing however, the rotors were not held in place by the snap-off tabs. It was found that bonds were not well established between the pillar and beam which form the mechanical link, and is attributed to insufficient polishing for such a small bonding area.

Complete 5-stack bonding Wafer bonding of the FEP-rotor pair to the other wafers was also hindered by surface quality problems. The stator surface was repeatedly polished until trial bonding runs demonstrated good contact over most of the device area. The conformal

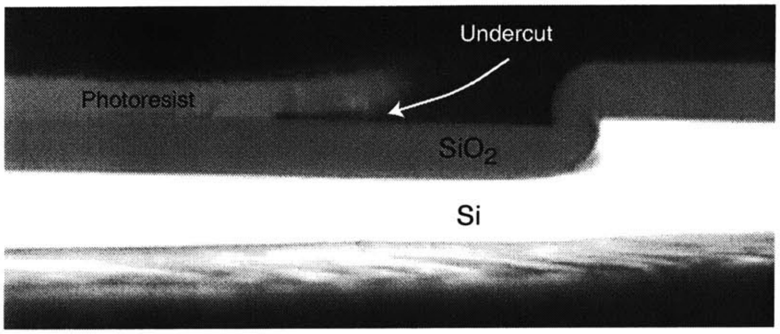

Figure 3-23: Optical photograph of cleaved rotor wafer with photoresist, showing a region of possible undercut where the film is curling.

CMP settings were used in order to minimizing the erosion of the electrodes, especially the 1 μm elevations created when they cross over the interconnect rings. After sufficient polishing for bonding, the electrode thickness at the intersection was reduced from 1.1 μm to 0.8 μm , which does not affect the electrical characteristics of the stator. The entire 5-wafer stack was successfully bonded, yielding a large contact area in the center of the wafers, as shown in Figure 3-25. The rotors were individually inserted in their housing during the bonding process. This manual process did not appear to hinder successful bonding and operation (as will be discussed in later chapters). This suggests that rotor retention and release of an enclosed rotor may not be necessary, if manual assembly is acceptable.

Consequences of CMP Repeated polishing of the etched wafers had the consequence of clogging the 10 μm in diameter thrust bearing nozzles with CMP slurry. This was only discovered after the wafer stack had been bonded and diced. A post-cleaning procedure, using an aqueous solution of 10% oxalic acid in an ultra-sound bath, was found to remove the dried CMP slurry. The dies were individually soaked in the oxalic acid solution, purged with filtered DI water, cleared with pressurized nitrogen, and dried in an oven at 110°C for 1 hour in an atmospheric pressure air ambient. This procedure, repeated twice on some devices, resulted in thrust bearing flow characteristics similar to those of the MC-Bearing Rigs, hence suggesting that the nozzles were cleared. This post-cleaning step could be avoided by cleaning the wafers with oxalic acid after each CMP step and preventing the wafers to dry before they have been thoroughly cleaned. This could be avoided altogether if polishing were not necessary for bonding.

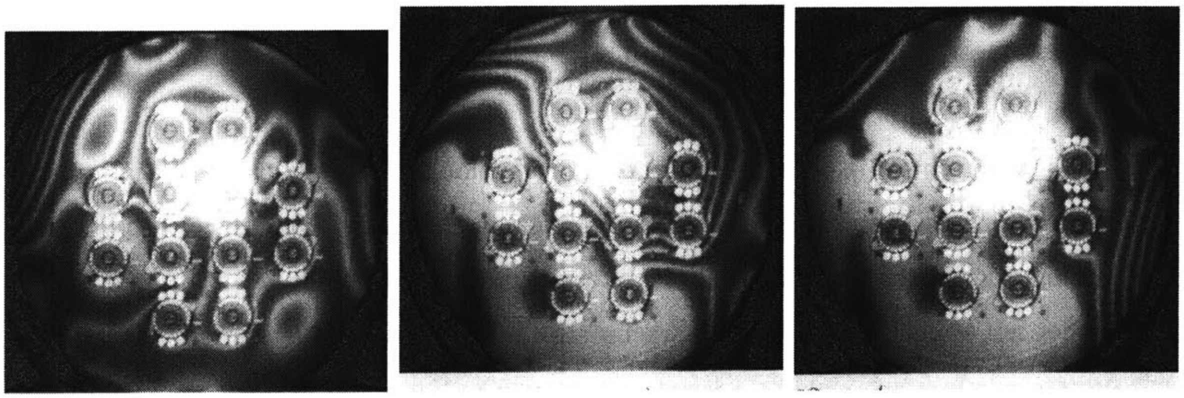

(a) after 1^{st} bonder run (b) after 2^{st} bonder run (c) after 4^{st} bonder run

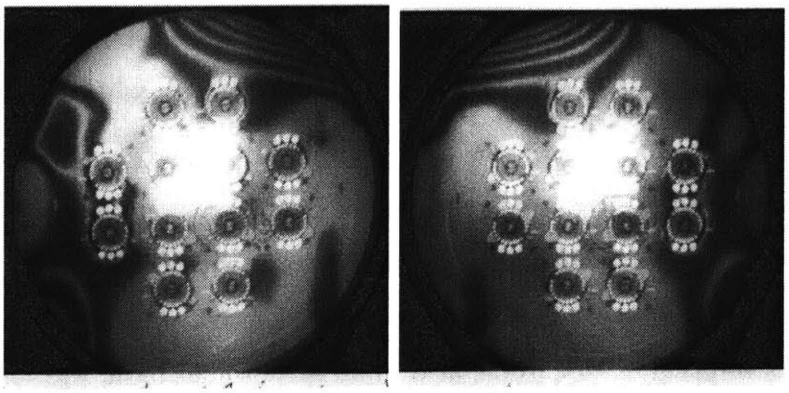

(d) after 6^{st} bonder run (e) final contact, after anneal

Figure 3-24: Quality of contact improvement after repeated cycles of compression (4000 mbar) at moderate temperature in a N_2 low pressure ambient. Fringes are indicative of poorly contacted areas.

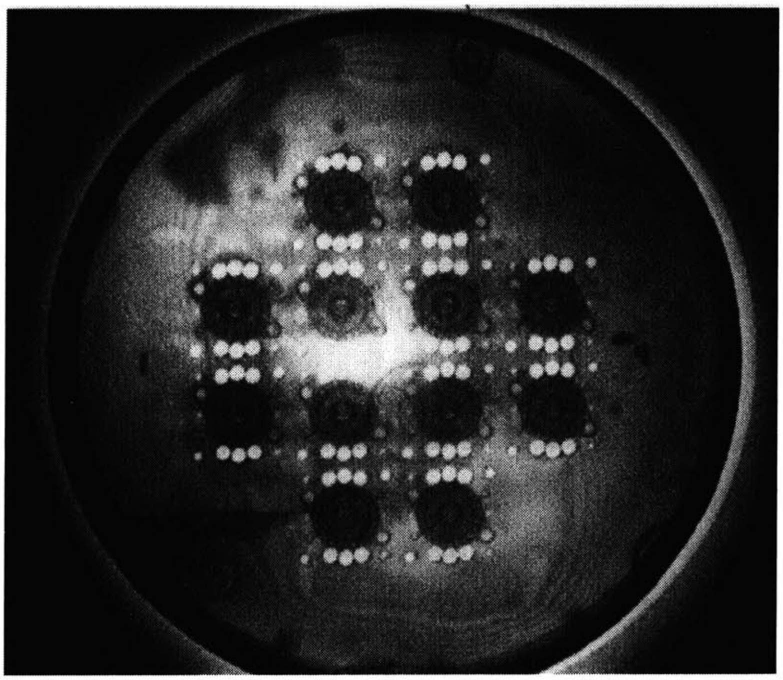

Figure 3-25: Infrared picture of the bonded Motor-Compressor 5-wafer stack (*MC1*).

3.4 Process Development

3.4.1 Thick PECVD SiO_2 insulating layers

The high operating voltage of the electrostatic motor introduces the requirement for thick insulating layers under the electrical components in order to improve the electrical efficiency and motoring power. Plasma-enhanced chemical-vapor-deposited (PECVD) oxide films typically range from 1000 Å to 1-2 microns. PECVD film thicknesses were pushed to more than 10 μm for the motor-compressor fabrication, providing the requisite insulation under the rotor and stator electrical structures.

Before describing the fabrication development of the thick SiO_2 films, requirements for thick insulators will be justified.

Thick rotor insulator increases the torque delivered by the electric motor, everything else being kept constant. With infinitely thick rotor insulation, the induced electric fields are concentrated in the rotor conducting film and no leakage occurs in the underlying silicon substrate.

The stator structure benefits from thick insulation mostly for efficiency reasons. Parasitic capacitance between the stator conductors, excited at ±300V, and the underlying silicon substrate tends to draw more current than necessary through the power electronics and stator structure, incurring additional losses and reducing the system efficiency.

The design insulating thicknesses were a result of trade-off between performance and fabrication complexity and risk.

Thick insulator development

Practically, film thicknesses are limited by their capability to withstand high stresses. In-plane Stress in the PECVD $Si0_2$ films come from three sources:

1. In-situ stress: introduced during the deposition;
2. Film shrinkage: after deposition, the film is densified at 1100C for 1 hr in a nitrogen ambient in order to lower the hydrogen content in the film. Densification is necessary

in order to prevent release of hydrogen during subsequent processing such as etching, bonding, and film deposition;

3. Thermal expansion mismatch: the lower thermal expansion coefficient of SiO_2 compared to the Silicon substrate induces compressive stresses in the film when it is cooled from the deposition temperature (400°C) to room temperature.

Using the Novellus Concept One PECVD system in MTL, silane-based SiO_2 films have been deposited up to thicknesses of 20 μm until film cracking started to occur. Upon densification, such films thicker than 14 μm typically exhibited cracks. This behavior of these films is reported by Ghodssi et al [65] and will not be discussed further here. From the system design perspective, deposited thickness of 14 μm is a practical limit on the insulating layers. In addition, a safety margin was adopted for the initial experimental devices to reduce the risk of cracking by limiting the thicknesses to 10 μm , as a trade-off with performance.

In addition to cracking problems, high stresses in the films induce excessive wafer bow[3]. The compressive film on one side of the wafer applies a bending torque on the substrate, curving the wafer. These oxide films are typically compressive, bowing the wafer with the film on the convex surface.

Measured wafer bow is shown in Figure 3-26 as a function of film thickness, for PECVD silane-based SiO2 deposited on one side of 525 μm wafers using the Novellus Concept One system [39]. Each data point is the average of 3 wafers, and the solid line and dashed lines represents the measurements before and after densification respectively. We notice that the densification process increases the bow by approximately a factor of 4. The stress is calculated using the Stoney formula [56] to be approximately constant over the range of thicknesses, at a value of -50 MPa for the undensified films and -200 MPa after densification. The densification process is necessary in order to reduce the hydrogen content in the deposited film, which would otherwise be deleterious to the electrical properties of subsequent deposited layers [58].

Wafer bonding of excessively bowed wafers with thick film was found to be extremely challenging, for three main reasons:

---

[3] Wafer bow is defined as the deflection at the center of the wafer, measured with respect to the edge of the wafer.

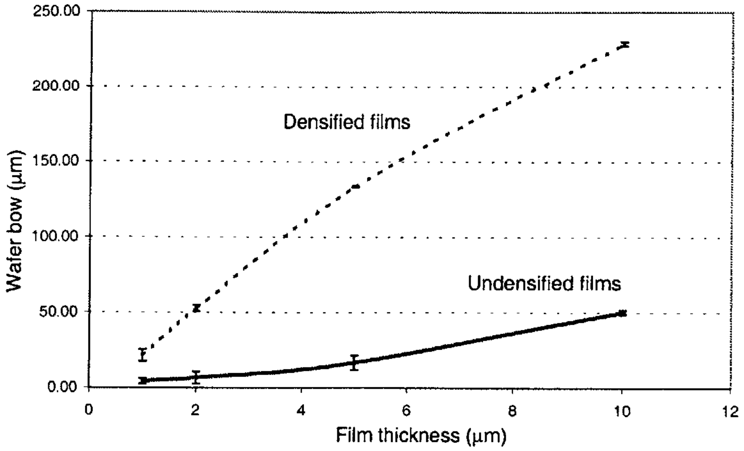

Figure 3-26: Wafer bow due to thin film stress as a function of film thickness. Novellus Concept1 silane-based SiO_2 film deposited on one side of a 525 μm silicon wafer [21].

- Excessive bow prevented the wafer manipulation by critical processing equipment;
- Large normal contact forces are necessary in order to prevent the wafers from returning to their original bowed state;
- Thick films must be polished to reduce the as-deposited surface roughness to acceptable levels for bonding.

Having determined these challenges for thick oxide films, alternate geometries were engineered to allow for their integration into multi-wafer bonded stacks. The films were patterned in order to clear the bonding and other non-electrical regions. Two variants of this approach are presented in Sections 3.3.3 and 3.3.4, which have demonstrated a 5× reduction in bow compared to a uniform film covering the entire wafer. The second approach, Recessed Oxide Islands, was furthermore successfully bonded in the 5-wafer stack Motor-Compressor.

3.4.2 High aspect ratio DRIE

The journal bearing geometry pushes the requirements on DRIE. A 10 μm wide and 300 μm deep trench needs to be etched, maintaining a straight wall profile throughout. These high aspect ratio and form accuracy requirements are beyond standard MEMS processing capabilities, and therefore required extensive development to satisfy the design needs of many devices part of the Microengine project. The DRIE development of 300 μm deep journal etching lead by Ayón *et al.* and is presented elsewhere ([3, 4]). This section presents the etching experience gained during the MC-Bearing Rig and Motor-Compressor. A tailored journal bearing etch was used for these devices, as proposed by Ayón.

Tailored DRIE For constant plasma conditions, the ion flux and mass transport at the bottom of the trench reduces as the trench reaches depths of more than 200 μm, at widths of 10-20 μm[4]. The etching conditions at that point therefore change, affecting the anisotropy. One approach to maintain the vertical wall profile, is to increase the ion flux by changing the plasma conditions.

Journal bearing etch experience The *MCBR1* journal implemented this approach by opening the throttle valve downstream of the chamber. Since the etch and passivation gas flows were kept constant, the chamber pressure was reduced and the driving potential, increasing the ion flux by reducing the ion collisions in the plasma and increasing their kinetic energy.

Figure 3-27 shows an optical photograph of the etched journal on Die #12 of *MCBR1*. Using recipe MIT56 as a baseline, and reducing the pressure in the chamber by opening the exhaust valve by 1.2° every 30 min, over a total etch time of 4h30min. It was noticed that the trench profile remained tapered, maintaining 13-15 μm over the first 230 μm , but then tapering to 9 μm at 300 μm .

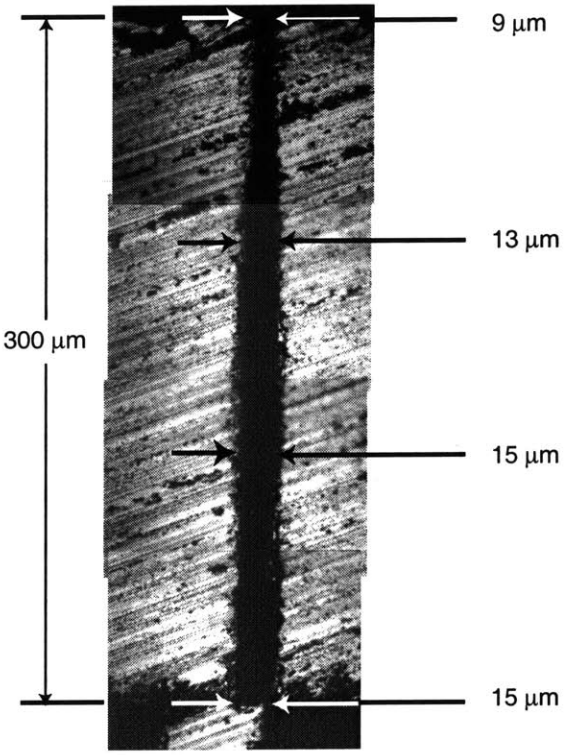

Figure 3-27: Cross-section of the journal bearing of Die #12 of *MCBR1*. The trench is etched from the bottom side.

3.5 Rotor Retention and Mechanical Release

An on-going challenge in the fabrication of micro-rotors is a reliable process flow to create free parts within enclosed structures, without tedious manual assembly and risk of damage. This section summarizes the rotor release strategy and development for the MC-Bearing Rig and Motor-Compressor. A discussion of the requirements and possible options is first presented, followed by the experimental development of *snap-off tabs*, the chosen approach.

3.5.1 Rotor retention and release strategies

Ideally, the wafers would be processed individually, starting with the most critical etches first. Once all etches completed, wafers with dimensions within tolerances can be chosen from those processed, and the 5-stack assembled. The advantage of this approach is to push low yield processes upstream in the process flow, minimizing the value of a wafer before it reaches a critical point. In this scenario, the rotor must be held in place at the wafer level, a challenging requirement.

A less ideal scenario from a yield standpoint, consists of bonding one of the end plates to the rotor plate before a final etch creating the rotor. The rotor can be held by a mechanical link between the rotor and the adjacent wafer. This approach was previously demonstrated by C. C. Lin [29] on the first generation micro-bearing rig. The mechanical link, or *tab*, was created between the FEP and the rotor plate (wafers #2 and #3) near the center hub on the rotor. Before testing, the rotor was released by laser ablation of the silicon tab. This technique was shown to be viable, but resulted in a low yield, which has a dramatic effect since it is at the end of the process. An alternate strategy was therefore pursued for the MC-Bearing Rig and Motor-Compressor.

A variety of options were originally considered, and discarded for the following reasons:

1. Sacrificial thin oxide film between the rotor and FEP or AEP (wafers #2-3 or #3-4) or sacrificial thick oxide filling the journal bearing gap: entrain the risk of etching the oxide films forming the micromotor;
2. Handle wafer supporting the rotors with photoresist or polymer: would not withstand

the high silicon-to-silicon bonding temperatures;

3. Silicon bridge crossing the journal bearing, formed during the blade etch: difficult access for laser ablation and high risk of particles entering the journal bearing gap if removed by fracture.

3.5.2 Snap-off experimental development

The approach adopted was similar to that of the first generation bearing rig. As shown in Figure 3-28, a silicon pillar extending from the rotor bonds to a horizontal beam on the forward end plate. The journal bearing is then etched and the remaining three wafers are aligned and fusion bonded to complete the five-stack. The silicon links are then mechanically fractured to release the rotor before testing, acting as *snap-off tabs*. This differs from the first generation bearing rig process [29], which used a laser assisted etch to remove the tabs.

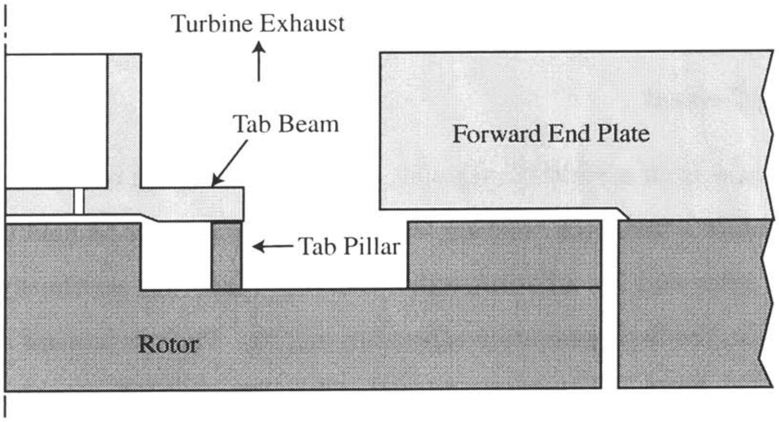

Figure 3-28: Schematic cross-section of wafers #2 and #3 showing the snap-off tab configurations.

The tab geometry was designed to provide a solid support against axial and in-plane motion of the rotor, while allowing a controlled failure mode upon lateral force. Four tabs were located around the forward trust bearing hub, directly accessible through the compressor inlet. They were positioned in pairs, on each side of the center supports.

An array of configurations were designed using simple beam theory and stress concentration relations, and tested aiming for a clean fracture at the roots of the pillar and beam. In order to reduce the implementation uncertainty, the test geometries were fabricated in the actual device structure.

Figure 3-29 shows such a snap-off tab structure before and after being fractured. The fractured surfaces are raised from the disk surface, which is important so as not to introduce stress concentrations. Figure 3-30 shows an SEM of a tab pillar before bonding, which illustrates the local accelerated etching at the sharp corners of the structure. This can be avoided by rounding the corners on the mask.

This snap-off tabs approach has been successfully used in two five-stack builds.

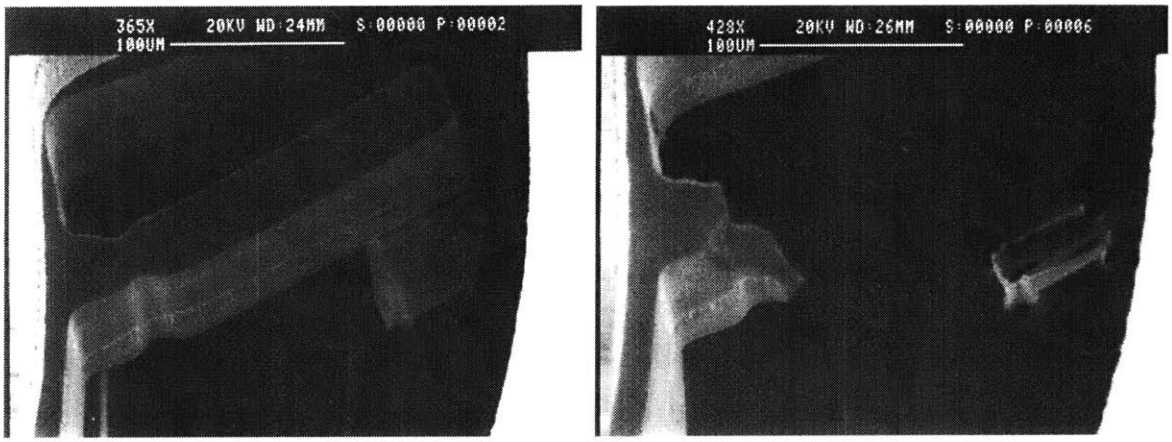

(a) Before fracture

(b) After fracture

Figure 3-29: SEM of a silicon snap-off tab before and after fracture, viewed through the center inlet port.

Silicon needles: a snap-off tool

Micromachined silicon needles were specially designed to reach down the main exhaust port and apply the necessary lateral force to snap the silicon tabs. The needles are fabricated using the aligned double-side DRIE process. First, one side of a 450 μm wafer was patterned and etched locally down 350 μm, where the needles will be formed. the wafer is then reversed and the needles are cut out through the remaining 100 μm . The optimal geometry consisted in square 100×100 μm needles, 2 mm long with a 60° beveled tip, formed during the second etch. Such a small tip was necessary in order to reach into the inlet, without obstructing the view.

The needle is then held with a set screw onto a fixture, which is attached to a three-axis micrometer positioning stage. A stereo-microscope is used to view at an angle down the

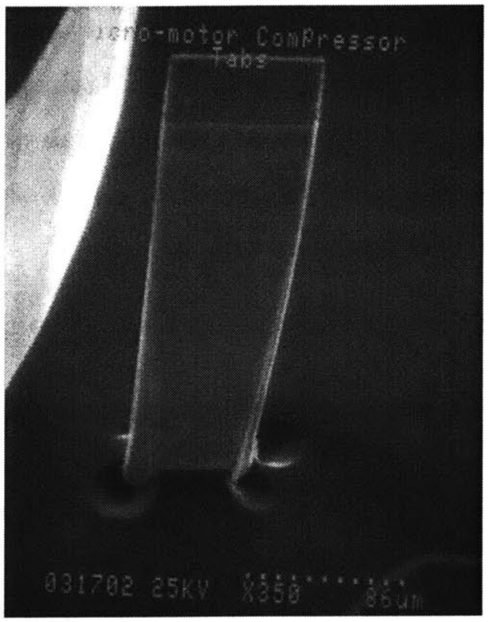

Figure 3-30: SEM of a silicon pillar before bonding.

inlet, as the needle is lowered towards the snap-off tab. As the beveled edge of the needle is brought into contact with the top edge of the tab, the needle is lowered vertically, until the tangential component of the contact force is sufficient to induced fracture at the roots of the pillar and beam.

Particles generated during snap-off were removed by blowing nitrogen radially inward through the main flow path and out of the center port. The impeller blades essentially act as a fence, protecting the critical journal gap from the debris. The tab was usually found to break in one large piece, also generating some microscopic particulates. Before spin testing the device, pressurized gases are flow through the aft thrust bearing, the motor gap, the journal bearing, the impeller and out the center port, as a precaution. Finally, observation with an infrared microscope through the silicon die confirms that no particles remain.

CHAPTER 4

MICROFABRICATED BEARING DEVELOPMENT

A pivotal effort in the development of the Motor-Compressor was in the area of *bearings and rotordynamics*. This section describes the experimental development of microfabricated air bearings used for the Motor-Compressor, mostly focusing on the hydrostatic journal bearing operation at high-speeds. The supporting disciplinary research has been conducted by previous researchers in the MIT Microengine project, namely: D.J. Orr [41] experimentally investigated the hydrostatic and hydrodynamic plain journal bearing behavior on a 26x scaled-up low-aspect ratio bearing rig; E.S. Piekos [44] numerically modeled the dynamics of such microfabricated gas bearings; N. Savoulides [50] investigated the rotordynamics of hybrid (hydrostatic and hydrodynamics) journal bearings using low order models, all with the support of S. Jacobson, K. Breuer, and F. Ehrich.

Experimental bearing development at the micro-scale has been centered around a microturbine-driven bearing rig. As detailed by Lin [29], the first generation *microbearing rig* played a major role in developing the microfabrication techniques as well as characterizing the hydrostatic thrust bearings and demonstrating rotation up to 60,000 RPM. Further unpublished work by S. Jacobson demonstrated sustained rotation rates for some microbearing rigs up to 296,000 RPM. Repeatable operation at higher speeds was however desirable for the motor-compressor, and motivated further bearing development as part of this work.

The objective of this experimental effort was to demonstrate sustained high-speed rotation and define an operating protocol which would be applicable to the Demo Motor-Compressor.

This section presents this follow-up effort in the development of microfabricated gas bearings. The approach has been to fabricate and test a second generation microbearing rig based on the silicon structure designed for the Demo Motor-Compressor, which will be referred to as the *MC-Bearing rig*. As detailed in the previous chapter, two sets of 12 devices were built as part of this work (*MCBR1* and *MCBR2*). The following sections will sequentially review the MC-Bearing rig device, present the experimental set-up, and present the experimental results in operating the MC-Bearing rig to rotational speeds greater than 1 million RPM. Of main interest will be the original effort in understanding and demonstrating high speed operation of the microfabricated hydrostatic journal bearing. Operation of the micro-turbine will also be discussed in Section 4.5, as an additional outcome from the MC-Bearing rig testing.

4.1 MC-Bearing rig description

The MC-Bearing rig device, shown in Figures 4-1 and 3-9 (105), consists of a 4.2 mm diameter rotor enclosed in a fusion-bonded stack of five aligned, through-etched wafers. Pressurized gases are supplied through the fluidic ports on the top and bottom surfaces of the die for the hydrostatic bearings and the turbine. The bearing design and secondary flow piping configuration was described in Section 2.4. The turbine operation and design has not been discussed, so it will be summarized next.

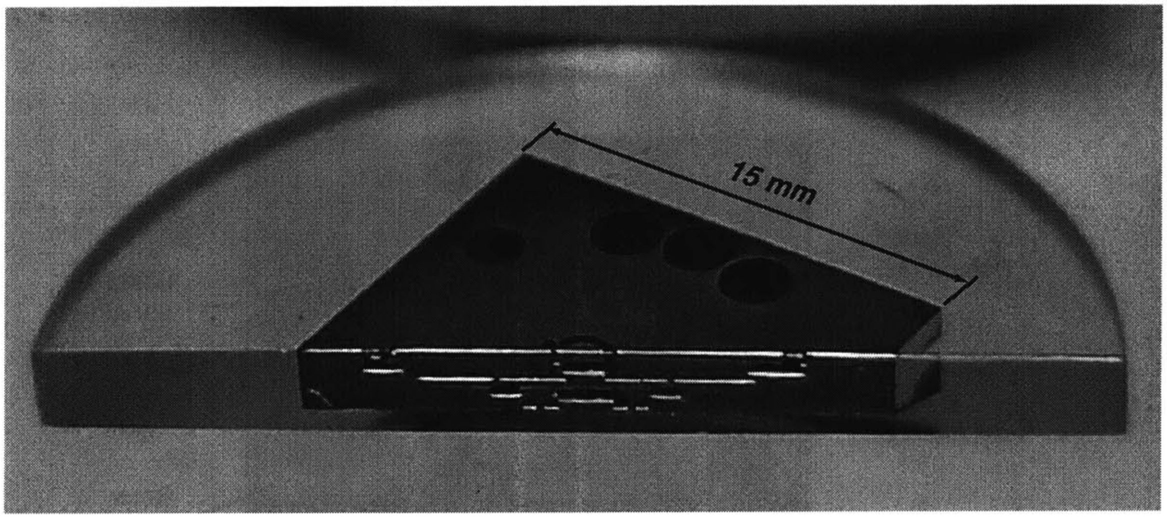

Figure 4-1: Photograph of an MC-Bearing rig die, which has been casted in epoxy and diced through its center. We notice the internal flow paths, created by deep etching and bonding a stack of 5 wafers.

Microturbine

Pressurized air enters the device near the outer edge and flows radially inward, first through a set of stationary (stator) vanes and then through the rotor blades, exhausting axially near the center of the device. The stator vanes, shown in Figure 4-2, are curved, turning the flow away from purely radial, imparting angular momentum to the flow as it accelerates. The turbine rotor blades turn the flow back toward radial, extracting angular momentum in the process. The angular momentum change across the rotor produces a torque. The power transferred to the rotor is the product of this torque and the angular rotation rate of the rotor.

The turbomachinery was designed by Stuart Jacobson using MISES, a two-dimensional computational fluid dynamics code developed at MIT [9], and is shown in Figure 4-2. MISES is a two-dimensional Euler solver coupled to an integral boundary layer formulation. The actual flow through the turbine is expected to be three-dimensional, mainly due to boundary layer growth on the end-walls. However, because the turbine flow is accelerating, the three-dimensional effects are not expected to be substantial [33]. The particular challenge in the design of microturbomachinery results from the microfabrication constraint that limits the design to constant blade height. A more traditional design for centrifugal turbomachinery would allow the blade height to vary inversely with radius to compensate for the increase in circumference with radius. As will be demonstrated herein, this limitation does not preclude the successful operation of microturbomachinery.

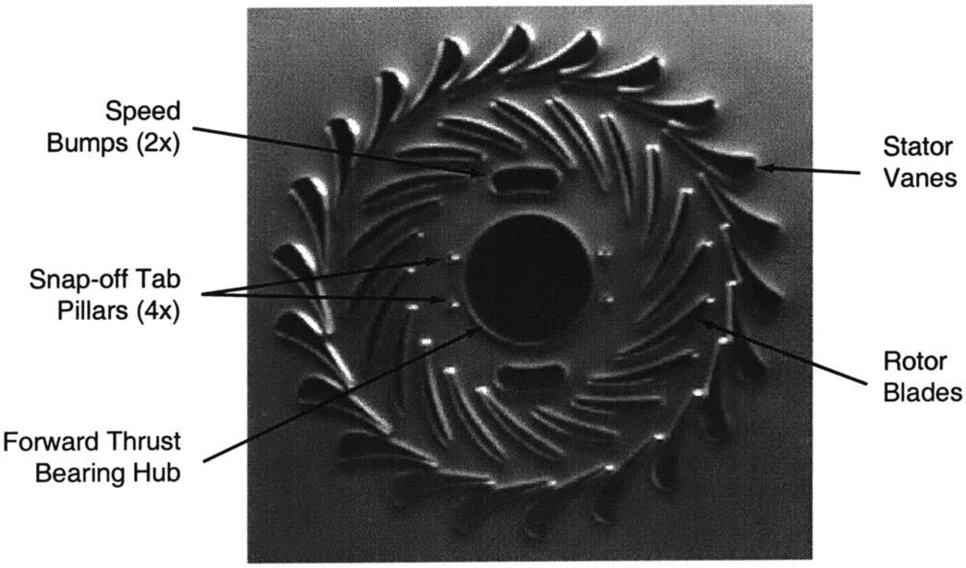

Figure 4-2: Photograph of the 4.2 mm diameter microturbine showing the 150 μm tall stator and rotor blades, two symmetric speed bumps, and four pillars for the snap-off tabs. In this picture, the journal bearing gap remains to be etched.

For this application, the turbine was designed to provide sufficient power to overcome the viscous drag in the bearings and on the back side of the rotor, which increases with the square of the rotation rate. The total drag is calculated as 13 W at a circumferential tip speed of 500 m/s. While viscous drag is relatively large in microsystems due to the small length scale, it is still quite small compared to the capabilities of high-speed turbomachinery [25]. The turbine for this device was intentionally designed to match the relatively low power requirements of the viscous drag. Alternative turbine designs that produce tens of watts of power beyond the drag requirements, while compatible with the current process and geometric constraints, have been designed for Power MEMS applications.

Device Operation

The rotor is set in rotation by applying controlled pressures to the bearings and to the turbine, by sequentially:

1. Applying pressures to the thrust bearings to float the rotor axially;
2. Applying pressures to the journal pressurization plena, flowing gases axially through the journal bearing to support the rotor in the radial direction;
3. Applying pressures to the turbine, to set the amount of torque imparted on the rotor and control the rotational speed.

The following section will describe the packaging and experimental apparatus which was assembled and used to test the MC-Bearing rig and Demo Motor-Compressor devices.

4.2 Experimental apparatus and packaging

Although the device is only millimeters in size, the experimental set-up necessary to adequately investigate its operation is considerably larger. Overall, the testing apparatus consists of: a gas handling system, speed and rotordynamics monitoring sensor, data acquisition system, and a package to interface the die with the macro world. The apparatus is located in a laminar flow, filtered air test room, and is illustrated in Figure 4-3.

The gas handling and data acquisition systems developed as part of this work are also being used for the testing of other devices in the Microengine Project, such as the μvalve, turbocharger, and eventually the turbine-generator. Packaging, discussed next, is however unique to each device.

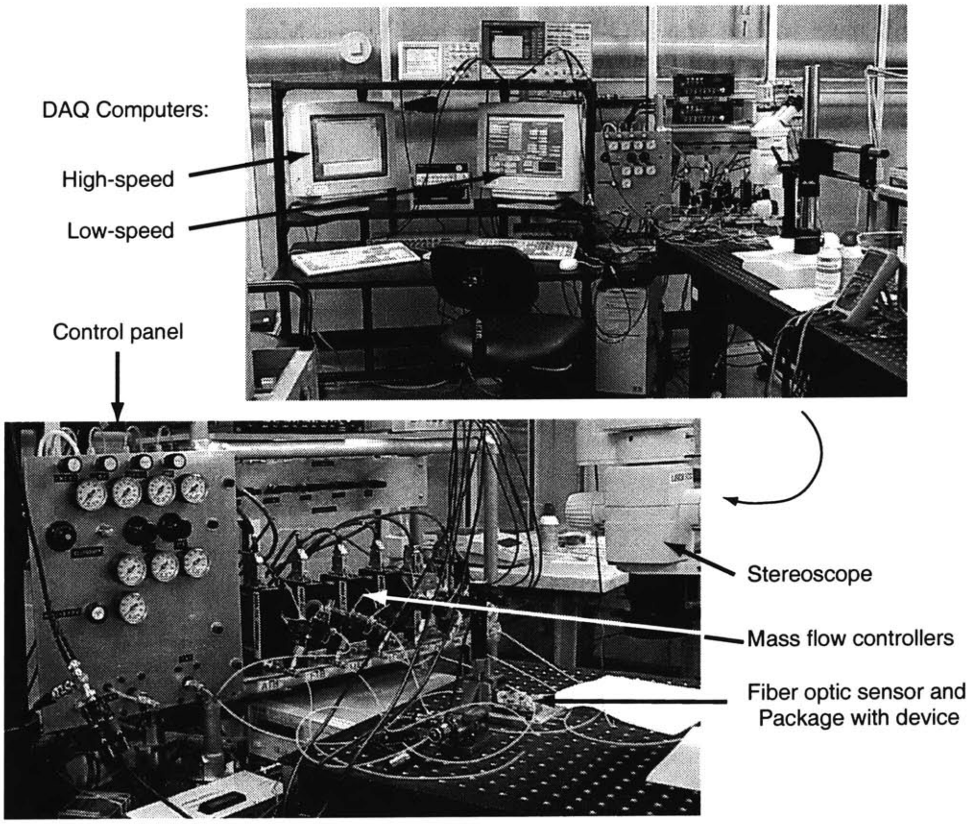

Figure 4-3: Photograph of the MC-Bearing Rig and Motor-Compressor test set-up.

4.2.1 Packaging

The microturbine-driven bearing rig die mounts in an acrylic package using o-rings to create sealed fluidic connections to the die. The package is largely based on the approach used by Lin [29] for the first generation microbearing rig. As shown in Figure 4-4, an aluminum spacer plate, with a square hole in the center to receive the die, is clamped between the top and bottom cover plates to hold the die in place and establish the fluidic connections. The spacer plate is slightly thicker than the device, such that the fragile silicon die does not come in contact with the top and bottom Plexiglas plates. Instead, the chip is supported by the rubber o-rings distributed over the front and back surfaces. Parker 2-002 and 2-004 o-rings were chosen, and the package was designed to create a 20% compression of the o-ring. This approach provided sealed fluidic connections up to at least 150 psig.

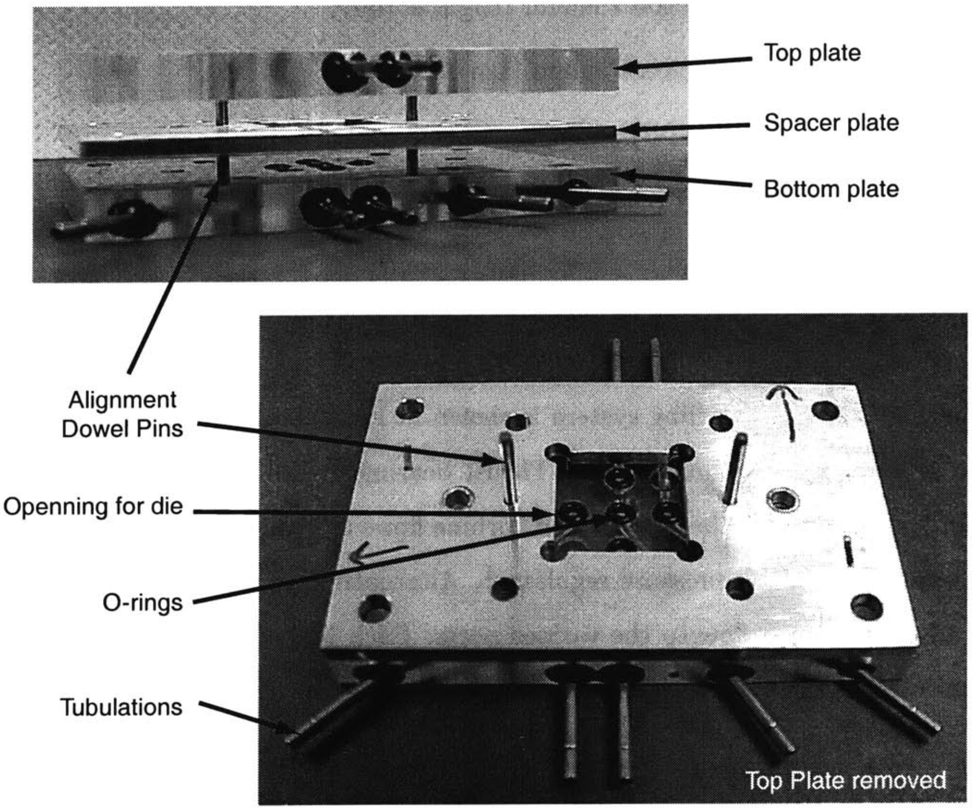

Figure 4-4: Photographs of the package.

The flow channels are machined in the top and bottom plates, such that ports are oriented radially outward. Standard 0.063" stainless steel bulged tubulations are then fixed in the Plexiglas plate (using medium stiffness epoxy), from which plastic tubing then connects the package to the gas handling system. Technical drawings of the packaging can be found in Appendix D.

4.2.2 Gas Handling system

The role of the gas handling system is to provide controlled pressures to the individual ports, and measurements of static pressure and mass flow. The die requires six independent pressure supplies, one static pressure tap, and two exhaust ports:

1. Main turbine inlet (or compressor exhaust);
2. Forward thrust bearing (FTB) supply;
3. Aft thrust bearing (ATB) supply;
4. High Journal Pressurization Plenum (High) supply;
5. Low Journal Pressurization Plenum (Low) supply;
6. Motor outer plenum (MOP) supply;
7. Inter-row pressure tap (Pir);
8. Main turbine exhaust;
9. Aft exhaust (for ATB and MOP).

A schematic of the gas handling system is shown in Figure 4-5. Pressurized nitrogen supplies the primary and secondary lines. Thrust bearing pressures are then controlled with pressure regulators, while the journal and turbine flows are controlled with metering valves downstream of a common pressure regulator[1]. Alternatively, the mass flow controllers can be used to set the mass flow to the various ports. Each line of the gas handling system is then connected to the package with plastic tubing.

4.2.3 Data acquisition system

The operating parameters are recorded using a PC-based data acquisition (DAQ) system. Two computers are used: a high-speed DAQ to acquire a single dynamic signal up to a rate

---

[1] This configuration allows simultaneous increase in bearing stiffness with speed, a useful feature in maintaining journal bearing stability.

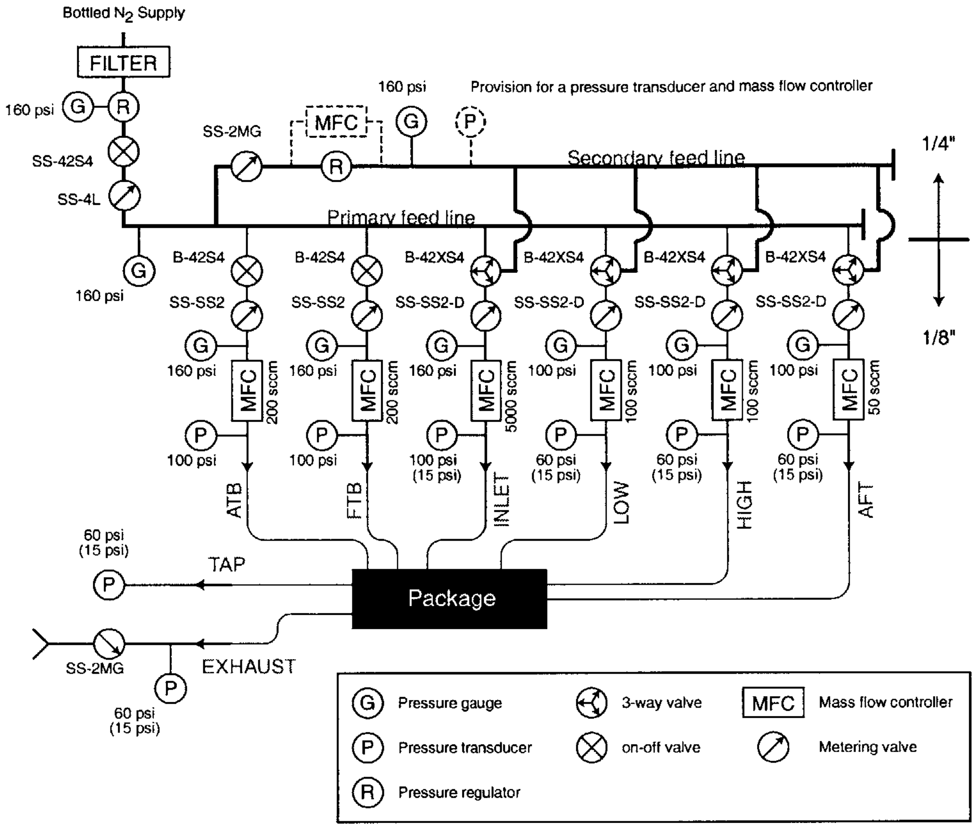

- MFC can be replaced with tube of length 5.167"
- All line are terminated with 1/16" tube connectors and connect to package with teflon tubing

Figure 4-5: Schematic of the gas handling system.

of 1.25 MSamples/sec (for short durations), and a low-speed DAQ for the complete quasi-steady data (usually recorded over the entire run). The low-speed DAQ records the mass flow and pressures on all fluidic ports, as well as the rotational speed. Labview software was used to implement the DAQ, and also to display the real-time data on the computer terminal. Measurements are sampled at 4 kHz and the average of every 1000 samples is recorded and displayed.

4.2.4 Optical speed and rotordynamics measurement

Speed is measured with a fiber optic sensor that detects the passage of two diametrically opposite features on the silicon rotor. These two features, referred to as speed bumps in Figure 4-2, are at the same level as the blades and the thrust bearing hub, and are located in the exhaust flow from the turbine. A fiber optic displacement measurement system, by Philtec Inc. [43], is positioned above the speed bumps with an XYZ stage. The Philtec sensor consists of a bundle of 12 collocated optical fibers, 6 fibers emitting light from a laser source, and 6 fibers capturing the reflected light and transmitting it to a photo diode. The light intensity is converted to a voltage and is amplified up to a level of 5V.

With the rotor spinning, the output from this sensor approximates a low duty cycle square wave with frequency twice that of the rotor rotation rate. The spectrum of this signal is processed by a spectrum analyzer, providing rotational speed and real-time monitoring of rotordynamics activity (which will be discussed in Section 4.4.2). The peak in the spectrum is tracked by the analyzer, and sent to the low-speed DAQ to determine the rotational speed.

4.3 Hydrostatic thrust bearings

The principle of operation and design of the hydrostatic thrust bearings were described in Chapter 2. Although the thrust bearings were redesigned for the Motor-Compressor load requirements, their operation remains similar to that demonstrated and characterized in the first generation microbearing rig by Lin [29]. The main difference is the size and asymmetry. In the current design, the Aft Thrust Bearing (ATB) was made larger than the Forward Thrust Bearing (FTB) in order to counteract the downward forces from the electrostatic motor. This section will summarize the characterization and operation of these thrust bearings.

4.3.1 Static flow characterization

Flow characteristics through the thrust bearings, at the condition of maximum gap, are shown in Figure 4-6. In these tests, the rotor is pushed either completely up or down, by applying the pressure to one bearing at a time. We notice that some devices from the first MC-Bearing build (*MCBR1*) show excessive flow, which was due to leakage from the forward thrust bearing plenum.

As shown in Figure 3-11, the bonding surface of the plenum wall was damaged by ion backscattering during deep etching, creating a leakage flow path. Fortunately, the pitting was not so severe as to effect all dies from this build. Backside protection was improved in the second built (*MCBR2*), resulting in consistent flow characteristics. The measured flow rates are similar to those predicted by the flow model of Jacobson [24]. Of greater importance is the axial stiffness of the thrust bearing pair, necessary in order to allow sufficient operating range during testing, as discussed next.

4.3.2 Axial stiffness and position sensor

The approach first presented by Lin [29] to characterize the axial stiffness is repeated here on the MC-Bearing rig and Motor-Compressor devices. It consists of applying a constant pressure on one bearing, and varying the pressure on the other. Increase in the forward thrust bearing (FTB) pressure for example, pushes the rotor downward, closing the aft thrust bearing (ATB) gap, until the pressure in the gap is sufficient to balance the axial forces on the rotor.

Figure 4-7 shows a typical measurement of ATB flow versus FTB pressure for two different ATB pressures. The slope of the curves between the open and closed positions is a measure of thrust bearing stiffness. Broad curves depict high stiffness, while a sharp transition from open to close is characteristic of low stiffness.

Also of interest is the axial position of the rotor. In this experiment, the forward thrust bearing can be viewed as an actuator and the aft thrust bearing, as an axial position sensor. Using the flow model, mass flow as a function axial position (i.e. gap) can be calculated, and mapped on the flow versus pressure curve. It was found that the flow rate for a centered rotor is approximately 1/3 of the maximum flow rate, for a given pressure.

4.3.3 Axial thrust bearing operating protocol

The approach developed to successfully operate the thrust bearings consists of the following steps:

1. Choose an ATB pressure (from previous experience), usually in the range of 35-60 psig;
2. Map the ATB flow versus FTB pressure from fully open to closed, as described previously;
3. Note the FTB pressure at which the mass flow is approximately 1/3 of the fully open flow;
4. If the FTB pressure is above 100 psig, choose a lower ATB pressure and repeat steps 1 to 3.

The typical pressures chosen resulted in a ratio of ATB to FTB pressure in the range of 0.55-0.65, and approximately identical mass flows on the order of 10-20 sccm, depending on the pressure level chosen.

While operating the device, the FTB pressure or MOP pressure are adjusted in order to keep the ATB flow constant, hence maintaining the axial position of the rotor. In parallel, the journal bearing pressure must also be monitored during a run, as discussed in the next section.

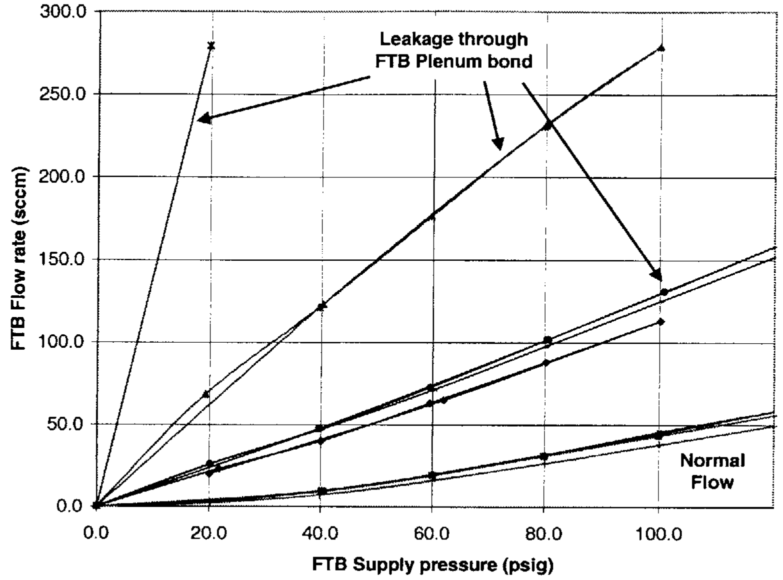

(a) Forward thrust bearings, *MCBR1*

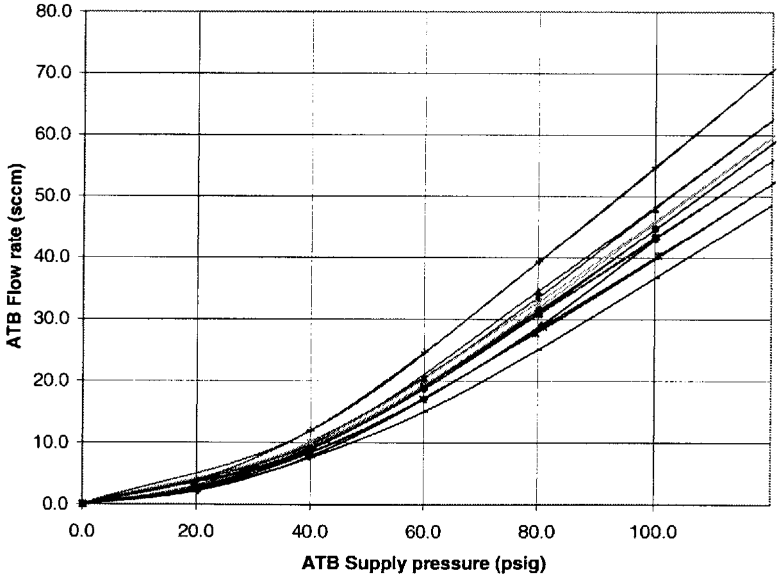

(b) Aft thrust bearings, *MCBR1*

Figure 4-6: Thrust bearing characterization at condition of maximum gap, shown for the dies tested from the first MC-Bearing rig build.

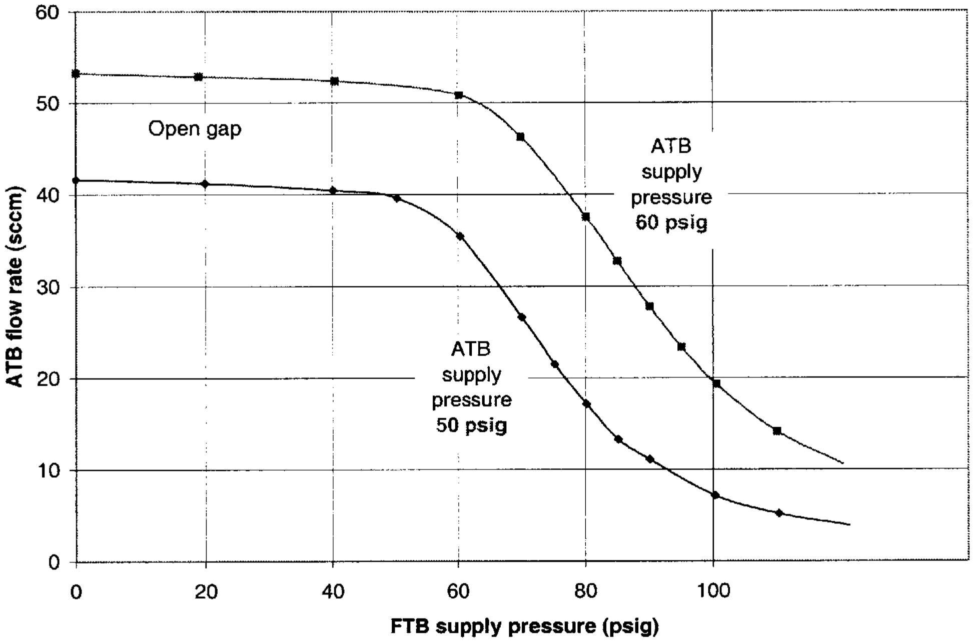

Figure 4-7: Aft thrust bearing flow rate as a function of FTB pressure.

4.4 Hydrostatic Journal Bearing Testing

The principle of operation of the hydrostatic journal bearing was described in Figure 2-23. This type of operation had not been repeatedly demonstrated to high speeds before this work, and therefore constituted a critical element in the development of the Motor-Compressor.

Experiments on the 26x scaled bearing rig by Orr [41] first demonstrated the approach of flowing gases axially through the journal bearing gap to create a radial spring. This section describes the successful implementation of this approach in a microfabricated device. Focus will be on the critical experimental advances which enabled a better control of the bearing system and eventually high speed operation. First, static flow characterization of the journal bearing will be presented, then rotordynamics optical monitoring approach will be described, leading to the experimental spin results, and mapping of the stability boundary.

4.4.1 Review of journal bearing configuration and operation

The journal bearing, formed in the gap between the rotor and the stator at the periphery of the rotor, acts as a radial spring. The journal bearing gap is 300 microns deep and has a width of 10-15 microns with the rotor centered. A pressure differential is maintained across the gap, generating an axial through-flow. On the front side of the rotor, the journal bearing boundary pressure is set by the stator exit/rotor inlet pressure, called the inter-row pressure. On the back side of the rotor, the journal bearing opens into a large plenum whose pressure can be set externally. The current implementation splits the back side plenum into two symmetric journal pressurization plena (High JPP and Low JPP), as shown in Figure 2-18, although for current testing these two plena are set to the same pressure.

The pressure supplied to the journal pressurization plena is maintained higher than the inter-row pressure so that there is an axial flow across the journal bearing from the back side to the front side. As discussed in Section 2.4.4, when the rotor is perturbed to create a smaller gap on one side, higher local pressures are induced, re-centering the rotor.

The stiffness of this radial spring typically increases with pressure, and has been analyzed by others [44, 41]. Mass flow through both journal pressurization plena is monitored during operation. Static flow characteristic are obtained before the spin test to assess the symmetry through both flow paths. In these characterization experiments, a similar pressure is applied to the High JPP, Low JPP and MOP, and the flow rate through each channel is measured. A typical result is shown in Figure 4-8 illustrating the symmetry between the low and high sides.

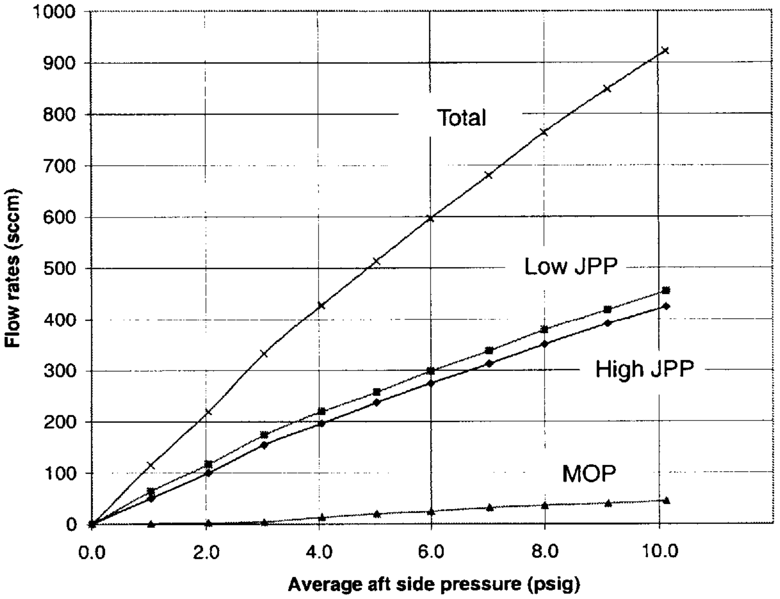

Figure 4-8: Journal bearing static flow characterization, showing the symmetry in the flow rates through the *high* and *low* journal pressurization flow channels.

Radial stiffness from the journal bearing is a function of the axial pressure difference (hence mass flow) across the bearing. This value is externally controlled with the gas handling system, in order to maintain stable operation. Monitoring of the rotordynamics activity will be discussed next.

4.4.2 Optical rotordynamics monitoring

During operation, the signal from the speed sensor is monitored on a spectrum analyzer to determine the frequency content of the signal. The spectrum shows a strong peak at twice the rotation rate (two speed bumps per rotation), at the rotation rate (due to asymmetry), and also at higher harmonics. Under certain conditions, extra peaks also appear, as shown in Figure 4-9. As will be discussed next, these peaks are evidence of precession, or resonance at the bearing natural frequency. The ability of the optical sensor to pick up this rotordynamics information has been an important diagnostic tool.

As mentioned earlier, the hydrostatic journal bearing acts like a spring, and as such has a natural frequency associated with it. Oscillations of the rotor at the natural frequency of the bearing results in additional motion of the speed bumps, which appears as a pulse width modulation of the signal at the whirl frequency. To better understand this principle, let us consider a disk rotating at a rate Ω about its geometric center. The response from the fiber optic sensor as a function of time is a simple square wave, with a constant pulse width Δt equal to the arc length of the speed bump divided by the tangential velocity at that radial location r_s:

$$\Delta t = \frac{s}{V_\theta} = \frac{s}{\Omega r_s} \tag{4.1}$$

For this analysis, let us consider a precession of the rotor, represented by a motion of the center of the disk along a circular orbit of radius r_p and at a frequency ω. The instantaneous velocity of the tab as it goes by the sensor is now modified by the precession velocity. Depending on whether the velocities add or subtract, the pulse width will vary in the range:

$$\Delta t|_{prec} = \frac{s}{\Omega r_s \pm \omega r_p} \tag{4.2}$$

Furthermore, this pulse width modulation will occur at the frequency ω, and will appear as a peak in the spectrum at the frequency ω. Due to the nature of the signal, peaks in the spectrum will also occur at the combinations of the oscillation frequency and the rotational speed, as identified in Figure 4-9.

This interpretation of the bands in the spectrum was validated in two ways. First, the raw signal was acquired using the high speed DAQ, and processed. The possible effect of axial motion was removed by chopping the signal, and extracting the pulse width directly. The second approach was to simulate the precession scenario by a simple kinematic model of the precessing disk. The spectrum of the simulated square waveform exhibited the same features as the measured signal, namely additional peaks at the combinations of the precession frequency and the rotational speed.

Spectral analysis of the signal generated from the speed bump configuration is therefore a tool to assess if the rotor is at a steady-state point or if it is whirling along an orbit or oscillating. Acknowledgments are extended to F. Ehrich for his valuable discussions and suggestions which led to this interpretation of the signal. The following section will describe how this rotordynamics information was used to successfully operate the MC-Bearing rig to high rotational speeds.

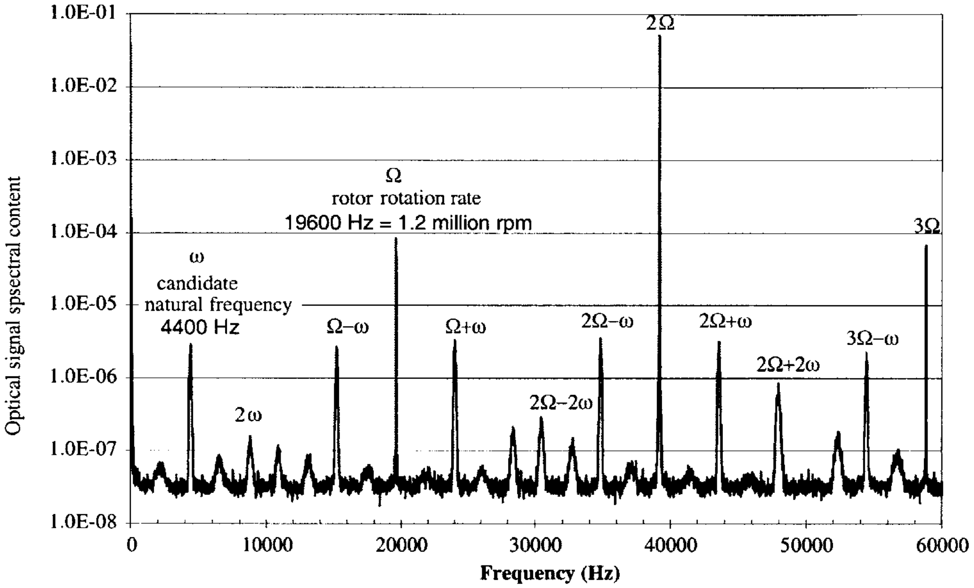

Figure 4-9: Power spectrum of the optical speed sensor signal showing the speed bump frequency (2Ω) and the rotor rotation rate (Ω), as well as other peaks corresponding to the natural frequency (ω) and its combinations with the rotation frequency. Courtesy of Jacobson [24].

4.4.3 High-Speed Journal Bearing Operation

The approach to achieve high-speed stable operation was to experimentally explore the operating space for stable operating regions, identified by the absence of spectral activity.

The main focus of the initial experiments with the *MCBR1* devices was not only to achieve high speed operation, but also to determine the regions of instability. The following paragraphs summarize the effect of two important parameters: the rotational speed and the pressure differential ΔP, across the journal bearing.

Effect of rotational speed

Figure 4-10 shows the spectrum as a function of time, for Die 1 from the *MCBR1* build. Initially, only the strong signal at 2Ω, the natural frequency ω_n, and their sums and differences are seen (the absence of a band synchronous is a sign of perfect symmetry of the speed bump geometry). The speed is then increased while the bearing pressures are maintained constant (illustrated by the constant natural frequency, ω). Immediately before the rotor speed drastically decreases (crash), we notice that the intensity of the natural frequency band increases and combinations with the rotational speed also appear. This behavior strongly suggests that the crash is of rotordynamics nature. The lubricating film is eventually reestablished by lowering the rotational speed (through a reduction in turbine inlet pressure).

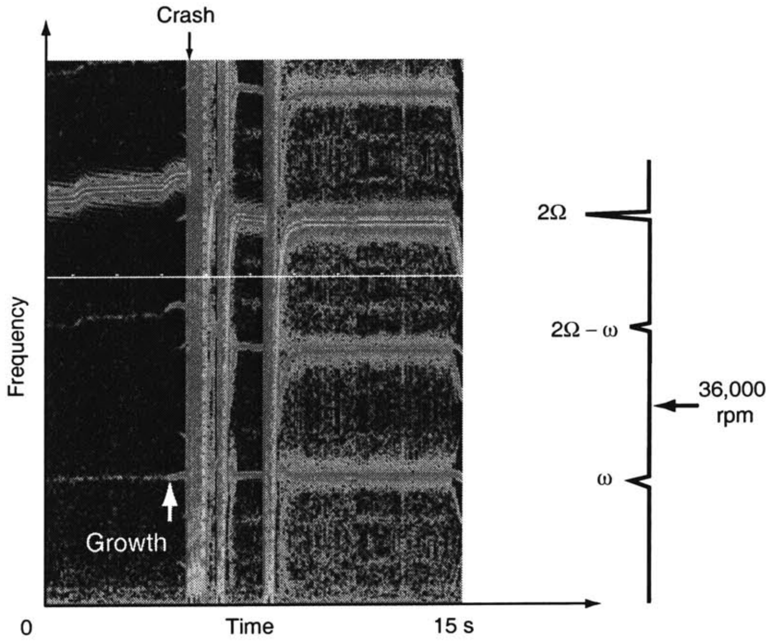

Figure 4-10: Spectrum as a function of time, showing the increased magnitude of oscillations immediately before crash, relating both events.

Effect of journal bearing pressure differential

Figure 4-11 shows a spectrum when ΔP is reduced from 0.23 to 0.20, at a speed of 246 Hz. In this case, stronger spectral activity intensifies when the pressure differential is reduced, instead of the speed being increased. We also notice a slight reduction in frequency due to the reduction in ΔP.

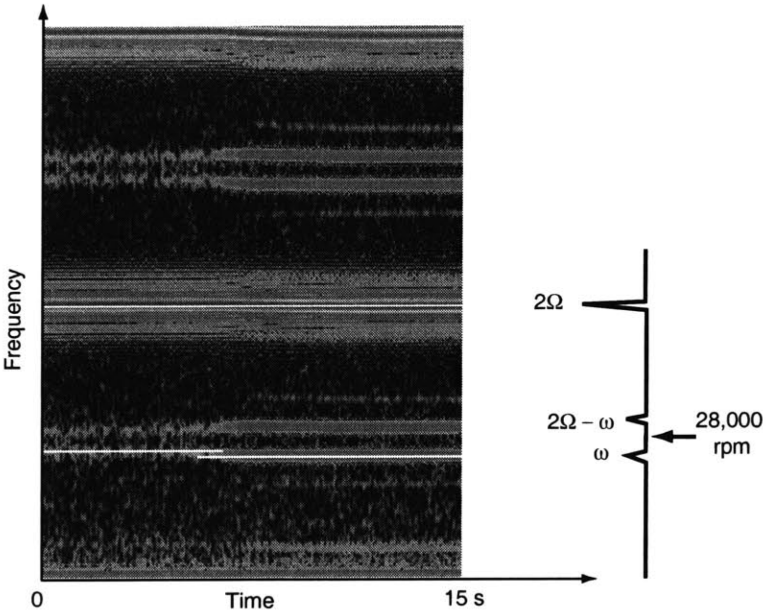

Figure 4-11: Spectrum as a function of time, showing the effect of reducing the journal bearing pressure differential.

In summary, as the rotor speed increases or the radial stiffness is reduced, the unsteady motion of the rotor increases, up to the point of instability. Imbalance is thought to have an important effect on this relation, in two different, yet related ways. First, the journal bearing may simply not supply the sufficient load capability to withstand the radial imbalance loads. Since the imbalance loads increase with the square of the speed, the radial stiffness needs to be increased accordingly.

The second viewpoint considers the destabilizing nature of hydrodynamics forces. When the bearing operates at rotation rates higher than the journal bearing natural frequency (supercritically), as it does through most of its operating range, the rotor spins around its center of mass rather than its geometric center. This offset of the rotor produces a non-uniform circumferential gap, causing the development of hydrodynamic forces in the journal bearing gap. These forces tend to be destabilizing unless the rotor operates at more than 90% eccentricity 2.4.4. In order to stabilize the rotor in this case, the natural frequency of the bearing w_n is best kept near the rotational speed. The critical speed ratio, Ω/ω_n, is often considered as a stability metric, and is limited to a ratio of 2.

From either viewpoint, the pressure differential ΔP should be increased along with the rotational speed. The following experimental results will quantify this relation.

Initial high speed operation: 510,000 RPM

This preliminary understanding of the hydrostatic journal bearings, and use of the spectral tool to monitor the rotordynamics activity guided the test to achieve high rotational speeds. The approach was to monitor the spectral activity as the speed was increased, and accordingly raise the pressure differential to prevent the bands from appearing. This approach was successful in operating the first die from the *MCBR1* build up to a speed of 510,000 RPM. At this point, the rotor suddenly crashed, and was found to be fractured, as shown by the collage of micro-photograph in Figure 4-12. This top view of the rotor was achieved by casting the fractured die in epoxy, and grinding the surface down to the level of the blades.

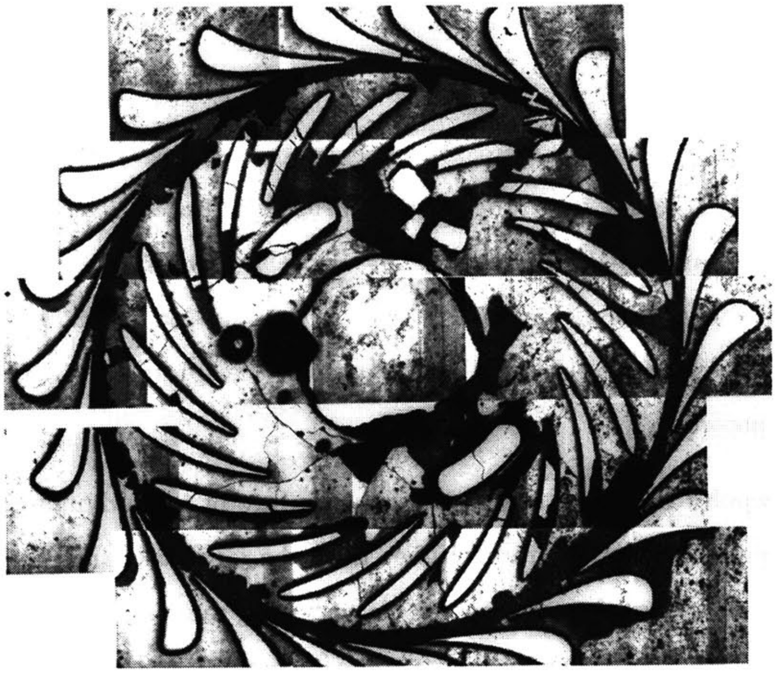

Figure 4-12: Assembly of optical pictures of the crashed rotor after crashing at 510,000 RPM (first die of *MCBR1* build)

Figure 4-13 shows the spectrum before, and at the moment of the crash. We notice the presence of a band at $\sim$ 900 Hz, which vanishes after the crash. It can be tracked back in time (using other recorded spectra), and identified as the same natural frequency previously discussed in Figures 4-11 and 4-10. Near the end of the run, the intensity of this band was continuously increasing, suggesting that the crash may have been due to rotordynamics instabilities.

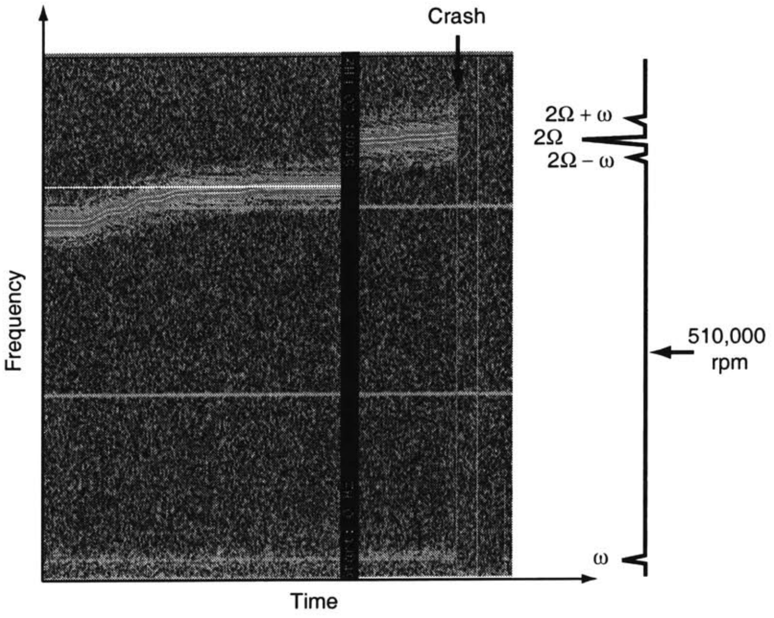

Figure 4-13: Spectrum of the 510,000 RPM bearing rig run, before and at crash

Post-analysis of the pressure information acquired during the run showed that a value of $\Omega/\Delta P^2$ was kept approximately constant at a value of 50,000 RPM/psi^2 throughout the run except near the end, when the bands reappeared. The stability parameter, $\Omega/\Delta P^2$, increased up to a value of 117,000 RPM/psi^2 before the crash. This information was extracted from the experimental results by S. Jacobson and has been taken as a protocol for subsequent bearing rigs runs. Since the rotation rate at crash was $\sim$ 8510 Hz, the maximum critical speed ratio achieved was $\frac{\Omega}{\omega_{crit}} \sim 9$.

Pursuit of high speed operation: 1,400,000 RPM

The second set of MC-Bearing rig devices built as part of this work (*MCBR2*) were tested to achieve higher rotational speeds, using the knowledge gained through the initial experimental investigation. Testing was pursued by S. Jacobson and C.W. Wong, while the main effort for the Motor-Compressor project was redirected towards the fabrication of the 5-stack devices with the integrated micromotor, since a viable journal bearing protocol had been determined.

Figure 4-14 shows the rotation rate of two *MCBR2* devices as they are slowly accelerated in a stable manner. As the turbine supply pressure increases, the pressures applied to the hydrostatic journal bearing are also increased to maintain $\Omega/\Delta P^2 \approx 50,000$ RPM/psi^2. Device 1 was brought up to a tip speed of 260 m/s (1.2 million RPM) and was held there for 20 minutes (a pressure leak resulted in a slight deceleration). The rotor was then rapidly decelerated to stop. Device 2 reached a tip speed of 303 m/s (1.4 million RPM) prior to going unstable and crashing. Both devices achieved of order 10^8 revolutions. The operating schedule is one suspect in the cause of the crash of Device 2. Other dies from both *MCBR1* and *MCBR2* builds have also been tested, but they have only been able to reach tens to hundreds of thousands of RPM prior to instability. They typically required ΔP up to 6 psi, at which point further increasing ΔP did not allow higher speeds. Additional MC-Bearing rig devices have also been built by X. Zhang since then, paying increased attention to minimize the as-fabricated imbalance. Test results to date (by S. Jacobson and C.W. Wong) have repeated stable operation above 1 million RPM.

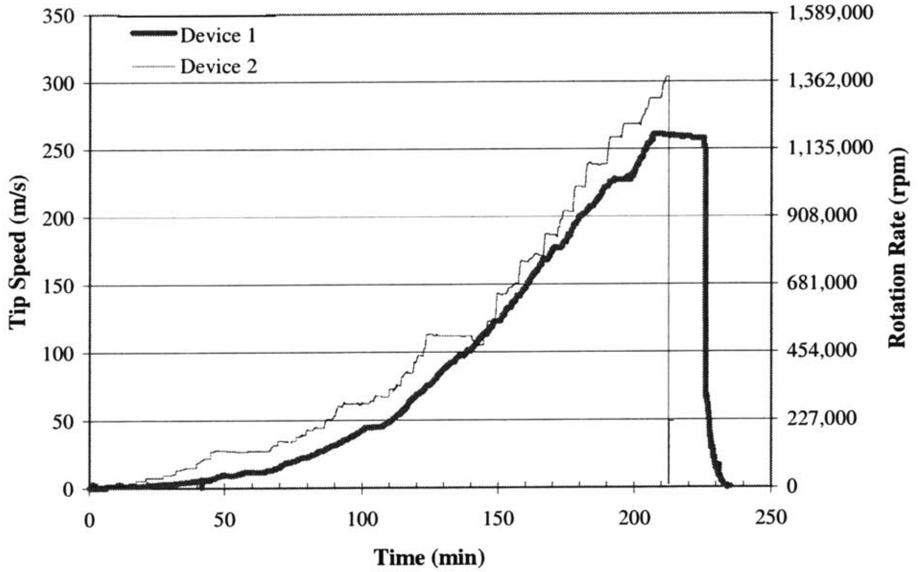

Figure 4-14: MC-Bearing rig speed evolution over time. Uncertainty in the tip speed measurement is 0.5% of the measured speed. Courtesy of Jacobson and Wong [24].

4.4.4 Investigation of the stability boundary

In order to allow a wider operating range than the previously described pressure schedule, the stability boundary was experimentally probed. Using a turbine die from the Motor-Compressor build (M/T #1), rotational speed and journal bearing pressure differential were varied, up to the point where side bands became apparent. In contrast to previous investigations, the goal was to define the operating space at high-speeds. In these experiments, the pressure differential was reduced while keeping the speed constant. Figure 4-15 illustrates the stable operating points, and the stability boundary for speeds up to 300,000 RPM. Fitting a curve of the form $\Omega_{crit} = C\Delta P^{a}$ through the least stable points at 100,000 RPM, 200,000 RPM, and 300,000 RPM, we find C = 223,000 and a = 1.7 ($\Omega_{crit} = 223,000\Delta P^{1.7}$) for Ω_{crit} in RPM and ΔP in psi. This trend suggests that a safe operating protocol would consist in maintaining $\Omega/\Delta P^{1.7} < 223,000 RPM/psi^{1.7}$. It should be noted however that the boundary is a strong function of rotor imbalance, which may be different for each device, and build.

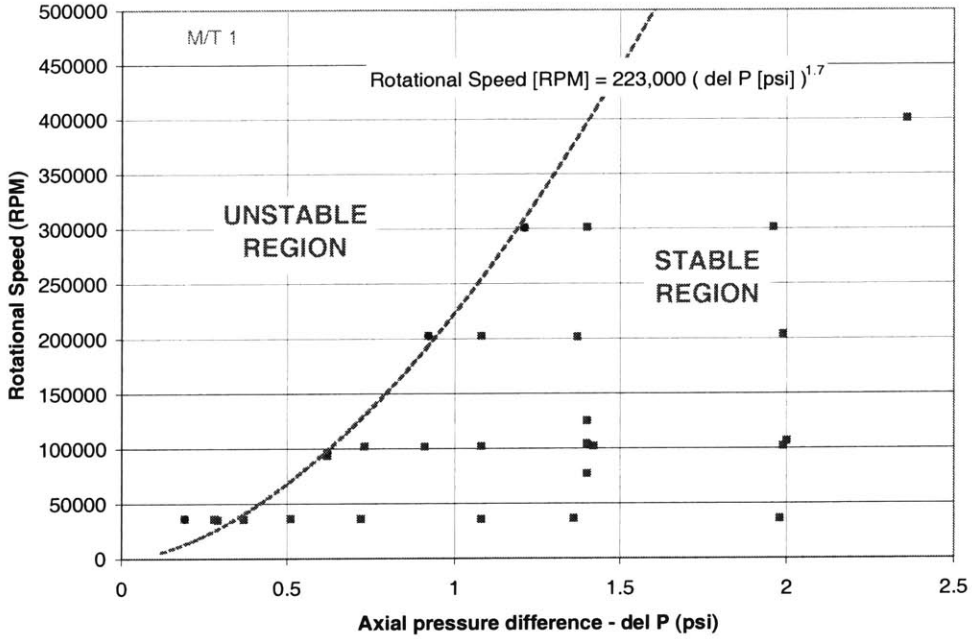

Figure 4-15: Experimentally determined stability boundary for the Motor/Turbine device #1.

4.4.5 Conclusions on hydrostatic journal bearing

This bearing development effort demonstrated sustained rotation of the microfabricated rotor at speeds greater than 1 million RPM. The experimentally established operating protocol reduces the operational risk from the bearings for the Motor-Compressor.

4.5 Microturbine Operation

In addition to demonstrating the high-speed operation of microfabricated gas-lubricated bearings, the MC-Bearing rig tests provided an assessment of the microturbomachinery. Figure 4-16 shows the turbine operating line for Devices 1 and 2 previously presented. These operating lines are comparable in shape to those observed for macro-scale turbines. Also shown in this figure are three data points calculated by S. Jacobson, using MISES and simple viscous drag models. At 1.4 million RPM, the microturbine is predicted to deliver nearly 5 W of mechanical power with a torque of over 30 μm N-m. The computational results are dependent on the axial position of the rotor, which affects the amount of drag. The uncertainty bars on the MISES data points are associated with an expected +/- 0.5 μm uncertainty in the axial position of the rotor. The MISES results do not compensate for the decrease in mass flow due to blockage from boundary layer growth on the end-walls (three-dimensional effect), which likely explains why the actual device required a somewhat higher turbine pressure for a given speed to generate sufficient torque.

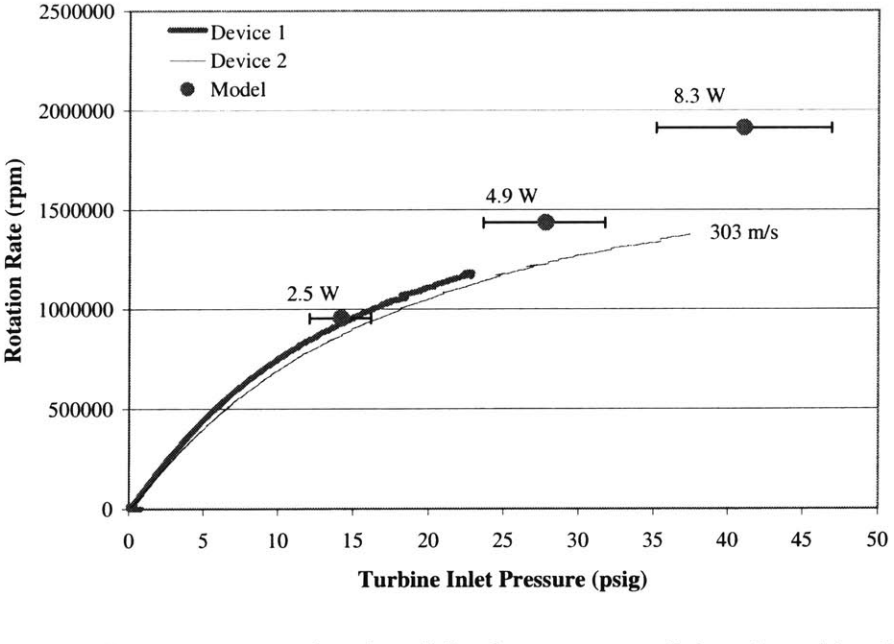

Figure 4-16: Rotation rate as a function of the air pressure supplied to the turbine. There is a 0.8 psi uncertainty in the pressure. Courtesy of Jacobson [24].

4.6 Hydrostatic bearing flows

At 1.4 million RPM, the differential pressure across the journal bearing was about 5 psi. The mass flow rates supplied to Device 2 are shown in Figure 4-17. Here the experimental turbine flow rate (Qmain) is somewhat higher than predicted in MISES, due to the increased pressure required to operate the turbine. The flow rates supplied to each journal pressurization plenum (Qjp1 and Qjp2) are essentially equal, lying on top of each other in Figure 4-17. The thrust balance plenum was sealed with negligible leakage. Also shown in Figure 4-17 is an aggregate of the back plenum flows normalized by the main turbine flow. This ratio peaks at a value of 0.3 at low speed, but decreases to 0.13 at the highest speed. The trend suggests that this flow ratio would further decrease at higher speeds. Thus, for high-speed applications, the flow needed to operate the hydrostatic journal bearing is small compared to the main turbine flow. The thrust bearings proved sufficiently stiff so as not to require much manipulation during a run. For Device 2, the aft thrust bearing ran with a constant supply pressure of 35 psig while the forward thrust bearing was varied from about 60 - 85 psig. Each thrust bearing required about 10 sccm of nitrogen, which is negligible in the scale of the other flow rates (Figure 4-17).

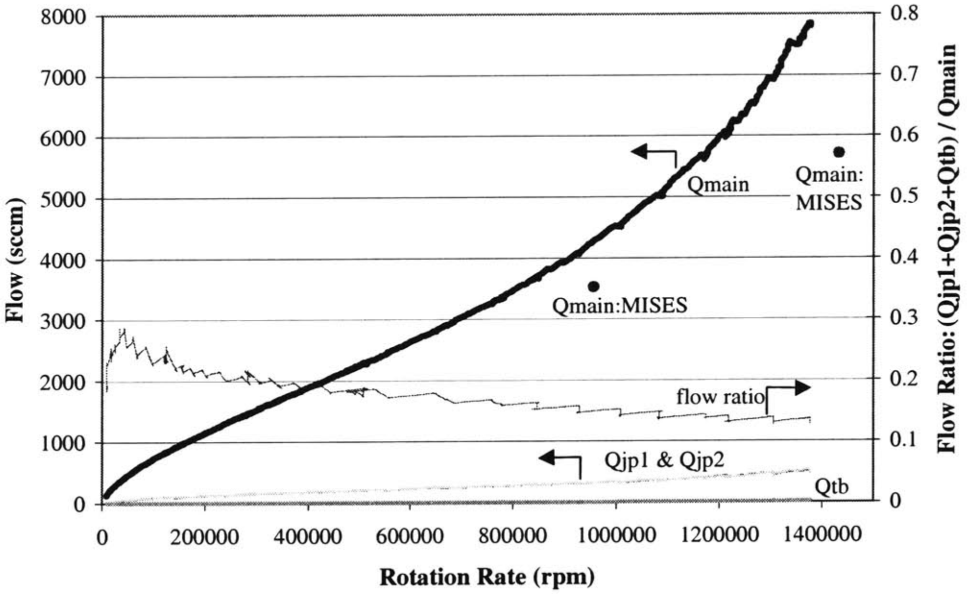

Figure 4-17: Turbine and bearing flow rates over the range of operating speeds for Device 2. Uncertainty in the main flow is 200 sccm, in the journal pressurization plena (jp1 and jp2) is 50 sccm, and in the thrust balance plenum (tb) is 0.5 sccm. Courtesy of Jacobson [24].

4.7 Summary

An approach for real-time monitoring of the rotordynamics activity has been investigated and used. Experimental investigation using these tools has given critical insight on the operation of the microfabricated hydrostatic journal bearings. It confirmed the benefit of increasing the pressure differential across the journal bearing gap in order to remain away from the stability boundary while increasing in speed.

A viable operating protocol for the hydrostatic journal bearing was experimentally determined: $\Omega/\Delta P^2 \approx 50,000$ RPM/psi^2, while the stability boundary on another device was mapped out as: $\Omega_{crit} = 223,000 \Delta P^{1.7}$ (for Ω_{crit} in RPM and ΔP in psi), up to a rotational speed of 300,000 RPM. These guidelines, and the understanding of hydrostatic journal bearings gained during these experiments, provide a reasonable base for operating the bearings in the motor-driven devices.

The 4.2 mm diameter silicon rotor supported on gas bearings demonstrated sustained rotation at speeds over 1 million RPM, above the design speed for the Demo Motor-Compressor. This demonstration validates the technological approach of microfabricated silicon rotors and air bearings.

In addition, these experiments demonstrate the operation of high-speed microturbomachinery. The microturbine has reached tip speeds of 300 m/s, corresponding to rotation rates of 1.4 million RPM. At this speed, the turbine provides nearly 5 W of power and achieves a power density greater than 4,000 MW/m^3 (based on turbomachinery volume), which is comparable to the power density of conventional-scale modern aircraft engine turbine technology.

CHAPTER 5

MICROMOTOR DEVELOPMENT AND SYSTEM DEMONSTRATION

This chapter presents the experimental investigation of the motor-driven devices. The objective is to demonstrate the micromotor operation, validate the viscous and electrical motor models, and determine the viable design space. First, the experimental apparatus used to test the devices is described, followed by the experimental spin test results and their interpretation; an experimental determination of the viscous loads; an assessment of the micromotor design space delineated by these experiments, and finally, a discussion concerning the system level operation.

For investigation purposes three different motor-driven devices are were built and tested: a motor-driven disk (no blades), a motor-assisted turbine (with turbine blades), and a motor-driven compressor (with compressor blades). As described in Chapter 3, they were build in the same 5-wafer stack, sharing an identical fabrication processes, only differing by their blading (or absence thereof). Although the results presented herein constitute original work, the contributions of S. Nagle, J. Lang, S. Umans, and E. P. Warren were greatly appreciated in developing the power electronics and helping to carrying out the experiments.

5.1 Experimental apparatus

The motor-driven devices were tested using the same experimental apparatus assembled for the MC-Bearing rig testing, and described in Section 4.2. Additional power electronics and modifications to the packaging were necessary, as described in this section.

5.1.1 Power electronics

By design, the micromotor requires a high voltage, high-frequency voltage source to excite the stator electrodes. The specifications for the power electronics can be summarized as:

- 6-channel sinusoidal output, phase shifted by 60° relatively to each other;
- Voltage up to 300V amplitude (600V peak-to-peak);
- Frequency up to 3-5 MHz;
- Current up to 0.1A per channel.

The efficiency and size of the drive electronics are also important, especially for portable applications. These two criteria were however not an issue for the initial bench-top demonstration of the Motor-Compressor. The three different drives used for the tests presented herein will be described next.

Resonant power electronics One approach to drive the micromotor was to combine efficient low voltage switching, with a resonant LC circuit. Control circuitry alternately excites six inductors, each connected to a phase of the motor which acts as a series capacitance. As illustrated in Figure 5-1, tunable capacitors and resistors are added to the circuit in order to balance the six phases. At resonance, voltages 30-50 times larger than the switching voltages can be delivered to the motor, depending on the Quality factor of the inductors (Quality factor: $Q = \omega L/R$). This approach can provide sinusoidal voltages up to 300V and in the megahertz range. Practically, only the voltage can be varied during a test, since the frequency is set by the dynamic characteristics of the resonant circuit components.

This approach holds the promises of miniaturization, making it amenable for portable applications. Special development was however necessary in order to achieve compact, high Q inductors (30-100) in the range of $100 - 400\mu H$. The minimal size of such an inductor was found to be on the scale of the micro-device: a few millimeters per side. As a result resonant power electronics would be at least six times the size of the device it drives, limiting but not preventing their prospects for portable applications.

The resonant drive electronics used in these experiments were developed and fabricated by J. Lang, S. Umans, E. P. Warren with the support of Lincoln Labs, while the inductors were developed and fabricated by S. Umans.

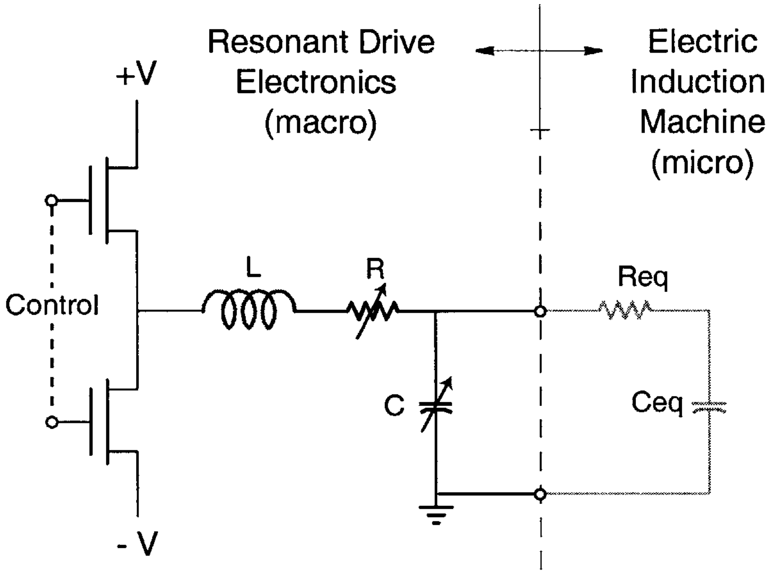

Figure 5-1: Schematic of one phase of the resonant power electronics.

Operational amplifier drive An alternative approach for bench top investigation of the micromotor was to use a set of six high voltage operational amplifiers, driven by control circuitry. Compared to the resonant power electronics, the Op-Amp drive is limited in voltage ($< 70V$) and frequency ($< 700kHz$), before the output waveforms degenerates.

Although this approach is not desirable for future application due to the low efficiency and large size, it is useful for experimental investigations. It provides the flexibility of varying both the voltage and excitation frequency. These electronics were developed and built by S. Umans, and modified by S. Nagle [37].

Synchronized function generators In order to cover the experimental space at higher frequencies, six HP33120A function generators were synchronized together. This approach provided phase shifted sinusoidal signals up to 5 MHz, but limited in amplitude to 10V. The output waveforms for 4 or the 6 phases are shown in Figure 5-2, at 2 MHz and 5 MHz. It was found that the accuracy of the phase differences degrades at high frequencies. At 5MHz, the phasing oscillates about the set value by up to ±35°, which may reduce the magnitude of the stator fundamental harmonic. Furthermore, the voltage amplitude drops gradually as a function of frequency, as shown in Figure 5-3. This calibration curve will be used to normalize the torque obtained with this drive.

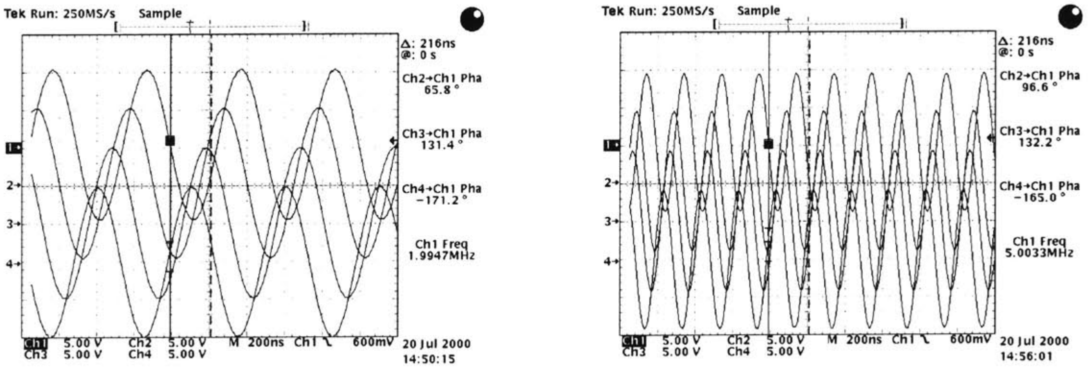

(a) 2 MHz - 10 V Amplitude

(b) 5 MHz - 10 V Amplitude

Figure 5-2: Output waveforms from the set of phase shifted function generators (4 out of 6 phases shown).

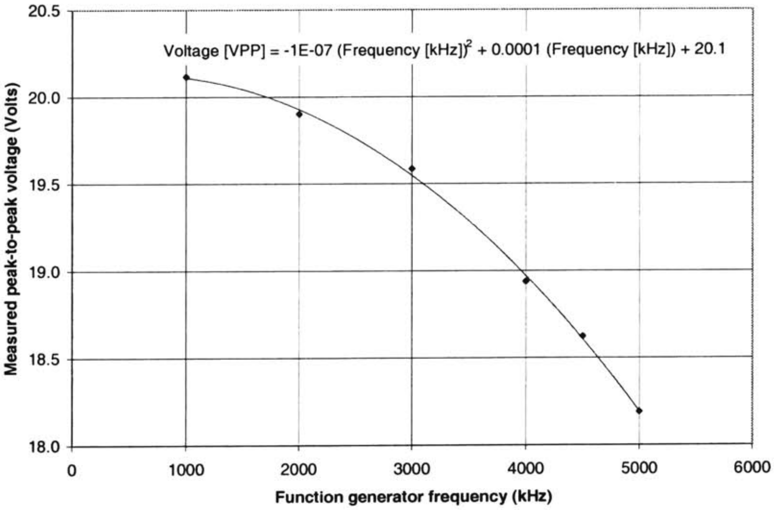

Figure 5-3: Peak-to-peak voltage from the HP33120A function generators as a function of excitation frequency, showing a gradual drop off at high frequencies.

5.1.2 Electrical packaging

These driving signals are brought to the stator through spring loaded, precision contact probes, by Interconnect Devices Inc., which come in contact with the stator electrical leads. They are held in place by an extra Plexiglas plate, which is aligned to the other parts of the packaging (and therefore to the die) through dowel pins.

Contact resistance between pogo pins and the polysilicon was initially found to be on the order of $100k\Omega$. This could be improved by scratching the polysilicon surface, but was not practical given the packaging approach. Instead, gold balls (on the order of 100 μmdiameter) were bonded to the contact pads using a standard wire bonder. Maximum force and power settings were used, and the chip was heated to 350°C in order to ensure adhesion of the gold ball to the polysilicon. This approach reduced the resistance of the connection from the pogo pin, to the gold ball, and to the lead reduced to $< 1\Omega$. This process was done after the die had been cleaned and was otherwise ready for testing.

5.2 Experimental Results

This section presents the test results for the set of motor-driven devices, using different motor excitation approaches. Discussion of the results and comparison to the models will be presented in the following section.

5.2.1 Op-Amp drive results

The results from three devices are presented, using the Op-Amp drive electronics. Figures 5-4 and 5-5 show the rotational speed achieved as a function of stator excitation frequency and voltage amplitude respectively. We notice the linear trend of speed versus excitation frequency, which is characteristic of operation at frequencies lower than the motor torque curve peak frequency. When the frequency or voltage are pushed beyond the viable range of the Op-Amp drive, the speed decreases due to the problems of excitation waveform. This result suggests that higher rotational speeds could be achieved at higher excitation frequency.

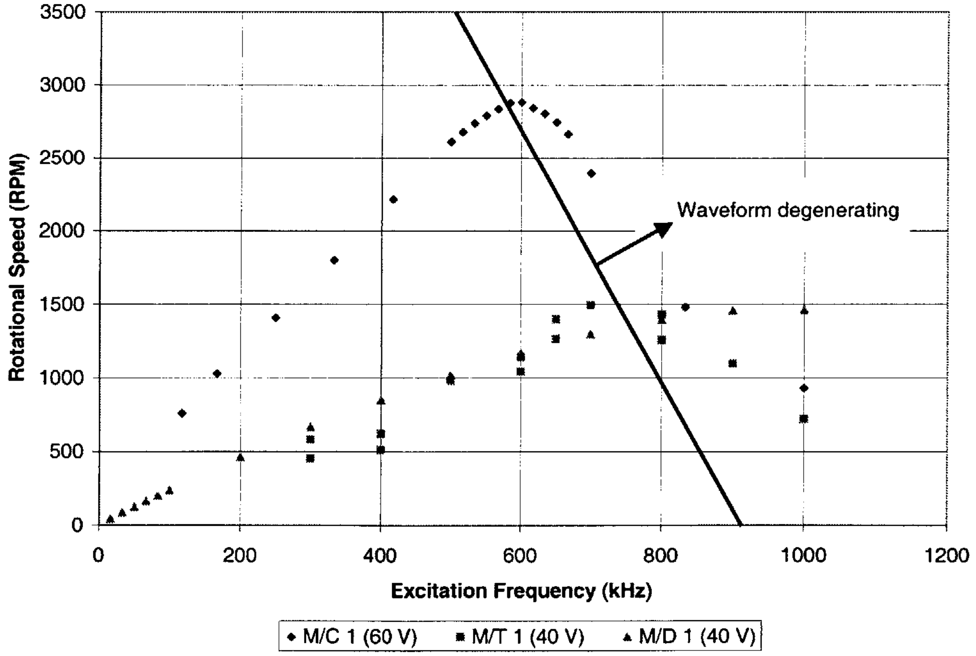

Figure 5-4: Rotational speed as a function of excitation frequency, using the Op-Amp drive at 40 V amplitude. Above 700 kHz, the driving waveform begins to generate, resulting is a lower motor torque.

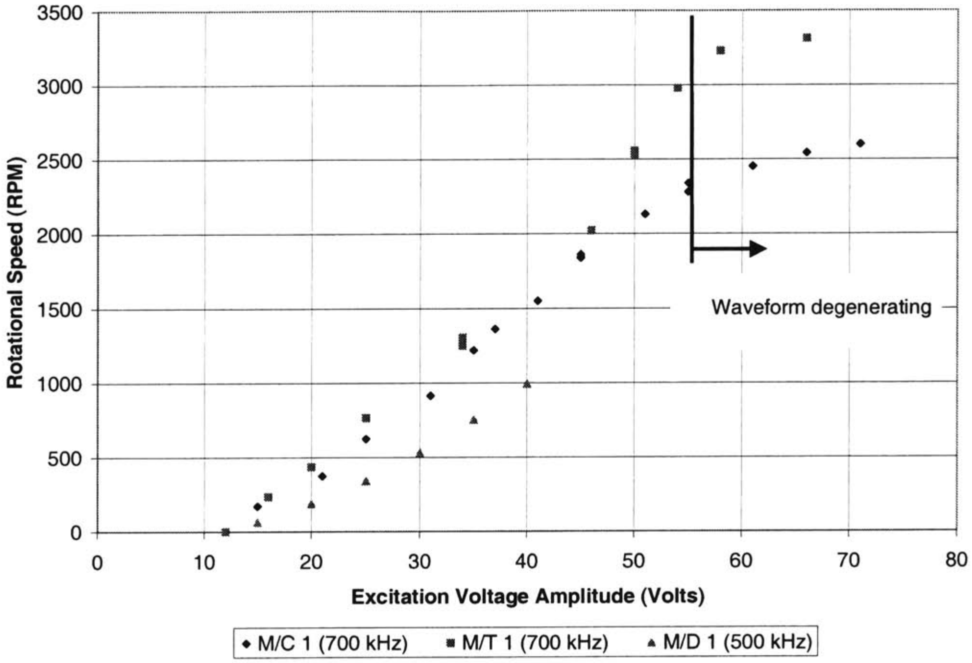

Figure 5-5: Rotational speed as a function of voltage amplitude, using the Op-Amp drive at 700 kHz. Above 60 V, the driving waveform begins to generate, resulting is a lower motor torque.

5.2.2 Resonant drive results

The resonant power electronics were then used to achieve higher speeds by allowing increased voltages at a fixed excitation frequency of 1.8 MHz. Figure 5-6 shows the experimental results for the Motor/Turbine device #1. Initial excitation at 100V drove the rotor to 15,000 RPM. In a second ramp-up (identified by the arrow), speed initially increased in an exponential fashion (up to 50-60V), and then leveled off to 12,000 RPM. At a voltage of 90V, the currents drastically fluctuated, a behavior which is indicative of breakdown occurring in the motor. The rotational speed after the breakdown event was lower than during the ramp-up, as shown by two data points indicated in Figure 5-6.

When compared to the Op-Amp drive results, we notice that the linear trend of increasing speed with frequency is maintained. For example, at a voltage of 40V the Op-Amp drive drove the rotor to 1140 RPM for 600 kHz excitation, while the Resonant drive achieved three times the speed (3700 RPM) at three times the frequency (1.8 MHz). This suggests that the peak of the motor torque curve was not yet been reached, and motivated the use of the function generators to assess the motor operation at higher frequencies.

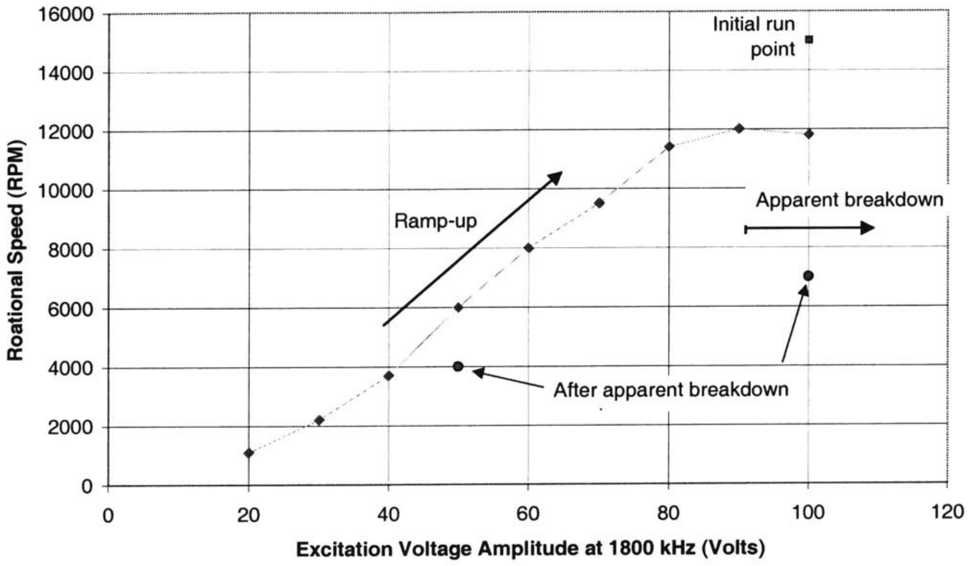

Figure 5-6: Rotational speed as a function of voltage amplitude, using the Resonant Drive at 1800 kHz. The initial operating point at 100V shows a maximum rotation rate of 15,000 RPM. Subsequent ramp up resulted in degradation in torque due to apparent breakdown.

5.2.3 Function Generator drive results

The set of six synchronized function generators was then use to drive the Motor/Disk device #1. Given that the voltage is limited to 10 V amplitude, lower speeds than previously achieved are expected. However, this drive allows the shape of the motor torque curve to be investigated at higher frequencies.

Figure 5-7 presents the measured speed as a function of electrical frequency, up to 5 MHz. Since the voltage magnitude decreases slightly at high frequencies (as shown in Figure 5-3), corrected values of speed are also plotted to simulate a constant voltage source. The corrected speed is based on the assumption of a square dependence on voltage, such that: $\Omega_{corr} = \Omega_{meas}\frac{10^2}{V_{meas}^2}$. The data is characteristic of induction motors, for which the torque curve is initially linear with frequency, and then curls over, reaching a maximum value.

The dependence on voltage was also investigated using the function generator drive, as shown in Figure 5-8. Similarly to the Op-amp and resonant drive results, the trend is quadratic with voltage. The data can be bound by quadratics with coefficients of 3.1 and 3.7 RPM/V^2.

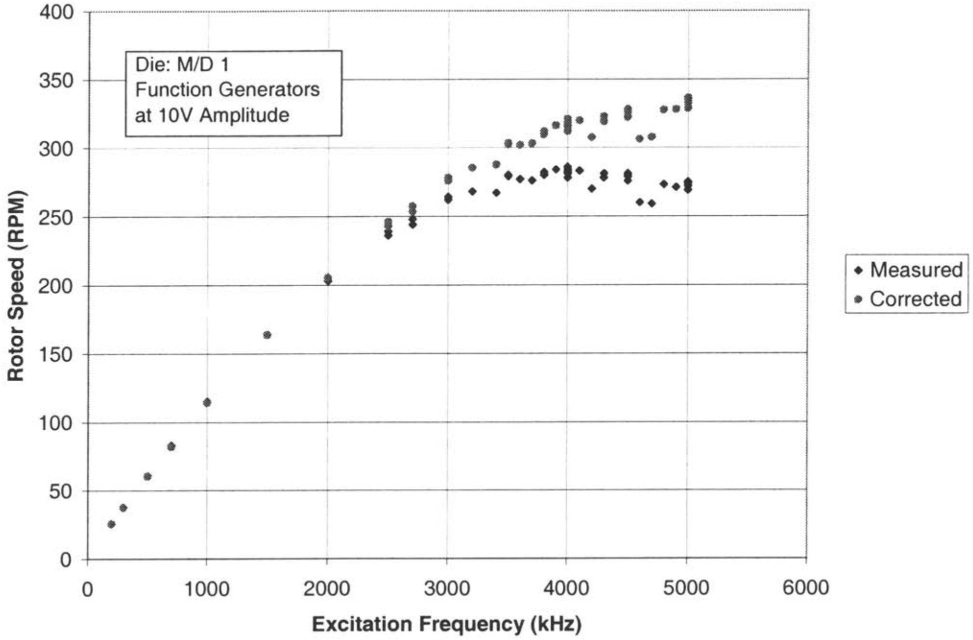

Figure 5-7: Rotational speed as a function of excitation frequency, using the Function Generator drive at 10 V amplitude. In addition to the direct speed measurement, the corrected speed is also shown, compensating for gradual voltage drop at high frequencies.

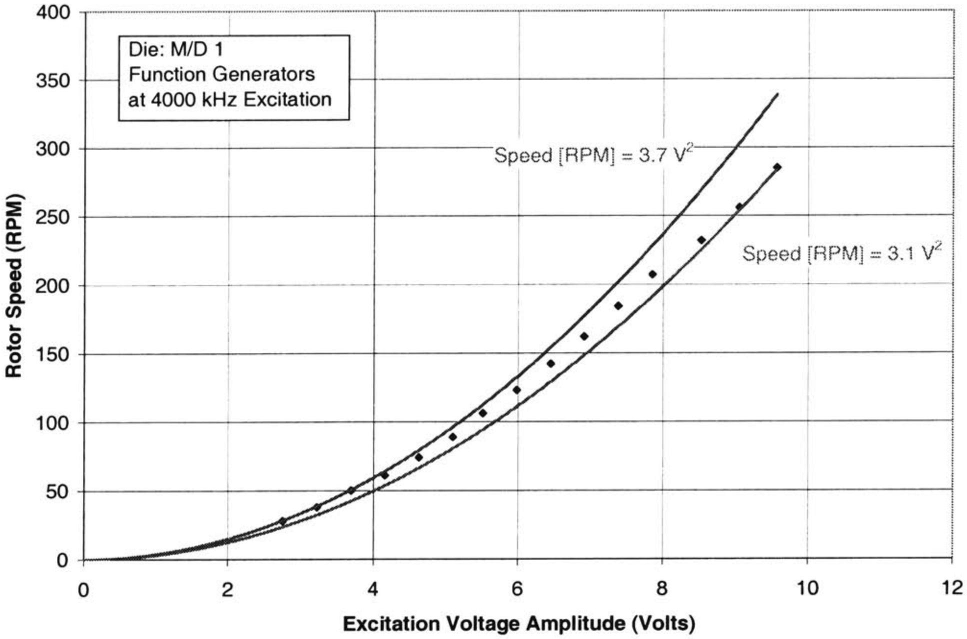

Figure 5-8: Rotational speed as a function of voltage amplitude, using the Function Generator drive at 4 MHz. Also shown are curves which bound the measurements, illustrating the quadratic dependence on voltage.

5.3 Assessment of Micromotor Performance

As exemplified by the previous results, the micromotor operates with the expected trends of electrostatic induction machines, such as the shape of the motor torque curve as a function of slip, and the square dependence on voltage. A quantitative assessment of the micromotor performance will be presented in this section.

5.3.1 Model comparison

The measured operating line can be simulated with the models, by calculating the intersection of the viscous load curve and the motor torque curve, as the electrical frequency is varied.

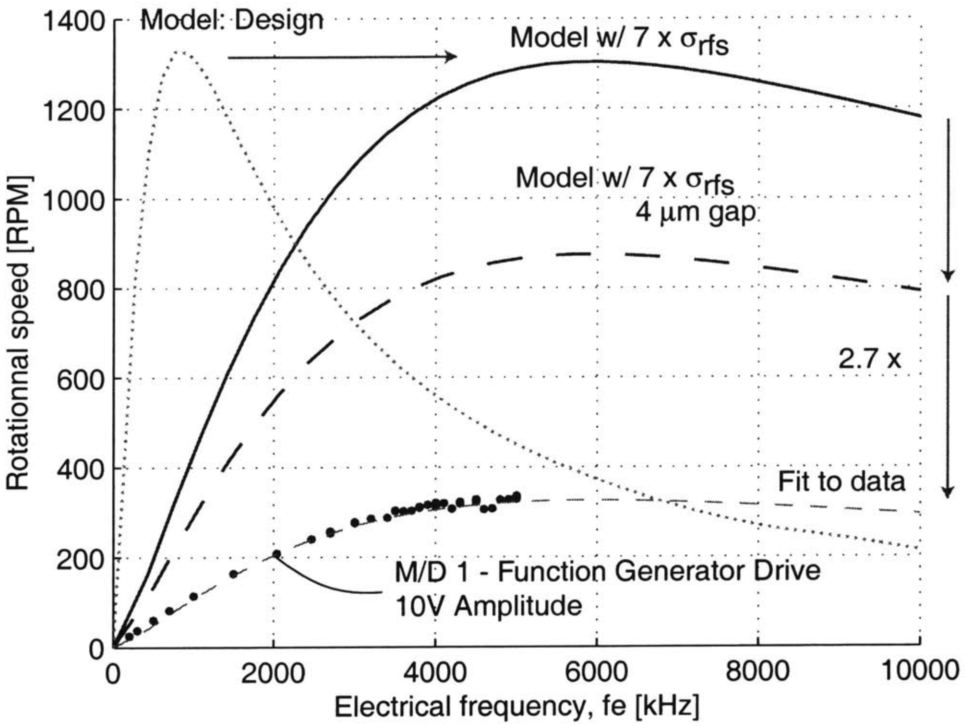

Figure 5-9: Comparison of predicted and measured rotational speed as a function of frequency for 10 v amplitude, for the Motor/Disk device #1 driven with the function generator drive. Indicates that the the rotor film conductivity is 7 times larger than expected, and that the electrostatic torque is 37% (1/2.7) of the predicted value for this rotor conductivity.

Figure 5-9 re-plots the experimental results for the Motor/Disk device #1 (from Figure 5-7, corrected speed for constant voltage supply), along with four model predictions. The dotted line represents the expected operating line based on the Demo Motor-Compressor nominal design parameters. We notice that the maximum speed was expected near a frequency of 700 kHz while the data reaches a maximum near 5 MHz. This change in peak frequency can be explained if the rotor film conductivity (σ_{rfs}) is approximately *seven* times greater than the design value (30 $\mathrm{M}\Omega_{\square}$ instead of 200 $\mathrm{M}\Omega_{\square}, intermsofresistivity$), shifting the operating points to the solid curve.

Based on measurement taken during the rotor and stator fabrication, the motor gap is expected to be 4 μm instead of the design value of 3 μm (the larger gap was a result of oxide left on the stator bonding areas, intended to improve the bonding yield). Taking the larger gap into consideration, the model predicts a factor of 1.5 reduction in speed (33% reduction), as shown by the dashed line in Figure 5-9.

The experimental results however, are lower than the model predictions by a factor of 2.7 (63 % reduction). A fit to the data (thin dashed line) can be obtained by reducing the electrostatic torque by a factor of ≈ 2.7, in addition to the $7\times$ increase in rotor film conductivity. This suggests that the motor is 2.7 times less powerful than expected or that the viscous drag is 2.7 times larger.

In the current results, the rotational speed is much less than the electrical frequency $w \gg m\Omega$, resulting in a value of slip approaching unity. This is illustrated by the calculated torque curves in Figure 5-10, shown for the nominal design with $7 \times \sigma_{rfs}$ (solid lines), and the fitted model (dashed lines), for frequencies up to 5 MHz. The viscous load line practically overlays the vertical axis, extending linearly from the origin. This scenario has two impacts. First, high slip results in low electromechanical energy conversion efficiency in the rotor. Second, this indicates that the motor torque curves will bare the same shape as the operating curves mapped out experimentally. The peak motor torque as a function of slip will therefore occur at the same frequency as the peak in speed as a function of frequency (5 MHz in Figure 5-9). The experimental operating lines presented earlier therefore directly represent the shape of the motor torque curve.

From a qualitative point of view, the motor behaves as a typical electrostatic induction motor, both with respect to the functionality versus slip, as well as the square dependence on voltage (described in section 2.3). Quantitatively however, the speed achieved is less than expected, which may be due to higher viscous drag or lower electrostatic forces. The following two sections will investigate the possible electrical and fluidic causes of this discrepancy.

5.4 Electrical characterization

This section will summarize the electrical measurements aimed at characterizing the possible sources of lower micromotor performance. The potential causes discussed are: voltage drop to the electrodes, reduced electrode active area, and lower inter-electrode area. Viscous drag will be assessed in Section 5.5.

Stator polysilicon resistivity

Lower torque could be caused by a voltage drop from the leads to the electrodes. The resistivity of the polysilicon forming the stator leads, interconnects and electrodes was measured on an open die, using a 4-point probe technique.

During fabrication, the stator polysilicon resistivity was measured to be 390 $\mu\Omega - cm$, while the resistivity on the stator of an open die was 1400 $\mu\Omega - cm$ for the leads, 2000 $\mu\Omega - cm$ for the electrodes, and 630 $\mu\Omega - cm$ for the interconnects. On average, the stator polysilicon resistivity was 4 times larger than the design intent. Probable causes for this change in conductivity are the high temperature anneals ($1100°C$) incurred during bonding or the chemical-mechanical-polishing (CMP) of the stator surface. One indication that CMP may be a cause is the fact that the interconnect layer maintained a higher conductivity than the electrode and lead layer, consistent with the fact that it was not directly exposed to the CMP process (the inter-level dielectric oxide covers the interconnect polysilicon).

The effect of increased resistivity was simulated in a circuit model of the stator [37], using the measured values of resistivity. The model indicated a lag of the signal by up to 5° as it reaches the electrodes on the opposite side from the input lead. This asymmetry has for effect of introducing undesired backward traveling waves, which were calculated to reduce the torque by 1-3%, which does not account for the 63% reduction in measured torque.

Electrode potential

To confirm that the high voltage, high frequency signal reaches the electrodes unperturbed, a direct measurement from the end of a lead to a connected electrode was done using probe tips. Four probes were used in the measurement: Ch2 - supplying the signal at the far end of the lead; Ch1 - measuring the voltage along the lead, near the electrodes; Ch4 - measuring the voltage on the electrodes, located at 90° from the lead; and Ch3 - extra probe contacted to the electrode to add capacitance. The main difficulty with this measurement is the capacitance added to the stator circuit by the probes contacting the electrodes. To quantify the impact of the measuring probe (Ch4), measurements are taken with and without a second probe on the electrodes. Figure 5-11 shows the results for two configurations. A significant phase shift (36°) and reduction in magnitude (to 80%) is measured when 2 probes are contacting the electrodes. When the second probe is removed, the lag is reduced to 20° and the magnitude rises to 97% of the supplied voltage. Presence of the measurement probe (Ch4) can therefore account for the remaining phase lag and slight voltage drop. This high voltage, high frequency test confirms that the signal applied to the leads should remain essentially unaffected as it reaches the electrodes.

Active electrode area

Motor torque is directly proportional to the active area, so disconnected electrodes would also cause lower torque. Measurements however suggest that all electrodes are active. Conduction was measured with the probe tip, from the lead to over 100 electrodes on an open stator die, without finding a disconnected electrode. Furthermore, capacitance measurements between phases and the ground plane have shown to be consistently in the range of 6.6-7.8 pF for all phases (7.8 pF for adjacent phases down to 6.6pF for opposite phases), suggesting symmetry. In addition, equal participation of each phase to the stator waveform was confirmed by disconnecting the leads to each of the six phases, one at a time. Rotational speed consistently dropped from 275 ± 5 RPM to 175 ± 5 RPM when either phase was disconnected (which is approximately a $(5/6)^2$ reduction).

Inter-electrode potential

Although current experiments have validated the potential on the electrodes, the inter-electrode potential remains a possible cause for lower power. As discussed in the design chapter, it can have a strong impact on the delivered torque, and has not yet been experimentally verified. The inter-electrode gap for these devices was larger by 1 μm (from the design value of 4 μm) and the thick insulating oxide was only 8 μm instead of 10 μm . A larger gap and closer ground plane may allow the ground and rotor potentials to have a greater effect on the inter-electrode potential, reducing the magnitude of the fundamental. Further analysis is necessary in order to determine the probability of the cause.

Conclusions on electrical characterization

The characterization results seem to indicate that the stator structure built is expected to serve its functions adequately, namely to distribute the high voltage, high frequency signals and create the traveling waveform. It is not known for a fact however if the waveform has the desired shape, since the inter-electrode potential remains unknown.

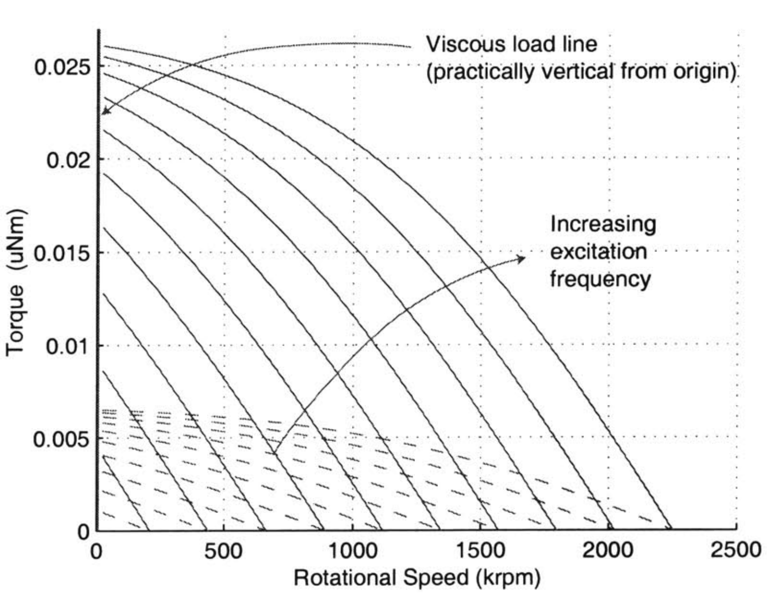

Figure 5-10: Viscous load curve and motor torque curves for the M/D #1 at different stator excitation frequencies and constant 10V amplitude. The solid line is for the nominal Demo Motor-Compressor design parameters with 7 times larger rotor film conductivity, while the dashed line corresponds to the 4 times lower electrostatic torque.

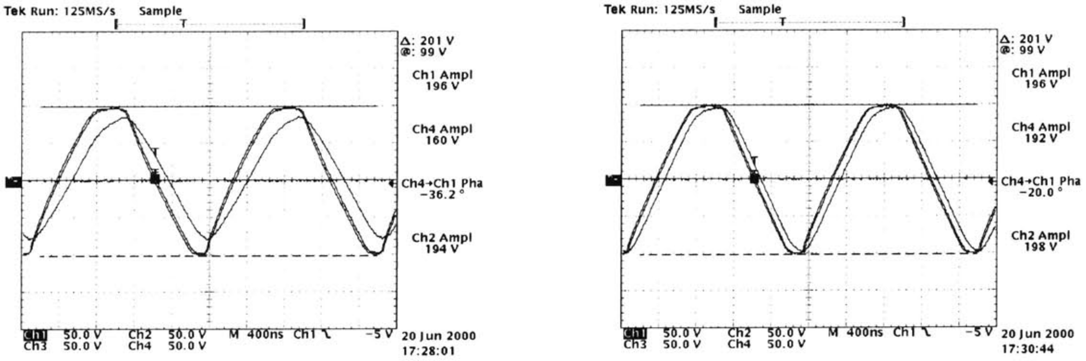

(a) With extra probe and coax cable (78pF)

(b) Without the extra probe and cable

Figure 5-11: Stator electrode characterization, showing that the supplied potential reaches the electrodes with minor phase delay and magnitude reduction, once the presence of the sensing probe is accounted for. The shifted waveform corresponds to that measured on the electrode.

5.5 Experimental measurement of viscous drag

In this section, the prediction of viscous drag will be assessed experimentally. The breakdown of torques on the Motor/Disk rotor is presented in Figure 5-12. Measurement of the total drag on the rotor is presented here.

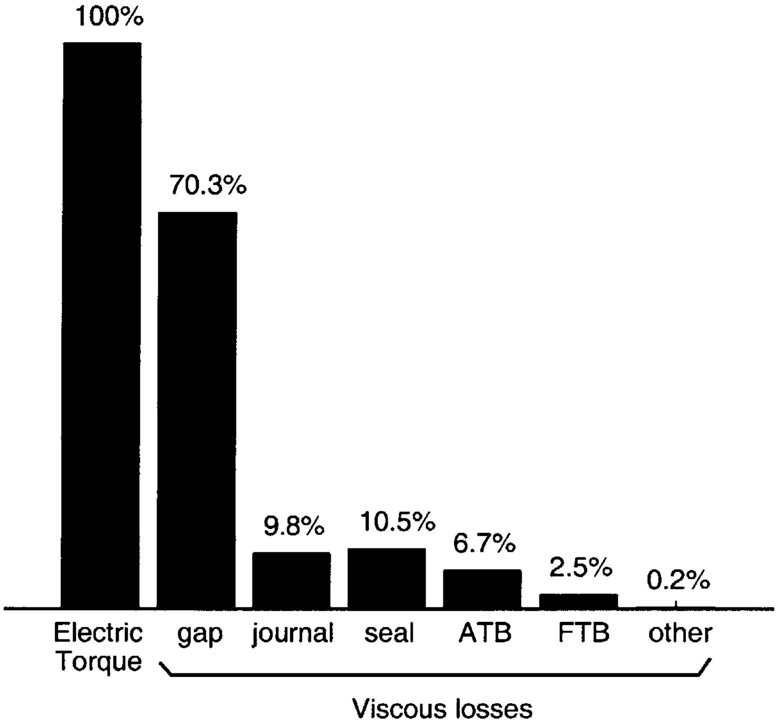

Figure 5-12: Torque balance in the Motor/Disk device.

Spindown approach

In order to quantify the effects of viscous drag independently from the motor electrostatic torque, spin down experiments were done on the Motor/Disk device #1. The procedure consisted of:

1. Spinning the rotor up to the highest steady-state speed possible using the motor, at which point the viscous torques are equal to the torque of electrostatic origin: $Tvisc = Telec$
2. Start the high-speed acquisition of the fiber optic sensor signal, which is aimed at the rotor surface;

3. Suddenly stop the drive signal to the motor ($Telec = 0$), allowing the disk to decelerate smoothly[1];
4. Stop the data acquisition once the rotor has came to a rest.

Since the only torque on the disk during spindown is viscous drag, the deceleration rate will be set by the rotor moment of inertia J and the viscous torque $T_{visc} = -K_v\dot{\theta}$:

$$J\frac{d\dot{\theta}}{dt} = -K_v\dot{\theta} \tag{5.1}$$

The instantaneous rotation rate therefore takes the form of an exponential decay from the steady-state speed, Ω:

$$\dot{\theta} = \Omega\, e^{-\frac{K_v}{J}t} \tag{5.2}$$

which expressed logarithmically is:

$$ln(\dot{\theta}) = -\frac{K_v}{J}t + ln(\Omega) \tag{5.3}$$

Spindown results

The Motor/Disk device #1 was driven with the Op-Amp electronics at a voltage of 65V and a frequency of 1 MHz, to a speed of 3580 RPM. At this point, recording of the fiber optic sensor output was started (50,000 samples/sec for 10 seconds), during which the frequency signal to the Op-Amp drive circuitry was disconnected, halting the stator excitation. The rotor completes less than 10 revolutions before stopping, in $\sim 1/2$ sec. A typical signal is shown in Figure 5-13, generated by non-uniformities on the rotor surface. A quasi-instantaneous rotational speed can be determined for each period, by noting the time interval Δt of each revolution. Based on Equation 5.3, the logarithm of this rotational speed is plotted as a function of time in Figure 5-14. Given the relatively long periods with

---

[1] Along with the electrostatic torque, the attraction force will vanish upon stopping the drive signal. At high power operation, the rotor will move upwards (away from the stator), changing the motor gap and the related viscous torque. In the current experiments, the electrostatic attraction force was negligible compared to the thrust bearing stiffness, such that the gap can be assumed to remain constant. This effect is confirmed during the experiment by monitoring the change in thrust bearing flows, for constant pressures.

respect to the overall deceleration time, the choice of the time associated to each quasi-instantaneous value of speed is a source of uncertainty. Nominally, it was taken as the time halfway through each revolution. Uncertainty bounds can be drawn, by plotting the speed with respect to the time at the beginning and at the end of each revolution.

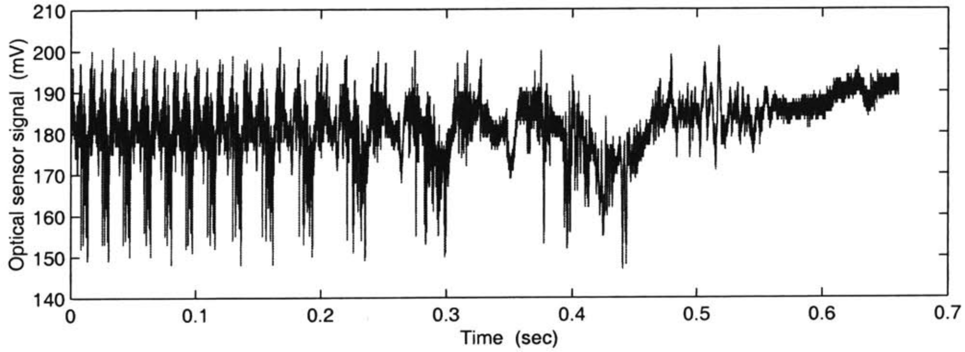

Figure 5-13: Raw signal from the fiber optic sensor during spindown.

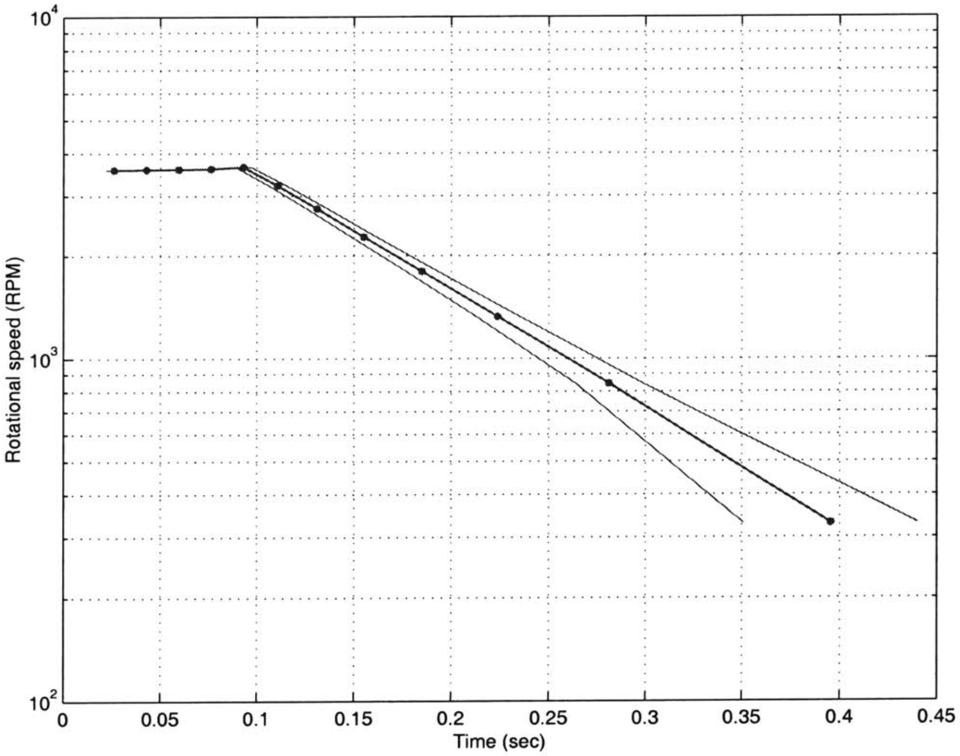

Figure 5-14: Quasi-instantaneous speed as a function time during the spindown - die M/D #1. Uncertainty on the speed as a function of time is shown by the bounding lines.

The slope of the curve on this log scale is directly the ratio of viscous torque constant K_v to rotor moment of inertia J: $-K_v/J$. The value of the slope was calculated at each point using a finite difference method. From the known moment of inertia of the disk

$(2.1 \times 10^{-11} kg\ m^2)$, the viscous torque constant K_v is calculated and plotted in Figure 5-15, along with the values predicted by the drag models for motor gaps of 3.5, 4.0 and 4.5 μm. We note agreement between the model and data for a motor gap of 4.0 μm, which is within the expected fabrication results. Another representation of this data is a plot of the viscous torque ($T_{visc} = K_v * \Omega$) as a function of rotational speed, shown in Figure 5-16. It is interesting to note that this micro-spindown approach was capable of measuring torque levels down to 0.02 μNm (20 nNm).

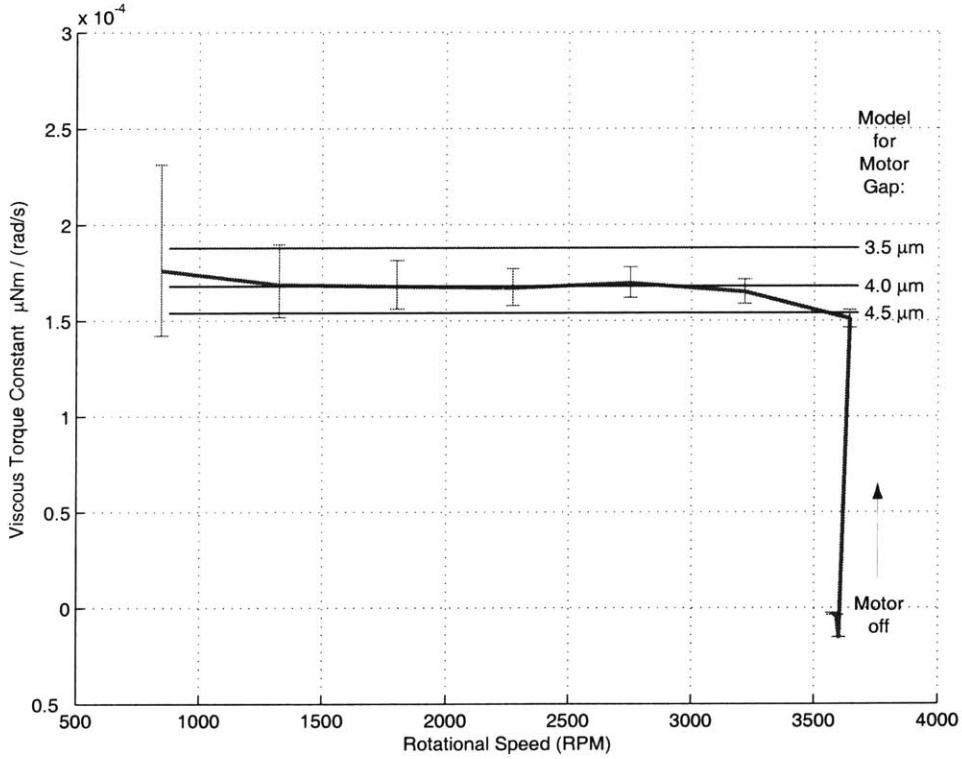

Figure 5-15: Viscous torque constant: $T_{visc} = K_v \Omega$, derived from the spindown data for die M/D #1. Uncertainty bars result from the uncertainty on the instantaneous speed.

Error bars on the data are once again determined from the uncertainty on the time. The low speed data points are characterized by a larger uncertainty, since one revolution occupies a larger portion of the deceleration time. Testing at higher speeds is expected to improve the accuracy of the results and increase the number of data points. More sophisticated signal processing of the optical sensor signal might results in higher accuracy.

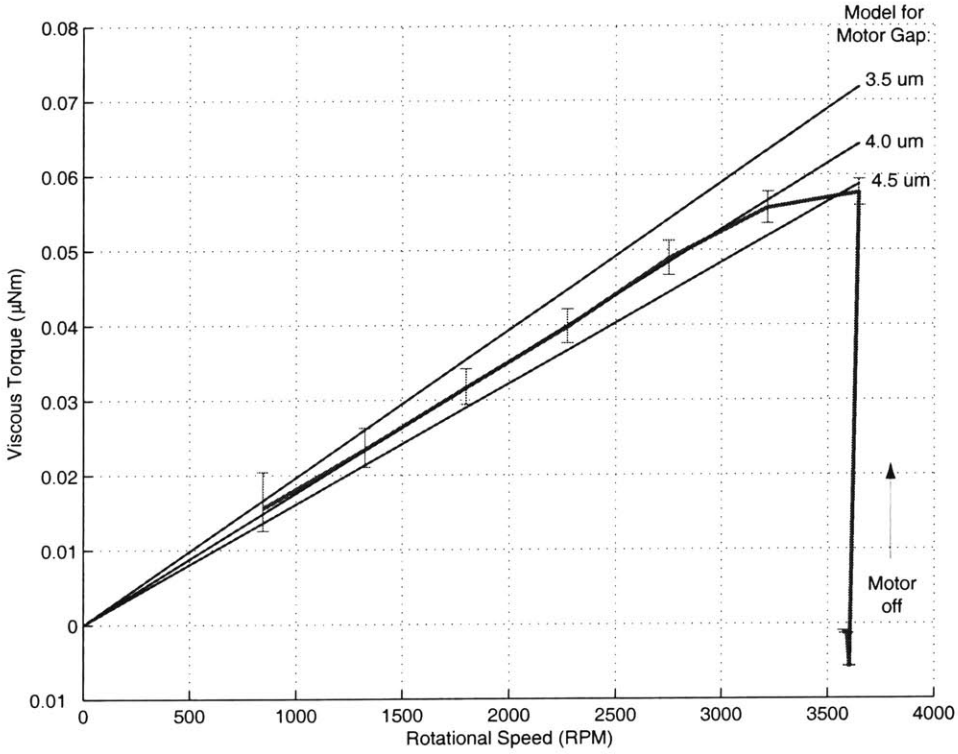

Figure 5-16: Viscous torque derived from the spindown data for die M/D #1. Uncertainty bars results from the uncertainty on the instantaneous speed.

Assessment of viscous modeling

The results presented indicate that the simple flow models seem to be adequate for design purposes, at least in the range of speeds investigated. In the high-speed regime, the MC-Bearing rig results presented in Section 4.5 (up to 300 m/s tip speed) have shown reasonable agreement with the models. Although the uncertainty was larger than for the spindown experiments (since the turbine torque is part of the prediction), there is no indication at this point in time that viscous drag in these high speed micro-devices is anything other than expected from standard theory.

This spindown approach could also prove useful in experimentally measure microturbomachinery efficiency, especially since parallel MEMS processing allows the fabrication of similar rotors with and without blades, hence providing a mean to separate the viscous drag in the motor and bearings from the turbomachinery torque.

5.6 Summary of Performance Assessment

Results from this experimental effort indicate that the viscous drag closely matches the simple flow models. The lower than expected speeds are therefore attributed to the electrostatic motor by elimination.

The peak torque delivered by the motor can be separated in two parts: the voltage squared, and the torque per unit voltage squared (μNm / kV^2). Both limited the motor torque.

Maximum voltage

The maximum voltage is ultimately limited by breakdown. Although test structures have reached the design value of 300V, the current devices exhibited breakdown in the range of 90-100V. This lower maximum voltage results in a factor of ~ 10 decrease in torque.

The fact that similar structures have withstood higher voltages implies that improved stator design and/or processing of the stators is needed to reach the design values of torque.

When tuned to match the frequency at the peak of the motor curve, the resonant electronics should allow operation at high torque.

Torque per unit voltage squared

Torque per unit voltage squared is a measure of the performance of the motor, and of the variations off-design in the geometry and the electrical characteristics of the motor. Maximum torque is however not affected by the rotor film conductivity (it simply shifts the peak to different frequencies, as shown in Figure 5-9). From the calculations of torque presented in Figure 5-10 for the designed and measured motor performance, the torque per unit voltage squared is found to be 260 μNm / kV^2 for the design and 170 μNm / kV^2 when accounting for the 4 μm motor gap. The measured value is more on the order of 65 μNm / kV^2. The discrepancy can result from un-modeled phenomena, or electrical characteristics which have not been characterized. Further characterization of the devices built as part of this work would require destructive approaches, and will be reported to later.

Furthermore, although the value for torque per unit voltage squared is consistent across the different tests at low voltage, it may tend to drop at high voltages. As shown by the resonant drive results in Figure 5-6, the speed (hence the motor torque) tails off from the V^2 trend, above 50-60 V. The cause of this reduction in torque per unit voltage squared may be associated with the breakdown in the polysilicon stator structure which manifested itself at 90V. High voltage operation over a range of frequencies would be necessary in order to further investigate the voltage dependence.

Rotor conductivity / slip

As fabricated these micromotors exhibited a rotor conductivity 7 times larger than expected. Although this does not directly impact the maximum torque, it changes the optimal operating point, and affects the system operation. For the current set of experiments, the power electronics did not along peak operation at high voltage. the resonant drive electronics were limited to 1.8 MHz, corresponding to only half the peak torque. A better understanding of the effects of high temperature anneals on the rotor film conductivity is necessary, in order to fabricate a device which operates with predictable slip. Also, the system should be designed to accommodate variations in rotor film conductivity. A slip in the range of 30%, as chosen in the Demo Motor-Compressor design, seemed appropriate for ease of operation. The drive electronics should also be designed to accommodate variations in slip to achieve peak power operation.

Discrepancy in the motor performance is summarized in Table 5.1, identify the factors which reduced the achieved motor torque and power.

Engineering Issue	Impact on Torque	Impact on Power	Approach
Breakdown - High voltage operation	9x	81x	Further investigation
Rotor Conductivity - Peak operation	2x	4x	High freq electronics or new build
Motor Gap - Torque/V^2	1.5x	2x	New build
Undetermined factor - Torque/V^2	2.7x	7x	Further investigation
Factor from design	70x	5300x	

Table 5.1: Summary of motor performance assessment

5.7 System-level Operation

5.7.1 Motor-Compressor Operation

At the maximum speed achieved of 15,000 RPM (tip speed of 3.3 m/s), the Demo Motor-Compressor is expected to provide a pressure rise of only 0.03" $H_2 0$, based on the pressure ratio of 1.17 at 168 m/s, demonstrated on the macro-scale compressor test rig.

Furthermore, the corresponding mass flow through the compressor should only be of the order of 10 sccm in order to match the velocity triangle. A minimum flow rate on the order of 20 sccm is typically necessary through the hydrostatic journal bearing for startup, which combines with the compressor main flow. At these low speeds, the bearing configuration largely impacts the compressor operation, and further investigation of the compressor operation was not pursued. The focus was mostly directed towards increasing the operating speed.

5.7.2 Integrated System Demonstration

Nevertheless, demonstration of the integrated system at high speeds was possible, using the turbine to supply additional torque. Simultaneous operation of the gas-lubricated bearings, micromotor, and microturbomachinery was demonstrated up to 200,000 RPM with die M/T #1. The device was run as an MC-Bearing rig, but with the micromotor acting as a brake or secondary source of torque. Changes in speed in the thousands of RPM were measured using the Op-Amp drive, similarly to the results shown in Section 5.2 (without air assist). The same die was also spun up to 400,000 RPM, as was shown in Figure 4-15. These high-speed runs demonstrate that the incorporation of thin film structures on the rotor does not preclude high-speed operation. Although not quantified, the issues of strength of the composite rotor and imbalance due to thin film processing appear not to be limiting aspects for high-speed operation, at least up to 400,000 RPM.

5.7.3 Projected performance

Given the current status of the technology as demonstrated here, a maximum speed of 36,000 RPM is expected for the Motor/Disk device excited at 5 MHz and 100V amplitude. Although current power electronics do not allow such operating conditions, devices should operate at these conditions, since operation has been demonstrated up to 100V, and at 5 MHz, but not simultaneously. The Demo Motor-Compressor is predicted to rotate at 32,000 RPM and deliver a pressure rise of 0.08" $H_2 0$, under this excitation.

If it were possible to operate the motor up to 300V without breakdown, the current demonstrated technology (65 $\mu Nm/kV^2$) would spin a Motor/Disk up to 330,000 RPM and a Motor/Compressor at 260,000 RPM, delivering 1000 sccm at 5" $H_2 0$.

CHAPTER 6

SUMMARY AND CONCLUSIONS

This chapter summarizes the research presented in this thesis and outlines the main contributions. Recommendations for future work are also presented.

6.1 Summary

This thesis presented the design and micro-scale development effort of a silicon microfabricated motor-driven compression system, and its components. The research focused on the system design, fabrication, and testing of the hydrostatic journal bearing, the electrostatic induction micromotor, and the integrated system.

Component and system design - System modeling was initially undertaken to determine the main design trade-offs and define viable configurations. Modeling of the electrostatic and fluidic forces in the micromotor identified that the viscous dissipation in the motor gap can negate the electrical torque, if the motor geometry is not designed appropriately. System modeling then allowed the exploration of this and other trade-offs, and the determination of viable configurations for μCompressor (2:1 pressure ratio, 0.1 g/s of air) and μBlower (20" H_20 pressure rise, 0.1-0.3 g/s of air) applications, with expected overall efficiencies up to 20%. The configuration of an experimental device to be used through this work was also defined, as a compromise between maximum performance and risk in fabricating and operating such an unconventional device.

Microfabrication - Experimental development work was then undertaken to define a viable fabrication approach to integrate thin and thick (up to 10 μm) patterned films with deep reactive ion etched precision features in a stack of 5 fusion bonded wafers. This led to the successful fabrication of three sets of devices: two sets of all silicon microturbine-driven bearing rigs (no thin or thick films), and one set of micromotor-driven devices (which integrated the thin and thick film motor components). The main challenges were:

- Wafer bonding with thin and thick films: overcome through a recessed design of the motor components, which includes removing the films in specified bonding areas (reducing wafer bow) and polishing the surfaces.
- Retention of the rotor during wafer processing and release: accomplished by a new snap-off tab approach, consisting of a mechanical link between the rotor and static structure created while bonding, which is controllably fractured to release the rotor before testing.
- Precision fabrication of the rotor and bearing components: accomplished through iterative development of deep reactive ion etching techniques, which resulted in geometries proven to be adequate for high speed rotation.

High-speed bearing operation - The all silicon bearing rigs, driven with an air turbine, were then used to demonstrate repeatable, sustained high speed rotation. Critical to this work was the use of a fiber optic sensor to monitor the rotordynamics and bearing stability in real-time. This information was used to determine experimentally a pressure schedule for stable operation of the hydrostatic journal bearing, which is new to this type of device. These microrotors have been spun up to 1.4 million RPM (300 m/s tip speed) in stable and sustained manner, using the pressure schedule developed. This speed is beyond the design value of the specific motor-driven devices. This experimental demonstration confirms that the microfabricated single crystal silicon rotor structure can sustain the centrifugal forces up to 300 m/s tip speed.

High power density microturbomachinery was also demonstrated during these experiments, since the microturbine delivered 5W of net mechanical power, which corresponds[1] to 4000

---

[1] The power density is based on the volume of the turbomachine, enclosing the blades and the flow path,

MW/m^3.

Micromotor testing - The set of motor-driven devices were then tested to investigate the electrostatic induction micromotor and demonstrate operation of the integrated system. The motor torque curves were measured and found to exhibit typical induction machine characteristics, such as a peak in torque as a function of frequency (at 5 MHz), and a quadratic dependence on voltage. Voltage amplitudes were however limited to 100V, since electrical breakdown occurred beyond that point. Practically, this reduced the available torque achievable in these devices by almost one order of magnitude. The maximum speed achieved by a motor-driven device was 15,000 RPM (3 m/s tip speed) at 100V amplitude and 1.8 MHz, at which point the motor is calculated to deliver a torque of 0.3 μNm and a shaft power of 0.5 mW.

The speeds achieved were approximately one third of that predicted by the analytical models, for a given voltage. To help identify the cause of lower speed, the viscous drag on a bladeless rotor was experimentally determined using a transient spindown approach. It was found to compare well with the simple flow models, suggesting that the electrostatic induction torque must be lower than expected. The predicted peak torque per unit voltage squared for this micromotor was $170\mu Nm/kV^2$, while the experimental value derived from the viscous drag measurement was $65\mu Nm/kV^2$. Although the electrical structure has been characterized, the exact cause for reduced motor performance has however not yet been determined.

System demonstration - Integrated fabrication and simultaneous operation of the gas-lubricated bearings, turbomachinery, and micromotor were demonstrated. Rotation at low speed (15,000 RPM; solely using the micromotor as a drive) and up to high speed (300,000 RPM; using the turbine as a secondary source of torque) was achieved for the integrated device. No pressure rise was however measured from the compressor, since the motor-driven devices operated at low tip speed, 3 m/s, versus the design intent of 200 m/s. However, since the compressor has been successfully demonstrated at design aerodynamic conditions at large length-scale, the proposed MEMS motor-driven compressor would work,

---

but not the disk, shaft, and bearing assembly.

if the voltage can be raised to the intended 300V and the electrostatic induction torque discrepancy resolved.

6.2 Overview of Contributions

The research presented in this thesis opens the road for the development of a new type of compression system, characterized by high performance, compact size, and potentially low cost. The contributions of this work can be viewed as:

1. First demonstration of the operation of a silicon microfabricated MEMS device integrating turbomachinery, gas-lubricated bearings, and electromechanical energy conversion.
2. Development and demonstration of the fabrication process for a Motor-Compressor device, consisting of a 5-wafer bonded stack integrating thin and thick film processing with precision deep reactive ion etching;
3. Development of a rotordynamic monitoring approach and an operating protocol for high speed operation of microfabricated hydrostatic journal bearings;
4. Demonstration and characterization of an electrostatic induction micromotor supported on gas-lubricated bearings, designed for high power density;
5. System level design of a high-power density micromotor-driven compressor within the unique component and device design space allowed by silicon microfabrication;

6.3 Lessons learned

Various lessons learned have been listed throughout the thesis, but the main ones will be summarized here, along with overarching observations.

Design

- Viscous drag takes a major role in the operation of high speed micro-devices, and must be accommodated for in the system design.

- Design for simplicity, robustness, and flexibility is a rule to follow in MEMS design. This lowers the development risk, but may come to the cost of less performant design.
  - The operation of critical components should be decoupled, as much as possible;
  - The design should provide independent control over as many operating parameters as possible, to provide flexibility during testing;
  - Tight tolerances should not be introduced unless necessary, in order to allow processing flexibility (such as wet or dry etching for film patterning);
  - The parallel processing nature of micromachining suggest that only one critical feature should be designed per mask, for which the process can be optimized;
  - Simple geometries, with rounded corners, are preferable, since limited familiarity with micromachining may often introduce unexpected peculiarities in complex geometries.
- Characterization should be an integral part of the mask and process flow design. Specially designed features should be included on the masks (between die, or outside the device area) for critical thin film, small gap, and deep etch characterization. These could allow monitoring of the various steps during processing and non-destructive characterization of the devices built.

Fabrication

Guidelines were presented in Sections 3.2.3 and 3.2.3 for the design and fabrication of micromachined silicon structures, and of integrated thin films, respectively, and will not be repeated here. In addition:

- Particular attention must be dedicated to the fabrication of critical components, in order to ensure proper device operation. In particular, functional requirements must be defined for the bearing geometries, and respected during fabrication. This implies that the design should be within the reproducible capabilities of microfabrication; an overly aggressive design will introduce large uncertainty in the time estimate to reach the specified requirements.

- Due to long fabrication times for complex MEMS devices, it is useful to understand the cause of unsuccessful device operation before building new devices. Non-ideal devices can often be tested and useful information gained, which will increase the probability of success for the following build. Iterative fabrication without such a feedback loop may not be as productive.

Experimental development of power MEMS

- Similar to any other MEMS device, testing apparatus and packaging of power MEMS devices are critical to successful operation. They should be developed along with the micro-device, since they are closely interfaced.
- The testing apparatus should allow the investigation of the device over a wide operating range, since the operating conditions often deviate from the predicted design due to large tolerances common in new microfabricated devices.
- Instrumentation should not only be intended to quantify the level of performance achieved, but also to provide insight on the device operation. This information can be critical in operating the device and reach the intended levels of performance.
- Although a component is designed for high speed or high power operation, there is significant insight to be gained by operating it at lower levels of performance.

Complex system development in an academic environment

Although academic research has been traditionally oriented towards scientific developments in disciplinary fields, development of an integrated system (product) can also find its place. The device creates a platform for scientific development, and provides the student or researcher with a unique opportunity to experience the implementation of his/her work, and gain a multi-disciplinary background through collaborative work. In order to maximize the benefits of this approach and comply with the academic environment, it was found that:

- Involvement of the student or researcher in all critical aspects of the device development is beneficial (multi-disciplinary design, fabrication, and testing), in order to understand the components interactions and requirements, and promote original thinking. It comes at the expense of less depth in the disciplinary fields, which is acceptable if the desired level of performance does not require such a depth. Devices requiring simpler component design and analysis should be preferred in order to allow the multi-disciplinary experience.

- A faster development cycle (design, fabrication, testing) will result from a development plan formed of many small steps as opposed to one large leap. The cycle may however need to be repeated in order to reach the performance objectives, leading to a longer development plan. The iterative approach will however reduce the uncertainty on the time and probability of achieving the milestones.
- Use of components or processes from other devices allows a greater focus on the new aspects of the current device, but often to the expense of non-optimal performance.

6.4 Recommendations for Future Research and Development

This experimental effort has served to develop and demonstrate Power MEMS technologies, but also to identify areas where future work could contribute to the advancement of this technology. Given the primitive state of this research area, various aspects were identified during the design, fabrication, and testing stages, but were only pursued to the depth necessary in order to complete the entire life cycle of this first generation motor-driven compressor. Important areas of future work on the system development and disciplinary research are:

1. Microfabrication
   (a) Increased experience in bonding wafers with patterned thin films, in order to establish repeatable processes and requirements for successful bonding;
   (b) Further development of the rotor film fabrication process to ensure less variability of its conductivity, and a better understanding of the effects of high temperature cycling or other process step necessary to integrate the motor in a bonded wafer stack;
   (c) Develop an approach to build balanced rotors over the entire wafer, such that low yield would not negate the advantages of parallel processing, and rise the

unit cost;

   (d) Develop alternate approaches for the insulation of the stator and rotor electrical components, to expand on the current technology;

2. *Electromechanics*

   (a) A better understanding and control of the breakdown phenomena in the motor would be necessary in order to specify the requirements on the operating environment and fabrication in order to securely approach the design value of 300V between adjacent electrodes;
   (b) Electrostatic modeling and experimental assessment of the potential in the region between adjacent electrode during motor operation would be necessary in order to better assess the electrostatic induction torque;
   (c) Characterization of the axial electrostatic forces and tilting moments in order to validate the motor models for future thrust bearing designs;
   (d) Development of flexible high voltage, high frequency, multi-phase power electronics would be beneficial, and should include simultaneous measurement of currents and voltages to monitor the motor operation and quantify the motor efficiency;
   (e) Design of miniaturized power electronics and system level design including them as a main component, since they can effect the system efficiency, size, and micro-device configuration.

3. Turbomachinery

   (a) Exploration of a broader range of compressor designs, providing a prediction of compressor efficiency, pressure rise, and mass flow as a function of blade trailing edge angle. This would be useful for system design purposes by decoupling the pressure ratio from the rotational speed, currently constrained by a single blading design.
   (b) Further understanding and improvements in compressor efficiency would be beneficial. Current values, measured in the range of 25-40% (macro-compressor test rig) are lower than predicted numerically and so reduce the achievable speed and pressure rise of a motor-driven compressor;

   (c) Experimental characterization of the micro-compressor performance, such as pressure ratio, mass flow, and torque as a function of speed (possibly by using the spindown approach for torque measurement, using the micromotor as the drive - only possible once higher levels of power are achieve from the micromotor).

4. Bearings and secondary flows

   (a) Pursued experimental characterization of the stability boundaries using variants of the current configuration, in order to identify the various types of bearing failure, determine safe operating protocols, and more complete monitoring techniques;
   (b) Low-order modeling of the rotordynamics, including: hydrodynamic forces during supercritical (inverted) operation and hydrostatic stiffness and lag, would be useful to gain physical insight in the rotordynamics of the current generation of devices;
   (c) Design study of the effect of hydrostatic journal bearing geometry, on its stability and its requirements of pressure drop and mass flow, in order to open the design space and re-evaluate the current journal bearing fabrication requirements;
   (d) Experimental development of hydrodynamic, or hybrid, thrust and journal bearings to allow self-sustained operation (without externally supplied pressurized gases);
   (e) Experimental development of non-plain journal bearing configurations to reduce the destabilizing hydrodynamic forces;
   (f) Characterization of the thrust bearing flow versus position relation to extend the use of the thrust bearings as accurate axial position sensors;
   (g) Dynamic characterization of the thrust bearings in order to identify their role, if any, in the high-speed crashes;
   (h) Modeling of the tilt stiffness and stability of the bearing system, including the thrust bearings and the hydrostatic and hydrodynamic forces in the motor gap, to identify other critical speeds and sources of instability.

5. Structures and Materials

    (a) Understand and quantify the impact that stress in composite thin film / bonded structures has on the final operating gaps of the diced device;
    (b) Develop a post-failure analysis method of the crashed rotors to identify probable failure mechanisms;

6. System design and device testing:
    (a) Pursue testing of the current set of devices at higher voltages and high frequency;
    (b) Build and test a second set of devices which can operate up to the design value of 300V (once the breakdown problem is addressed) to reach high speed and demonstrate the compressor;
    (c) Review the system design once the assessment of the micromotor performance is completed, before pursuing the development of devices for specific applications;
    (d) Study the trade-off of compressor efficiency with motor efficiency as a function of tip speed (predictions or measurements of compressor performance for various designs are first necessary);
    (e) Develop and test metal stators in order to achieve higher device efficiency;
    (f) Develop magnetic micromotors as an alternative technology path, which offers the possibility of larger clearances, reducing the viscous losses in the motor;
    (g) Develop and integrate a rotor motion sensor for speed measurement and rotordynamic characterization;
    (h) Integrate a heat exchanger with the package and a temperature sensor (in the chip or in the package) in order to monitor and control the viscous losses and electrical characteristics of the motor components;
    (i) Further assess the impact of heat addition to the compressor flow path, originating from the dissipation in the rotor film, motor gap, and stator.

APPENDIX A

VISCOUS DRAG IN THE MOTOR GAP: PREDICTION AND REDUCTION STRATEGIES

Induction micromotor modeling states that the applied torque is inversely proportional to the motor gap, such that system design pushes the motor gap to very small values (3-5 microns) in order for the motor to produce the required amount of power. In addition, the turbomachinery requires high tangential velocities to provide the required pressure ratio. Unfortunately, this combination of a high speed rotating disk over a very small air gap results in large viscous losses. The power viscously dissipated in the motor gap has two main impacts on the system:

1. Reduces the net power output from the motor (limiting the available power for compression work);
2. Increases the temperature of the device, since the viscous dissipation acts as a heat source.

This section focuses on the first item by presenting the approach used to calculate the motor gap viscous dissipation and strategies to reduce it. First, the analysis of the motor gap flow with a smooth stator is summarized, followed by the flow between a spinning disk and a grooved stator (radial grooves). Other strategies for drag reduction are then presented and discussed. The focus is on understanding the origin of the drag on the disk in order to, as accurately as possible, predict and eventually reduce the dissipated power. The methods used to for calculating the flow field are both analytical and numerical, which details will not be presented herein. The numerical results presented were obtained using a commercial CFD package (Fluent) which solves the Navier-Stokes equations using a pressure-based segregated solution scheme with a second order accurate, cell centered, finite-volume discretization. For the calculations presented in this document, the flow in the motor gap is assumed to be steady and laminar[1].

Since viscous heating will affect the drag through changes in viscosity (and in some cases density), the predicted drag will be a function the thermal balance of the device. To concentrate on the flow field, this aspect will be factored out here by assuming a constant viscosity.

For reference, the nominal motor-compressor parameters relevant to the motor gap flow are summarized in Table A.1.

Parameter		Dimensions
Motor outer radius,	r_{mo}	2 mm
Motor inner radius,	r_{mi}	1 mm
Motor gap,	g_m	3 μm
Rotational speed,	Ω	1.9×10^6 RPM
Wheel speed,	Ωr_{mo}	400 m/s
Outer radius pressure,	$P2$	2 atm.
Inner radius pressure,	$P1$	1 atm.

Table A.1: Motor gap parameters for the nominal motor-compressor configuration.

---

[1] No turbulence is therefore used, such that the Navier-Stokes are solved directly

A.1 Smooth stator motor gap flow

The motor gap can be modeled as an annular disk extending from r_{mi} to r_{mo} and rotating over a flat surface. Static pressures are applied at the outer radius ($P2$) and inner radius ($P1$), where $P2 > P1$ for the nominal motor-compressor configuration. The following sections will discuss the flow features in the motor gap for a smooth stator configuration and derive simple approximations for drag prediction.

A.1.1 Simplified flow field

First, the flow will be assumed incompressible and the effects of rotation will be neglected. The following sections describe the motor gap flow under these conditions, then introduces the effects of rotation and entrance lengths.

Radial velocity profile When rotation is neglected, radial flow in the motor gap is similar to *Poiseuille flow* with varying area. The radial velocity profile is then parabolic, formed by the balance between the radial pressure gradient and the radial shear on both the disk and the stator (which impose $V_r = 0$ at these boundaries). This radial velocity profile determines the mass flow through the motor gap, but does not affect the tangential drag on the disk (when rotation is neglected).

Tangential velocity profile Flow in the tangential direction is similar to *Couette flow*, where velocity varies linearly between a stationary plate and a parallel plate moving at a velocity $U = \Omega r$. The shear stress on the moving plate corresponds to a drag force, (or torque on the disk). The force (or torque) multiplied by the plate velocity (or rotation rate) is the power required to sustain motion. Reduction of the shear stress is therefore a metric for comparing drag reduction approaches.

Furthermore, this power is dissipated as heat in the fluid, which increases the temperature, the viscosity and therefore the torque. Conceptually, the proportional trend of the viscosity coefficient with temperature is a vicious circle amplifying the detriment of a high viscous drag motor design.

Simple power dissipation model When rotation is neglected, the solution for drag on the disk is found by integrating the tangential shear stress due to Couette flow on the motor gap. We can express the torque (T) as the integral of the shear stress (τ_θ) from the inner to outer radius[2]:

$$\tau_\theta = \mu\frac{\delta V_\theta}{\delta z} = \mu\frac{\Delta V_\theta}{\Delta z} = \mu\frac{\Omega r}{g_m} \tag{A.1}$$

$$T = \int_{r_{mi}}^{r_{mo}} r\tau_\theta dA = \int_{r_{mi}}^{r_{mo}} \tau_\theta \times 2\pi r^2 dr$$

$$T = \int_{r_{mi}}^{r_{mo}} \mu\frac{\Omega r}{g_m} \times 2\pi r^2 dr = \mu\frac{2\pi\Omega}{g_m}\int_{r_{mi}}^{r_{mo}} r^3 dr$$

$$T = \mu\frac{\pi\Omega}{2g_m}(r_{mo}^4 - r_{mi}^4) \tag{A.2}$$

The viscous work done by the disk on the motor gap fluid is then :

$$\dot{W}_{visc} = T\Omega$$

$$\dot{W}_{visc} = \mu\frac{\pi\Omega^2}{2g_m}(r_{mo}^4 - r_{mi}^4) \tag{A.3}$$

The dissipated power, which reduces the net output power of the motor, is therefore proportional to the fluid viscosity (i.e. temperature), inversely proportional to the motor gap (g_m), and proportional to the rotational speed squared. To make the radius dependence more explicit, Eqn A.3 can be formulated as a function of area and wheel speed at the outer radius (Ωr_{mo}) by setting $r_{mi} = 0$:

$$\dot{W}_{visc} = \mu\frac{(\pi r_{mo}^2)(\Omega r_{mo})^2}{2g_m} \tag{A.4}$$

The dissipated power therefore tends to be proportional to the area and to the square of Ωr_{mo} (as r_{mi} tends to zero).

---

[2] Variables are defined as: axial component (z), radial component (r), motor gap (g_m), rotation rate (Ω) and viscosity coefficient (μ), inner and outer radius r_{mi} and r_{mo} respectively

A.1.2 Effects of rotation

For high angular velocities, we can expect rotation to affect the velocity profiles. One approach to view the effects of rotation is to evaluate the magnitude of the Coriolis and centrifugal terms in a rotating reference frame. If the momentum equations are written in a frame rotating with the fluid at a given axial position (i.e. $\Omega_{r.f.} = V_\theta / r$), then the relative tangential velocity (V_θ') is zero. The fictitious centrifugal and Coriolis forces per unit mass, due to the non-inertial frame, are then:

$$\vec{F}_{cent} = -\vec{\Omega}_{r.f.} \times (\vec{\Omega}_{r.f.} \times \vec{r}) = \frac{V_\theta^2}{r}\hat{e}_r \tag{A.5}$$

$$\vec{F}_{cori} = -2\vec{\Omega}_{r.f.} \times \vec{V}_r = -2\frac{V_\theta V_r}{r}\hat{e}_\theta \tag{A.6}$$

where the unit vector $\hat{e}_r$ is in the outward direction, and $\hat{e}_\theta$, in the direction of disk rotation.

Since these forces depend on the magnitude of the tangential velocity (V_θ), they will be more prevalent near the disk (where V_θ is large) than near near the stator (where V_θ tend to zero). When these forces are important, they will modify the tangential and radial velocity profiles so the drag may not be accurately predicted by the Couette flow approximation. The following paragraphs quantify the importance of these forces.

Centrifugal force The centrifugal force will change the radial velocity profile. Since the centrifugal force is directed outward (Eqn A.5), it creates larger radial velocities near the disk compared to the expected parabolic profile. The analytical solution for the radial velocity profile[3] at different pressure ratios ($P2/P1$) are shown in Figure A-2 (as the solid line), along with a numerical solution from Fluent (as the × symbols) for incompressible flow. They confirm the expected trends and show that the radial velocity is noticeably affected only when the external pressure ratio is less than 1.5, for the nominal speed and geometry of the motor-compressor.

The centrifugal force affects the mass flow through the motor gap, but will only affect the drag on the disk (tangential velocity profile) through V_r in the Coriolis force expression (Eqn A.6). It is therefore important for drag prediction only when the Coriolis force is also

---

[3] The analytical solution is not presented in this document.

important.

Coriolis force The Coriolis force will directly change the linear tangential velocity profile into a profile similar to a combined Couette-Poiseuille flow, as shown in Figure A-1. From Eqn A.6, the force will be in the direction of rotation for inward radial velocities ($V_r < 0$) and opposite to rotation for outward radial velocities ($V_r > 0$). Inward radial velocities (when $P2 > P1$) have the effect of reducing the tangential velocity gradient near the disk, therefore reducing the drag. The opposite applies for outward radial velocities, in which case the shear stress will increase. The Coriolis force can be detrimental if $P2 < P1$, and should be avoided not to increase the drag.

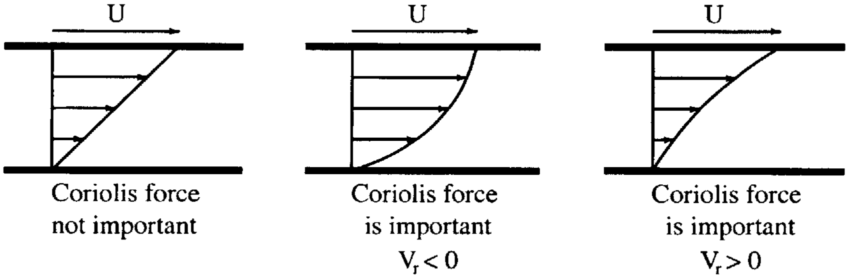

Figure A-1: Three tangential velocity profiles for situations where the Coriolis force is negligible, acting in the direction of rotation, or acting opposite to the direction of rotation.

This effect can also be described using conservation of angular momentum in an absolute reference frame. As a swirling inviscid fluid moves radially inward, angular momentum is conserved by increasing the tangential velocity ($V_\theta r$ = constant). However, the no-slip condition at the disk reduces the tangential velocity of the fluid as it flows inward ($\frac{V_\theta}{r}$ = constant). The ratio of viscous forces to angular inertial forces will determine which effect dominates. If the inertial forces are important enough, the tangential velocity profile will be similar to a combined Couette-Poiseuille flow, reducing (or increasing) the shear stress at the disk.

By comparing the magnitudes of the relevant inertial and viscous terms in the momentum equation, we can define a non-dimensional (Reynolds-like) number[4]. The convective inertial

---

[4] The literature on rotating flows normally uses the Rossby number ($R_o = \frac{Inertial \quad forces}{Coriolis \quad forces}$) and the Eckman number ($E_k = \frac{Viscous \quad forces}{Coriolis \quad forces}$) to describe the importance of the Coriolis effects. The non-dimensional ratio used here is actually a combination of both these numbers: $\frac{Inertial \quad forces}{Viscous \quad forces} = \frac{R_o}{E_k}$.

term can be approximated as:

$$V_r \frac{\delta V_\theta}{\delta r} \sim W \frac{\Omega r}{r} = W\Omega \tag{A.7}$$

where W is a representative radial velocity. The viscous term can be approximated as:

$$\nu \frac{\delta^2 V_\theta}{\delta z^2} \sim \nu \frac{\Omega r}{g_m^2} \tag{A.8}$$

The ratio of these two terms is then:

$$\frac{inertial \quad forces}{viscous \quad forces} \sim \frac{W g_m^2}{\nu r} \tag{A.9}$$

More insight can be gained however by expressing the ratio as:

$$\frac{inertial \quad forces}{viscous \quad forces} \sim \frac{W\Omega}{\nu \frac{\Omega r}{g_m^2}} = \frac{W}{\Omega r} \frac{g_m^2}{\nu/\Omega} \tag{A.10}$$

We can identify $\sqrt{\nu/\Omega}$, which characterizes a viscous diffusion length, so the non-dimensional ratio can be written as:

$$\frac{inertial \quad forces}{viscous \quad forces} \sim \left(\frac{W}{\Omega r}\right) \left(\frac{g_m}{\sqrt{\nu/\Omega}}\right)^2 \tag{A.11}$$

We can therefore state that the Coriolis force will gain importance, as the motor gap (g_m) increases compared to the viscous diffusion length[5] ($\sqrt{\nu/\Omega}$) and when the radial velocity (W) increase compared to the tangential velocity (Ωr). For the nominal motor-compressor configuration, the value of the above non-dimensional number is:

$$\frac{W}{\Omega r} \sim \frac{15m/s}{300m/s} = 0.05 \tag{A.12}$$

$$\frac{g_m}{\sqrt{\nu/\Omega}} \sim \frac{3}{\sqrt{\frac{2.2e-5}{1\times 200000}}} \sim \frac{3\mu m}{10\mu m} = 0.3 \tag{A.13}$$

$$\frac{inertial \quad forces}{viscous \quad forces} \sim \left(\frac{W}{\Omega r}\right) \left(\frac{g_m}{\sqrt{\nu/\Omega}}\right)^2 \sim 0.05 \times 0.3^2 = 0.0045 \tag{A.14}$$

---

[5] For the Rayleigh problem, where a plate is suddenly put into translation, the thickness of the boundary layer develops in time proportionally to $\sqrt{\nu t}$. Similarity with our case is found by replacing t by $1/\Omega$.

Since this number is small, the Coriolis force is not expected to modify the tangential velocity profile, or in other words, the viscous forces will overcome the inertial (or Coriolis) forces and impose a linear tangential velocity profile. The drag can therefore be approximated by the Couette flow solution for our nominal motor-compressor configuration.

Since the non-dimensional ratio is proportional to the square of the gap, and since increasing g_m allows for higher radial velocities (larger V_r), increasing the motor gap will make the Coriolis effect more prevalent. These effects are confirmed by Figure A-3, which shows numerical results for the tangential velocity profile at mid-radius for $3\mu m$ and $10\mu m$ gaps.

A.1.3 Entrance length effects

The previous analytical solution neglected the development of boundary layers as the flow enters at the outer radius. Two types of entrance lengths characterize the motor gap problem:

- distance over which the *tangential velocity profile* develops into a Couette flow (affects the torque on the disk);
- distance over which the *radial velocity profile* develops into a Poiseuille flow; (affects the mass flow through the motor gap).

Numerical solutions of the axisymmetric flow in the motor gap are shown in Figure A-4. The curves show the tangential velocity versus radius at mid-gap, for $3\mu m$ and $10\mu m$ gaps. Flow enters at the outer radius with zero tangential velocity. We notice the very short entrance length for the nominal $3\mu m$ gap[6]. In the entrance region, the shear stress at the disk is larger than Couette flow since the tangential velocity of the fluid in the gap is initially zero, while at the disk $V_\theta = \Omega r$. More work is done on the entering fluid since angular momentum must be imparted to the core flow.

To quantify the magnitude of rotation and entrance length effects, numerical results for axisymmetric flow are compared to the Couette flow approximation. Table A.2 summarizes

---

[6] Since the gap is orders of magnitudes less than the radius, the effect of this entrance length is expected to be secondary for small gaps

the power needed to sustain rotation ($T \times \Omega$) for $3\mu m$ and $10\mu m$ gaps with pressure ratios of 2:1 and 4:1.

Configuration			Power (W)		
Gap	Pressure ratio	Inlet V_θ	2-D axisymmetric computation	Couette flow approximation	% reduction from Couette flow
$3\mu m$	2:1	0 m/s	6.95	6.91	0.5%
	4:1	0 m/s	6.95	6.91	0.5%
$10\mu m$	2:1	0 m/s	2.16	2.07	4%
	4:1	0 m/s	2.27	2.07	10%
	4:1	150 m/s	1.93	2.07	-7%

Table A.2: Viscous drag on the disk from 2-D axisymmetric computations and the Couette flow approximation (Eqn A.3).

We first notice that the deviations from the Couette flow approximation are negligible for the nominal motor-compressor configuration ($3\mu m$ gap). Entrance length and rotation effects are apparent for the $10\mu m$ gap. We notice that the drag reduction due to the Coriolis effect is overtaken by the increase in drag due to the entrance length, so the drag is actually larger than the Couette flow approximation. When the entrance length is reduced ,by applying a uniform inlet tangential velocity of $\Omega r/2$, the calculations show a net reduction in drag. In this case, the Coriolis drag reduction is larger than the entrance drag increase. Comparing the results as a function of pressure ratio, we notice the insensitivity of the nominal configuration, while the larger motor gap drag is affected.

Conclusion To summarize, the Coriolis and centrifugal forces as well as the entrance lengths do not significantly affect the tangential velocity profile for the motor-compressor nominal configuration. The viscous dissipation can therefore be predicted by Eqn A.3, which assumes a linear tangential velocity profile (Couette flow).

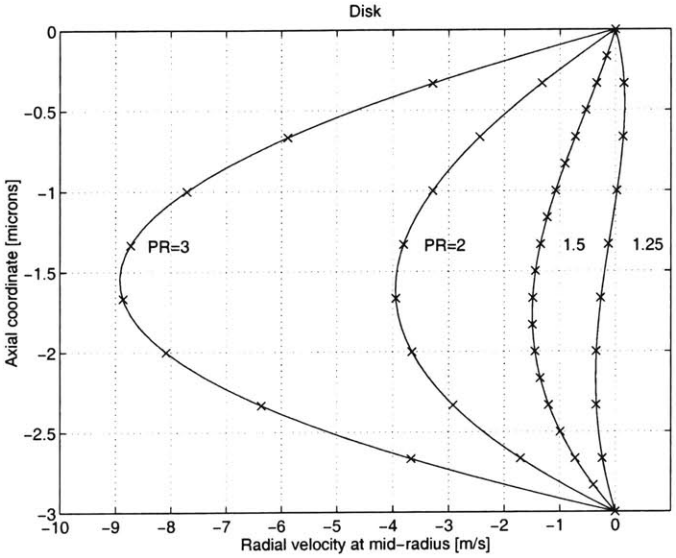

Figure A-2: Radial velocity profiles across the gap (mid-radius) for different pressure ratios ($P2/P1$). The centrifugal force tends to induce outward radial flow ($V_r > 0$) near the disk, opposite to the inward radial flow created by the external pressure ratio.

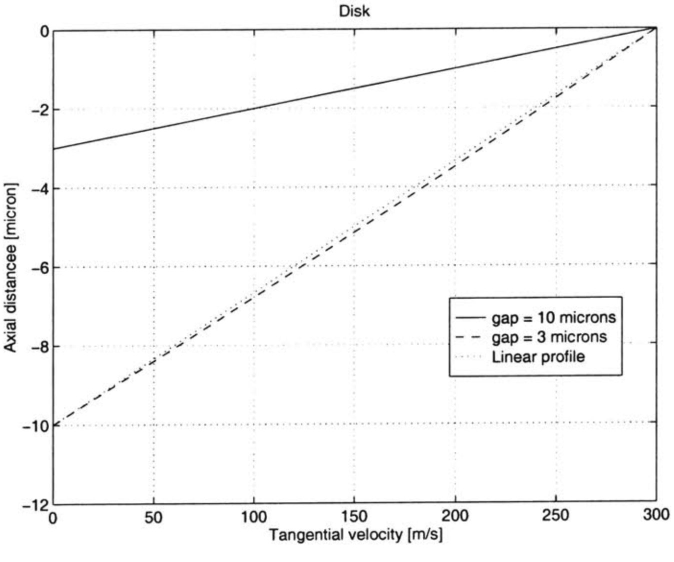

Figure A-3: Tangential velocity at mid-radius across $3\mu m$ and $10\mu m$ gaps. Larger gap shows a slight decrease in shear stress on the disk which is due to the Coriolis force (dotted line is a linear velocity profile).

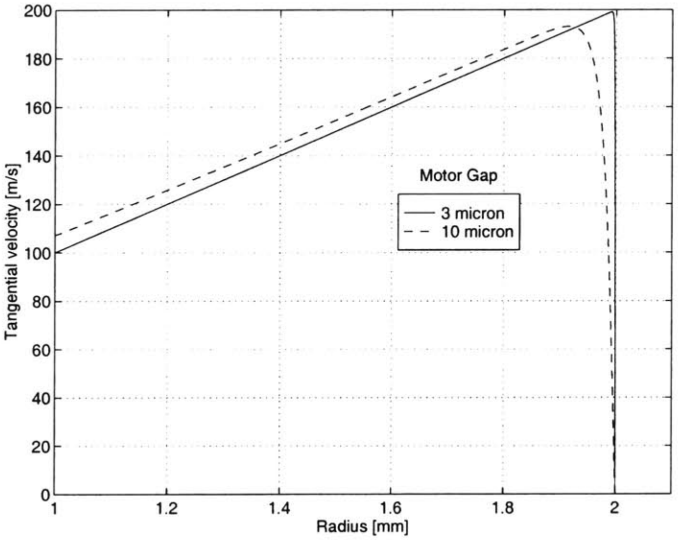

Figure A-4: Tangential velocity versus radius at mid-gap, for motor gaps of $3\mu m$ and $10\mu m$. Entrance length for the nominal motor-compressor configuration ($3\mu m$) is negligible. (Results from 2-D axisymmetric calculations with $V_\theta = 0$ at the inlet - $r = 2mm$).

A.2 Grooved stator motor gap flow

One feature to reduce the drag on the disk consists of locally increasing the motor gap wherever possible. Given the requirement for the stator electrodes to remain near the rotor, all other area under the disk other than electrodes can be recessed. In particular, the radial strips between each electrode can be etched, creating 300-500 thin radial trenches on the stator surface. This section first summarizes the flow features of a grooved motor gap, based on a nominal geometry. Then, a parametric method for predicting the drag given any geometry is presented. Such a prediction tool is useful to assess design trade-offs between electric power and viscous drag while designing the motor-compressor.

A.2.1 Geometry

A cross section (normal to the radial direction) of the motor gap region is shown in Figure A-5, labeled with the main geometric parameters describing the geometry at a given radius: the motor gap height (g_m), the electrode and trench widths (w_e and w_t respectively) and the trench depth (h_t).

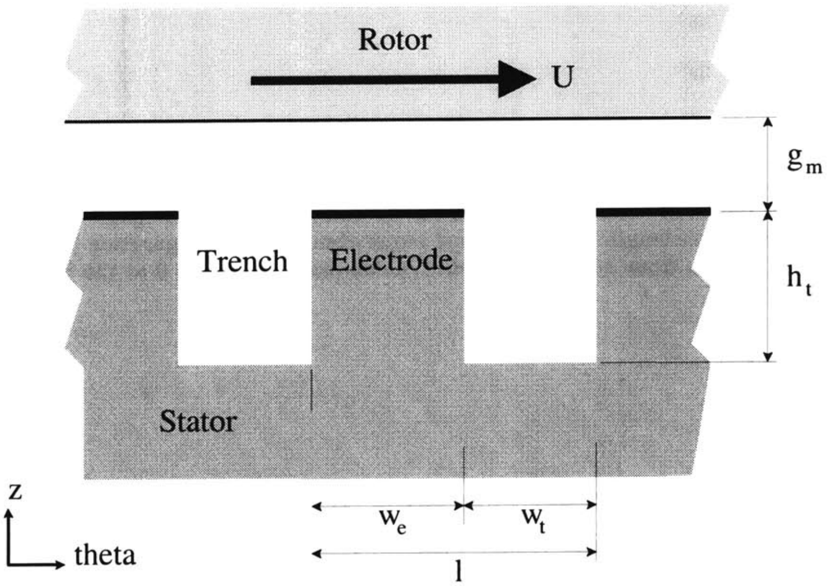

Figure A-5: Cross-section of the motor gap and the stator electrodes (view is normal to the radial direction)

Instead of directly using the widths w_e and w_t, it is convenient to use the width of an electrode-trench pair ($l = w_e + w_t$) and the following ratio, referred to as the duty-cycle

(dc):

$$dc = \frac{w_e}{w_e + w_t} = \frac{w_e}{l}$$

The duty-cycle will tend to 100% as the electrodes are wider and the trenches are narrower.

A.2.2 Grooved stator flow features

A 3-D numerical solution of the motor gap flow for the nominal motor-compressor parameters was first calculated to identify the physical features. The computational domain consisted of the fluid gap between the spinning disk and the stator, extending circumferentially over one electrode-trench pair (with periodic boundary conditions in the tangential direction) and extending radially from the motor inner to outer radius (with a pressure of 2 atm. at the outer radius and 1 atm. at the inner radius).

Figure A-6 shows the velocity vectors in a cross section of the motor gap for a nominal trench geometry ($dc = 50\%$, $h_t = 20\mu m$, $l = 20\mu m$, $\Omega r = 300 m/s$). The resulting flow field is characterized by a Couette-type flow in the gap region and a vortex in the trench.

The drag mechanism of high shear at the disk surface remains present, although slightly modified, as shown by the tangential velocity profiles in Figure A-7. Each curve corresponds to a different circumferential location, identified by vertical lines in the right view of Figure A-6. The disk is located at $z = 0$, the electrode surface, at $z = -3\mu m$, and the bottom of the trench, at $z = -20\mu m$. The point to notice is the uniformity of the slope of tangential velocity at the disk, over the electrode as well as over the trench. The desired reduction in drag is therefore not expected to be noticeable. Once again we can assume that the radial flow does not affect the tangential velocity profile near the disk when the Coriolis and centrifugal forces are negligible in the gap region. To confirm this, tangential velocity profile from the 3-D calculation are compared to those from a 2-D calculation in Figure A-7. The 2-D calculation is obtained for the flow in a cross section at mid-radius (as illustrated in Figure A-5). The profiles are shown to be almost identical, confirming the assumption that the effects of rotation are negligible for the grooved stator nominal configuration of the motor-compressor.

The flow in the trench is characterized by a radial vortex aligned along the trench and positioned near the gap region (top of the trench). Figure A-8 illustrates this by tracking fluid particles seeded across the gap and trench. The vortex is shown by swirling particles in the top region of the trench. Radial through-flow near the bottom of the trench is illustrated by the lower particle paths.

Radial velocities in the trench (not shown here) form profiles similar to Poiseuille flow in a rectangular pipe (once developed).

A.2.3 Drag prediction with a grooved stator

The complex 3-D problem can be simplified for means of drag prediction while designing the motor-compressor system. The total torque on the disk can be determined by numerically integrating the torque for annular slices of width dr. The drag per unit radius, $f = \frac{force}{dr}$, can be determined by calculating the 2-D flow in many cross sections as shown in Figure A-5 but with the parameters depending on the radial location of the cross section. In this approach, the rotation and entrance effects are neglected. Empirical corrections could however be applied.

To be useful for design, the drag per unit radius will be expressed as a function of the minimal non-dimensional numbers. The dependence of drag on these non-dimensional numbers will then be determined computationally by varying the numbers in the expected ranges, creating an table for drag per unit radius for the various configurations.

Non-dimensionalization

The drag in a 2-D cross section of the grooved stator motor gap depends on the following 7 independent parameters, which have units formed by 3 fundamental dimensions: mass (M), length (L) and time (T):

The dependent variable, drag per unit radius (f), can be expressed generally as a nonlinear function of the 7 independent variables:

$$f = \Psi(g_m, l, h_t, dc, U, \mu, \rho) \tag{A.15}$$

Parameter		Dimensions
Gap height,	g_m	L
Electrode+trench width,	l	L
Trench depth,	h_t	L
Duty-cycle,	dc	-
Velocity of the disk,	$U = \Omega r$	L/T
Viscosity coefficient,	μ	M/LT
Density,	ρ	M/L^3

Table A.3: Independent parameters .

Based on the Buckingham-Π theorem, we can reduce the number of independent variables by the number of fundamental dimensions. In this case, we can reduce the number of independent variables from 7 to 4. The dimensionally independent subset of the independent variables is chosen as $\{g_m, U, \mu\}$. The drag per unit radius (f) and the 4 remaining independent variables can be defined in dimensionless form as:

$$f^* = \frac{f}{\mu U} \tag{A.16}$$

$$l^* = \frac{l}{g_m} = \frac{w_e + w_t}{g_m} \tag{A.17}$$

$$h^* = \frac{h}{g_m} \tag{A.18}$$

$$dc = \frac{w_e}{w_e + w_t} \quad \text{(already non-dimensional)} \tag{A.19}$$

$$\rho^* = \frac{\rho U g_m}{\mu} = Re_g \tag{A.20}$$

The functionality is therefore reduced to:

$$f^* = \Psi^*(l^*, h_t^*, dc, Re_g) \tag{A.21}$$

Non-dimensionalized solution for the smooth stator It is informative to apply this non-dimensionalization to the motor gap flow with a *smooth stator*. Without the trenches, the drag per unit radius is only a function of 4 independent variables: g_m, l, U, μ. The analytical dependence of drag per unit radius is given by Eqn A.1 for τ_θ, multiplied by the length l:

$$f_{smooth} = \mu \frac{U}{g_m} l = \Psi_{smooth}(g_m, l, U, \mu) \tag{A.22}$$

which is written in non-dimensional from by dividing both sides by μU and noting that $l^* = l/g_m$:

$$\tag{A.23}$$

$$f^*_{smooth} = l^* = \Psi^*_{smooth}(l^*) \tag{A.24}$$

We notice that the Reynolds number, Re_g, is not a parameter in the Couette flow solution since density (representing inertial forces) does not affect the drag. Therefore, the Reynolds number mainly characterizes the trench flow (i.e. the vortex) as opposed to the flow in the gap region. The ratio of viscous to inertial forces will however determine the entrance lengths in the gap region for both the smooth or grooved stators.

Numerical results

The drag on the disk for the grooved stator configuration was calculated over a test matrix with 27 components formed by varying each of the 3 geometric non-dimensional number (l^*, h^*_t, and dc) over 3 values in their expected range. For this initial data set, the Reynolds number was kept constant to a nominal value of 55:

$$Re_{g,nom} = \frac{\rho U g_m}{\mu} = \frac{1.225 kg/m^3 \times 300 m/s \times 3 \mu m}{2.2 \times 10^{-5} kg/ms} = 55 \tag{A.25}$$

since the effect of Reynolds number is proposed to be of second order. Future work should extend the test matrix to include the dependence on Reynolds number.

The calculated drag for the grooved stator configuration (f^*) is best expressed as a drag reduction coefficient (C_d) applied to the drag for the smooth stator configuration (f^*_{smooth}, given by Eqn A.24):

$$f^* = (1 - C_d) f^*_{smooth} \tag{A.26}$$

$$C_d = 1 - \frac{f^*}{f^*_{smooth}} = 1 - \frac{f^*}{l^*} \tag{A.27}$$

The computational results for f^* as a function of l^*, h_t^*, and dc are shown in Figures A-9, A-10, and A-11. First and foremost, we notice that the maximum drag reduction levels below 30% for low duty-cycles, deep trenches and wide electrodes (and trenches). *This drag reduction approach is therefore limited.* The following paragraphs comment on the trends of drag reduction with respect to the 3 geometric parameters.

Duty-cycle, dc We notice from Figure A-9, that the drag reduction is larger at low duty-cycle (wide trenches compared to electrodes), which is intuitively expected since more disk area is at a larger gap when the duty-cycle is lowered. Also, the drag reduction is approximately linear with duty-cycle. We must also note that the drag reduction tends to zero for a duty-cycle of 90%. Very thin trenches compared to the electrodes are therefore not useful.

Trench depth, h_t^* The drag reduction as a function of trench depth (shown in Figure A-10) increases rapidly at shallow depths but asymptotes as the trenches are deeper. Although more calculations at low h_t^* are needed to better define maximum useful depth, it can be approximated as 1 to 3 gap heights, depending intuitively on the aspect ratio of the trench (w_t/h_t).

Sector length, l^* The effect of increasing the electrode+trench length as shown in Figure A-11 appears to increase drag reduction, approximately following a linear trend.

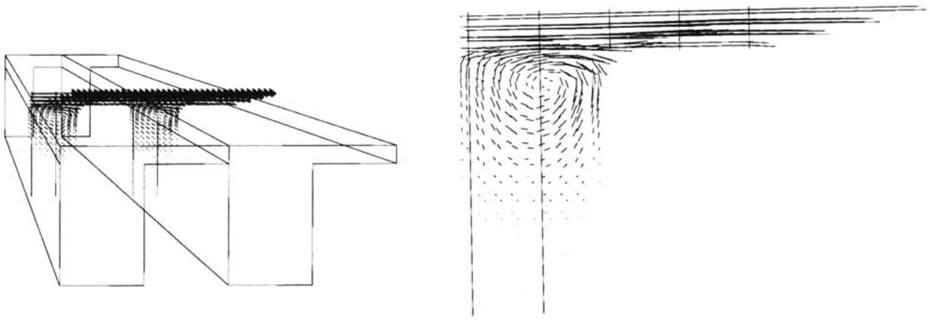

Figure A-6: Velocity vectors in a cross section of the motor gap for a nominal trench geometry ($dc = 50\%$, $h_t = 20\mu m$, $l = 20\mu m$, $\Omega r = 300m/s$). The left view shows two trenches and electrodes directed radially out of the page. The top surface is the rotating disk.

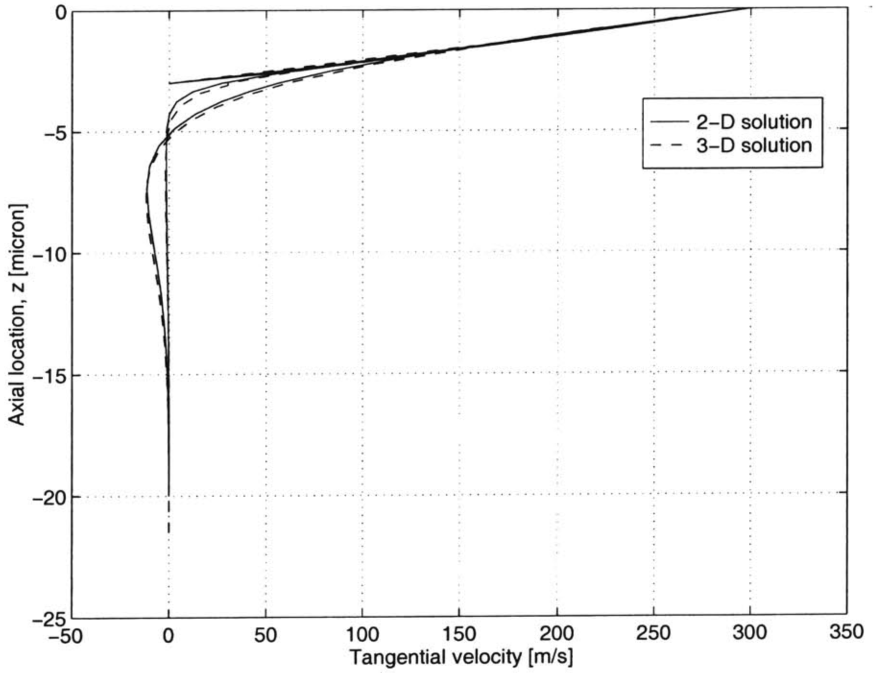

Figure A-7: Tangential velocity profiles from 3-D and 2-D calculations, showing that the 2-D solution predicts well the shear stress. Curves correspond to different circumferential location identified by the vertical lines in the cross section of Figure A-6

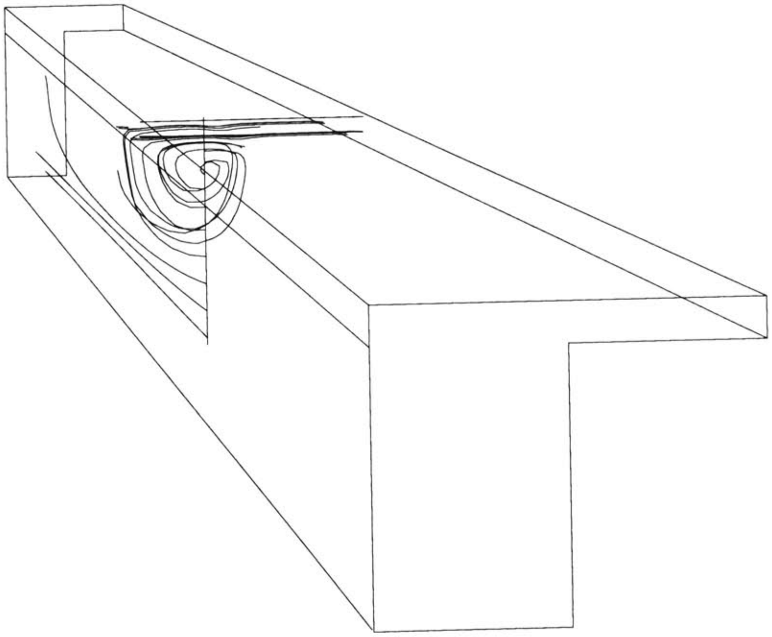

Figure A-8: Particle traces showing the vortex on the top region of the trench and the through-flow at the bottom of the trench.

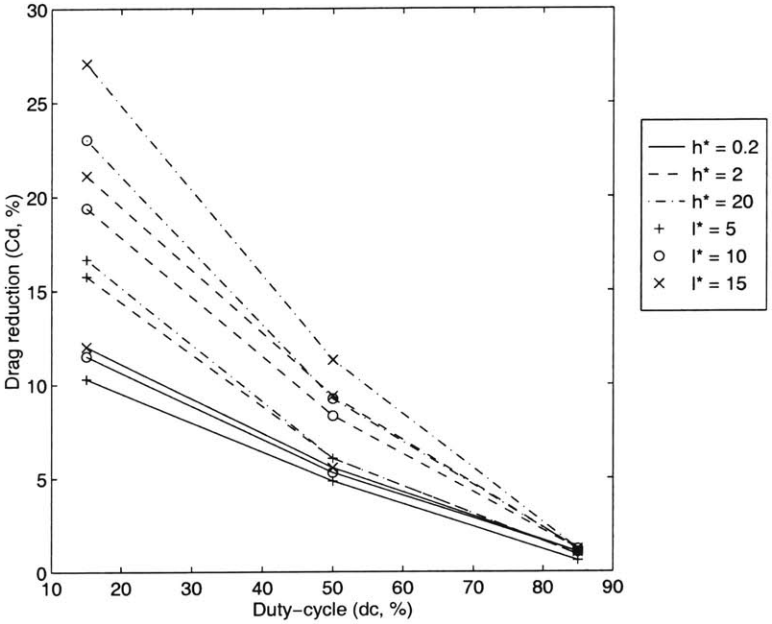

Figure A-9: Drag reduction coefficient as a function of duty-cycle (100% duty-cycle corresponds to the smooth stator).

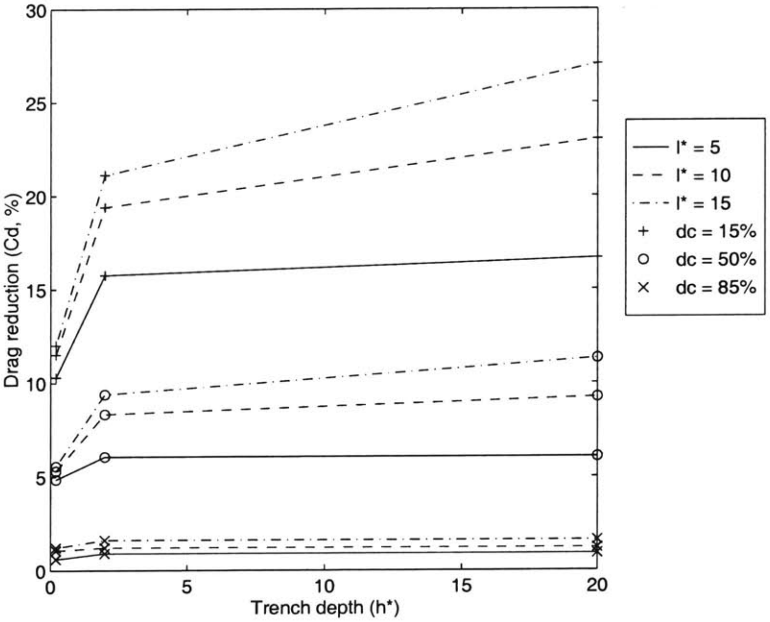

Figure A-10: Drag reduction coefficient as a function of non-dimensional trench depth ($h_t^* = h_t/g_m$).

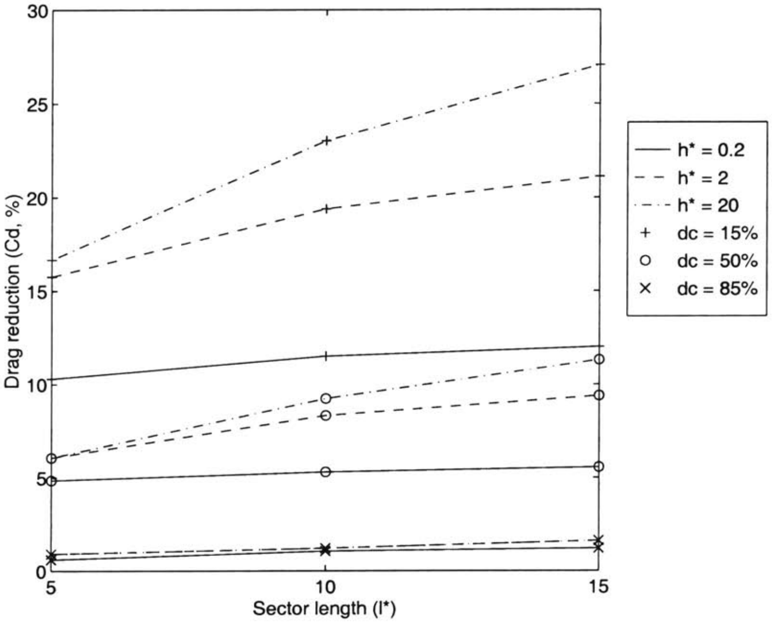

Figure A-11: Drag reduction coefficient as a function of non-dimensional sector length of an electrode+trench pair ($l^* = (w_e + w_t)/g_m$).

A.3 Conclusion

Overall, drag in this motor gap is mainly dominated by the Couette flow established between the stationary electrodes and the rotating disk. Locally increasing the gap between the electrodes, such to produce a radially grooved stator, does not dramatically decrease the drag. The constraint of small gaps imposed by the motor electrical design combined with the high speeds desired for a high power-density device seem intrinsically detrimental. Various modifications to the simple grooved stator configuration (not presented here) have also been evaluated but without much more drag reduction than the simple grooved stator. Further investigation on these and other possible drag reduction features are however necessary before implementing them in a device. Many other components of the motor-compressor already introduce large uncertainty in successful operation of the device, so extra risk incurred by uncertain motor gap fluid dynamics should be avoided, unless the proposed drag reduction is considerable.

The first version of the motor-compressor will therefore feature radial grooves between the electrodes. The trench geometry will be defined from an overall system design perspective, which considers trade-offs between the motor electrical power and the viscous losses. The modeling approach described in the last section will be used to evaluate the motor gap viscous losses.

APPENDIX B

OVERVIEW OF IC AND MEMS MICROFABRICATION TECHNOLOGY BASE

This appendix provides a quick overview of the basic set of microfabrication techniques borrowed from the IC and MEMS fields to build the MC-Bearing Rig and Motor-Compressor devices. Additional techniques developed specifically for these devices, such as thick insulating layers and deep reactive ion etching of high aspect ratio trenches, as well as rotor release strategies are described in sections 3.4 and 3.5.

B.1 IC processing technology

The set of standard IC fabrication technologies used throughout the motor-compressor fabrication is now briefly described for completeness. Further details can be found in standard textbooks [62, 20].

Photolithography - Transfer of the designed geometry on the wafer in the form of a patterned mask which exposes only regions to be etched :

A photo-sensitive polymer, photoresist, is used to mask certain regions of the wafer, locally protecting the underlying thin films or substrate against the etchant. The thickness is varied depending on the specific etching conditions; thicker photoresist withstand deeper etches, but reduces minimum achievable feature. The photolithography process consists of:

1. Prepare wafer surface
2. Spin coat the photoresist
3. Pre-bake to drive solvents out of the film
4. Expose desired features through a mask
5. Develop the exposed features, photoresist remains where unexposed
6. Post-bake to de-sensitize the photoresist to light and harden the mask

Etching - Removal of material in the exposed areas of the mask :

Chemical etching using a liquid solution (wet) or plasma (dry) isotropically removes material from the exposed surface, resulting in an etched recess larger than the opening in the mask. Anisotropic profiles can be obtained by the bombardment accelerated ion from a plasma, which usually results in a lower selectivity to the masking photoresist.

Polysilicon thin films - Deposition of a thin polycrystalline silicon film and doping to provide the necessary level of electrical conductivity :

Deposition is carried out by chemical vapor deposition in a low pressure ambient (LPCVD), flowing Silane at a temperature of 625°C and a pressure of 200 mbar. Conductivity of the film is enhanced by doping the film with boron or phosphorus either through *diffusion* or *implant*. The implant process consists of bombarding the thin film of ions, driving them into the film, then annealing the wafer to drive-in the dopant and electrically activate it. The polysilicon film can be patterned using photolithography and etching described previously.

Silicon Dioxide films - Deposition of insulating SiO_2 films :

Insulating layers are deposited in a plasma enhanced chemical vapor deposition process, by flowing silane at reduced pressure ambient and a temperature of 400 °C . Hydrogen content in the film is reduced by then annealing the wafer at 1100°C for 1 hour in an atmospheric pressure nitrogen ambient. The final state of the film for these conditions is under compressive stress. The SiO_2 film can then be selectively patterned relatively to silicon.

Chemical-mechanical planarization (CMP) - Removal of surface topology :

The wafer surface can be planarized, reducing the height of protrusions from the average wafer surface. The process consists of rubbing the wafer face down on a polishing pad, which is covered with a chemically activating slurry. A uniform pressure is applied on the wafer, which is transmitted as a contact pressure between the surface to be polished and the pad. Higher local pressure will increase the polishing rate of the protrusions, with respect to the average wafer surface. Similarly, this process also reduces the surface roughness of planar films, which is necessary for adequate bonding. After polishing and adequate cleaning, further thin film processing can proceed.

Wafer dicing - Cutting of the wafer into dies :

After all the fabrication steps at the wafer level have been completed, devices are separated from each other by cutting up the wafer between dies. The wafer, or bonded wafer stack, is temporarily fixed to a thin film of tape and held down on a vacuum chuck. An additional layer of tape is also applied on the front side of a wafer stack in order to prevent debris from entering the device. An array of perpendicular linear cuts are done through the wafer(s), down to the underlying tape, using a circular blade with diamond grit and water as the cutting fluid. The blades used to cut a 5-wafer stack have inner and outer radii of 42mm and 50mm respectively, a thickness from 150μm to 250 μm , and a grit size ranging 2-4μm . The cut wafer is then rinsed with DI water, dried, and the tape peeled off.

B.2 MEMS processing technology

Over the past few decades, the IC microfabrication techniques have been extended and new technologies have emerged to build the structural components of microelectromechanical systems. Two main technologies enable the use of silicon to create three-dimensional microstructures: *deep reactive ion etching (DRIE)* and *Wafer-level bonding.*

Deep reactive ion etching (DRIE) - Anisotropic bulk etching of silicon :

Deep silicon etches or cavities with vertical walls are directly etched into the substrate using the Bosch patented process for DRIE. The process consists of an iterative 2-step etching and passivation cycle. The first step isotropically etches the exposed area using a SF_6 high density plasma. A passivation step then conformally covers the entire wafer surface with a Teflon-type thin film using C_4F_8 chemistry. When the etching cycle resumes, ion bombardment preferentially removes the passivation film from the line-of-sight (i.e. horizontal) surfaces, allowing the unmasked horizontal surface to be once again isotropically etched. This cycle is repeated to create anisotropic geometries. The profile varies to a certain degree between negatively or positively sloped vertical walls (re-entrant cavity or not). Controlling the perpendicularity of the side wall within a few microns over hundreds of microns deep remains a challenge.

Wafer Bonding - Fusion bonding of contacted wafer surfaces :

Wafers can be permanently bonded by bringing the prepared, smooth surfaces in contact and elevate to high temperature to promote molecular diffusion. This creates an irreversible bond between the silicon wafers, which can have a strength up to the level of the bulk material. Previously etched wafers can be bonded to create quasi-three-dimensional geometries, as long as the surface remains clean and smooth to the nanometer level. Micron-level alignment is possible with recent commercial bonding tools. Other type of bonding have also been developed, but are not used in the motor-compressor fabrication.

APPENDIX C

MOTOR-COMPRESSOR AND MC-BEARING RIG PROCESS FLOW

This Appendix complements the process flow presented in the body of this thesis, with more detailled processing information. Recipe names refer to previously developped processes in the Microsystems Technology Laboratories.

Common process steps

Thick Photo (in TRL)	
HMDS	std: 17 min
Coater: adapt spin speed for desired thickness	Resist: AZ4260 Spin: 9s @ 1700, 60s @ [speed], 10s @ 7000 rpm Manual static dispense, finish w/ swab edge wipe
Pre-bake	1 hr @ 90C
Ksaligner2: adapt time according to thickness	power: 6.0
Develop: adapt time according to thickness	AZ440 MIF
Post-bake	1hr @ 110C (small oven)

Thin Photo (in TRL)	
HMDS	std: 17 min
Coater: adapt spin speed for desired thickness	Resist: OCG825 Spin: 6s @ 500, 6s @ 750, 30s @ 2500 rpm (for 1 um) Automatic dynamic dispense, finish w/ swab edge wipe
Pre-bake	0.5 hr @ 90C
Ksaligner2: adapt time according to thickness	power: 6.0, 45 sec for 1 um
Develop: adapt time according to thickness	OGC934, 2-2.5 min for 1 um
Post-bake	0.5 hr @ 120C

Alignment marks	
Thin Photo (or ICL photo)	standard thin photo-resist (1 um)
Etcher-1 or AME or STS	1-2 um deep
Asher or Piranha	

Bond handle wafer	Attach quartz handle wafer prior to postbake
Coater	Resist: AZ4260
Target mount: coat wafer, clear during spin using acetone, leaving a center dot of 1-2 cm in diameter. Then coat 1-2 cm outer rim	Spin: 9s @ 1700, 60s @ [speed], 10s @ 7000 rpm
Contact device wafer to quartz handle wafer (use jig)	
Compress rim area (pressing with a swab on each side)	
Post-bake	same bake step as device resist

Back coat	Protect the backside of wafer with PR during handling

After develop, before post-bake: spin standard thin resist on backside of wafer, using the teflon chuck

Oxide protective coating	
Piranha	ICL
Concept 1	0.1 um thick novellus oxide, unless otherwise noted
Densification (tube B6 in ICL)	1100 C for 1 hr

Steps which are necessary to be included for Motor-Compressor are labeled in the left column:

m	to include the motor (skip these steps for MC-Bearing Rig)	20 extra steps
*	Indicates which must (or should) be included in all variants, but may have different parameters depending on the variant	

Figure C-1: Common process steps

Forward Foundation Plate (A):

Wafer: Silicon <100>, n-type prime, thickness=450 um, double-side polished

Measure wafer bow and thickness	
Alignment marks (front side) - expose all the mask for writing	Mask A0-Marks-1; expose all the mask
Alignment marks (back side)	Mask A0-Marks-1; expose only the alignment marks
Oxide protective coating (front side)	0.1 um (standard)
Deep Si etch through wafer: 450 um (back side)	Mask A1b-Foundation-1 (dark field)
Thick Photo - IR (hide align. marks) + Handle wafer	TRL thick resist: AZ4620 12 um thick
STS	450 um (through wafer), MIT69 (~3:35) + MIT48 for 10 min
Piranha	

Figure C-2: Forward Foundation Plate - Wafer #1

Forward End Plate (B):

Wafer: Silicon <100>, n-type prime, thickness=450 um, double-side polished

Measure wafer bow and thickness

Alignment marks (front side)	Mask A0-Marks-1; expose only the alignment marks
Shallow Si etch for FTB gap: 1.5 um (back side)	Mask B1b-FTB-Gap (dark field)
Thin Photo - IR (expose alignment marks) + coat back	standard thin photo-resist (1 um)
AME5000	"UNDOPED-POLY-ETCH" 1.5 um deep (~175 s, use monitor to set time)
Piranha	ICL strip bath
Shallow Si etch for Tip Clearance : 12.5 um, (back side)	Mask B2b-Tip-clearance (dark field)
Thick Photo (hide alignment marks) + coat back	TRL thick resist: AZ4620 8 um thick
STS	recipe SF6_5 for 6 min (use monitors to set time)
Piranha	ICL
Deep Si etch for collector and FTB plenum: 350 um (front side)	Mask B5-Collector (dark field)
Thick Photo (hide alignment marks) + coat back (protect from residue)	TRL thick resist: AZ4620 10 um thick
STS	350 um deep, MIT59 (~2h40)
Piranha	TRL
Oxide protective coating (front side)	Thicker then standard: 0.5 um to prevent back side pitting
Deep Si etch for FTB orifices: 100 um (back side)	Mask B4b-FTB-orifices (dark field)
Thick Photo (hide alignment marks) + handle wafer	TRL thick resist: AZ4620 6 um thick
STS	100 um deep, MIT59 (~1h45)
Piranha	TRL
BOE to remove the front side oxide	1 min for 1000A

Figure C-3: Forward End Plate - Wafer #2

Rotor Plate (C):

	Wafer: Silicon <100>, n-type prime, thickness=500 um, double-side polished	
	Measure wafer bow and thickness	
*	Shallow Si etch for ATB gap: 2.0 um (1.5 w/o motor) (back side)	Mask C1b-ATB-gap (dark field)
	Thin Photo (expose alignment marks) + coat back	standard thin photo-resist (1 um)
	AME5000	2.0 um, "UNDOPED-POLY-ETCH", (~175s for 1.5 um, use monitor to set time)
	Piranha	ICL
	Alignment marks (front side) - Send to EV in Arizona	Mask A0-Marks-1; expose only the alignment marks
*	Shallow Si etch for pits: 12 um (or 1.5 um w/o motor) (back side)	Mask C2b-Rot-pits (dark field)
	Thick Photo (hide alignment marks) + coat back	TRL thick resist: AZ4620 8 um thick
	STS	12 um deep, SF6_5 for 6 min 15 sec (1.5 um w/o motor, see previous etch)
	Piranha	TRL or ICL
	Oxide protective coating (front side)	
m	Thick oxide deposition for rotor insulator: 10 um (back side), no densification	
	Piranha	ICL
	Concept 1	10 um thick novellus oxide, no densification
m	BOE field oxide down to Silicon (back side)	Mask C4b-Rot-clearox (light field)
	Thick Photo (clear align. mark region)	TRL thick resist: AZ4620 6 um thick
	BOE to Si surface	ICL Doped BOE bath for 50 min
	Piranha	ICL
m	Thin oxide depositions over rotor insulator: 0.5 um (front and back sides)	
	Piranha	ICL
	Concept 1	0.5 um thick novellus oxide
	Oxide protective coating (front side)	1000 A
	Densification (tube B6 in ICL)	recipe 190, 1100 C for 1 hr
m	PolySi deposition and doping for rotor conductor (back side)	
	RCA clean	ICL
	TRL PolySi deposition	40 min at 625C, 0.5 um thick
	Piranha	ICL
	Concept 1	Passivation oxide: 2400 A thick
	Densification (tube B6 in ICL)	rec 295, 30 min, 950C
	Implant	Ion Implant Services, 5e12, 180 keV
	Piranha	TRL or ICL
	Drive-in and anneal (tube B6 in ICL)	rec 195, 25 min, 1000C
	BOE to clear implant shield	Doped BOE bath in ICL for 3 min (clear 2400A)
m	Clear PolySi from front side	
	Thick photo (back side)	no mask
	Etcher-1	rec 12 (SF6), 2 min, rotate, 1 min
	Piranha	ICL
m	Pattern PolySi for rotor film (back side)	Mask C3b- Rot-film (light field)
	Thick Photo (clear align. mark region) + coat back	TRL thick resist: AZ4620 6 um thick
	Etcher-1	rec 12 (SF6), 3 min
	Piranha	TRL
m	Pattern oxide to clear bonding areas (back side)	Mask C5b-Bond-clear (light field)
	Thick Photo (clear align. mark region)	TRL thick resist: AZ4620 8 um thick
	BOE (partial)	ICL Doped BOE bath for 1 min
	Etcher-1 to ensure that polysilicon is completely removed	rec 12 (SF6), 2 min on back side
	BOE to Si surface	ICL Doped BOE bath for 5.5 min
	Piranha	
m	CMP for bonding (to improve contact quality)	
	CMP	1 min
	Piranha	TRL
	RCA clean	TRL
*	Deep Si etch for blades: 200 um (front side)	Mask C6-Blades or C6-Turbine or C6-noBlades (dark field)
	Thick Photo (hide alignment marks)	TRL thick resist: AZ4620 8 um thick
	STS	200 um deep, MIT69 for 90 min + SF6_5 for 1 min
	Piranha	TRL or ICL
	Bond B-C to create rotor combo	
	RCA clean	TRL
	EV aligner/bonder	Aligned fusion bond of B to C, Nitrogen ambiant, 1e-4 Torr
	Anneal in TRL tube B3	1100 C for 1 hr
	Deep Si etch for journal: 300 um (back side)	Mask C7-Journal (dark field)
	Thick Photo (hide alignment marks) + handle wafer and PR ring	TRL thick resist: AZ4620 10 um thick
m	BOE	Clear >0.5 um of field oxide
	STS	300 um deep, through wafer, tailored recipe based on MIT56, reduce pressure
	Piranha	TRL

Figure C-4: Rotor Plate - Wafer #3

Aft End Plate (D) - Recessed Oxide Island Stator

Wafer: Silicon <100>, n-type prime, thickness=450 um, double-side polished

	Alignment marks (front side)		Mask A0-Marks-1; expose only the alignment marks
	Alignment marks (back side)		Mask A0-Marks-1; expose only the alignment marks
	Shallow Si etch for stator pits: 10 um (front side)		Mask D1-Stat-pits (dark field)
		Thick Photo - IR (expose alignment marks) + coat back	TRL thick resist: AZ4620 10 um thick
		STS	rec SF6_5 for 5 min 10 sec
		Piranha	TRL
m	Thick oxide deposition to fill pits (front side), no densification		10 um
		Piranha	ICL
		Concept 1	10 um thick novellus oxide
m	Etch field oxide to Silicon surface (front side)		Mask D2-Stat-Clearox -3 (light field)
		Thick Photo (clear align. mark region) + coat back	TRL thick resist: AZ4620 10 um thick
		BOE	ICL, 33 min, outer oxide rim remains and will be removed later
		Piranha	ICL
		Densification (tube B6 in ICL)	1100 C for 1 hr
		BOE (additional, to recess the electrical area by 2 um)	ICL, 16 min (device area lower than field by 1.9-2.0 um)
m	Thin oxide deposition over oxide islands (front and back sides)		PolySi etch stop
		Piranha	ICL
		Concept 1	1000 A (PolySi etch stop)
		Densification (tube B6 in ICL)	1100 C for 1 hr
m	PolySi 1 deposition and doping for interconnects (front side)		
		RCA clean	TRL
		TRL PolySi	75 min for 1 um
		POCL tube in ICL	Phosphorous doping, Tube A4, rec 304
		BOE to remove native film	ICL doped BOE bath for 3 min
m	Pattern PolySi 1 to form interconnect rings (front side)		Mask D3-Intercon (light field)
		Thin Photo (clear align. mark region) + coat back	ICL thin resist: OGC825-35CS for 2.2 - 2.6 um thick
		Etcher-1 (two step etching: anisotropic, then isotropic)	rec 19, step1 CCl4 for 1 min 20 sec (0.75 um); Step 2 SF6 1 min 30 sec (0.25 um
m	Strip PolySi 1 from back side		
		Etcher-1	rec 12 (SF6 with 02), 4 min
		Piranha	TRL
m	Oxide deposition of inter-level dielectric (front side)		use TEOS for conformality (prevent stringers)
		Piranha	TRL
		Concept 1	1.0 um thick novellus TEOS
		Densification (tube B6 in ICL)	1100 C for 1 hr
m	Pattern isolation TEOS to open vias (front side)		Mask D4-via (dark field)
		Thin Photo (hide alignment marks) + coat back	TRL thin resist: OGC825-35CS for 2.2-2.6 um thick
		AME5000	1 um (until PolySi is reached), rec "Nagle-CHF3"
		Piranha	ICL
m	PolySi 2 deposition and doping for electrodes (front side)		1 um
		RCA clean	TRL
		TRL PolySi	75 min for 1 um
		POCL tube in ICL	Phosphorous doping, Tube A4, rec 304
		BOE to remove native film	ICL doped BOE bath for 3 min
*	Pattern PolySi 2 to form electrodes (front side)		Mask D6-Electrodes (light field) (optional Si etch for bearing rig variant)
		Thin Photo (clear alignment marks) + coat back	TRL thin resist: OGC825-35CS for 2.2-2.6 um thick
		Etcher-1	rec #10, 1 min 40 sec
m	Strip PolySi 2 from back side		OPTIONAL - only if it will help wafer bow, otherwise can strip PolySi 2 later
		Piranha	ICL
		Etcher-1	rec #12, SF6 for 4 min
m	Oxide deposition for protection (back side)		0.9 um
		Piranha	TRL
		Concept 1	0.9 um thick novellus oxide
		Densification (tube B6 in ICL) - can densify after patterning	1100 C for 1 hr
m	CMP oxide for bonding (front and back side)		Reduce surface roughness for bonding
		CMP	manual CMP, applying pressure around periphery
		Piranha	
		RCA clean	
	Deep Si etch for aft piping: 350 um (back side)		Mask D8b-Piping -2 (dark field)
		Thick Photo (hide alignment marks) + coat back	TRL thick resist: AZ4620 10 um thick
		BOE	TRL 10 min
		STS	350 um deep, MIT69 for 2h 30 min
		Piranha	TRL
	Deep Si etch for ATB orifices: 100 um (front side)		Mask D7-ATB-Orifices (dark field)
		Thick Photo (hide alignment marks) + coat back	TRL thick resist: AZ4620 8 um thick
m		BOE to clear oxide	10 min to clear field, 5 min with ultrasound to clear nozzles (> 5 um undercut)
		Attach handle wafer	coat, attach, and bake 30 min at 100C
		STS	100 um deep, MIT59 for 1 h 28 min
		Piranha	TRL
		Asher	TRL

Figure C-5: Aft End Plate (Stator) - Wafer #4

Aft Foundation Plate (E)	
Wafer: Silicon <100>, n-type prime, thickness=450 um, double-side polished	
Alignment marks (both sides recommended, back side necessary)	Mask A0-Marks-1; expose only the alignment marks
oxide protection of back side	
Deep Si etch for holes: 200 um (back side)	Mask E2b-Foundation (dark field)
Thick Photo (hide alignment marks)	TRL thick resist: AZ4620 10 um thick
STS	200 um deep, MIT59 (~1h30)
Piranha	TRL
Deep Si etch for aft piping: 250 um	Mask E1-Piping (dark field)
Thick Photo - (hide alignment marks)	TRL thick resist: AZ4620 10 um thick
STS	250 um deep, MIT59 (~2h00)
Piranha	TRL

Figure C-6: Aft Foundation Plate - Wafer #5

Device assembly and completion	
Bond entire stack in one process: MC-Bearing Rigs	
Asher in TRL	To completely clear photoresist from small features
Piranha	TRL
RCA clean	TRL
EV aligner, silicon-direct-bonding	Contact A-BC by inserting A first. Don t remove from aligner
EV aligner, silicon-direct-bonding	Contact ABC-D by resending ABC back in, then inserting D
EV aligner, silicon-direct-bonding	Contact ABCD-E by resending ABCE back in, then inserting E
EV Bonder (this step was not done on first 2 MCBR builds)	Bond stack with "minustwo" recipe, to improve contact
Inspect alignment visually before anneal	Speed sensor contacts, inlet tabs,
Anneal in TRL tube A2	1100 C for 1 hr
Bond stack in two steps (Motor-Compressor)	
Asher in TRL	To completely clear photoresist from small features
Piranha	TRL
RCA clean	TRL
EV aligner, silicon-direct-bonding	Contact A-BC by inserting A first
EV Bonder	Bond stack with "minustwo" recipe, to improve contact
EV aligner, silicon-direct-bonding	Contact D-E
EV Bonder	Bond stack with "minustwo" recipe, to improve contact
Anneal in TRL tube A2	1100 C for 1 hr, ABC and DE
EV aligner, silicon-direct-bonding	Contact ABC-DE
EV Bonder	Bond stack with "minustwo" recipe, to improve contact
Anneal in TRL tube A2	1100 C for 1 hr
Separate dies	
Die saw	
Rotor release	
Snap-off tabs	After flow characterization

Figure C-7: Device assembly and final processing

APPENDIX D

PACKAGING DRAWINGS

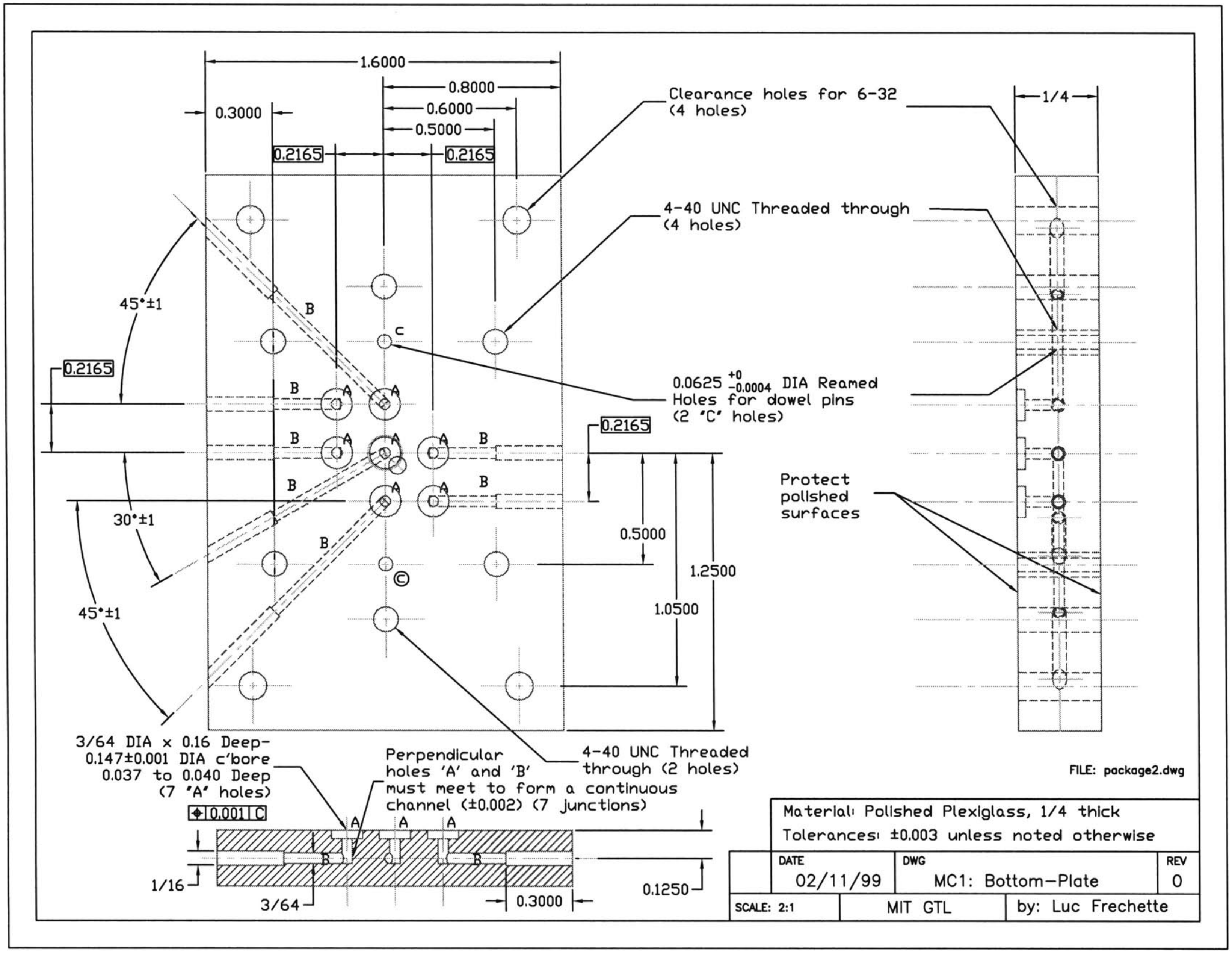

Figure D-1: Technical drawings of the MC-Bearing rig and Motor-Compressor package - Bottom plate

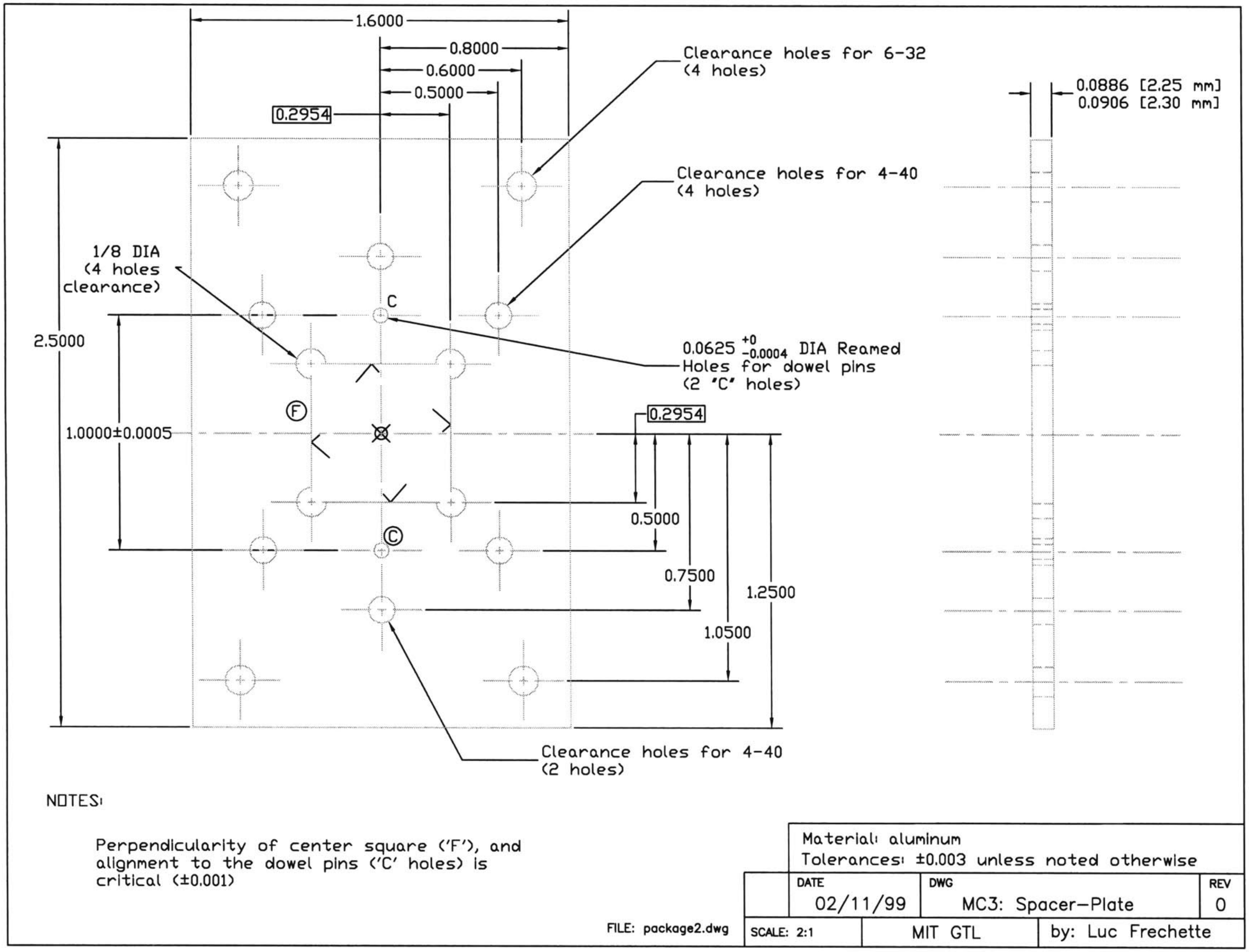

Figure D-2: Technical drawings of the MC-Bearing rig and Motor-Compressor package - Spacer plate

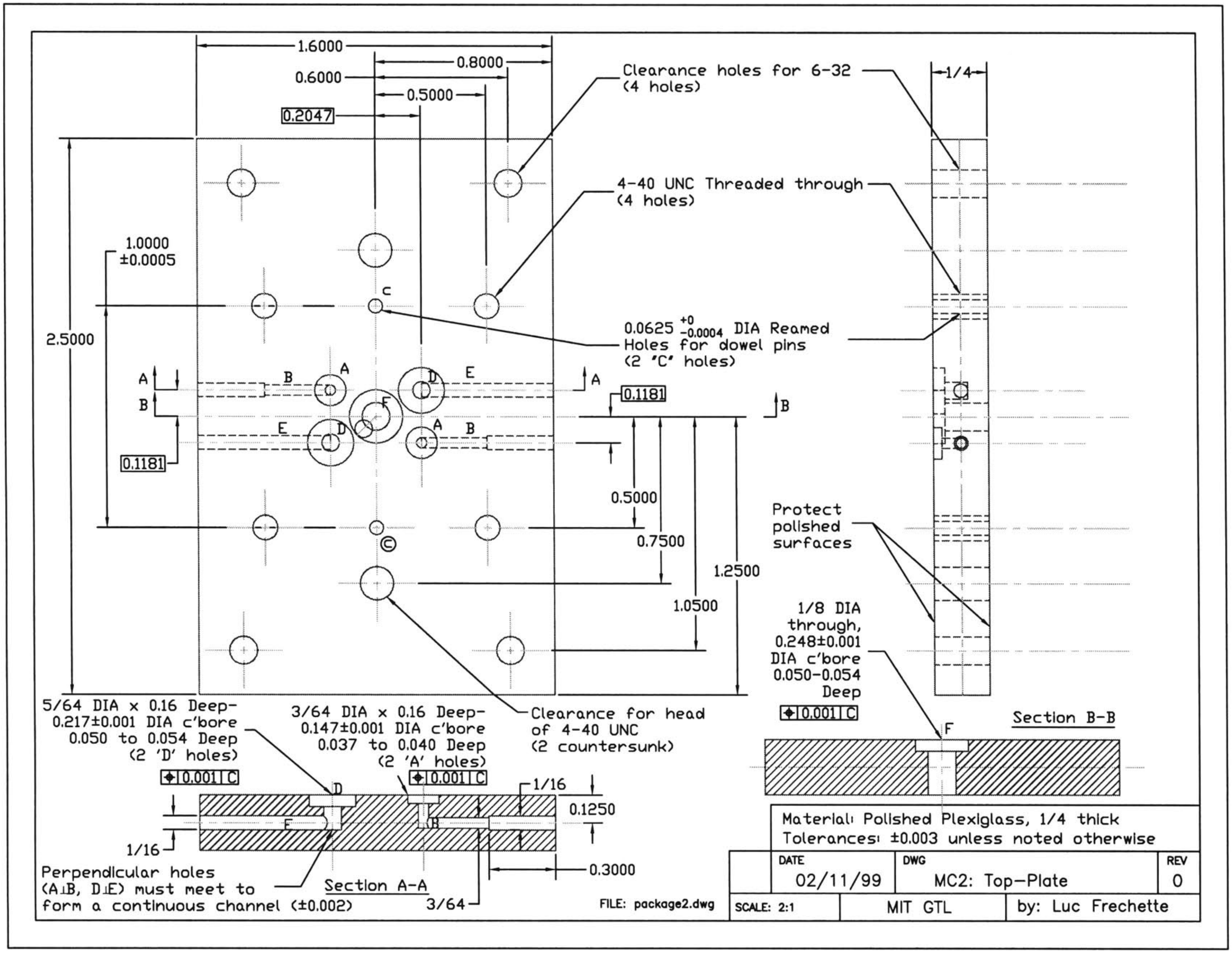

Figure D-3: Technical drawings of the MC-Bearing rig and Motor-Compressor package - Top plate

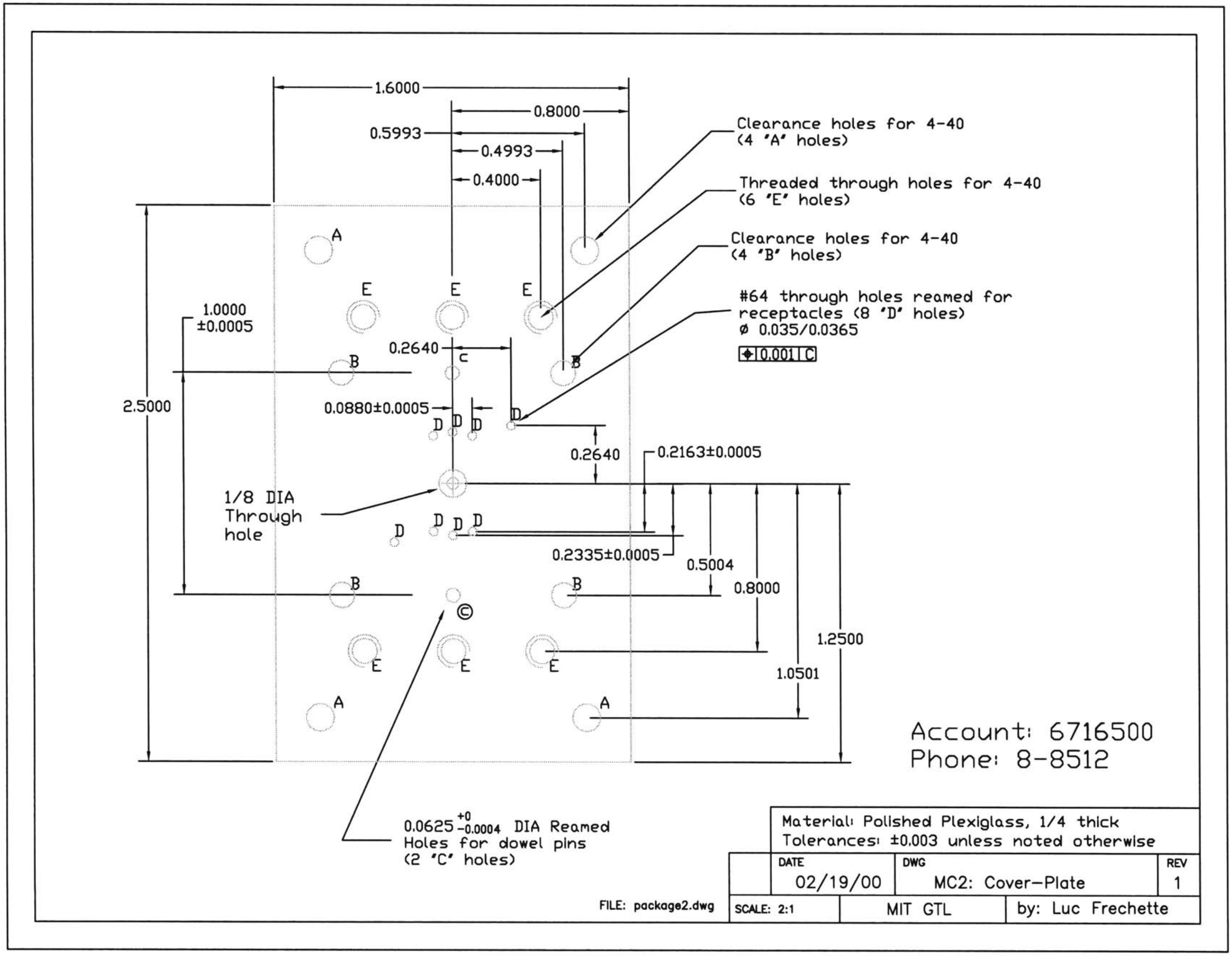

Figure D-4: Technical drawings of the MC-Bearing rig and Motor-Compressor package - Electrical cover plate

BIBLIOGRAPHY

[1] AHN, C., AND ALLEN, M. "Fluid micropumps Based on Rotary Magnetic Actuators". IEEE MEMS Conference Proceedings, 1995.

[2] AYÓN, A. A. personnal communication, unpublished work.

[3] AYÓN, A. A., BRAFF, R., LIN, C. C., SAWIN, H. H., AND SCHMIDT, M. A. "Characterization of a Time Multiplexed Inductively Coupled Plasma Etcher". *Journal of the Electrochemical Society, Vol. 146*, No. 1 (January 1999), pp. 339–349.

[4] AYÓN, A. A., ZHANG, X., AND KHANNA, R. "Ultra Deep Anisotropic Silicon Trenches Using Deep Reactive Ion Etching (DRIE)". Poster presented at the Solid-State Sensor and Actuator Workshop, Hilton Head Is. SC, June 2000.

[5] BART, S. F., AND LANG, J. H. "An analysis of electroquasistatic induction micromotors". *Sensors and Actuators, Vol. 20* (November 1989), pp. 97–106.

[6] BARTH, P., BEATTY, C., FIELD, L., BAKER, J., AND GORDON, G. "A Robust Normally-Closed Silicon Microvalve". Solid-State Sensor and Actuator Workshop Proceedings, 1994.

[7] CHEN, K.-S. *Materials Characterization and Structural Design of Ceramic Micro Turbomachinery.* PhD thesis, Massachusetts Institute of Technology, February 1999.

[8] CREARE. Inc. PO Box 71, Etna Rd, Hanover, NH 03755 U.S.A.

[9] DRELA, M., AND YOUNGREN, H. "A User's Guide to MISES 2.1". Tech. rep., Massachusetts Institute of Technology, June 1995.

[10] EPSTEIN, A., SENTURIA, S., AL-MIDANI, O., ANATHASURESH, G., AYON, A., BREUER, K., CHEN, K.-S., EHRICH, F., ESTEVE, E., FRÉCHETTE, L., GAUBA, G., GHODSSI, R., GROSHENRY, C., JACOBSON, S., KERREBROCK, J., LANG, J., LIN, C.-C., LONDON, A., LOPATA, J., MEHRA, A., MIRANDA, J. M., NAGLE, S., ORR, D., PIEKOS, E., SCHMIDT, M., SHIRLEY, G., SPEARING, S., TAN, C., TZENG, Y.-S., AND WAITZ, I. "Micro-Heat Engines, Gas Turbines, and Rocket Engines - The MIT Microengine Project". presented at the 28th AIAA Fluid Dynamics Conference and the 4th AIAA Shear Flow Control Conference, Snowmass Village, CO No. 97-1773 (June 1997).

[11] EPSTEIN, A. H. "Micro-Gas Turbine Generators". ARO / DARPA Annual Progress Report, 1997.

[12] EPSTEIN, A. H., JACOBSON, S. A., PROTZ, J. M., L, LIVERMORE, C., AND SCHMIDT, M. A. "Shirtbutton-Sized Micromachined Gas Turbine Generators". presented at the 39^{th} Power Sources Conference, Cherry Hill, NJ (June 2000).

[13] EPSTEIN, A. H., AND SENTURIA, S. D. "Macro Power from Micro Machinery". *Science, Vol. 276* (May 23, 1997).

[14] ESASHI, M., SHOJI, S., AND NAKANO, A. "Normally Closed Microvalve and Micropump Fabricated on a Silicon Wafer". *Sensors and Actuators, Vol. 20* (1989), pp. 163–169.

[15] FAN, L. S., TAI, Y. C., AND MULLER, R. S. "IC-processed electrostatic micromotors". Proceedings from the IEEE International Electron Devices Meeting, IEEE Electron Devices Society, San Francisco, CA, December 11-14 1988.

[16] FEYNMAN, R. P. "There's Plenty of Room at the Bottom". *Journal of Microelectromechanical Systems, Vol. 1*, No. 1 (March 1992), pp. 60–66.

[17] FLUENT. Inc., 10 Cavendish Court, Centerra Park Lebanon, New Hampshire 03766, U.S.A.

[18] FRANCIS, R. J. "A Systems Study of Very Small Launch Vehicles". Master's thesis, Massachusetts Institute of Technology, September 1999.

[19] Fréchette, L. G., Jacobson, S. A., Breuer, K. S., Ehrich, F. F., Ghodssi, R., Khanna, R., Wong, C. W., Zhang, X., Schmidt, M. A., and Epstein, A. H. "Demonstration of a Microfabricated High-Speed Turbine Supported on Gas Bearings". Proceedings of the Solid-State Sensor and Actuator Workshop, Hilton Head Is. SC, June 4-8 2000.

[20] Ghandhi, S. K. *VLSI Fabrication Principles*, 2 ed. Wiley, 1994.

[21] Ghodssi, R., Fréchette, L. G., Nagle, S. F., Zhang, X., Ayón, A. A., Senturia, S. D., and Schmidt, M. A. "Thick Buried Oxide in Silicon (TBOS): An Integrated Fabrication Technology for Multi-Stack Wafer-Bonded MEMS Processes". presented at Transducers '99, Sendai, Japan, June 1999.

[22] Gong, Y. personal communication, unpublished work.

[23] Huang, J.-B., Mao, P.-S., Tong, Q.-Y., and Zhang, R.-Q. "Study on Si electrostatic and electroquasistatic micromotors". *Sensors and Actuators A, Vol. 35* (1993), pp. 171–174.

[24] Jacobson, S. A. personal communication, unpublished work.

[25] Jacobson, S. A. "Aerothermal Challenges in the design of a Microfabricated Gas Turbine Engine". presented at the 29th AIAA Fluid Dynamics Conference, Albuquerque, June 1998.

[26] Kerrebrock, J. L. *Aircraft Engines and Gas Turbines*, 2nd ed. The MIT Press, Cambridge, Massachusetts, 1992.

[27] Khanna, R. personal communication, unpublished work.

[28] Li, H. Q., Roberts, D. C., Steyn, J. L., Turner, K. T., Carretero, J. A., Yaglioglu, O., Su, Y. H., Saggere, L., Mlcak, R., Breuer, K. S., Hagood, N. W., Spearing, S. M., and Schmidt, M. A. "A High Frequency High Flow Rate Piezoelectrically Driven MEMS Micropump". Proceedings of the Solid-State Sensor and Actuator Workshop, Hilton Head Is. SC, June 4-8 2000.

[29] Lin, C. C. *Development of a Microfabricated Turbine-Driven Air Bearing Rig.* PhD thesis, Massachusetts Institute of Technology, June 1999.

[30] LIN, C. C., GHODSSI, R., AYÓN, A. A., CHEN, D. Z., JACOBSON, S. A., BREUER, K. S., EPSTEIN, A. H., AND SCHMIDT, M. A. "Fabrication and Characterization of a Micro Turbine/Bearing Rig". presented at the 13th IEEE International Micro Electro Mechanical Systems Conference, January 1999.

[31] LIN, C. C., GHODSSI, R., AYÓN, A. A., CHEN, D. Z., AND SCHMIDT, M. A. "Fabrication and Characterization of a Turbine/Bearing Rig". Late News Poster presented at the Solid-State Sensor and Actuator Workshop, Hilton Head Is. SC, June 1998.

[32] LONDON, A. P. *Development and Test of a Microfabricated Bipropellant Rocket Engine.* PhD thesis, Massachusetts Institute of Technology, June 2000.

[33] MEHRA, A. "Computational Investigation and Design of Low Reynolds Number Micro-Turbomachinery". Master's thesis, Massachusetts Institute of Technology, June 1997.

[34] MEHREGANY, M., NAGARKAR, P., SENTURIA, S. D., AND LANG, J. H. "Operation of microfabricated harmonic and ordinary side-drive motors". Proceedings from the IEEE Workshop on Micro Electro Mechanical Systems, Napa Valley, CA, February 12-14 1990.

[35] MTI. (Mechanical Technology Incorporated), Latham, New York, U.S.A.

[36] MUNTZ, E., SHIFLETT, G., ERWIN, D., AND KUNC, J. "Transient Energy-Release Pressure-Driven Microdevices". *Journal of Microelectromechanical Systems* (September 1992).

[37] NAGLE, S. F. *Analysis, Design, and Fabrication of an Electric Induction Micromotor for a Micro Gas-Turbine Generator.* PhD thesis, Massachusetts Institute of Technology, (to be submitted, 2000).

[38] NAGLE, S. F., AND LANG, J. H. "A Micro-Scale Electric-Induction Machine for a Micro Gas Turbine Generator". presented at the 27th Annual Meeting of the Electrostatics Society of America, June 1999.

[39] NOVELLUS. Systems Inc., 81 Vista Montana, San Jose, CA 95134.

[40] Olson, A., Enosksson, P., Stemme, G., and Stemme, E. "Micromachined flat-walled valveless diffuser pumps". *Journal of Microelectromechanical Systems, Vol. 6*, No. 2 (June 1997), pp. 161–166.

[41] Orr, D. J. *Macro-scale Investigation of High Speed Gas Bearings for MEMS Devices.* PhD thesis, Massachusetts Institute of Technology, February 2000.

[42] Petersen, K. E. "Silicon as a Mechanical Material". *Proc. IEEE, Vol. 70*, No. 5 (1982), pp. 420–457.

[43] Philtec. Inc. Anapolis, Maryland, U.S.A.

[44] Piekos, E. S. *Numerical Simulation of Gas-Lubricated Journal Bearings for Microfabricated Machines.* PhD thesis, Massachusetts Institute of Technology, February 2000.

[45] Piekos, E. S., Orr, D. J., Jacobson, S. A., Ehrich, F. F., and Breuer, K. S. "Design and Analysis of Microfabricated High speed Gas Journal Bearings". presented at the 28th AIAA Fluid Dynamics Conference, Snowmass Village, CO, Paper No. 97-1966 (June 1997).

[46] Protz, C. S. "Systems Analysis of a Microfabricated Storable Bipropellant Rocket Engine". Master's thesis, Massachusetts Institute of Technology, February 2000.

[47] Reid, R. P., Mamin, J., and Rugar, D. "Air-Bearing Sliders and Plane-Plane-Concave Tips for Atomic Force Microscope Cantilevers". *Journal of Microelectromechanical Systems, Vol. 9*, No. 1 (March 2000), pp. 52–57.

[48] Richter, A., and Sandmaier, H. "An Electrohydrodynamic Micropump". IEEE MEMS Conference Proceedings, 1990.

[49] RMB. Roulements Miniatures SA, Eckweg 8, CH-2500 Biel/Bienne 6, Switzerland.

[50] Savoulides, N. "Low Order Models for Hybrid Gas Bearings". Master's thesis, Massachusetts Institute of Technology, February 2000.

[51] Shirley, G. "An Experimental Investigation of a Low Reynolds Number, High Mach Number Centrifugal Compressor". Master's thesis, Massachusetts Institute of Technology, September 1998.

[52] SMITS, J. "Piezoelectric Micropump with Three Microalves Working Peristaltically". *Journal of Sensors and Actuators* (1990).

[53] SNIEGOWSKI, J. J., AND GARCIA, E. J. "Surface-Micromachined Gear Trains Driven by an On-Chip Electrostatic Microengine". *IEEE Electron Device Letters, Vol. 17*, No. 7 (July 1996), pp. 366–368.

[54] STEMME, E., AND STEMME, G. "A Valve-less Diffuser Nozzle based Fluid Pump". Sensors and Actuators, 1993.

[55] SYSTEM. Planning Corporation, MEMS 1999 - Emerging Applications and Markets, 1000 Wilson Boulevard, Arlington, Virginia 22209-2211, 1999.

[56] TENCOR. Inc., User Manual to Tencor FLX-2320, 2400 Charleston Road, Mountain View, CA 94043.

[57] TIMKEN. 1835 Dueber Ave. SW, P.O. Box 6932, Canton, Ohio 44706-0932, U.S.A.

[58] VEPREK-HEIJMAN, M. G. J., AND BOUTARD, D. "The Hydrogen Content and Properties of SiO2 Films Deposited from Tetraethoxysilane at 27 MHz in Various Gas Mixtures". *J. Electrochem Soc., Vol. 138*, No. 7 (1991), pp. 2042–2046.

[59] VON ENGEL, A. *Ionized Gases.* Oxford University Press, Oxford, England, 1965, p. 195.

[60] WEGENG, R. S., CALL, C. J., AND DROST, M. K. "Chemical System Miniaturization". Presented at the 1996 Spring National Meeting of the American Institute of Chemical Engineers, New Orleans, LA, February 25-29 1996.

[61] WIEGELE, T. G. "Micro-Turbo-Generator Design and Fabrication: A Preliminary Study".

[62] WOLF, S., AND TAUBER, R. N. *Silicon Processing for the VLSI Era*, vol. 1 - Process Technology. Lattice Press, 1986.

[63] WOODSON, H., AND MELCHER, J. *Electromechanical Dynamics - Part I: Discrete Systems.* Robert E. Krieger Publishing Company, Inc., Malabar, Florida, 1968.

[64] Zbedlick, M., Anderson, R., Jankowski, J., Kline-Schoder, B., Christel, L., Miles, R., and Weber, W. "Thermopneumatically Actuated Microvalves and Integrated Electro-Fluidic Circuits". Solid-State Sensor and Actuator Workshop Proceedings, 1994.

[65] Zhang, X., Chen, R. G. K.-S., Ayón, A. A., and Spearing, S. M. "Residual Stress Characterization of Thick PECVD TEOS film for Power MEMS Applications". Poster presented at the Solid-State Sensor and Actuator Workshop, Hilton Head Is. SC, June 2000.